TUM School of Engineering and Design
Technische Universität München

Hybridizable Discontinuous Galerkin Methods for time-domain electromagnetic diffusion in conductive media

Luca Berardocco

Vollständiger Abdruck der von der TUM School of Engineering and Design der Technischen Universität München zur Erlangung des akademischen Grades eines

Doktors der Ingenieurwissenschaften (Dr.-Ing.)

genehmigten Dissertation.

Vorsitzender:
    Prof. Dr.-Ing. Wolfgang A. Wall

Prüfende der Dissertation:
    1. Prof. Phaedon-Stelios Koutsourelakis, Ph.D.
    2. Prof. Dr. Martin Kronbichler,
       Uppsala University

Die Dissertation wurde am 10.06.2021 bei der Technischen Universität München eingereicht und durch die Fakultät für Machinenwesen am 28.09.2021 angenommen.

"O frati," dissi, "che per cento milia
perigli siete giunti a l'occidente,
a questa tanto picciola vigilia

d'i nostri sensi ch'è del rimanente
non vogliate negar l'esperïenza,
di retro al sol, del mondo sanza gente.

Considerate la vostra semenza:
fatti non foste a viver come bruti,
ma per seguir virtute e canoscenza"

Inferno, XXVI, 112-120

Abstract

The simulation of electromagnetic phenomena in geophysical applications has benefited from the continued evolution of computers and numerical methods. However, despite the great success that high-order methods experienced in other engineering fields over the last decades, their application in the field of geophysics remains largely unexplored.

It is the goal of this thesis to lay the groundwork for the application of high-order methods in the numerical investigation of electromagnetics in geophysical applications. The focus is on the spatial discretization of Maxwell's equations by means of the Hybridizable Discontinuous Galerkin (HDG) method.

In the first part of the thesis, an HDG method based on a mixed-equation formulation, for the solution of electromagnetic wave propagation problems in dielectric and conductive media, is proposed. Perfect Electric Conductor (PEC) boundary conditions and Absorbing Boundary Conditions (ABC) are developed and implemented to allow the simulation of wave and diffusion phenomena. The spatial and temporal convergence properties of the proposed method are assessed and the problem of electromagnetic diffusion in a unit cube containing a current source is used as a validation scenario. The method is then tested with a benchmark problem for wave propagation and scattering by a dielectric obstacle. Finally, the problem of scattering by means of a conductive sphere is solved.

In the second part, an HDG method for the solution of electromagnetic diffusion phenomena is proposed. This novel method is based on the electromagnetic diffusion equation and is obtained neglecting the displacement current term with respect to the conduction current term in the full-wave equation. Additionally, an HDG method for the solution of the direct current resistivity problem is proposed. This method can be used to obtain the initial condition for the electromagnetic diffusion initial value problem. To improve the efficiency of the novel method, the properties of the linear system of equations are investigated. The proposed formulation is modified such that the condition number of the linear system's matrix improves in the range of parameters typically found in geophysical applications. Finally, the method is shown to achieve optimal convergence rates of the primary variables and an improved convergence rate of the post-processed variable.

Next, a real-world application scenario, for which an analytical solution is available, is used to validate the proposed method. The scenario models a controlled-source electromagnetic survey in which the transient response of the electromagnetic field to a submerged current source is measured by surface receivers.

Finally, the method is used to simulate the transmission of an electromagnetic signal in an example of a Measure-While-Drilling application. In this model, an arbitrarily oriented current source is buried in a conductive stratum and the effects of different simulation parameters on the received signal are explored.

Zusammenfassung

Die Simulation elektromagnetischer Phänomene in geophysikalischen Anwendungen profitiert von der kontinuierlichen Weiterentwicklung von Computern und numerischen Methoden. Trotz des großen Interesses, das Methoden höherer Ordnung in den vergangenen Jahrzehnten in anderen Bereichen erfahren haben, bleibt ihre Anwendung im Bereich der Geophysik weitestgehend unerforscht.

Ziel dieser Arbeit ist die Entwicklung von Methoden höherer Ordnung zur numerischen Untersuchung elektromagnetischer Fragestellungen in der angewandten Geophysik. Dabei liegt der Schwerpunkt auf der räumlichen Diskretisierung der Maxwell-Gleichungen mit Hilfe der Hybridizable Discontinuous Galerkin (HDG) Methode.

Im ersten Teil der Arbeit wird eine HDG-Methode zur Lösung elektromagnetischer Wellenausbreitung in dielektrischen und leitenden Medien präsentiert. Die Methode basiert auf einer Mixed-Equation-Formulierung. Um die Simulation von Wellen- und Diffusionsphänomenen zu ermöglichen, werden sowohl Perfect Electric Conductor (PEC) Randbedingungen als auch Absorbing Boundary Conditions (ABC) entwickelt und implementiert. Räumliche und zeitliche Konvergenzeigenschaften der präsentierten Methode werden anaylsiert. Als Validierungsszenario wird die elektromagnetische Diffusion in einem Einheitswürfel mit Stromquelle verwendet. Danach wird die Methode mit einem Benchmark-Problem für Wellenausbreitung und Streuung an einem dielektrischen Hindernis getestet. Abschließend wird die Streuung an einer leitenden Kugel untersucht.

Im zweiten Teil der Arbeit wird eine HDG-Methode zur Lösung von elektromagnetischen Diffusionsproblemen präsentiert. Diese neuartige Methode basiert auf der elektromagnetischen Diffusionsgleichung und wird unter Vernachlässigung des Verschiebungsstroms in der full-wave Gleichung hergeleitet. Zusätzlich wird eine HDG-Methode zur Lösung des Gleichstrom-Widerstandsproblems vorgestellt. Die Lösung dieses Problems dient als Anfangsbedingung des elektromagnetische Diffusions-Anfangswertproblems. Um die Effizienz der neuen Methode zu verbessern, werden die Eigenschaften des linearen Gleichungssystems untersucht. Daraufhin wird die Formulierung so angepasst, dass sich die Konditionszahl der Matrix des linearen Gleichungssystems im Bereich von, für geophysikalische Anwendungen, typischen Parameterwerten verbessert. Schließlich wird gezeigt, dass sowohl die zu erwartenden optimalen Konvergenzraten der Primärvariablen als auch eine verbesserte Konvergenzrate der nachbearbeitet Variable erreicht werden.

Anschließend wird ein reales Anwendungsszenario, für das eine analytische Lösung verfügbar ist, zur Validierung der vorgeschlagenen Methode verwendet. Das Szenario modelliert eine elektromagnetische Vermessung mit gesteuerter Quelle, bei der die transiente Reaktion des elektromagnetischen Feldes auf eine versunkene Stromquelle mittels Oberflächenempfängern gemessenen wird.

Zusammenfassung

Abschließend wird die Methode zur Simulation der Übertragung eines elektromagnetischen Signals in einer Bohrlochvermessung verwendet. In diesem Modell wird eine beliebig orientierte Stromquelle in einer leitenden Schicht vergraben und die Auswirkung verschiedener Simulationsparameter auf das empfangene Signal wird untersucht.

Contents

Glossary and symbols

Acronyms

HDG$_\mathbf{H}$	High quality HDG mesh
HDG$_\mathbf{L}$	Low quality HDG mesh
ABC	Absorbing boundary conditions
AMG	Algebraic MultiGrid
BC	Boundary Conditions
BDF	Backward differentiation formula
CG	Continuous Galerkin
CGS	Conjugate Gradient Solver
CSEM	Controlled source electromagnetics
DC	Direct current
DFT	Discrete Fourier Transform
DG	Discontinuous Galerkin
DOFs	Degrees of Freedom
EM	Electromagnetic
EMD	Electromagnetic diffusion
FD	Finite Differences
FEM	Finite Element Method
FFT	Fast Fourier Transform
HDG	Hybridizable Discontinuous Galerkin
HSM	Homogeneous seabed model
IE	Integral Equation
IMEX	Implicit-Explicit schemes
LoTEM	Long-offset transient electromagnetics
MoM	Method of Moments
MRI	Magnetic Resonance Imaging
MWD	Measure-While-Drilling
ODE	Ordinary differential equation
PDE	Partial differential equation
PEC	Perfect Electric Conductor
PMC	Perfect Magnetic Conductor
PML	Perfectly Matched Layer
SI	*Système international d'unités* International system of units

Variables

B	Magnetic flux density or magnetic induction field

Glossary and symbols

D   Electric displacement field
E   Electric field
$\hat{\mathbf{E}}$ Electric field's trace value
H   Magnetic field
$\hat{\mathbf{H}}$ Magnetic field's trace value
Λ   Hybrid variable
ϕ Electric potential
$\hat{\phi}$ Electric potential's trace value
u   Auxiliary variable
$\hat{\mathbf{u}}$ Auxiliary variable's trace value

Source terms

$\partial_t \mathbf{i}_\mathrm{s}$ Electric current density source time derivative
$\mathbf{i}_\mathrm{s}$ Electric current density source
$\mathbf{I}_s$ Total electric current source
$\mathbf{i}$ Electric current density

Electromagnetic properties

ρ_c Electric charge density
$\boldsymbol{\varepsilon}$ Electric permittivity tensor
ε Electric permittivity
ε_s Electric permittivity of the scatter
ε_0 Electric permittivity of vacuum
$\boldsymbol{\mu}$ Magnetic permeability tensor
μ Magnetic permeability
μ_s Magnetic permeability of the scatterer
μ_0 Magnetic permeability of vacuum
σ Electric conductivity
σ_a Air electric conductivity
σ_s Scatterer/soil electric conductivity
σ_w Water electric conductivity

Wave properties

ω Angular frequency
c Speed of light
c_0 Speed of light in vacuum
f Linear frequency
T Oscillation period
λ Wavelength
k   Wave vector

Lens properties

f_L Focal length

n Refractive index

Function spaces and sets

$H^{\mathrm{curl}}(\Omega)$ Space of square integrable functions with bounded curl over the domain Ω

$H^{\mathrm{div}}(\Omega)$ Space of square integrable functions with bounded divergence over the domain Ω

$L^2(\Omega)$ Space of square integrable functions over the domain Ω

$\mathcal{P}_m(\Omega)$ Space of polynomials of degree of at most m on Ω

$\mathcal{P}_m^d(\Omega)$ Space of polynomials of degree of at most m on Ω in d dimensions.

$\mathbb{R}^d$ Space of real numbers in d-dimensions

Mathematical operators

i Immaginary unit

$\delta(\cdot)$ Dirac delta function

$(\cdot)^{\mathrm{h}}$ Discrete quantity

$\nabla \cdot (\cdot)$ Divergence operator

$\partial_t(\cdot)$ Time derivative

$\nabla(\cdot)$ Gradient operator

$\|\cdot\|_{H^{\mathrm{curl}}}$ H^{curl}-norm

$\|\cdot\|_{H^{\mathrm{div}}}$ H^{div}-norm

$[\![\cdot]\!]$ Jump operator

$\Delta(\cdot)$ Laplacian operator

$\|\cdot\|$ L^2-norm

$\overline{(\cdot)}$ Maximum value over time

$\mathbf{n}$ Surface unit normal vector

$\nabla \times (\cdot)$ Rotor operator

$\langle \cdot, \cdot \rangle_{\partial\Omega}$ Surface integral over the boundary of the volume Ω

$\mathbf{t}$ Surface tangential vector

$(\cdot)^T$ Transpose operator

$\hat{(\cdot)}$ Trace value

$(\cdot, \cdot)_{\Omega}$ Volume integral over the volume Ω

Numerics parameters

k Polynomial approximation order

h Characteristic element size

τ Stabilization parameter

Δt Time-step size

1 Introduction

Electromagnetic (EM) phenomena permeate all aspects of our lives. Literally. We could, as a matter of fact, consider life in our planet as a direct consequence of the presence of the EM radiation. It is in fact believed that, a key ingredient in the origin of life on Earth was the presence of an energetic radiation, such as ultraviolet light, to form radicals in the primitive atmosphere [1, 2]. Again, the EM radiation plays a role in the evolution of species as it can cause random variations in the genetic code of an organism, modifying the new generations of such organism [3]. We, together with most of the complex life forms in this planet, breathe the oxygen that is produced by the plants surrounding us, harvesting energy from the EM radiation.

Nonetheless, despite the important role these phenomena play in the everyday life and the fact that electric and magnetic effects were already known to the ancient Greeks, it was only in the late eighteenth century that quantitative research in electricity and magnetism began [4, 5]. An interesting overview of the history of research on the topic can be found in [4]. Then, in the course of a century, with the contributions from scientists of the kind of Cavendish, Coulomb, Faraday and Maxwell, our knowledge of the topic deepened, opening limitless technological opportunities.

Nowadays, the application spectrum of EM phenomena is vast and covers most, if not all, engineering fields. Probably, the most known applications of electromagnetism are in the energy sector, in which electric power is generated, distributed and utilized, informatics, where information is generated and processed and, finally, in the telecommunication sector, where EM signals are used to transmit information. Additionally, EM phenomena are used in imaging and remote sensing in a range of applications such as medicine [6–8] and geophysics [9–12].

Regardless of the application field, EM phenomena can be accurately modelled by the equations of *classical electrodynamics*[1] [5, 13], a set of Partial Differential Equation (PDE)s, used to quantitatively describe and predict such phenomena. However, given the complexity of most of the engineering problems, it is often prohibitive to tackle the problem of finding solutions analytically. In these instances it is then necessary to introduce the field of *computational electromagnetics* that is concerned with the research of accurate and efficient ways to solve EM problems numerically.

This work aims to provide novel, efficient methods for the numerical solution of electromagnetic problems arising from real-world engineering problems.

---

[1]With the exception of quantum processes.

1.1 Computational electromagnetics

Before the advent of computers, the solution to the equations modelling electromagnetism could only be obtained analytically or empirically. Although analytical, closed-form, solutions are preferable with respect to approximate computer solution, analytical solutions can usually only be obtained for simple configurations or approximate set of equations, therefore reducing their range of application in engineering fields. Successively, with the evolution of performances, and increased availability, of computer systems coupled with advances in numerical analysis, the need to manipulate solutions and simplify the model equations, to reduce the computational cost, diminished, see, e.g. [14, 15]. The increased computational power finally allowed the numerical solution of the equations modelling electromagnetic phenomena.

A solution method of great importance in the field of computational electromagnetics is the Method of Moments (MoM), in which the original functional equation is transformed in a matrix equation that can be solved by a computer by means of linear solvers. The solution of the MoM converges to the exact solution when the expansion function forms a complete set of basis function [14]. However, the details of the solution via MoM vary greatly from problem to problem [15] and, furthermore, the matrices obtained by the method are usually full [16], making the solution of these linear systems computationally more expensive than those obtained by other methods.

An efficient solution method for the time-dependent Maxwell equations is by means of Finite Differences (FD), first introduced by Yee [17]. In this method, the approximated values of electric and magnetic fields, are computed in the nodes of staggered computational grids. Finite differences can be used to solve problems in the time-domain as well as in the frequency-domain, where it is assumed that the electromagnetic fields are harmonic in time. The choice of a time-domain rather than a frequency-domain approach mostly depends on the field of application and on the research interest, see e.g. [18–23]. A disadvantage of the finite difference approach is given by the structured nature of the computational grid required to compute the solution. While such grids efficiently discretize regular domains, they fall short when employed in the discretization of irregularly shaped domains or domains containing geometrical entities with characteristic sizes that span different order of magnitude. In fact, while it is possible to discretize complex geometries [24–26] and make use of mesh adaptivity [27–29], this typically leads to more complex discretizations or inhomogeneous accuracy of the solution.

The successful application of the Finite Element Method (FEM) in computational electromagnetics was only possible more recently thanks to the seminal work of Nédélec [30,31], where a new family of mixed finite element has been developed and investigated. These elements, often called edge elements, can be used in presence of geometrical complexities of the domain or discontinuous electrical properties that can cause discontinuities in the EM fields. In fact, when these features are present in the domain, the discretization of the domain with nodal elements can lead to spurious solutions [32–34]. However, using edge elements does not ensure a correct solution of the Maxwell system by itself if the formulation is not properly chosen. Additionally, edge elements generate more unknowns with respect to nodal elements on the same mesh, for the same accuracy [33,35]. A few

examples of the application of the finite element methods in the field of computational electromagnetics can be found in [34, 36–39].

A different approach to the solution of PDEs by means of the FEM method, is provided by the introduction of Discontinuous Galerkin (DG) methods, see, e.g. [40, 41]. In the DG method the continuity requirement on the inter-element boundary is relaxed and jumps in the values of the unknowns are allowed. The coupling between elements is enforced defining numerical fluxes that relate the values of the unknowns on the different elements. The inter-element continuity is therefore only enforced weakly, providing an intrinsic stabilization of the method, allowing the discretization of discontinuous fields and removing the requirement for additional stabilization techniques. Additionally, DG methods are well suited for higher-order discretizations and polynomial adaptivity thanks to the discontinuous nature of the approximation functions used. These methods have been successfully used in several fields of application as computational fluid mechanics [42–45] and computational electromagnetics [46–51], to cite a few. Despite the advantages of the DG methods, they are usually criticised for the increased number of unknowns introduced by the interface fluxes, making such methods computationally more expensive than standard FEM.

The drawbacks of DG methods are addressed by the so called HDG methods, introduced by Cockburn et al. in [52] and further investigated in [53, 54]. HDG methods are derived from DG methods employing definitions of the numerical fluxes that ensure the numerical traces to be single-valued on the faces of the discretization. Hence, the number of Degrees of Freedom (DOFs) on element interfaces of HDG methods is reduced with respect to the DG methods from which are derived. Moreover, the resulting HDG methods exploit the piecewise continuity of the approximation functions, retaining the advantages of DG methods with respect to the standard FEM. The ability of HDG methods to construct high-order discretizations can be exploited to reduce the number of globally coupled DOFs to the point where the number of unknowns of HDG methods is smaller than that of standard FEM, see e.g. [55, 56]. Moreover, HDG methods have the interesting property to achieve superconvergence via local post-processing techniques, see, e.g. [53, 54, 57–62]. It has been suggested to exploit superconvergence to reduce the order of the polynomial approximation, therefore reducing the DOFs number, without loosing solution accuracy [55, 56] or as an inexpensive a priori error estimator for FEM adaptivity schemes [61].

The HDG method has successfully been applied to the field of computational electromagnetics in a range of applications. Methods for the solution of problems expressed in time-domain and time-harmonic forms have been developed, see e.g. [63–67]. However, to the best of the author's knowledge, high-order HDG methods have not yet been applied in the field of geophysics until the work of the author. In fact, while most of the methods developed are concerned with wave propagation in dielectric media, in [68] the author introduces novel HDG formulations that are well suited for the propagation of electromagnetic waves in both dielectric and conductive media and subsequently, in [69], the author further investigates one of the formulations previously introduced in its applications to the field of electromagnetic propagation in underground strata formations.

1.2 Geophysical applications of computational electromagnetics

One of the interests of geophysicists is to explore and discover underground geological formations for both research purposes and commercial exploitation. As it is not always possible, or economically viable, to physically explore the crust by coring or by directly accessing the formations, other exploration means have been developed such as seismic tomography [70–72], Controlled Source Electromagnetics (CSEM) [11,73,74], magnetotelluric methods [12,75–78] and others, each of which has a different field of application. For an overview of time-domain EM methods of explorations see, e.g. [79] and, more specifically, for an overview of CSEM surveys, see e.g. [11].

In its geophysical applications, one of the main topic of computational electromagnetics is the development of efficient EM diffusion solvers that can either be used directly to experimental data or to solve inverse problems, see e.g. [21, 80–84]. Inverse problems are used to compute the electrical properties of the formations that produced the given experimental data. The electrical properties can be used to reconstruct the distribution of different media, such as metals, natural gas and oil reservoirs, in the crust.

In the past, the results of in situ surveys were interpreted with the help of analytical solutions [85–87] and lookup tables [88]. The analytical solutions of EM transient problems are typically expressed in the form of Integral Equations (IEs), see e.g. [82,89–93]. Within the IE framework, the Maxwell equations are written in integral form and simplified, where possible, with considerations that are specific for the problem at hand. The equations arising from such treatment are usually not in closed form as, integrating the known quantities in complex geometries, is non-trivial. In fact, closed solutions to the Maxwell equations can usually only be found in cases where the domains are regular and/or have some symmetry that can be exploited to simplify the problem. Therefore, to obtain a solution in complex domains, the integrals have to be solved numerically.

The numerical solution to this problem can be obtained via the MoM, in which the domains are discretized in several smaller domains. In these subdomains the unknowns of the IE are discretized with basis functions and tested by testing functions obtaining a set of linear equations that can be written in matrix form and solved by a computer [14,15,82,89]. However, both the IE and the MoM have limitations that can reduce their range of applicability to simpler problems. For example, the derivation of IE solutions for very complex problems can require considerable effort and, in some cases, prove unworthy. The MoM, on the other hand, can become computationally very expensive as the discretization matrices are usually large and full [82,94].

The need to simulate more complex geometries moved the focus of many researchers to the field of FD in which, instead of deriving an integral equation to describe the problem at hand, the Maxwell equations are discretized directly in each point of the numerical domain. FD discretizations of large domains result, just as in the solution of IEs via the MoM, in large linear systems of equations. However, because of the local nature of FD stencils, the discretization matrices obtained with the FD method are typically sparse and well suited for the solution by efficient linear solvers, therefore improving the overall efficiency of these methods.

It is worth to point out that it is possible to make assumptions based on the problem at hand also when using FD methods, hence allowing the development of different formulations, each with different pros and cons. In fact, similarly to the IE approach, it is possible to derive FD formulations for stationary field solutions [95–98], time-domain solutions, obtaining the so called FDTD methods, [20,21,99] and in the frequency-domain [83,100–102]. Moreover, if necessary, it is possible to obtain a time-dependent solution from a solution in the frequency-domain, and vice-versa, applying a direct or inverse Fourier transform. Furthermore, it is possible to obtain stationary solutions by means of FDTD methods by integrating over long time. However, this approach can lead to poor results in the static limit and particular precautions have to be implemented, such as including divergence conditions on the fields [99].

Unfortunately, even though FD methods allow to represent structures that would otherwise be prohibitively expensive by means of IE methods, they still fall short in the discretization of large, complex, domains. In fact, the structured meshes required by FD methods can include a considerably higher number of cells than an unstructured mesh, for the discretization of the same domain.

The solution to this problem was finally brought by the development of finite element formulations for EM prospecting [103,104]. Even though this method was computationally more expensive for the computers available at the time [97,104], the possibility to discretize geometrically complex geometries and include anisotropic and heterogeneous electrical parameters rendered this approach very attractive. The possibility to use unstructured meshes greatly helps improve the discretization in the vicinity of sources, receivers or areas in which a greater accuracy is needed. Additionally, the ability to selectively refine the element size in certain areas allows the mesh size to grow in areas where such additional accuracy is not needed. Indeed, the possibility to coarsen the mesh can also be used to increase the dissipation introduced by the discretization in the vicinity of the boundaries of the domain, in order to reduce unwanted reflections and reducing the need of more complex mixed Boundary Conditions (BC) [84,96,105–107]. Different finite element formulations were developed, each with a different application in mind as stationary resistivity modelling [84,108–111], finite element time-domain (FETD) methods [105–107] and finite element frequency-domain (FEFD) methods [112–114], to cite a few.

Finally, although high-order methods such as the DG and HDG methods have already been investigated in their applications in the field of computational electromagnetics, to the best of the author's knowledge no such method has been applied to model the electromagnetic phenomena typical of geophysical applications until the author's publications [68,69]. Nevertheless, similarly to the other fields that have greatly benefited by the advantages of these novel methods, the author believes that further investigation of these methods can lead to improved discretization techniques in the field of geophysics.

1.3 Scope and objectives

The vast amount of different modelling techniques such as IE, FD and standard FEM introduced in Section 1.2, developed in the last decades for use in the field of geophysics, starkly contrasts the vacuum of application of high-order DG and HDG methods in the same field. However, given the advantages of high-order methods in terms of accuracy and flexibility, it seems only natural to investigate how such methods apply to the field at hand. It is therefore the goal of this work to lay the groundwork for a thorough investigation of HDG methods and, perhaps, prompt renovated interest in high-order methods from the geophysics community.

The first step in such an endeavour is to develop the mathematical formulations that are best suited for the solution of the Maxwell equations in conductive environments. Fortunately, as a vast literature exists, it is possible to extend the approaches already used in conjunction with other discretization techniques and extend them for use in the HDG framework. To explore all the different approaches would be prohibitive and, therefore, only a few could be explored in this thesis. Mainly, the focus of this work is on the simulation of transient electromagnetic fields with the goal to model electromagnetic signal propagation, hence the time-domain approach is chosen.

An obvious choice in this regard is the development of a HDG mixed-equations formulation in which a solution in terms of both electric and magnetic fields is obtained. In this formulation the Maxwell equations in their complete form are discretized and can, therefore, be applied to a range of different applications, from wave propagation in dielectric media to electromagnetic diffusion in conductive media. The generality of this method is however balanced by the necessity of an initial conditions in terms of both the electric and magnetic fields, potentially reducing its advantages. In fact, if the initial conditions are not trivial, identically zero electric and magnetic fields, the solution of a Direct Current (DC) problem is required to compute the initial electric field and the solution of a magnetostatic problem is required to compute the initial magnetic field. Even though ABCs are not commonly used in the geophysical applications, a set of first-order ABC called Silver–Müller BC is implemented.

The proposed method is thoroughly tested with simple test cases in a unit cube, making use of both structured and unstructured meshes, and with more complex wave propagation and scattering problems. For the latter, an unstructured mesh is used to discretize a domain bounded by ABCs and containing both dielectric and conductive media.

Another common choice for time-domain approaches is the electromagnetic diffusion equation written in terms of the electric field. This equation is derived from the full-wave equation for the electric field in which the displacement current term is dropped. Indeed, in the low-frequency regimes encountered in geophysical applications, the displacement current term can be safely neglected with respect to the conduction current term. While this formulation is more problem-specific with respect to the mixed-equation formulation, it has the advantage of only requiring an initial condition in terms of the electric field, therefore removing the need for a magnetostatic solution. Furthermore, an extensive collection of efficient preconditioners and linear solvers is available for the solution of diffusion problems, possibly providing an edge over the mixed-equation formulation.

In order to compare the solutions obtained by the novel method with those that can be found in the literature, the same test cases have to be simulated. To do so, it is necessary to compute an initial condition in terms of the electric field solving a DC problem. The DC resistivity problem can be solved either by means of a HDG method or by the standard FEM. Even though this feature is an interesting topic itself, only a superficial treatise is given in this work as it unfortunately falls outside the primary scope of this thesis.

The newly developed formulations' convergence properties have to be thoroughly tested with respect to the different type of discretizations, structured and unstructured meshes, and polynomial approximation order. Furthermore, a local post-processing technique is implemented in the most promising of the two formulations, the electromagnetic diffusion equation formulation, to prove the HDG method's superconvergence properties. Additionally, it is an important question to test whether the superconvergence properties can be exploited in real-world application scenarios, where complex unstructured discretizations are needed and the electrical parameters can be highly heterogeneous and can experience stark discontinuities.

Because of the complexity of the scenarios that are encountered in geophysical applications, their numerical discretization is traditionally known to result in ill-conditioned matrices, potentially impairing solution efficiency. To address these issues, the main causes affecting the matrices' condition number are investigated and a "formulation-preconditioning" is proposed.

To validate the proposed formulation, real-world application scenarios are used. A first example is that of a CSEM survey in which the method is used to simulate the transient electromagnetic response to a step-off signal. For the successful solution of this application scenario the different algorithms developed are put to test. In fact, the DC resistivity problem solver is used to compute the initial condition and the formulation-preconditioning is used to improve the condition number of the matrix and increase the performance of linear solvers. This scenario has been thoroughly investigated in the past and, therefore, reference solutions are available and can be used as a comparative metric to measure the accuracy of the proposed method.

Finally, an additional real-world scenario is that of a fracking site in which Measure-While-Drilling (MWD) tools are used to transmit data from the buried drill bit to the surface. The relations between the amplitudes of the signals received by antenna poles, placed on the surface, and the transmitted frequencies or the electrical properties of the transmission media, are investigated.

1.4 Outline

This work is organised following the same rationale followed in the introduction of the scope and objectives Section 1.3.

In Chapter 2 the mathematical foundations on which this work is based are provided. The Maxwell equations are introduced in their general form and the most important properties are provided. Within the chapter, in Section 2.1.2, a short overview of Ohm's law is provided, as this is the starting point for the derivation of DC resistivity problems. Starting from the general form of Maxwell's equations, on which the mixed-equation

formulation is based, the electromagnetic diffusion equation, on which the electromagnetic diffusion equation formulation is based, is derived in Section 2.1.5. In Section 2.2 the main concepts of computational electromagnetics, with a special focus on HDG methods, are presented. An overview of the boundary conditions and time-integration schemes used in this work is also provided.

Chapter 3 provides a thorough derivation of the mixed-equation formulation. The different aspects of the proposed formulation such as time discretization Section 3.1.1 and matrix condensation Section 3.1.2 are discussed. Finally, the spatial and temporal convergence properties of the method are investigated with a range of different tests in Section 3.2.1, Section 3.2.2 and Section 3.2.3.

Chapter 4 is devoted to the application of the proposed mixed-equations formulation to wave propagation and scattering phenomena. Initially, in Section 4.1, the propagation of a plane wave in a homogeneous spherical domain is simulated. Subsequently, the scattering of the same plane wave by means of a spherical scatterer of different materials is simulated. A dielectric scatterer is employed in Section 4.2 whilst a conductive scatterer is used in Section 4.3.

In Chapter 5 the electromagnetic diffusion equation formulation is developed. Again, details on the time discretization, Section 5.1.1, and condensation algorithm, Section 5.1.2, are provided. This formulation is complemented by a local post-processing algorithm, described in Section 5.2. Then, an overview of the DC current problem is provided in Section 5.3 and the HDG method employed to solve it is described in Section 5.3.1. An important addition to the electromagnetic diffusion equation formulation is the algorithm used to reduce the condition number of the discretization matrix, described in Section 5.4. Finally, in Section 5.5, the spatial convergence rates achieved by the proposed electromagnetic diffusion equation formulation are shown.

Chapter 6 addresses the validation of the method by simulating a real-world application scenario that can be found in the literature and for which both an integral equation and a finite element solutions are available. In this test case a large and complex unstructured mesh is employed to discretize a domain with heterogeneous electrical properties. The response of the system, whose initial condition can be obtained by the solution of a DC resistivity problem, to a ramp-off source is investigated. The solution is provided in terms of the transient electromagnetic field at given receivers locations. In Section 6.3 an overview of the validation is provided.

Chapter 7 expands on the applications of the proposed methods in real-world applications with an example of a possible fracking scenario. In this application the interest is on the propagation of a downhole generated signal to the surface. The influence of different parameters is investigated, and the results presented in Section 7.2.

Finally, in Chapter 8, the most important conclusions and achievements of this work are summarized. Moreover, an outlook of interesting additional research topics and approaches is provided.

2 Introduction to classical electrodynamics and computational electromagnetics

The physical phenomena that are studied in this work can be described within the framework of *classical electrodynamics*. Therefore, in this chapter, an introduction to the fundamental notions of this branch of physics is provided. However, while the theory of classical electrodynamics covers many engineering fields, in this thesis, only the main concepts useful for our geophysical applications are treated. Furthermore, it is important to point out that, while in classical electrodynamics there is an extensive literature using Gaussian units, in this work only SI units are used.

It is often difficult, if not impossible, to obtain a closed form solution of the equations of classical electrodynamics for practical engineering problems. In these instances, it is necessary to compute approximate numerical solutions. It is the goal of this thesis to develop novel solutions methods for these problems by means of the hybridizable discontinuous Galerkin method. Consequently, in this chapter, an introduction of the main properties of the HDG method are presented.

The chapter is organised as follows. First, in Section 2.1, the equations of classical electrodynamics are introduced and discussed. In this section, the equations of classical electrodynamics are introduced in their general form. Then, different forms of the equations, more suitable for the description of stationary, wave propagation and electromagnetic diffusion problems, are derived and examined. In Section 2.2, the basic concepts of computational electromagnetics are reviewed. First, the main characteristics of hybridizable discontinuous Galerkin methods are provided. Next, the notation and definitions used throughout this work are introduced. An overview of the main boundary conditions used in the field of computational electromagnetics is then provided. Finally, the time-integration schemes used in this work are presented.

Given the complexity and broad spectrum of Section 2.1 and Section 2.2, a more detailed outline of these sections is provided in the section's introductory paragraphs.

2.1 Classical electrodynamics

The mathematical framework on which classical electrodynamics is based are the *Maxwell equations*, a set of partial differential equations that allow, given an initial state and proper boundary conditions, to determine the state of the electromagnetic field at any point in time and space. In classical electrodynamics the electromagnetic field is generated by the motion of electrical charges. On the electromagnetic field, *electromagnetic waves*

9

propagate at a speed called *speed of light*, that is a property of the material the field permeates. In vacuum, and in most other media, the Maxwell equations are linear, and therefore the *superposition principle* holds. Linearity is an important property for many technological applications of electromagnetic fields.

It is important to distinguish between *lossless* or *dielectric media*, such as vacuum and air, and *lossy* or *conductive media*, such as (saline) water and metals. Lossless media are characterized by low values of electric conductivity and therefore no currents are generated in the presence of an electric field. In the second case, when the medium has higher conductivity values, the electric field generates electric currents in the material. The flow of an electric current in a material dissipates the electric field's energy. It has to be noticed that the two extreme cases of zero conductivity, perfect dielectric, and infinite conductivity, superconductors, are only limit cases and can not, or are extremely hard to, be obtained in realistic applications. The distinction between dielectric and conductive media is important as the range of phenomena observed in the two different media varies. The goal of this work is to develop efficient solvers for the propagation of electromagnetic signals in conductive media and therefore special assumptions are made considering the conductive nature of the materials encountered.

While a thorough discussion of classical electrodynamics can be found in several textbooks, see, e.g. [5], the following sections give an insight of the fundamental concepts that are needed for the development of this work. In Section 2.1.1, the Maxwell equations in their general form are shown. Section 2.1.2 introduces the generalized form of Ohm's law necessary to model the relation between electric fields and currents in conductive materials. Successively, in Section 2.1.3, Ohm's and Maxwell's laws are used to obtain an equation for the description of the so called direct current resistivity problem. In Section 2.1.4 the wave equation for the electric field is shown. Finally, in Section 2.1.5, the full vector wave equation is simplified to obtain a damped vector wave equation, also called electromagnetic diffusion equation.

2.1.1 Maxwell equations

The mathematical model that describes the interaction of the *electric field*, $\mathbf{E}$, and the *magnetic field*, $\mathbf{H}$, in anisotropic, heterogeneous media, is provided by the Maxwell equations

$$\nabla \cdot \mathbf{B} = 0, \tag{2.1a}$$

$$\nabla \cdot \mathbf{D} = \rho_c, \tag{2.1b}$$

$$\partial_t \mathbf{B} + \nabla \times \mathbf{E} = \mathbf{0}, \tag{2.1c}$$

$$\partial_t \mathbf{D} - \nabla \times \mathbf{H} + \mathbf{i} = \mathbf{0}. \tag{2.1d}$$

Equation (2.1a) is called *Gauss' law for magnetism* and states that the divergence of $\mathbf{B}$, called *magnetic flux density* or *magnetic induction field*, is identically zero. This equation is justified by the absence of *magnetic monopoles*. *Gauss' law of electrostatics* (2.1b) relates the divergence of the *electric displacement field*, $\mathbf{D}$, to the electric charge density, ρ_c. *Faraday's law* (2.1c) and *Maxwell-Ampere's law* (2.1d) describe the time evolution of the electric and magnetic fields in the presence of an *electric current density* $\mathbf{i}$.

It can be shown that if the initial condition provided to (2.1c) and (2.1d) satisfies (2.1a) and (2.1b), then, the solution of (2.1c) and (2.1d) satisfies (2.1a) and (2.1b) at any time. We can show that

$$\nabla\cdot\mathbf{B}|_{t=0} = 0 \;\Rightarrow\; \nabla\cdot\mathbf{B} = 0 \quad \forall t, \tag{2.2}$$

taking the divergence of (2.1c)

$$\nabla\cdot(\partial_t\mathbf{B} + \nabla\times\mathbf{E}) = \partial_t(\nabla\cdot\mathbf{B}) = 0, \tag{2.3}$$

that means that the divergence of $\mathbf{B}$ is constant in time. We therefore have (2.2).

To show that

$$\nabla\cdot\mathbf{D}|_{t=0} = \rho_c \;\Rightarrow\; \nabla\cdot\mathbf{D} = \rho_c \quad \forall t, \tag{2.4}$$

we proceed in a similar manner, taking the divergence of (2.1d)

$$\nabla\cdot(\partial_t\mathbf{D} - \nabla\times\mathbf{H} + \mathbf{i}) = 0. \tag{2.5}$$

Substituting the equation of *continuity of charges*

$$\partial_t\rho_c + \nabla\cdot\mathbf{i} = 0, \tag{2.6}$$

in (2.5), we obtain

$$\partial_t(\nabla\cdot\mathbf{D} - \rho_c) = 0. \tag{2.7}$$

Again, being the term $(\nabla\cdot\mathbf{D} - \rho_c)$ constant in time, for the same argument used in (2.3), we have (2.4).

This property has important implications in computational electrodynamics as, usually, (2.1a) and (2.1b) are not directly enforced. Therefore, if the initial condition does not satisfy these constraints, the numerical solution will not be a solution of the Maxwell equations [115]. Nonetheless, because of the finite accuracy of the numerical methods, especially in long-term integration of the equations, it might be necessary to actively enforce the divergence free constraints (2.1a) and (2.1b) by means of divergence-free methods [50] or divergence cleaning techniques, see e.g. [116, 117].

To close the system of equation (2.1), constitutive relations between $\mathbf{E}$ and $\mathbf{D}$ and between $\mathbf{H}$ and $\mathbf{B}$ have to be introduced. If the response of the material to the applied fields is linear, the constitutive relations can be written as

$$\mathbf{D} = \boldsymbol{\varepsilon}\mathbf{E}, \tag{2.8a}$$

$$\mathbf{B} = \boldsymbol{\mu}\mathbf{H}, \tag{2.8b}$$

where $\boldsymbol{\mu}$ is the *magnetic permeability tensor* and $\boldsymbol{\varepsilon}$ is the *electric permittivity tensor*. If the material is isotropic, the tensors $\boldsymbol{\mu}$ and $\boldsymbol{\varepsilon}$ can be substituted by the scalars μ and ε

$$\mathbf{D} = \varepsilon\mathbf{E}, \tag{2.9a}$$

$$\mathbf{B} = \mu\mathbf{H}. \tag{2.9b}$$

For isotropic media, the Maxwell equations can then be written as

$$\nabla \cdot (\mu \mathbf{H}) = 0, \qquad (2.10a)$$

$$\nabla \cdot (\varepsilon \mathbf{E}) = \rho_c, \qquad (2.10b)$$

$$\partial_t \mathbf{H} + \frac{1}{\mu} \nabla \times \mathbf{E} = \mathbf{0}, \qquad (2.10c)$$

$$\varepsilon \partial_t \mathbf{E} - \nabla \times \mathbf{H} + \mathbf{i} = \mathbf{0}. \qquad (2.10d)$$

2.1.1.1 Electromagnetic fields in heterogeneous media

An important aspect of the description of electromagnetic fields in heterogeneous media is the possibilty to have discontinuities in the fields at material interfaces. This feature proved to be the main source of difficulties in the numerical solution of Maxwell equations.

Assume a domain Ω, containing two materials with different electrical permittivities ε_1 and ε_2 and different magnetic permeabilities μ_1 and μ_2, as shown in Figure 2.1.
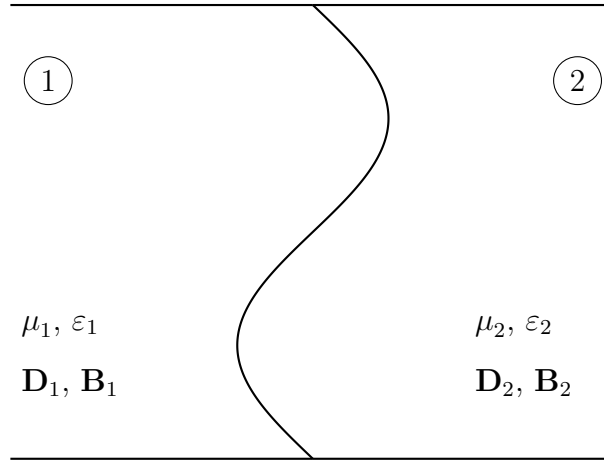

Figure 2.1: Interface between materials with different electrical properties.

In this configuration, the tangential and normal components of the electric and magnetic fields behave differently and can present discontinuities across the material interface.

Tangential components

To investigate the behaviour of the tangential component of the fields in the proximity of the interface we take a section of the domain containing the interface, as shown in Figure 2.2. Integrating the stationary form of (2.10c) and (2.10d) over the encircled area gives

$$\int_\Sigma \nabla \times \mathbf{E} \, \mathrm{d}\Sigma = 0, \qquad (2.11a)$$

$$\int_\Sigma \nabla \times \mathbf{H} \, \mathrm{d}\Sigma = \int_\Sigma \mathbf{i} \, \mathrm{d}\Sigma. \qquad (2.11b)$$
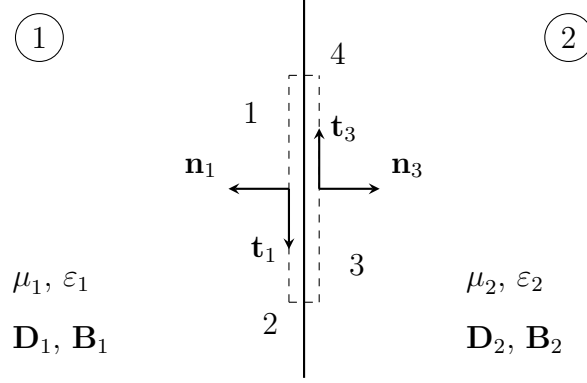
Figure 2.2: Integration area across material interface.

Applying Stokes' theorem to the left-hand side of the equations, a relation between the tangential components of the electric and magnetic fields in the two different materials is obtained

$$\oint_{\partial\Sigma} \mathbf{E} \cdot \mathbf{t} \; \mathrm{d}l = 0, \tag{2.12a}$$

$$\oint_{\partial\Sigma} \mathbf{H} \cdot \mathbf{t} \; \mathrm{d}l = \int_{\Sigma} \mathbf{i} \; \mathrm{d}\Sigma. \tag{2.12b}$$

Neglecting the contributions from the sides 2 and 4, and introducing the relation $\mathbf{t}_1 = -\mathbf{t}_3$, (2.12) can be written as

$$E_{1,\mathrm{t}} - E_{2,\mathrm{t}} = 0, \tag{2.13a}$$

$$H_{1,\mathrm{t}} - H_{2,\mathrm{t}} = \frac{1}{l} \int_{\Sigma} \mathbf{i} \; \mathrm{d}\Sigma, \tag{2.13b}$$

where l is the length of the interface.

Equation (2.13) shows that the tangential component of the electric field is always continuous across material discontinuities while the tangential component of the magnetic field experiences a discontinuity proportional to the surface current on the interface. If there is no surface currents, the tangential component of the magnetic field is also continuous across material interfaces.

Normal components

Considering again Figure 2.2, it is possible to study the behaviour of the normal components of the electric and magnetic fields integrating (2.10a) and (2.10b) over the surface Σ, obtaining the following relations

$$\int_{\Sigma} \nabla \cdot (\mu\mathbf{H}) \; \mathrm{d}\Sigma = 0, \tag{2.14a}$$

$$\int_{\Sigma} \nabla \cdot (\varepsilon\mathbf{E}) \; \mathrm{d}\Sigma = \int_{\Sigma} \rho_c \; \mathrm{d}\Sigma. \tag{2.14b}$$

Applying the divergence theorem, equation (2.14) becomes

$$\oint_{\partial\Sigma} (\mu\mathbf{H}) \cdot \mathbf{n} \; \mathrm{d}l = 0, \tag{2.15a}$$

$$\oint_{\partial\Sigma} (\varepsilon\mathbf{E}) \cdot \mathbf{n} \; \mathrm{d}l = \int_{\Sigma} \rho_c \; \mathrm{d}\Sigma. \tag{2.15b}$$

Finally, substituting in (2.15) the relation $\mathbf{n}_1 = -\mathbf{n}_3$, a relation between the normal components of the electric and magnetic fields in the different materials is obtained

$$\mu_1 H_{1,n} - \mu_2 H_{2,n} = 0, \tag{2.16a}$$

$$\varepsilon_1 E_{1,n} - \varepsilon_2 E_{2,n} = \frac{1}{l} \int_{\Sigma} \rho_c \; \mathrm{d}\Sigma. \tag{2.16b}$$

Assuming no surface charges are present at the interface, $\rho_c = 0$, equation (2.16) can also be written as

$$\frac{H_{1,n}}{H_{2,n}} = \frac{\mu_2}{\mu_1}, \tag{2.17a}$$

$$\frac{E_{1,n}}{E_{2,n}} = \frac{\varepsilon_2}{\varepsilon_1}. \tag{2.17b}$$

Equation (2.17) states that the ratio between the normal components of the magnetic field in the two materials is inversely proportional to the ratio between the magnetic permeabilities of the materials. Similarly, the ratio between the normal components of the electric field in the two materials is inversely proportional to the ratio between the electric permittivities of the materials. Additionally, similarly to what happens for the tangential component of the magnetic field in presence of a surface current, equation (2.16b) indicates that even if the two materials have the same electrical permittivity, $\varepsilon_1 = \varepsilon_2$, a surface charge distribution on the interface generates a discontinuity in the normal component of the electric field.

Consequences on numerical solution methods

The presence of field discontinuities carry consequences for the numerical methods used to solve Maxwell's equations. In fact, for the solution of Maxwell's equations, it is necessary to employ methods that are able to correctly represent discontinuous fields. Most standard solution techniques, in fact, compute all the components of the fields in each node of the discretization and assume the fields to be continuous. However, while the continuity assumption may hold for a variety of different mathematical models, it is usually not the case in electromagnetic applications, as shown in Section 2.1.1.1.

To address these shortcomings and avoid the appearance of spurious solutions, specific FD stencils, such as Yee cells [17], and a new family of finite elements, the edge-based elements [30, 31], have been developed for use in electromagnetic applications. Additionally,

as DG and HDG methods only weakly enforce the inter-element continuity, standard node-based elements can be used. Figure 2.3 provides a schematic description of the collocation of the unknowns and of the continuity requirements of different types of discretizations.
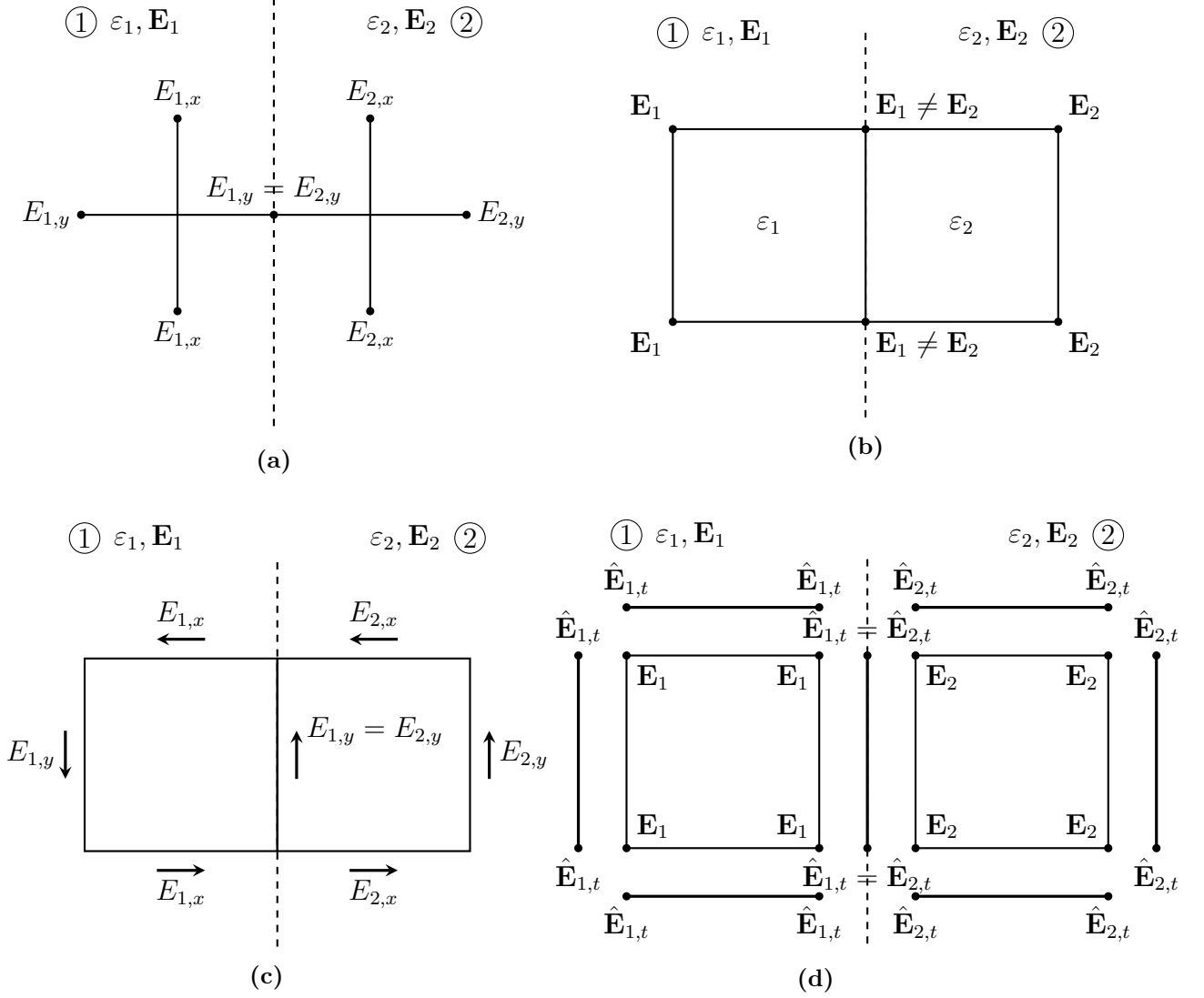

Figure 2.3: Comparison between different discretization techniques. (a) Finite differences; (b) Node-based finite elements; (c) Edge-based finite element; (d) Hybridizable discontinuous Galerkin method.

In the finite difference method using staggered cells, Figure 2.3(a), only the tangential component of the electric field is computed on the interface between different materials, while the normal component is computed on nodes away from the interface. In the standard finite element method using node-based elements, Figure 2.3(b), all the components of the electric field are computed in each node. As the FEM strongly enforces inter-element continuity, it is impossible to discretize the discontinuity in the normal component of the electric field. With edge-based elements Figure 2.3(c) instead, the DOFs are assigned to the edges, rather than the nodes, of the discretization. Hence, similarly to

the finite difference staggered grid, only the tangential components of the electric field are computed on the material interface, therefore making it possible to have a discontinuity in the normal component of the field between distinct elements. Finally, with the HDG method, Figure 2.3(d), the solution is computed in terms of the single-valued tangential component of the trace value, $\hat{\mathbf{E}}_t$, and the inter-element continuity is only enforced weakly.

A more complete description of the properties of HDG methods in the field of computational electromagnetics is provided in Section 2.2.

2.1.2 Generalized Ohm law

In this work, the propagation of electromagnetic signals in conductive media is investigated. It is thereofore necessary to introduce a constitutive relation between electric currents and electric fields. In fact, while in dielectric media such as vacuum, the conduction current term $\mathbf{i}$ can be neglected, it holds particular importance in the description of electromagnetic fields in conductive media.

In nature, if an electric field is applied to an electric conductor, a current is generated. Vice-versa, forcing an electric current through a conductor, generates an electric field opposing the current. This phenomenon is modeled by the *generalized Ohm equation*

$$\mathbf{i} = \sigma\mathbf{E} + \mathbf{i}_{\mathrm{s}}, \tag{2.18}$$

where σ is the *electric conductivity* and $\mathbf{i}_{\mathrm{s}}$ is an externally applied *current density source*. Substituting (2.18) into (2.10d), the following for of Maxwell's equations, as used in this work, are obtained

$$\nabla\cdot(\mu\mathbf{H}) = 0, \tag{2.19a}$$

$$\nabla\cdot(\varepsilon\mathbf{E}) = \rho_c, \tag{2.19b}$$

$$\partial_t\mathbf{H} + \frac{1}{\mu}\nabla\times\mathbf{E} = \mathbf{0}, \tag{2.19c}$$

$$\varepsilon\partial_t\mathbf{E} + \sigma\mathbf{E} - \nabla\times\mathbf{H} = -\mathbf{i}_{\mathrm{s}}. \tag{2.19d}$$

The conduction current term, $\sigma\mathbf{E}$, mathematically represents a dissipative term in the equations. In fact, while a plane wave propagating in a perfect dielectric material travels without dissipation, the energy of a wave traveling in a conductive material is dissipated by the generated electric currents.

2.1.3 Direct current resistivity problem

In electrostatic problems there is no need to employ the full Maxwell equations to describe the behaviour of electric fields. In fact, we can obtain an equation describing a stationary field substituting (2.18) in (2.10b), obtaining

$$\nabla\cdot(\sigma\mathbf{E}) = -\nabla\cdot\mathbf{i}_{\mathrm{s}}. \tag{2.20}$$

However, (2.20) is typically not the equation that is used to numerically solve stationary fields problems. For stationary fields equation (2.19c) implies that

$$\nabla\times\mathbf{E} = \mathbf{0}, \tag{2.21}$$

and, therefore, there exists a potential function ϕ, called *electric potential*, such that

$$\mathbf{E} = -\nabla\phi. \tag{2.22}$$

Substituting (2.22) into (2.20) we obtain a diffusion equation for the electric potential

$$\Delta\left(\sigma\phi\right) = \nabla\cdot\mathbf{i}_{\mathrm{s}}, \tag{2.23}$$

that can be efficiently solved numerically. In fact, as the potential is a continuous scalar function over the domain, for the numerical solution of (2.23), standard finite elements can be used, reducing both the implementation complexity and the computational cost of the solver. Moreover, an extensive literature is available for the efficient solution of scalar diffusion problems.

Equation (2.23) is used to solve stationary problems called DC problems [98, 109]. The solution to these problems can be used per se to investigate the potential distribution due to electric current sources [95, 103] or used to initialize transient problems in geophysical applications [105, 106]. Additionally, it is possible to develop divergence-cleaning techniques based on (2.23), see, e.g. [106].

As the propagation of the magnetic field is not of primary interest in this work, magnetostatic and *magnetometric resistivity* problems will not be addressed. More information about this topic can be found in [9, 108, 118–120].

2.1.4 Electromagnetic wave equation

Although the description of electromagnetic wave propagation is already included in (2.10), it can be useful to write a wave equation for the electric or magnetic wave to immediately visualize the properties of the waves.

Considering for simplicity an isotropic, homogeneous medium, the wave equation can be obtained deriving (2.19d) in time and substituting the rotor of (2.19c) into the resulting equation, obtaining

$$\varepsilon\partial_{t^2}\mathbf{E} + \sigma\partial_t\mathbf{E} + \frac{1}{\mu}\nabla\times\nabla\times\mathbf{E} = -\partial_t\mathbf{i}_{\mathrm{s}}. \tag{2.24}$$

Equation (2.24) is called *damped vector wave equation* as it includes the dissipative conductive current term $\sigma\partial_t\mathbf{E}$. In dielectric media the conductive current term can be neglected with respect to the *displacement current* term $\varepsilon\partial_{t^2}\mathbf{E}$, obtaining the so-called *vector wave equation*. For non-conductive media, where $\sigma \to 0$, and no external current sources applied, the vector wave equation takes the form

$$\varepsilon\partial_{t^2}\mathbf{E} + \frac{1}{\mu}\nabla\times\nabla\times\mathbf{E} = \mathbf{0}. \tag{2.25}$$

Typically, however, (2.25) is written as

$$\frac{1}{c^2}\partial_{t^2}\mathbf{E} + \nabla\times\nabla\times\mathbf{E} = \mathbf{0}, \tag{2.26}$$

17

where c is the *speed of light* and is defined as

$$c = \frac{1}{\sqrt{\mu\varepsilon}}. \tag{2.27}$$

Moreover, considering a material without free charges nor currents, (2.19b) implies

$$\nabla \cdot \mathbf{E} = 0,$$

and, using the vector identity

$$\nabla \times \nabla \times \mathbf{E} = \nabla(\nabla \cdot \mathbf{E}) - \Delta\mathbf{E}, \tag{2.28}$$

equation (2.24) can be rewritten as

$$\varepsilon\partial_{t^2}\mathbf{E} + \sigma\partial_t\mathbf{E} - \frac{1}{\mu}\Delta\mathbf{E} = \mathbf{0}. \tag{2.29}$$

Following a similar rationale the same equation can be obtained for a magnetic field wave equation.

Notice that, while (2.26) is a linear equation, it is possible, in some applications, to have electrical properties dependent of the field variables, making the equation nonlinear. The linearity of (2.26) is important from a technological standpoint, as it allows for the independent propagation of different waves in the same domains and prevents the energy associated to the lower frequencies to be transferred to higher frequencies. Form a numerical point of view, the linearity of (2.26) removes the necessity of nonlinear iterations and, if the simulation parameters are well-defined, no aliasing can occur.

2.1.4.1 Electromagnetic wave equation in frequency-domain

Another, perhaps more convenient, way to describe wave phenomena is the frequency-domain approach. The transformation of the wave equation from the time-domain to the frequency-domain is achieved assuming that the fields oscillate harmonically in time with angular frequency ω, as

$$\mathbf{E}(\mathbf{x}, t) = \mathbf{E}_0(\mathbf{x})e^{i\omega t}, \tag{2.30a}$$
$$\mathbf{H}(\mathbf{x}, t) = \mathbf{H}_0(\mathbf{x})e^{i\omega t}. \tag{2.30b}$$

Substituting (2.30a) in (2.24) and neglecting the current source term, the following wave equation is obtained

$$\varepsilon\omega^2\mathbf{E}_0(\mathbf{x}) - i\sigma\omega\mathbf{E}_0(\mathbf{x}) - \nabla \times \nabla \times \mathbf{E}_0(\mathbf{x}) = \mathbf{0}. \tag{2.31}$$

Similarly, a wave equation in the frequency-domain can be obtained for the magnetic field.

Although this work is concerned with time-domain problems, the wave equation expressed in the frequency-domain can be helpful to investigate the effect of conductive materials on the propagation of electromagnetic waves.

Assume the propagation of a plane wave in a conductive domain. The propagation of the wave can be described by (2.29). Let's now assume a solution of the form

$$\mathbf{E}(\mathbf{x}, t) = \mathbf{E}_0 e^{i(\omega t - \mathbf{k} \cdot \mathbf{x})}, \tag{2.32}$$

and substitute it in (2.29), obtaining

$$-\varepsilon\omega^2 \mathbf{E}_0 + i\omega\sigma \mathbf{E}_0 + \frac{1}{\mu}\mathbf{k}^2 \mathbf{E}_0 = \mathbf{0}. \tag{2.33}$$

We can now write an equation for the wave vector as

$$-\varepsilon\omega^2 + i\omega\sigma + \frac{1}{\mu}\mathbf{k}^2 = 0, \tag{2.34}$$

and assuming the wave vector to have the form

$$\mathbf{k} = \mathbf{A} - i\mathbf{B}, \tag{2.35}$$

the following can be obtained

$$A = \omega\sqrt{\mu\varepsilon} \left[\frac{1}{2} + \frac{1}{2}\sqrt{1 + \frac{\sigma^2}{\omega^2\varepsilon^2}} \right]^{\frac{1}{2}}, \tag{2.36a}$$

$$B = \frac{\omega\mu\sigma}{2A}. \tag{2.36b}$$

From the definition (2.35) and relations (2.36) is possible to study the limit cases $\sigma \gg \omega\varepsilon$ and $\sigma \ll \omega\varepsilon$.

Before studying the two cases however, is important to introduce the relation, obtained from (2.19c), between the electric field and the magnetic field

$$\mathbf{H} = \frac{\mathbf{k}}{\mu\omega} \times \mathbf{E}. \tag{2.37}$$

From this relation is possible to notice how the magnetic field oscillates in a direction that is orthogonal to both the direction of oscillation of the electric field and the direction of propagation of the wave.

Non-conductive material

In the case of a non-conductive material, $\sigma \ll \omega\varepsilon$, (2.36) becomes

$$A \approx \omega\sqrt{\mu\varepsilon}, \tag{2.38a}$$

$$B \approx 0. \tag{2.38b}$$

In this case, therefore, the wave vector is real and, from (2.37), the electric and magnetic fields are in phase.

Moreover, substituting (2.35) in (2.32) the following is obtained

$$\mathbf{E} = \mathbf{E}_0 e^{i(\omega t - \mathbf{A}\mathbf{x})} e^{-\mathbf{B}\mathbf{x}}. \tag{2.39}$$

Considering for simplicity a wave propagating along the x-direction, with the coefficients $\mathbf{A}$ and $\mathbf{B}$ from (2.38), (2.39) can be rewritten as

$$\mathbf{E} = \mathbf{E}_0 e^{i\left(\omega t - \omega\sqrt{\mu\varepsilon}x\right)}, \tag{2.40}$$

or, introducing the wave velocity (2.27), as

$$\mathbf{E} = \mathbf{E}_0 e^{i\left(\omega t - \frac{\omega}{c}x\right)}. \tag{2.41}$$

Additionally, introducing the wavelength

$$\lambda = \frac{c}{f}, \tag{2.42}$$

equation (2.41) can be written as

$$\mathbf{E} = \mathbf{E}_0 e^{\frac{2\pi}{\lambda}i(ct-x)}. \tag{2.43}$$

Conductive material

For a conductive material instead, $\sigma \gg \omega\varepsilon$, (2.36) gives

$$A \approx \sqrt{\frac{\omega\mu\sigma}{2}}, \tag{2.44a}$$

$$B \approx \sqrt{\frac{\omega\mu\sigma}{2}}. \tag{2.44b}$$

In the conductive case the wave vector is complex and, from (2.37), follows that the electric and magnetic fields are out of phase.

As for the dielectric case, considering a wave propagating along the x-direction, with the $\mathbf{A}$ and $\mathbf{B}$ coefficients from (2.44), (2.39) can be rewritten as

$$\mathbf{E} = \mathbf{E}_0 e^{i\left(\omega t - \sqrt{\frac{\omega\mu\sigma}{2}}x\right)} e^{-\sqrt{\frac{\omega\mu\sigma}{2}}x}. \tag{2.45}$$

The term $e^{-\sqrt{\frac{\omega\mu\sigma}{2}}x}$ in (2.45) indicates, as expected, that in a conductive material the amplitude of the wave decreases as the wave travels further, in contrast to the dielectric case (2.40) where the wave propagates without dissipation.

Both the dissipation of the waves and the phase angle between the electric and magnetic fields can be observed in the numerical simulations presented in Chapter 4, where the propagation and scattering of a wave in both dielectric and conductive materials are investigated.

2.1.5 Electromagnetic diffusion equation

In conductive media in the low frequency spectrum, $\sigma \gg \omega\varepsilon$, the displacement current term $\varepsilon\partial_{t^2}\mathbf{E}$ in (2.24) can be neglected, obtaining the Electromagnetic Diffusion (EMD) equation

$$\sigma\partial_t\mathbf{E} + \frac{1}{\mu}\nabla\times\nabla\times\mathbf{E} = -\partial_t\mathbf{i}_{\mathrm{s}}. \tag{2.46}$$

This equation is often used in geophysics as, in applications such as CSEM, Long-offset Transient Electromagnetics (LoTEM) and subsurface signal propagation, the media is conductive and the frequency used are of the order of 1-10 Hz. In these scenarios, a good approximation for the values of permittivity and permeability are those of vacuum, $\varepsilon \approx \varepsilon_0$ and $\mu \approx \mu_0$. The speed of light in these media is then $c \approx c_0 \approx 3 \times 10^8$ m/s with wavelengths λ of approximately 3×10^7 m. These wavelengths are much bigger than the typical source-receiver offset $(1 - 10$ km), see, e.g. [11, 105, 106, 114], hence the problem can be safely approximated by an EMD problem.

Notice that, for divergence-free electric fields and no current sources, the identity

$$\nabla\times\nabla\times\mathbf{E} = \nabla\nabla\cdot\mathbf{E} - \Delta\mathbf{E},$$

becomes simply

$$\nabla\times\nabla\times\mathbf{E} = -\Delta\mathbf{E},$$

and the EMD equation (2.46) can be rewritten as

$$\sigma\partial_t\mathbf{E} - \frac{1}{\mu}\Delta\mathbf{E} = \mathbf{0}. \tag{2.47}$$

However, given the presence of current sources or charge densities, in geophysical applications the EMD equation in the form of (2.46) is typically used.

The EMD equation is typically used when large conductivity contrasts are present in the domain as, in the low-frequency domain, the mixed-equation formulation becomes loosely coupled, therefore requiring prohibitively small time-steps to make the methods stable [83, 99, 121].

2.2 Introduction to computational electromagnetics

In most cases it is only possible to find closed-form solutions for to the equations introduced in Section 2.1 for simple geometries and configurations. To obtain solutions to engineering problems, instead, it is necessary to develop numerical methods able to reliably find solutions for a range of applications. A short historical overview of the development of such methods is given in Chapter 1.

This work is focused on the development of novel HDG formulations for electromagnetic propagation in conductive environments. Hence, a brief overview of the main characteristics and properties of HDG methods are introduced. Additionally, other general, finite element concepts as boundary conditions and time-integration schemes are provided.

This section is organised as follows. In Section 2.2.1, a qualitative description of HDG methods and how these compare to standard FEM and DG methods, particularly with respect to the number of unknowns and distribution of DOFs, is given. Section 2.2.2 is devoted to the introduction of the approximation spaces and the notation used in the rest of the work. In Section 2.2.3 an overview of the boundary conditions used in this work is presented. Finally, in Section 2.2.4, the time-integration scheme chosen to discretize the equations in time is discussed.

2.2.1 Hybridizable Discontinuous Galerkin methods for electromagnetic signal propagation

The hybridizable discontinuous Galerkin method is a special case of the discontinuous Galerkin method, in which the numerical fluxes are defined such that these are single-valued on the faces shared by adjacent elements. This flux definition allows for a reduction of the number of unknowns of the HDG method with respect to the DG method from which it is derived.

In HDG methods, just as in DG methods, it is possible to distinguish two different set of unknowns, belonging to the so-called global and local problems. The global problem contains the DOFs belonging to the trace of the discretization, indicated by the red squares in Figure 2.4, that provides a schematical representation of the collocation of DOFs for an exemplary second-order, four-element, discretization. These DOFs are globally coupled, and it is therefore necessary to solve the problem considering the contributions of each elements' traces, similarly to the unknowns of the standard FEM.
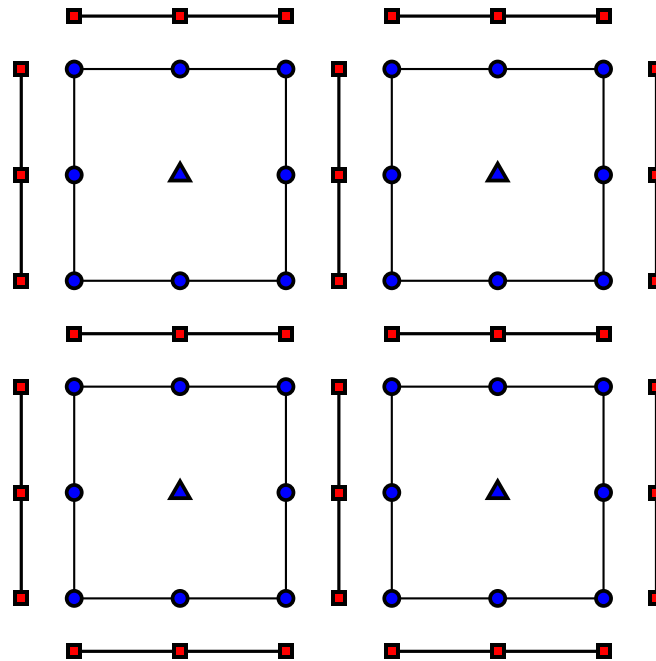

Figure 2.4: Schematical representation of local and global DOFs in a second-order quadrilateral element for a HDG discretization. The blue circles and triangles represent local DOFs while the red squares represent the global DOFs.

Comparing Figure 2.4 to Figure 2.3(b), it is easily noticeable how the HDG method has an increased number of globally coupled DOFs with respect to the standard FEM because of the duplication of the DOFs on the vertices of the elements and, in 3D, of the edges of the faces. However, from Figure 2.4, it is also possible to notice how, for higher-order discretizations, the DOFs internal to the elements, represented by the blue triangles, are effectively ignored by the global problem as they are not globally coupled. Therefore, as the order of the polynomial approximation increases, the ratio of the number of globally coupled DOFs of HDG and continuous Galerkin methods reduces [55, 56, 122].

The local problem, on the other hand, includes the DOFs of the distinct elements and are only coupled to the DOFs of the element's adjacent faces. Therefore, after the solution of the global problem is obtained, it is possible to compute the values of the unknowns of the local problem at an element level. The decoupling of the DOFs of different elements allows a fast computation of the local problem as it is possible to distribute the computational effort to independent computational units. It has to be noticed that, although the computation of the local problems is computationally less expensive than the solution of the global problem and is well suited for parallel computations, the local system necessarily introduces additional DOFs, increasing the size of the overall problem.

2.2.1.1 Local post-processing

A major advantage of HDG methods over other discretization techniques is the possibility to obtain solutions of increased accuracy by means of local post-processing procedures. In fact, it is possible to show that if the stabilization parameter of the HDG methods is chosen wisely [123], both the solution of the global and local problems converge optimally, that is, converge with order $k + 1$ where k is the order of the polynomial approximation. In turn, if the trace variable achieves optimal convergence, it is possible to compute an element-by-element improved solution that superconverges at a rate of $k + 2$.

Different use cases have been proposed for the additional accuracy of the post-processed solution. While some focus on the reduction of the computational cost of the method, reducing the order of the polynomial approximation necessary to obtain the same accuracy, see e.g., [55, 56, 123] others have proposed to use the post-processed solution as an error estimator for adaptivity algorithms [61, 124, 125].

2.2.1.2 Discussion of HDG methods

In recent years, high-order methods have gained interest in several fields of applications [44, 45, 126, 127], just to cite a few. The main advantage of using higher-order discretizations lies on the reduction of the number of elements and, typically, DOFs needed to achieve a given accuracy. In fact, by exploiting the higher convergence rates of higher-order polynomial approximations it is possible to use coarser meshes with a smaller number of unknowns to accurately represent complex fields. The convergence studies of the proposed formulations, presented in Section 3.2.1 and Section 5.5.1, provide a good example of such behaviour.

Nonetheless, the reduction of elements and DOFs counts is not the only performance measure that has to be taken into account when comparing different discretization meth-

ods. Other metrics that have to be considered when comparing different discretization methods is the possibility to obtain fast, scalable, implementations and well conditioned discretization matrices. In fact, for the efficient solution of any engineering problem, the properties of the discretization matrices have to satisfy certain requirements in order to benefit the most from existing linear solvers and preconditioners. Additional information on performance comparisons between continuous, discontinuous and hybridizable discontinuous finite element methods see, i.e., [55, 122, 123, 128], to cite a few.

Additionally, it is worth pointing out that the performance achievable by the methods are strongly dependent on the underlying equations in that each problem has a different number of DOFs assigned to each discretization node. For example, while the heat equation only has one scalar variable to solve for, incompressible fluid flow problems include scalar and vectorial unknowns. The formulations proposed in this work solve the tangential component of the electric field as a globally coupled variable and, hence, the dimension of the space in which the unknowns lay depends on the spatial dimensions of the problem.

Several performance comparisons between continuous Galerkin and HDG methods, see, e.g. [55, 56] or, similarly, DG and HDG methods [67], are based on node-based finite element. Therefore, the extensions of these results to the field of computational electromagnetics, where edge-based elements are necessary, is not straightforward. In fact, edge-based elements differ from node-based elements in several aspects, such as the number of DOFs per element and, for non consistently linear elements, the difference in local approximation order in the different components of the fields [33].

Finally, the performances of linear solvers and preconditioners developed for node-based elements can be affected by the discretization with edge-based elements and vice-versa. In addition, the high performances of efficient solution approaches such as matrix-free methods, that perform well in FEM [129, 130] and DG [131] methods, are not necessarily obtained when these methods are applied to HDG methods [123]. Therefore, to obtain a more precise picture of the performance difference between standard FEM with edge-based elements, DG and HDG methods, additional research would be necessary.

2.2.2 Notation and approximation spaces

As there is no unique notation shared in the FEM community, the notation used in this work is introduced. Most of the notation is the same used in [68].

Let Ω be the domain. We denote by $\mathcal{T}^{\mathrm{h}}$ the collection of n_e elements, Ω_e, that partitions Ω. The boundary of the domain, $\partial\Omega$, is divided in two disjoint portions: a portion where ABCs are applied, Γ_A, and a portion where PEC boundary conditions are applied, Γ_D. The portions are defined such that $\Gamma_A \cup \Gamma_D = \partial\Omega$. The boundary of the collection $\partial\mathcal{T}^{\mathrm{h}}$, consists of all element boundaries $\partial\Omega_i, \forall i \in [0, \ldots, n_e]$. The intersection of the boundaries of two neighboring elements i and j is called *interior face*, $F = \partial\Omega_i \cap \partial\Omega_j$. The intersection of the boundaries of an element i, with the boundary of the domain $F = \partial\Omega_i \cap \partial\Omega$ is called *boundary face*. The union of all interior faces is denoted by $\mathcal{E}^0$, while the union of all boundary faces is denoted by $\mathcal{E}^\partial$. The set $\mathcal{E} = \mathcal{E}^\partial \cup \mathcal{E}^0$ denotes the union of all faces.

Let D be an open domain in $\mathbb{R}^d$ and $L^2(D)$ be the space of square-integrable functions on D. Denoted by $\mathcal{P}_m(D)$ is the space of polynomials of degree of at most m on D and $\mathcal{P}_m^d \equiv [\mathcal{P}_m(D)]^d$.

In the given notation, the approximation spaces are defined as

$$V^h = \{r^h \in L^2(\mathcal{T}^h) : r^h|_{\Omega_e} \in \mathcal{P}_m(\Omega_e) \, \forall \Omega_e \in \mathcal{T}^h\}, \tag{2.48a}$$

$$\mathbf{V}^h = \{\mathbf{v}^h \in [L^2(\mathcal{T}^h)]^d : \mathbf{v}^h|_{\Omega_e} \in \mathcal{P}_m^d(\Omega_e) \, \forall \Omega_e \in \mathcal{T}^h\}, \tag{2.48b}$$

$$M^h = \{\mu^h \in L^2(\mathcal{E}) : \mu^h|_F \in \mathcal{P}_m(F) \, \forall F \in \mathcal{E}\}, \tag{2.48c}$$

$$\mathbf{M}^h{}_t = \{\boldsymbol{\eta}^h \in [L^2(\mathcal{E})]^{d-1} : \boldsymbol{\eta}^h|_F \in \mathcal{P}_m{}^{d-1}(F), (\boldsymbol{\eta}^h \cdot \mathbf{n})|_F = 0 \, \forall F \in \mathcal{E}\}, \tag{2.48d}$$

$$\mathbf{M}^h{}_t(\mathbf{f}) = \{\boldsymbol{\eta}^h \in \mathbf{M}^h{}_t : \boldsymbol{\eta}^h \times \mathbf{n} = \Pi(\mathbf{f} \times \mathbf{n}) \text{ on } \Gamma_D\}. \tag{2.48e}$$

Here $\Pi(\mathbf{f} \times \mathbf{n})$ is a projection of $\mathbf{f} \times \mathbf{n}$ onto $\mathbf{M}^h{}_t$.

2.2.2.1 Dimensions of approximation spaces and reference frames

This work is concerned with 3D solutions of electromagnetic fields, hence, $d = 3$ always. It is therefore worth to point out that, while the space $\mathbf{V}^h$ is defined within an element Ω_e, and has dimension d, the space $\mathbf{M}^h{}_t$ is defined on a face F, and thus has dimension $d-1$. The direct consequence of this property is that we can express any function $\boldsymbol{\eta}^h \in \mathbf{M}^h{}_t$, with respect to a 2D reference frame $\mathbf{R}'$, that lies on the plane of the face F, reducing the dimensionality and complexity of the problem. Notice that the definition of the face's reference frame $\mathbf{R}'$ is arbitrary. To define $\mathbf{R}'$, it is necessary to define a set of $d-1$, linearly independent, basis vectors.
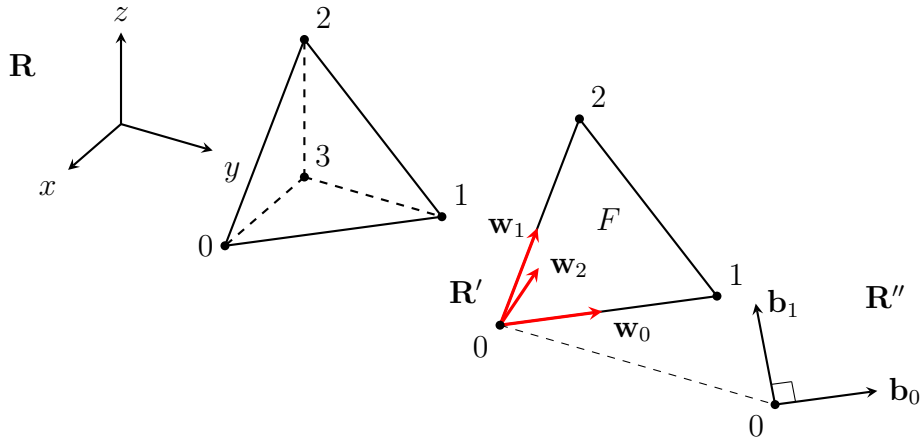

Figure 2.5: Construction of the face reference frame, $\mathbf{R}''$, for a tetrahedral element.

Let $\mathbf{v}_i = [x_i, y_i, z_i]$, with $i \in [0, \ldots, 2]$, be the coordinates of the ith vertex of the face F, expressed in the domain's reference frame $\mathbf{R}$. A possible choice of the basis vectors $\mathbf{W} = [\mathbf{w}_0, \mathbf{w}_1]$, such that the reference frame $\mathbf{R}' = \text{span}(\mathbf{W})$ lies on the face F, is given

by

$$\mathbf{w}_0 = \frac{\mathbf{v}_1 - \mathbf{v}_0}{|\mathbf{v}_1 - \mathbf{v}_0|},$$

$$\mathbf{w}_1 = \frac{\mathbf{v}_2 - \mathbf{v}_0}{|\mathbf{v}_2 - \mathbf{v}_0|}. \tag{2.49}$$

The transformation between $\mathbf{R}$ and $\mathbf{R}'$ can be obtained as

$$\mathbf{R} = \mathbf{W}\mathbf{R}', \tag{2.50a}$$

$$\mathbf{R}' = \mathbf{W}^{-1}\mathbf{R}. \tag{2.50b}$$

While such reference frame satisfies the requirements and is therefore perfectly acceptable, it was found that it is not the most advantageous choice from an implementation point of view. The cons of using such definition is given by the computation of the inverse transformation matrix $\mathbf{W}^{-1}$. As the matrix $\mathbf{W}$ is non-square, it is also a *non-invertible* matrix. Consequently, to obtain the inverse transformation matrix $\mathbf{W}^{-1}$, it is necessary to extend the set of basis vectors as $\mathbf{W} = [\mathbf{w}_0, \mathbf{w}_1, \mathbf{w}_2]$, where

$$\mathbf{w}_2 = \frac{\mathbf{w}_0 \times \mathbf{w}_1}{|\mathbf{w}_0 \times \mathbf{w}_1|}, \tag{2.51}$$

is a unit vector orthogonal to both $\mathbf{w}_0$ and $\mathbf{w}_1$. The extension of the matrix with an additional basis vector makes the matrix $\mathbf{W}$ *nonsingular* and therefore *invertible*. Notice that, while it is necessary for $\mathbf{w}_2$ to be linearly independent from $\mathbf{w}_0$ and $\mathbf{w}_1$, the orthogonality property is not a necessary requirement. Nonetheless, (2.51) was the definition initially adopted to generate the additional basis vector.

It is worth to point out that, the external product always provides a linearly independent vector while, if the other vertices of the element are to be used to create the additional basis vector $\mathbf{w}_2$, it is necessary to find a vertex that does not lie on the plane defined by span$(\mathbf{w}_0, \mathbf{w}_1)$. Although finding the necessary additional vertex can be trivial for a tetrahedral element, it can prove more complex for other elements such as hexahedra, especially when higher order elements are used.

To avoid such problem and simplify the implementation, we can use an *orthonormal reference frame* as, in this case, the following identity holds

$$\mathbf{B}^{-1} = \mathbf{B}^T. \tag{2.52}$$

An orthonormal reference frame is a reference frame in which the basis vectors are unit vectors, $|\mathbf{b}_0| = 1$ and $|\mathbf{b}_1| = 1$, and mutually orthogonal, $\mathbf{b_0} \cdot \mathbf{b_1} = 0$.

We can obtain the basis vectors, $\mathbf{B}$, of the orthonormal frame $\mathbf{R}''$, applying the *Gram–Schmidt orthonormalization process* [132, 133] to the basis vectors $\mathbf{W}$, as follows

$$\mathbf{b}_0 = \mathbf{w}_0,$$

$$\mathbf{b}_1 = \frac{\mathbf{w}_1 - (\mathbf{b}_0 \cdot \mathbf{w}_1)\mathbf{b}_0}{|\mathbf{w}_1 - (\mathbf{b}_0 \cdot \mathbf{w}_1)\mathbf{b}_0|}.$$

The transformation matrix $\mathbf{B}$ can therefore be used to transform vectors expressed in the domain's reference frame to vectors expressed in the face's reference frame and vice-versa. For example, it is possible to project the boundary condition expressed in terms of a global reference frame $\mathbf{R}$ into the boundary faces' reference frames $\mathbf{R}''$.

Figure 2.5 provides a graphical representation of the construction of the frame $\mathbf{R}''$.

2.2.2.2 Definition of mathematical operators

To simplify the notation it is useful to introduce some additional notation for the operators that are most used.

The integral of the inner product on the volume $\Omega \in \mathbb{R}^3$, is denoted as

$$(\mathbf{u}, \mathbf{v})_\Omega = \int_D \mathbf{u}\mathbf{v}, \tag{2.53}$$

and, consequently,

$$(\mathbf{u}, \mathbf{v})_{\mathcal{T}^{\mathrm{h}}} = \sum_{\Omega_e \in \mathcal{T}^{\mathrm{h}}} (\mathbf{u}, \mathbf{v})_{\Omega_e}. \tag{2.54}$$

Boundary integrals over an element are denoted as

$$\langle \mathbf{u}, \mathbf{v} \rangle_{\partial D} = \int_{\partial D} \mathbf{u}\mathbf{v}, \tag{2.55}$$

and the boundary integral over the entire domain is defined as

$$\langle \mathbf{u}, \mathbf{v} \rangle_{\partial \mathcal{T}^{\mathrm{h}}} = \sum_{\partial \Omega_e \in \partial \mathcal{T}^{\mathrm{h}}} \langle \mathbf{u}, \mathbf{v} \rangle_{\partial \Omega_e}. \tag{2.56}$$

It is also useful to introduce the *jump operator*, defined for interior faces as

$$[\![\mathbf{u}]\!] = \mathbf{n}^+ \times \mathbf{u}^+ + \mathbf{n}^- \times \mathbf{u}^-, \tag{2.57}$$

where the symbols $\pm$ indicates the face's two neighboring elements and $\mathbf{n}$ is the face's outward pointing vector. For boundary faces the jump operator is defined as

$$[\![\mathbf{u}]\!] = \mathbf{n} \times \mathbf{u}. \tag{2.58}$$

The value of the field $\mathbf{u}$ on a face, its *trace value*, is denoted as $\hat{\mathbf{u}}$.

Additionally, we define the error in the L^2-norm as

$$\|\mathbf{u}^{\mathrm{a}} - \mathbf{u}^{\mathrm{h}}\| = \left(\sum_{\mathcal{T}^{\mathrm{h}}} \int_{\Omega_e} \|\mathbf{u}^{\mathrm{a}} - \mathbf{u}^{\mathrm{h}}\|^2 \right)^{\frac{1}{2}}, \tag{2.59}$$

the error in the H^{curl}-norm as

$$\|\mathbf{u}^{\mathrm{a}} - \mathbf{u}^{\mathrm{h}}\|_{H^{\mathrm{curl}}} = \left(\sum_{\mathcal{T}^{\mathrm{h}}} \int_{\Omega_e} \left(\|\mathbf{u}^{\mathrm{a}} - \mathbf{u}^{\mathrm{h}}\|^2 + \|\nabla \times \mathbf{u}^{\mathrm{a}} - \nabla \times \mathbf{u}^{\mathrm{h}}\|^2 \right) \right)^{\frac{1}{2}}, \tag{2.60}$$

and the error in the H^{div}-norm as

$$\|\mathbf{u}^{\mathrm{a}} - \mathbf{u}^{\mathrm{h}}\|_{H^{\mathrm{div}}} = \left(\sum_{\mathcal{T}^{\mathrm{h}}} \int_{\Omega_e} \left(\|\mathbf{u}^{\mathrm{a}} - \mathbf{u}^{\mathrm{h}}\|^2 + \|\nabla \cdot \mathbf{u}^{\mathrm{a}} - \nabla \cdot \mathbf{u}^{\mathrm{h}}\|^2 \right) \right)^{\frac{1}{2}}. \qquad (2.61)$$

It is important to recall the property of the Dirac delta function [132, 133].

$$\int_{-\infty}^{+\infty} u(x)\delta(x) = u(0). \qquad (2.62)$$

Finally we denote the maximum value of $\mathbf{u}(t)$ over time as

$$\bar{\mathbf{u}} = \max_{t \in [0, T_{\max}]} \mathbf{u}(t). \qquad (2.63)$$

2.2.3 Boundary conditions

There are many possible choices of boundary conditions in computational EM such as, for example, PEC, Perfect Magnetic Conductor (PMC), *impedance boundary conditions*, ABC, Perfectly Matched Layer (PML) etc. However, in geophysical applications, it is common to adopt PEC and PMC boundary conditions to obtain accurate solutions without adding complexity to the problem. When these Dirichlet-like boundary conditions are used, it is necessary to extend the boundaries away from the source or receivers to make sure that possible numerical artifacts caused by the boundary conditions do not interfere with the solution [21, 105]. Nonetheless, if a reduction in the number of unknowns is necessary, it is possible to introduce other boundary conditions, such as, for example, continuation boundary conditions that would allow to neglect the air layer in the discretization domain [20, 99].

In this work, despite the goal is to develop methods for the simulation of electromagnetic signal propagation in underground strata formation and, therefore, PEC boundary conditions would suffice, in order to demonstrate the broader range of application of the proposed formulation, both PEC and ABC boundary conditions are derived and implemented.

2.2.3.1 Perfect electric conductor boundary conditions

Perfect electric conductor boundary conditions are Dirichlet-like boundary conditions on the tangential component of the electric field and are expressed as

$$\mathbf{n} \times \mathbf{E} = \mathbf{0}. \qquad (2.64)$$

These boundary conditions are used to model a computational domain that is bounded by conductive material such as a metal sheet.

PEC boundary conditions can be derived applying Ohm's law to the interface represented by the BC. If the computational domain is bounded by a perfectly conductive material, that is $\sigma \to \infty$, from Ohm's law (2.18), reported here for convenience

$$\sigma \mathbf{E} = \mathbf{i}_{\mathrm{s}},$$

we notice that in order to have a bounded current density $\mathbf{i}_s$, the electric field has to be such that $\mathbf{E} \to 0$ [34, 36]. Given that $\mathbf{n} \times \mathbf{E}$ is always continuous across material discontinuities, that is, between the external conductor and the material contained in the domain, (2.64) is obtained.

Notice that this boundary condition model physical boundaries of a domain and, therefore, the waves reaching PEC boundary conditions are reflected. Additionally, PEC boundary conditions can be used to bound both the boundaries of a buried metal scatterer or the external boundaries of the domain. In the latter case, standing wave solutions can be obtained as the waves reaching the boundaries are reflected back towards the domain.

PMC boundary conditions follow the same rationale as (2.64) and are defined as

$$\mathbf{n} \times \mathbf{H} = \mathbf{0}. \tag{2.65}$$

However, since the proposed formulations follow an electric field approach, only PEC boundary conditions are enforced in the following sections.

2.2.3.2 Absorbing boundary conditions

Although it is possible to simulate phenomena happening in unbounded physical domains making use of the Infinite Elements method, see, e.g. [134–136], these methods can lead to an increased number of unknowns and poor matrix conditioning [134, 137]. A different approach to the solution of this class of problems involves truncating the discretization and bounding it by means of ABCs. Different types of Absorbing boundary conditions have been developed in the past to account for different scenarios [34, 36, 137, 138]. However, for simplicity, we only introduce a simple first-order ABC.

The ABCs implemented in this work are derived from the Silver–Müller condition in [139] that reads

$$\sqrt{\varepsilon\mu}\,(\partial_t\mathbf{E} \times \mathbf{n}) \times \mathbf{n} - \nabla\times\mathbf{E} \times \mathbf{n} = \mathbf{0}. \tag{2.66}$$

Substituting Faradays' law (2.19c) in (2.66), the following relation is obtained

$$\sqrt{\varepsilon\mu}\,(\partial_t\mathbf{E} \times \mathbf{n}) \times \mathbf{n} + (\mu\partial_t\mathbf{H}) \times \mathbf{n} = \mathbf{0}, \tag{2.67}$$

and can be manipulated into

$$\partial_t\left(\sqrt{\frac{\varepsilon}{\mu}}\,(\mathbf{E} \times \mathbf{n}) \times \mathbf{n} + \mathbf{H} \times \mathbf{n}\right) = \mathbf{0}. \tag{2.68}$$

We can now split the total field, the solution of the proposed formulation, as a sum of an incident radiation and a diffracted one as

$$\mathbf{E} = \mathbf{E}_{\text{inc}} + \mathbf{E}_{diff}, \tag{2.69}$$

and apply the Silver–Müller condition to each of the fields, obtaining

$$\partial_t\left(\sqrt{\frac{\varepsilon}{\mu}}\,(\mathbf{E} \times \mathbf{n}) \times \mathbf{n} + \mathbf{H} \times \mathbf{n} - (\mathbf{E}_{\text{inc}} \times \mathbf{n}) \times \mathbf{n} - \mathbf{H}_{\text{inc}} \times \mathbf{n}\right) =$$
$$\partial_t\left(\sqrt{\frac{\varepsilon}{\mu}}\,(\mathbf{E}_{diff} \times \mathbf{n}) \times \mathbf{n} + \mathbf{H}_{diff} \times \mathbf{n}\right) = \mathbf{0}. \tag{2.70}$$

To absorb the diffracted radiation on the boundary, we impose

$$\sqrt{\frac{\varepsilon}{\mu}} \left(\mathbf{E}_{diff} \times \mathbf{n} \right) \times \mathbf{n} + \mathbf{H}_{diff} \times \mathbf{n} = \mathbf{0}, \tag{2.71}$$

obtaining the following relation between the total radiation and the incoming one

$$\sqrt{\frac{\varepsilon}{\mu}} \left(\mathbf{E} \times \mathbf{n} \right) \times \mathbf{n} + \mathbf{H} \times \mathbf{n} - \left(\mathbf{E}_{\mathrm{inc}} \times \mathbf{n} \right) \times \mathbf{n} - \mathbf{H}_{\mathrm{inc}} \times \mathbf{n} = \mathbf{0}. \tag{2.72}$$

The notation is simplified as

$$\sqrt{\frac{\varepsilon}{\mu}} \left(\mathbf{E} \times \mathbf{n} \right) \times \mathbf{n} + \mathbf{H} \times \mathbf{n} = \mathbf{g}_{inc} \tag{2.73}$$

where

$$\mathbf{g}_{inc} = \sqrt{\frac{\varepsilon}{\mu}} \left(\mathbf{E}_{\mathrm{inc}} \times \mathbf{n} \right) \times \mathbf{n} + \mathbf{H}_{\mathrm{inc}} \times \mathbf{n}, \tag{2.74}$$

is the incoming radiation imposed on the boundary Γ_a.

While PEC boundary conditions are used to model physical bounds to the domain, ABCs are used to bound the computational domain where no physical boundary is present and, therefore, the fields are expected to be unaffected by the boundary conditions. However, although no physical obstacle is being modeled, ABCs can still introduce unwanted reflections at the boundaries that can then propagate into the domain. To reduce the influence of these non-physical reflections on the solution it is possible to implement higher-order ABCs or more efficient PML boundary conditions. In addition, it is advantageous to extend the boundaries of the domain away the region of interest.

Finally, as PEC are Dirichlet-type BCs on the electric field, they can be strongly enforced on the trace variable. Absorbing boundary conditions on the other end, are weakly enforced and therefore have to be expressed in a form that suits our formulation.

2.2.4 Time integration

The spatial discretization of a set of PDEs results in a set of Ordinary Differential Equation (ODE)s. The resulting ODEs are discretized in time to obtain a set of algebraic equations that can finally be solved.

While the development of novel HDG formulations for the spatial discretization of the equations modelling electromagnetic phenomena is the main goal of this work, and is therefore shown in detail, the development of time discretization schemes goes beyond the scope of this work. Therefore, only the main reasons for our choice of time-integration schemes are given and the well-established Backward Differentiation Formula (BDF) is briefly introduced.

The choice of time-integration scheme is mostly dictated by the equations and the field of application. Typically, for wave equations in the high-frequency range, or applications with fast transients, where a small time-step is required to accurately discretize the time evolution, explicit time-integration schemes are employed due to their computational efficiency [62, 128, 140]. For long-term diffusion-dominated problems, such as those modeled

by the electromagnetic diffusion equation, implicit time-integration schemes are usually employed [105,141,142]. Therefore, given the field of application of the methods developed in this work, we employ the implicit BDF time-integration schemes.

The BDFs scheme is a linear s-step, implicit time discretization method of order s. Therefore, BDF1 denotes a single-step, first-order method, while BDF2 denotes a two-step second-order method. To define the BDF schemes, the following ODE is introduced

$$\dot{y} = f(y, t), \tag{2.75}$$

from which a generalized formula to express a family of BDF methods can be written as

$$\sum_{k=0}^{s} \alpha_{n-k} y^{n-k} = \beta \Delta t f(y^n, t^n), \tag{2.76}$$

where Δt is the chosen time-step, $y^n = y(n\Delta t)$ is the solution at the nth time step and the coefficients α_{n-k} are the coefficients of the backward finite difference of order s from y^n.

It is important to notice that, being the BDF a multistep method, for every $s > 1$, it is necessary to have more than one previous step to be able to advance in time. This property can reduce the range of application of such schemes as proper initialization procedures have to be developed to make sure that the initial conditions have the required accuracy. Once the scheme is initialized, however, the computational cost of a low-order and a high-order BDF scheme are approximately the same as the solutions in the previous time-steps are already known.

Fortunately, the BDF1 scheme has the property of being second-order accurate in the first time-step and can therefore be used to initialize the more accurate BDF2 scheme. Higher-order BDFs schemes with $s > 2$, instead, can only be used when the initial s-steps are given or an analytical solution is known.

In this work, BDF1 and BDF2 are used for the application scenarios while the BDF4 is implemented to speed up the convergence studies where the analytical solutions are known.

Table 2.1 provides the coefficients α_{n-k} and β for BDFs schemes with a number of steps $s \in [1, 4]$.

# of steps	Coefficients					
s	α_n	α_{n-1}	α_{n-2}	α_{n-3}	α_{n-4}	β
1	1	-1	-	-	-	1
2	1	$-\frac{4}{3}$	$\frac{1}{3}$	-	-	$\frac{2}{3}$
3	1	$-\frac{18}{11}$	$\frac{9}{11}$	$-\frac{2}{11}$	-	$\frac{6}{11}$
4	1	$-\frac{48}{25}$	$\frac{36}{25}$	$-\frac{16}{25}$	$\frac{3}{25}$	$\frac{12}{25}$

Table 2.1: BDFs time-integration scheme coefficients.

3 Electromagnetic mixed equation formulation

In this chapter, a general HDG formulation based on a mixed form of the Maxwell equations is developed and implemented. This formulation allows the simulation of a wide variety of physical scenarios, such as wave propagation and scattering in both conductive and non-conductive media, EM diffusion in conductive environments, etc. In this formulation the solution is given in terms of the electric, $\mathbf{E}$, and magnetic, $\mathbf{H}$, fields. The solution of both fields makes the formulation suitable for a broad range of applications.

In addition to geophysical applications, that are the main interest of this work, additional possible applications are in the medical fields, where computer simulations are used to improve diagnostic instruments such as Magnetic Resonance Imaging (MRI) machines [7], electrical engineering and physics where FEM tools are used for the design of electric machines and tools [39, 143].

To make the mathematical problem well-posed, it is necessary to assign boundary conditions on the boundaries of the computational domain. Depending on the modelling purposes, different kind of BC can be derived and used. As the goal is to develop a general purpose formulation for EMs, two different boundary conditions are shown, the PEC boundary condition to model physical boundaries of the domain and ABC used in wave propagation applications to model unbounded physical domains.

This chapter is based on the original publication from Berardocco et al. [68] and is organised as follows: in the first section, Section 3.1, the formulation is derived from the Maxwell equations. Then, in Section 3.2, the developed HDG method is applied to the solution of a simple problem to show the convergence properties of the proposed formulation.

3.1 Formulation derivation

The first formulation proposed, the *mixed-equations formulation*, is based on the Maxwell equations for conductive media (2.19). As already discussed in Section 2.1.1, equation (2.19b) and (2.19a) are not directly solved for as they are automatically satisfied if the initial fields satisfy the divergence-free conditions.

Using the notation introduced in Section 2.2.2, equations (2.19c) and (2.19d) are multiplied by (discrete) weighting functions $(\mathbf{v}^{\mathrm{h}}, \mathbf{w}^{\mathrm{h}}) \in \mathbf{V}^{\mathrm{h}} \times \mathbf{V}^{\mathrm{h}}$, respectively, and integrated over one element Ω_e with boundary $\partial\Omega_e$:

$$\left(\mathbf{v}^{\mathrm{h}}, \mu\partial_t\mathbf{H}^{\mathrm{h}}\right)_{\Omega_e} + \left(\mathbf{v}^{\mathrm{h}}, \nabla\times\mathbf{E}^{\mathrm{h}}\right)_{\Omega_e} = \mathbf{0}, \tag{3.1a}$$

$$\left(\mathbf{w}^{\mathrm{h}}, \varepsilon\partial_t\mathbf{E}^{\mathrm{h}}\right)_{\Omega_e} + \left(\mathbf{w}^{\mathrm{h}}, \sigma\mathbf{E}^{\mathrm{h}}\right)_{\Omega_e} - \left(\mathbf{w}^{\mathrm{h}}, \nabla\times\mathbf{H}^{\mathrm{h}}\right)_{\Omega_e} = -\left(\mathbf{w}^{\mathrm{h}}, \mathbf{i}_{\mathrm{s}}^{\mathrm{h}}\right)_{\Omega_e}. \tag{3.1b}$$

3 Electromagnetic mixed equation formulation

Here $(\mathbf{E}^{\text{h}}, \mathbf{H}^{\text{h}}) \in \mathbf{V}^{\text{h}} \times \mathbf{V}^{\text{h}}$ are approximations, in the element Ω_e, of the electric and magnetic fields $\mathbf{E}$ and $\mathbf{H}$ while $\mathbf{i}_{\text{s}}^{\text{h}}$ a projection of $\mathbf{i}_{\text{s}}$ onto $\mathbf{V}^{\text{h}}$.

Integration by parts of (3.1) yields

$$\left(\mathbf{v}^{\text{h}}, \mu \partial_t \mathbf{H}^{\text{h}}\right)_{\Omega_e} + \left(\nabla \times \mathbf{v}^{\text{h}}, \mathbf{E}^{\text{h}}\right)_{\Omega_e} + \left\langle \mathbf{v}^{\text{h}} \times \mathbf{n}, \hat{\mathbf{E}}^{\text{h}} \right\rangle_{\partial\Omega_e} = \mathbf{0}, \tag{3.2a}$$

$$\left(\mathbf{w}^{\text{h}}, \varepsilon \partial_t \mathbf{E}^{\text{h}}\right)_{\Omega_e} + \left(\mathbf{w}^{\text{h}}, \sigma \mathbf{E}^{\text{h}}\right)_{\Omega_e} - \left(\nabla \times \mathbf{w}^{\text{h}}, \mathbf{H}^{\text{h}}\right)_{\Omega_e} - \left\langle \mathbf{w}^{\text{h}} \times \mathbf{n}, \hat{\mathbf{H}}^{\text{h}} \right\rangle_{\partial\Omega_e}$$
$$= - \left(\mathbf{w}^{\text{h}}, \mathbf{i}_{\text{s}}^{\text{h}}\right)_{\Omega_e}, \tag{3.2b}$$

where the numerical traces $(\hat{\mathbf{E}}^{\text{h}}, \hat{\mathbf{H}}^{\text{h}}) \in \mathbf{M}^{\text{h}} \times \mathbf{M}^{\text{h}}$ of the electric and magnetic field appear as additional variables.

We now define the hybrid variable, $\mathbf{\Lambda}^{\text{h}}$, as the tangential component[1] of the numerical trace of the electric field, $\hat{\mathbf{E}}^{\text{h}}$,

$$\begin{aligned} \mathbf{\Lambda}^{\text{h}} &:= \hat{\mathbf{E}}^{\text{h}}{}_{\text{t}} \ \forall F \in \mathcal{E}^0, \\ \mathbf{\Lambda}^{\text{h}} &:= \mathbf{0} \quad \forall F \in \mathcal{E}^{\partial} \cap \Gamma_D, \end{aligned} \tag{3.3}$$

such that $\mathbf{\Lambda}^{\text{h}} \in \mathbf{M}^{\text{h}}{}_{\text{t}}(\mathbf{0})$.

Substituting (3.3) in (3.2) and summing the contribution of each individual element, the following is obtained

$$\left(\mathbf{v}^{\text{h}}, \mu \partial_t \mathbf{H}^{\text{h}}\right)_{\mathcal{T}^{\text{h}}} + \left(\nabla \times \mathbf{v}^{\text{h}}, \mathbf{E}^{\text{h}}\right)_{\mathcal{T}^{\text{h}}} + \left\langle \mathbf{v}^{\text{h}} \times \mathbf{n}, \mathbf{\Lambda}^{\text{h}} \right\rangle_{\partial\mathcal{T}^{\text{h}}} = \mathbf{0}, \tag{3.4a}$$

$$\left(\mathbf{w}^{\text{h}}, \varepsilon \partial_t \mathbf{E}^{\text{h}}\right)_{\mathcal{T}^{\text{h}}} + \left(\mathbf{w}^{\text{h}}, \sigma \mathbf{E}^{\text{h}}\right)_{\mathcal{T}^{\text{h}}} - \left(\nabla \times \mathbf{w}^{\text{h}}, \mathbf{H}^{\text{h}}\right)_{\mathcal{T}^{\text{h}}} - \left\langle \mathbf{w}^{\text{h}} \times \mathbf{n}, \hat{\mathbf{H}}^{\text{h}} \right\rangle_{\partial\mathcal{T}^{\text{h}}}$$
$$= - \left(\mathbf{w}^{\text{h}}, \mathbf{i}_{\text{s}}^{\text{h}}\right)_{\mathcal{T}^{\text{h}}}. \tag{3.4b}$$

The numerical trace of the magnetic field, $\hat{\mathbf{H}}^{\text{h}}$, is defined as

$$\hat{\mathbf{H}}^{\text{h}} = \mathbf{H}^{\text{h}} + \tau \left(\mathbf{E}^{\text{h}}{}_{\text{t}} - \mathbf{\Lambda}^{\text{h}}\right) \times \mathbf{n}, \tag{3.5}$$

where τ is a stabilization parameter that weights the difference between the tangential component of the discrete electrical field $\mathbf{E}^{\text{h}}{}_{\text{t}}$ and the hybrid variable $\mathbf{\Lambda}^{\text{h}}$.

The stabilization parameter is an empirical parameter and its choice is typically dictated by experience and by the problem at hand. Usually, values too close to zero yield ill-defined methods [54], while values that are too high can lead to ill-conditioned problems and therefore poor convergence of iterative methods [56]. Additionally, the value of the stabilization parameter affects the convergence properties of the method in the trace variables [55, 123].

In this work, the default value of the stabilization parameter is obtained by the relation

$$\tau = \sqrt{\frac{\sigma}{\mu \, t_{\text{c}}}}, \tag{3.6}$$

---

[1]Note that the tangential component of a vector, $\mathbf{v}_t$, can be obtained as $\mathbf{v}_t = \mathbf{n} \times (\mathbf{v} \times \mathbf{n})$ or subtracting the normal component, $\mathbf{v}_n = \mathbf{n}\,(\mathbf{v} \cdot \mathbf{n})$, from $\mathbf{v}$ as $\mathbf{v}_t = \mathbf{v} - \mathbf{v}_n$.

where t_c is a characteristic timescale.

To close the system of equations and to ensure that the numerical trace $\hat{\mathbf{H}}^h$ is single-valued, an additional equation is required. This equation is called *continuity equation* and enforces the tangential component of $\hat{\mathbf{H}}^h$ to be continuous across inter-element boundaries

$$\left[\!\!\left[\mathbf{n} \times \hat{\mathbf{H}}^h\right]\!\!\right] = \mathbf{0} \quad \text{on } \mathcal{E}^0, \tag{3.7}$$

to ensure that the method is locally conservative [66]. The proof that the definition (3.5) toghether with the condition (3.7) ensure the numerical flux of the magnetic field to be continuous can be found in Appendix A.

For an individual element boundary $\partial\Omega_e$, the variational form of (3.7), with weighting function $\boldsymbol{\eta}^h$, is given as

$$\left\langle \boldsymbol{\eta}^h, \mathbf{n} \times \hat{\mathbf{H}}^h \right\rangle_{\partial\Omega_e} = \mathbf{0}. \tag{3.8}$$

Integrating (3.8) over the whole domain and substituting the definition (3.5), the following is obtained

$$-\left\langle \boldsymbol{\eta}^h, \mathbf{H}^h \times \mathbf{n} \right\rangle_{\partial\mathcal{T}^h} + \left\langle \boldsymbol{\eta}^h, \tau\mathbf{E}^h \right\rangle_{\partial\mathcal{T}^h} - \left\langle \boldsymbol{\eta}^h, \boldsymbol{\Lambda}^h \right\rangle_{\partial\mathcal{T}^h} = \mathbf{0}. \tag{3.9}$$

To enforce the ABC (2.73) in (3.9), the latter is modified as

$$-\left\langle \boldsymbol{\eta}^h, \mathbf{H}^h \times \mathbf{n} \right\rangle_{\partial\mathcal{T}^h} + \left\langle \boldsymbol{\eta}^h, \tau\mathbf{E}^h \right\rangle_{\partial\mathcal{T}^h} - \left\langle \boldsymbol{\eta}^h, \boldsymbol{\Lambda}^h \right\rangle_{\partial\mathcal{T}^h} + \left\langle \boldsymbol{\eta}^h, \sqrt{\frac{\varepsilon}{\mu}}\boldsymbol{\Lambda}^h \right\rangle_{\Gamma_A} = -\left\langle \boldsymbol{\eta}^h, \mathbf{g}_{inc}^h \right\rangle_{\Gamma_A} \tag{3.10}$$

where $\mathbf{g}_{inc}^h$ is a projection of $\mathbf{g}_{inc}$ onto $\mathbf{M}^h_t$.

To show that (3.10) is equivalent to enforcing (2.73), it is possible to substitute the definition of the hybrid variable $\boldsymbol{\Lambda}^h$ (3.3) in (3.10), obtaining, for the faces belonging to the partition Γ_A

$$\left\langle \boldsymbol{\eta}^h, \sqrt{\frac{\varepsilon}{\mu}}\left(\hat{\mathbf{E}}^h_t \times \mathbf{n}\right) \times \mathbf{n} \right\rangle_{\Gamma_A} + \left\langle \boldsymbol{\eta}^h, \hat{\mathbf{H}}^h \times \mathbf{n} \right\rangle_{\Gamma_A} = \left\langle \boldsymbol{\eta}^h, \mathbf{g}_{inc}^h \right\rangle_{\Gamma_A}, \tag{3.11}$$

that is the discretized version of (2.73).

With the addition of (3.10) the system of equations (3.4) reads

$$\left(\mathbf{v}^h, \mu\partial_t\mathbf{H}^h\right)_{\mathcal{T}^h} + \left(\nabla\times\mathbf{v}^h, \mathbf{E}^h\right)_{\mathcal{T}^h} + \left\langle \mathbf{v}^h \times \mathbf{n}, \boldsymbol{\Lambda}^h \right\rangle_{\partial\mathcal{T}^h} = \mathbf{0}, \tag{3.12a}$$

$$\left(\mathbf{w}^h, \varepsilon\partial_t\mathbf{E}^h\right)_{\mathcal{T}^h} + \left(\mathbf{w}^h, \sigma\mathbf{E}^h\right)_{\mathcal{T}^h} - \left(\nabla\times\mathbf{w}^h, \mathbf{H}^h\right)_{\mathcal{T}^h}$$
$$- \left\langle \mathbf{w}^h \times \mathbf{n}, \mathbf{H}^h \right\rangle_{\partial\mathcal{T}^h} - \left\langle \mathbf{w}^h \times \mathbf{n}, \tau\left(\mathbf{E}^h_t - \boldsymbol{\Lambda}^h\right) \times \mathbf{n} \right\rangle_{\partial\mathcal{T}^h} = -\left(\mathbf{w}^h, \mathbf{i}_s^h\right)_{\mathcal{T}^h}, \tag{3.12b}$$

$$- \left\langle \boldsymbol{\eta}^h, \mathbf{H}^h \times \mathbf{n} \right\rangle_{\partial\mathcal{T}^h} + \left\langle \boldsymbol{\eta}^h, \tau\mathbf{E}^h \right\rangle_{\partial\mathcal{T}^h} - \left\langle \boldsymbol{\eta}^h, \boldsymbol{\Lambda}^h \right\rangle_{\partial\mathcal{T}^h} + \left\langle \boldsymbol{\eta}^h, \sqrt{\frac{\varepsilon}{\mu}}\boldsymbol{\Lambda}^h \right\rangle_{\Gamma_A}$$
$$= -\left\langle \boldsymbol{\eta}^h, \mathbf{g}_{inc}^h \right\rangle_{\Gamma_A}. \tag{3.12c}$$

Applying integration by parts to (3.12b) and rearranging the equations leads to the final form of the problem: find $\left(\mathbf{H}^{\mathrm{h}}, \mathbf{E}^{\mathrm{h}}, \boldsymbol{\Lambda}^{\mathrm{h}}\right) \in \mathbf{V}^{\mathrm{h}} \times \mathbf{V}^{\mathrm{h}} \times \mathbf{M}^{\mathrm{h}}{}_{\mathrm{t}}(\mathbf{0})$ such that

$$\left(\mathbf{v}^{\mathrm{h}}, \mu \partial_t \mathbf{H}^{\mathrm{h}}\right)_{\mathcal{T}^{\mathrm{h}}} + \left(\nabla \times \mathbf{v}^{\mathrm{h}}, \mathbf{E}^{\mathrm{h}}\right)_{\mathcal{T}^{\mathrm{h}}} + \left\langle \mathbf{v}^{\mathrm{h}} \times \mathbf{n}, \boldsymbol{\Lambda}^{\mathrm{h}}\right\rangle_{\partial \mathcal{T}^{\mathrm{h}}} = \mathbf{0}, \tag{3.13a}$$

$$\left(\mathbf{w}^{\mathrm{h}}, \varepsilon \partial_t \mathbf{E}^{\mathrm{h}}\right)_{\mathcal{T}^{\mathrm{h}}} + \left(\mathbf{w}^{\mathrm{h}}, \sigma \mathbf{E}^{\mathrm{h}}\right)_{\mathcal{T}^{\mathrm{h}}} - \left(\mathbf{w}^{\mathrm{h}}, \nabla \times \mathbf{H}^{\mathrm{h}}\right)_{\mathcal{T}^{\mathrm{h}}} - \left\langle \mathbf{w}^{\mathrm{h}} \times \mathbf{n}, \tau \mathbf{E}^{\mathrm{h}}{}_{\mathrm{t}} \times \mathbf{n}\right\rangle_{\partial \mathcal{T}^{\mathrm{h}}}$$

$$+ \left\langle \mathbf{w}^{\mathrm{h}} \times \mathbf{n}, \tau \boldsymbol{\Lambda}^{\mathrm{h}} \times \mathbf{n}\right\rangle_{\partial \mathcal{T}^{\mathrm{h}}} = - \left(\mathbf{w}^{\mathrm{h}}, \mathbf{i}_{\mathrm{s}}{}^{\mathrm{h}}\right)_{\mathcal{T}^{\mathrm{h}}}, \tag{3.13b}$$

$$- \left\langle \boldsymbol{\eta}^{\mathrm{h}}, \mathbf{H}^{\mathrm{h}} \times \mathbf{n}\right\rangle_{\partial \mathcal{T}^{\mathrm{h}}} + \left\langle \boldsymbol{\eta}^{\mathrm{h}}, \tau \mathbf{E}^{\mathrm{h}}{}_{\mathrm{t}}\right\rangle_{\partial \mathcal{T}^{\mathrm{h}}} - \left\langle \boldsymbol{\eta}^{\mathrm{h}}, \tau \boldsymbol{\Lambda}^{\mathrm{h}}\right\rangle_{\partial \mathcal{T}^{\mathrm{h}}} + \left\langle \boldsymbol{\eta}^{\mathrm{h}}, \sqrt{\frac{\varepsilon}{\mu}} \boldsymbol{\Lambda}^{\mathrm{h}}\right\rangle_{\Gamma_A}$$

$$= - \left\langle \boldsymbol{\eta}^{\mathrm{h}}, \mathbf{g}_{\mathrm{inc}}^{\mathrm{h}}\right\rangle_{\Gamma_A}. \tag{3.13c}$$

for all $\left(\mathbf{v}^{\mathrm{h}}, \mathbf{w}^{\mathrm{h}}, \boldsymbol{\eta}^{\mathrm{h}}\right) \in \mathbf{V}^{\mathrm{h}} \times \mathbf{V}^{\mathrm{h}} \times \mathbf{M}^{\mathrm{h}}{}_{\mathrm{t}}(\mathbf{0})$.

The system of equations (3.13) can be written in matrix-vector form as

$$\begin{bmatrix} \mathbb{A} & \mathbf{0} & \mathbf{0} \\ \mathbf{0} & \mathbb{E} & \mathbf{0} \\ \mathbf{0} & \mathbf{0} & \mathbf{0} \end{bmatrix} \begin{bmatrix} \dot{\mathbf{H}} \\ \dot{\mathbf{E}} \\ \dot{\boldsymbol{\Lambda}} \end{bmatrix} + \begin{bmatrix} \mathbf{0} & \mathbb{C} & \mathbb{D} \\ \mathbb{F} & \mathbb{G} & \mathbb{H} \\ \mathbb{I} & \mathbb{J} & \mathbb{L} \end{bmatrix} \begin{bmatrix} \mathbf{H} \\ \mathbf{E} \\ \boldsymbol{\Lambda} \end{bmatrix} = \begin{bmatrix} \mathbf{0} \\ -\mathbf{i}_{\mathrm{s}} \\ -\mathbf{g}_{inc} \end{bmatrix}, \tag{3.14}$$

where $\dot{\mathbf{H}}$, $\dot{\mathbf{E}}$ and $\dot{\boldsymbol{\Lambda}}$ denote the time derivatives of the magnetic, electric and trace fields respectively.

The obtained set of ODEs can now be discretized in time to obtain a set of algebraic equations that can be solved to obtain the approximation of the fields $\mathbf{H}^{\mathrm{h}}, \mathbf{E}^{\mathrm{h}}$ and $\boldsymbol{\Lambda}^{\mathrm{h}}$ over the discretized domain.

3.1.1 Time discretization

In Section 3.1 a novel HDG formulation (3.13) used to discretize the Maxwell equations in space is introduced. It is now necessary to discretize the ODEs, obtained from the spatial discretization, in time, in order to be able to numerically compute the solution.

The BDF method (2.76) introduced in Section 2.2.4 is applied to the matrix-vector formulation in equation (3.14) obtaining

$$\begin{bmatrix} \mathbb{A} & \mathbb{C} & \mathbb{D} \\ \mathbb{F} & \mathbb{G} + \mathbb{E} & \mathbb{H} \\ \mathbb{I} & \mathbb{J} & \mathbb{L} \end{bmatrix} \begin{bmatrix} \mathbf{H}^n \\ \mathbf{E}^n \\ \boldsymbol{\Lambda}^n \end{bmatrix} = \begin{bmatrix} \tilde{\mathbf{H}} \\ \tilde{\mathbf{E}} - \mathbf{i}_{\mathrm{s}}{}^n \\ -\mathbf{g}_{inc}^n \end{bmatrix}, \tag{3.15}$$

where the term $\frac{1}{\beta \Delta t}$ is included in the definition of the matrices $\mathbb{A}$ and $\mathbb{E}$, and the terms $\tilde{\mathbf{E}}$ and $\tilde{\mathbf{H}}$ are defined as

$$\tilde{\mathbf{H}} = - \sum_{k=1}^{s} \alpha_{n-k} \mathbb{A} \mathbf{H}^{n-k}, \tag{3.16a}$$

$$\tilde{\mathbf{E}} = - \sum_{k=1}^{s} \alpha_{n-k} \mathbb{E} \mathbf{E}^{n-k}. \tag{3.16b}$$

In equations (3.15) and (3.16), the order of the BDF integration scheme is denoted by s, the electric $\mathbf{E}^n$, magnetic $\mathbf{H}^n$ and trace fields $\mathbf{\Lambda}^n$ at the time $t = n\Delta t$ are the unknown variables. Finally, the vectors $\tilde{\mathbf{H}}$ and $\tilde{\mathbf{E}}$ are a linear combination of the magnetic and electric fields of the last s steps and $\mathbf{i_s}^n$ and $\mathbf{g}_{inc}^n$ are externally defined source functions.

Assembling the matrix (3.15) of each element into a global matrix leads to a system of the form

$$\mathbb{M}\mathbf{x} = \mathbf{b}, \tag{3.17}$$

that can be solved inverting the $\mathbb{M}$ matrix. The solution of (3.17) gives the solution to both the global, $\mathbf{\Lambda}^n$, and local, $[\mathbf{H}^n, \mathbf{E}^n]$, problems at the same time.

However, because of the simultaneous solution of both problems, the matrix $\mathbb{M}$ is unnecessarily large, making the solution of the system (3.17) computationally very expensive. To reduce the computational cost of the solution, it is possible to exploit the locality of the local system to reduce the size of the matrix $\mathbb{M}$, removing the local DOFs from the system in a process called condensation.

3.1.2 Matrix condensation

It is important to notice that (3.15) is valid from both a global point of view and an element point of view. However, assembling the element matrices as indicated by (3.15) in the global stiffness matrix is very expensive and results in a matrix that is unnecessarily large. Given that the computational complexity of the numerical solution of a linear system of equations increases notably with the size of the system, it is of great utility to reduce its size, where possible.

Fortunately, given the sparsity pattern of the element matrices resulting from HDG methods, it is possible to identify the blocks

$$\left[\begin{array}{cc|c} \mathbb{A} & \mathbb{C} & \mathbb{D} \\ \mathbb{F} & \mathbb{E}+\mathbb{G} & \mathbb{H} \\ \hline \mathbb{I} & \mathbb{J} & \mathbb{L} \end{array} \right] \left[\begin{array}{c} \mathbf{H}^n \\ \mathbf{E}^n \\ \mathbf{\Lambda}^n \end{array} \right] = \left[\begin{array}{c} \tilde{\mathbf{H}} \\ \tilde{\mathbf{E}} - \mathbf{i_s}^n \\ \mathbf{0} \end{array} \right], \tag{3.18}$$

and condense the matrix using the Schur complement obtaining the relation

$$\mathbb{K}\mathbf{\Lambda}^n = \mathbf{F}, \tag{3.19}$$

where

$$\mathbb{K} = \mathbb{L} - \begin{bmatrix} \mathbb{I} & \mathbb{J} \end{bmatrix} \begin{bmatrix} \mathbb{A} & \mathbb{C} \\ \mathbb{F} & \mathbb{E}+\mathbb{G} \end{bmatrix}^{-1} \begin{bmatrix} \mathbb{D} \\ \mathbb{H} \end{bmatrix}, \tag{3.20a}$$

$$\mathbf{F} = -\begin{bmatrix} \mathbb{I} & \mathbb{J} \end{bmatrix} \begin{bmatrix} \mathbb{A} & \mathbb{C} \\ \mathbb{F} & \mathbb{E}+\mathbb{G} \end{bmatrix}^{-1} \begin{bmatrix} \tilde{\mathbf{H}} \\ \tilde{\mathbf{E}} - \mathbf{i_s}^n \end{bmatrix}. \tag{3.20b}$$

Notice that, in this section, the term $\mathbf{g}_{inc}^n$ is set to zero for simplicity. A theoretical background, as well as possible applications of the Schur complement can be found in Appendix B.

It is possible to further reduce the size of the matrix that has to be inverted, using the identity

$$\begin{bmatrix} \mathbb{A} & \mathbb{C} \\ \mathbb{F} & (\mathbb{E} + \mathbb{G}) \end{bmatrix}^{-1} = \begin{bmatrix} 1 & -\mathbb{A}^{-1}\mathbb{C} \\ 0 & 1 \end{bmatrix} \begin{bmatrix} \mathbb{A}^{-1} & 0 \\ 0 & ((\mathbb{E} + \mathbb{G}) - \mathbb{F}\mathbb{A}^{-1}\mathbb{C})^{-1} \end{bmatrix} \begin{bmatrix} 1 & 0 \\ -\mathbb{F}\mathbb{A}^{-1} & 1 \end{bmatrix}, \quad (3.21)$$

obtaining the following relations

$$\mathbb{K} = \mathbb{L} - \mathbb{I}\mathbb{X} - \mathbb{J}\mathbb{Y}, \tag{3.22a}$$

$$\mathbf{F} = -\mathbb{I}\mathbf{x} - \mathbb{J}\mathbf{y}, \tag{3.22b}$$

where the matrices $\mathbb{X}$ and $\mathbb{Y}$ are defined as

$$\mathbb{X} = \mathbb{A}^{-1}(\mathbb{D} - \mathbb{C}\mathbb{Y}), \tag{3.23a}$$

$$\mathbb{Y} = ((\mathbb{E} + \mathbb{G}) - \mathbb{F}\mathbb{A}^{-1}\mathbb{C})^{-1}(\mathbb{H} - \mathbb{F}\mathbb{A}^{-1}\mathbb{D}), \tag{3.23b}$$

and the definitions of the vectors $\mathbf{x}$ and $\mathbf{y}$ are the following

$$\mathbf{x} = \mathbb{A}^{-1}(\tilde{\mathbf{H}} - \mathbb{C}\mathbf{y}), \tag{3.24a}$$

$$\mathbf{y} = ((\mathbb{E} + \mathbb{G}) - \mathbb{F}\mathbb{A}^{-1}\mathbb{C})^{-1}((\tilde{\mathbf{E}} - \mathbf{i}_{\mathrm{s}}{}^n) - \mathbb{F}\mathbb{A}^{-1}\tilde{\mathbf{H}}). \tag{3.24b}$$

The matrix $\mathbb{K}$ and the vector $\mathbf{F}$ are computed element-wise and assembled in a global matrix.

The global system of equations (3.19) can now be solved using either direct or iterative solvers to obtain the solution of the global problem in the form of the hybrid variable $\boldsymbol{\Lambda}^n$ over the whole domain.

Once $\boldsymbol{\Lambda}^n$ is known, the local problem

$$\begin{bmatrix} \mathbf{H}^n \\ \mathbf{E}^n \end{bmatrix} = \begin{bmatrix} \mathbb{A} & \mathbb{C} \\ \mathbb{F} & \mathbb{E} + \mathbb{G} \end{bmatrix}^{-1} \begin{bmatrix} \mathbf{h} \\ \mathbf{e} \end{bmatrix}, \tag{3.25}$$

where

$$\mathbf{h} = \tilde{\mathbf{H}} - \mathbb{D}\boldsymbol{\Lambda}^n, \tag{3.26}$$

$$\mathbf{e} = \tilde{\mathbf{E}} - \mathbf{i}_{\mathrm{s}}{}^n - \mathbb{H}\boldsymbol{\Lambda}^n, \tag{3.27}$$

can be solved element-wise, obtaining the local values of $\mathbf{E}^n$ and $\mathbf{H}^n$.

As done for the matrix $\mathbb{K}$, it is possible to substitute (3.21) in (3.25) reducing the size of the matrix that has to be inverted

$$\mathbf{H}^n = \mathbb{A}^{-1}\left(\mathbf{h} - \mathbb{C}\mathbf{E}^n\right), \tag{3.28}$$

$$\mathbf{E}^n = ((\mathbb{E} + \mathbb{G}) - \mathbb{F}\mathbb{A}^{-1}\mathbb{C})^{-1}(\mathbf{e} - \mathbb{F}\mathbb{A}^{-1}\mathbf{h}). \tag{3.29}$$

As the local problem can be solved individually for each element, it is well suited for parallelization.

Notice that reducing the size of the matrices to be inverted, the bottleneck of the specific implementation shifts from the solution of the linear system of equations to the matrix-matrix and matrix-vector multiplication operation. Therefore, to achieve efficient solvers, the characteristics of the available computational units have to be taken into consideration [123, 128].

3.1.3 Remarks on the choice of the hybrid variable

This formulation is similar to the one in [67], with the difference that here the hybrid variable is defined as the tangential component of the electric instead of the magnetic field. The main motivation for this choice lies in the fact that the tangential component of the electric field is always continuous. While charge density, surface currents and material heterogeneity can induce discontinuities in any component of the magnetic field or in the normal component of the electric field, $\mathbf{E}_t$ is always continuous, as emphasized in [5] (Chapter 4–5). There is not any notable difference in dielectric media, where surface currents are not allowed, but there might be one in conductive media, such as the ones encountered in geophysical applications. Furthermore, our choice of the electric field as primary variable is due to the importance of the electric field for our applications, that is, our interest is almost entirely in the propagation of the electric field. Most HDG methods have superconvergence properties in the L^2-norm, see e.g. [53, 54, 57, 58, 60, 66, 140] for the primary variable, $\mathbf{E}^{\mathrm{h}}$, while only optimal convergence for the mixed variable, in our case $\mathbf{H}^{\mathrm{h}}$. Therefore, in our following work, we will try to exploit this property to increase the accuracy of the approximated electric field.

3.2 Convergence studies

In order to show the convergence properties of the proposed method, the obtained numerical solution is compared to an analytical solution.

The test case considered here is the resonance of a standing wave in a cubic cavity, bounded by PEC boundary conditions, with frequency

$$f_{mnp} = \frac{1}{2\sqrt{\mu\varepsilon}} \left[\left(\frac{m}{a}\right)^2 + \left(\frac{n}{b}\right)^2 + \left(\frac{p}{d}\right)^2 \right]^{\frac{1}{2}}, \tag{3.30}$$

where the integers m, n and p indicate the modes of the wave in the $x-$, $y-$ and $z-$ directions, while a, b and c are the dimensions, in the three directions, of the cubic domain. The dimensions of the cubic domain in this test case are $a = b = c = 1$ m and the chosen modes are $m = n = p = 1$. Given these parameters, the values of permittivity and permeability are chosen as $\mu = \sqrt{3}$ H/m and $\varepsilon = \sqrt{3}$ F/m such that a frequency $f_{mnp} = \frac{1}{2}$ Hz, is obtained. It is finally possible to compute the period of oscillation as $T_{mnp} = \frac{1}{f_{mnp}} = 2$ s.

The analytical solution for the time evolution of the electric and magnetic fields, for the given set of parameters, is described by

$$\mathbf{E}^{\mathrm{a}} = \begin{bmatrix} -\sin(\pi x)\cos(\pi y)\cos(\pi z)\cos(\pi t) \\ 2\cos(\pi x)\sin(\pi y)\cos(\pi z)\cos(\pi t) \\ -\cos(\pi x)\cos(\pi y)\sin(\pi z)\cos(\pi t) \end{bmatrix},$$

$$\mathbf{H}^{\mathrm{a}} = \begin{bmatrix} -\sqrt{3}\cos(\pi x)\sin(\pi y)\sin(\pi z)\sin(\pi t) \\ 0 \\ \sqrt{3}\sin(\pi x)\sin(\pi y)\cos(\pi z)\sin(\pi t) \end{bmatrix}. \tag{3.31}$$

Equation (3.31) can now be used to initialize the fields and to compute the accuracy of the solution.

Notice that the fields described by (3.31) are divergence-free, a necessary condition on the initial fields, as described in Section 2.1.1.

3.2.1 Spatial convergence

In this first convergence study a dielectric media is considered, that is, $\sigma = 0\,\text{S/m}$. When a dielectric media is considered, the initial wave is reflected by the PEC boundary conditions and the resonance of the wave is self-sustained, hence, no forcing term is needed $\mathbf{i}_\text{s} = 0$.

To study the spatial convergence properties of the method, the domain is discretized with increasingly finer structured meshes consisting of hexahedral elements with polynomial approximation of different orders. The equations are discretized in time using the BDF2 time integration scheme with a time step $\Delta t = 10^{-4}$ s.
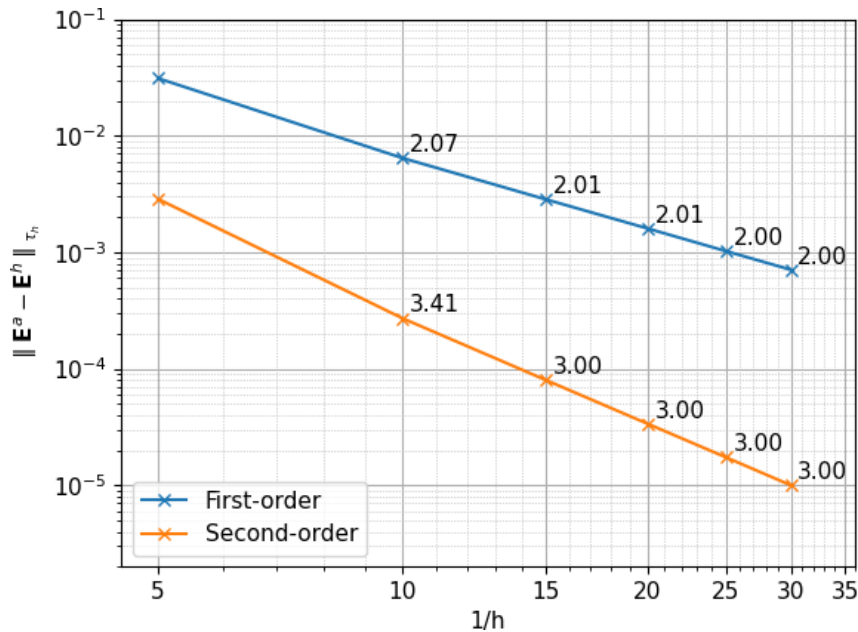
Figure 3.1: Spatial convergence plot ($\Delta t = 10^{-4}$ s). Convergence rates for first- and second-order hexahedral elements.

Figure 3.1 and Table 3.1 show the errors and the convergence rates of the approximate solution with respect to the analytic solution (3.31) in the L^2-norm. In this norm, the expected spatial convergence rate $k+1$, where k is the order of the polynomial interpolation, is indeed achieved.

To improve the accuracy of the solution in space it is possible to implement post-processing algorithms, as shown in [59]. However, for this formulation, no post-processing algorithm has been implemented in this work.

1/h	k = 1		k = 2	
	Error	Order	Error	Order
5	3.11e−2	−	2.86e−3	−
10	6.42e−3	2.07	2.70e−4	3.41
15	2.84e−3	2.01	7.98e−5	3.00
20	1.60e−3	2.01	3.37e−5	3.00
25	1.02e−3	2.00	1.73e−5	3.00
30	7.08e−4	2.00	1.00e−5	3.00

Table 3.1: Error table of the spatial convergence study.

3.2.2 Temporal convergence

Considering the same setup of Section 3.2.1, the time convergence properties are investigated. For the time convergence study, a fixed mesh consisting of fourth-order hexahedral elements with size $h = \frac{1}{15}$ m is used and the BDF1 and BDF2 time-integration schemes are tested.

The results of the convergence study are shown in Figure 3.2 and Table 3.2 where it is possible to notice that the expected first- and second-order convergence rates for the BDF1 and BDF2 time-integration schemes are indeed achieved.
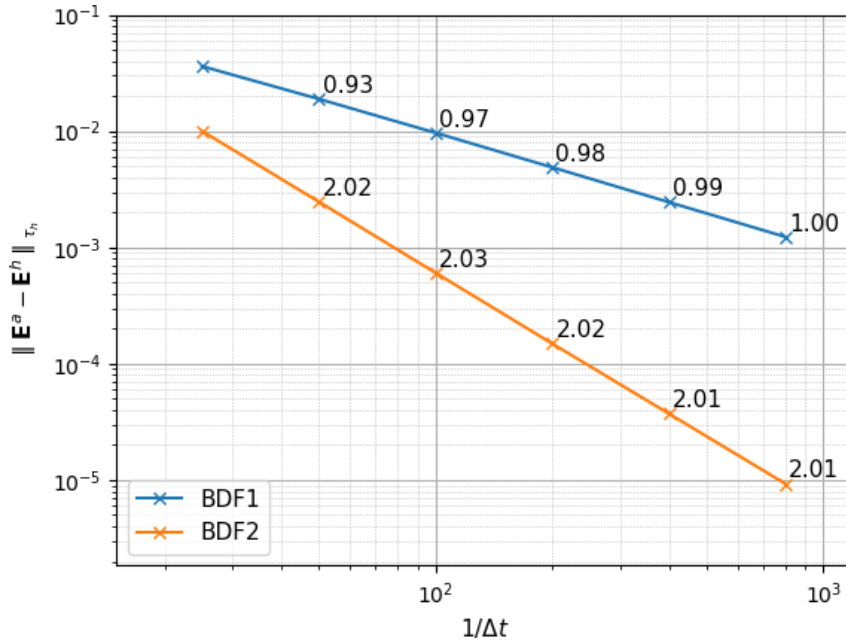
Figure 3.2: Temporal convergence plot ($h = 1/15$ m). L^2-norm error for BDF1 and BDF2 time-integration schemes.

	BDF1		BDF2	
$1/\Delta t$	Error	Order	Error	Order
25	$3.61e{-}2$	–	$1.00e{-}2$	–
50	$1.89e{-}2$	0.93	$2.47e{-}3$	2.02
100	$9.67e{-}3$	0.97	$6.05e{-}4$	2.03
200	$4.88e{-}3$	0.98	$1.49e{-}4$	2.02
400	$2.45e{-}3$	0.99	$3.72e{-}5$	2.01
800	$1.23e{-}3$	1.00	$9.25e{-}6$	2.01

Table 3.2: Error table of the time convergence study.

3.2.3 Conductive media test case

Finally, a conductive media with a conductivity $\sigma = 1.429$ S/m is introduced in the simulation scenario to test the novel method in a setting that more closely represents geophysical applications.

In conductive environments, to obtain a solution in the form of (3.31), it is necessary to introduce a current source $\mathbf{i}_s \neq 0$, to make up for the losses caused by the conductive media. Substituting (3.31) in (2.19), the following expression for the current source is obtained

$$\mathbf{i}_s = -\sigma \mathbf{E}^a. \tag{3.32}$$

Following this approach, it is possible to manufacture any solution satisfying the given boundary conditions and initial conditions by enforcing the correct right-hand side to the system of equations.

In this test case, different discretizations are used to investigate the convergence properties of the method. First, the same set of structured discretizations used in Section 3.2.1 are employed. Then, the structured meshes are substituted by a set of increasingly finer unstructured meshes, consisting of tetrahedral elements of slightly different sizes and shapes, as exemplary shown in Figure 3.3. The unstructured meshes are introduced to investigate the effects of different discretizations on the convergence properties of the method.

The solutions obtained with the structured discretizations are identical to those in Section 3.2.1. The errors and convergence rates computed are the same as those shown in Figure 3.1 and Table 3.1, indicating that the conductive current term, $\sigma \mathbf{E}$, is not a critical term for the spatial accuracy.

On the other hand, when unstructured meshes are used, although the approximation accuracy increases with a decreasing element size, the convergence rate only approximates the expected convergence rate for the given order of polynomial approximation, as seen in Figure 3.4 and Table 3.3. This behaviour is due to the non-uniform element size across the domain and is particularly evident for the mesh with elements of characteristic size $h = \frac{1}{15}$ where, for every degree of polynomial approximation used, the achieved convergence rate is lower than expected.
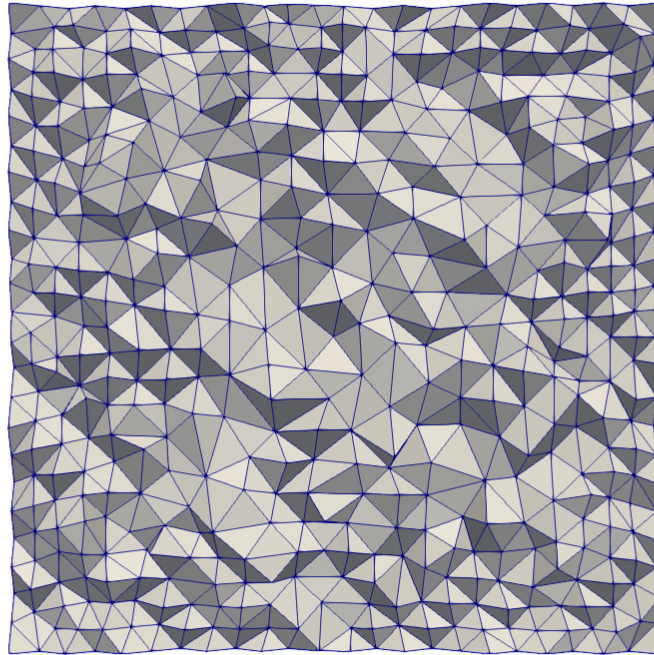
Figure 3.3: Midsection of unstructured mesh for the cubic cavity with conductive media (characteristic element size approximately $h = 1/20$ m).
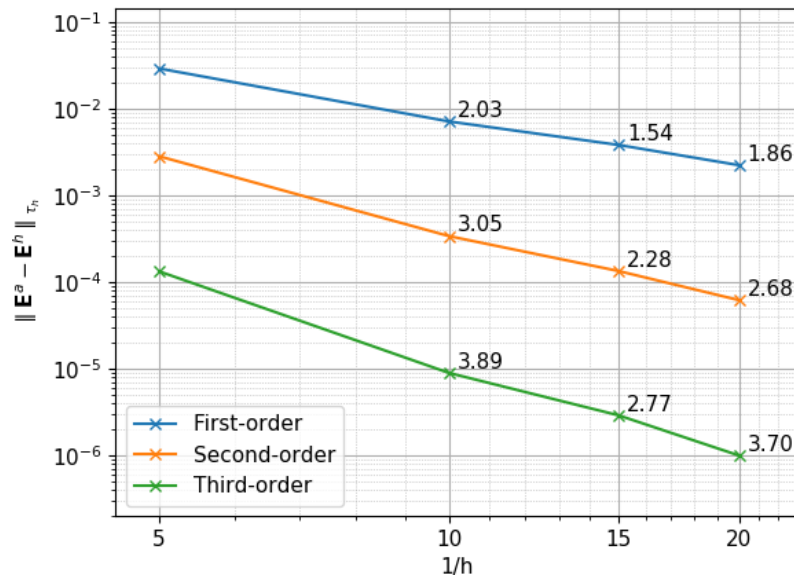

Figure 3.4: Spatial convergence plot ($\Delta t = 10^{-4}$ s). Convergence rates for first-, second- and third-order hexahedral elements.

1/h	$k = 1$		$k = 2$		$k = 3$	
	Error	Order	Error	Order	Error	Order
5	$2.89e - 2$	–	$2.82e - 3$	–	$1.33e - 4$	–
10	$7.10e - 3$	2.03	$3.39e - 4$	3.05	$9.01e - 6$	3.89
15	$3.81e - 3$	1.54	$1.34e - 4$	2.28	$2.93e - 6$	2.77
20	$2.23e - 3$	1.86	$6.22e - 5$	2.68	$1.01e - 6$	3.70

Table 3.3: Error table of the spatial convergence study of a cubic cavity with conductive media.

4 Wave propagation and scattering

In this chapter the numerical solutions of wave phenomena with the formulation introduced in 3.1 are shown. The wave propagation and scattering in dielectric media and conductive media are compared. While electromagnetic propagation in dielectric media is not the focus of this work, it is important to show that the method developed is general enough and can be applied to a range of different problems.

Wave propagation phenomena are inherently different from diffusion problems. In fact, while in diffusion problems disturbances in the field propagate immediately, in wave equations the signals propagate with a finite velocity. The hyperbolic nature of the wave equation also requires a careful design of initial and boundary conditions.

Not only the two problems are different from a physics point of view, but also the numerical solution approach is often different. Wave equations, for example, are often discretized in time using explicit time schemes as the time-step lengths required to properly discretize the waves are typically smaller than the time-step lengths required for the stability of the explicit scheme. Diffusion equations on the other hand, are typically discretized via implicit time-integration schemes as the time-steps lengths required to properly discretize diffusion phenomena are typically larger than the time-step length required for the stability of explicit time-integration schemes.

For the test cases proposed in this chapter an explicit time-integration scheme might have resulted in better performances than our implicit scheme. However, we chose an implicit scheme as the goal is the application of the mixed-equation formulation for diffusion phenomena as those modeled by the test cases shown in Chapter 6 and Chapter 7.

The wave propagation and scattering by a dielectric obstacle examples shown in this chapter were published in [68] and are used for a qualitative verification of the method by comparing these results to the ones reported in [67]. The scattering by conductive media is explored to investigate the ability of the proposed formulation to simulate wave propagation phenomena in conductive media.

The chapter is organised as follows. Section 4.1 introduces the main details of the spatial discretization and shows the results of the simulation of wave propagation in dielectric media. In Section 4.2 the scattering of plane waves of different frequencies by means of a spherical dielectric obstacle is investigated. Finally, in Section 4.3, the scattering of plane waves by a conductive scatterer is shown. The dependence of scattering and absorption on the wave's frequency is shown, and the results are compared to the expected behaviours introduced in Section 2.1.4.

4.1 Wave propagation

In this test case, the propagation of a plane wave in free space is simulated. The domain, Ω, is a dielectric sphere of radius $R = 1.5$ m, discretized with approximately $80,000$ linear tetrahedral elements, bounded by ABCs, defined by (3.11). A plane wave with frequency $f = 300$ MHz is forced to propagate through the domain along the y-direction. The electric and magnetic fields are defined as

$$
\mathbf{E}_{\text{inc}} = \begin{bmatrix} 0 \\ 0 \\ \cos\left(\sqrt{\varepsilon_0\mu_0}\,\omega y - \omega t\right) \end{bmatrix},
$$

$$
\mathbf{H}_{\text{inc}} = \begin{bmatrix} \sqrt{\frac{\varepsilon_0}{\mu_0}}\cos\left(\sqrt{\varepsilon_0\mu_0}\,\omega y - \omega t\right) \\ 0 \\ 0 \end{bmatrix},
$$

(4.1)

where ω is the angular frequency of the wave and is related to the linear frequency by the relation $\omega = 2\pi f$.

The electrical properties in the domain are set to those of free space, that is, $\varepsilon_0 = 8.854 \times 10^{-12}$ F/m, $\mu_0 = 1.257 \times 10^{-6}$ H/m and $\sigma = 0$ S/m. Given the material properties, we can compute the speed of light as $c_0 = \frac{1}{\sqrt{\varepsilon_0\mu_0}} \approx 3 \times 10^8$ m/s, that is, after approximately 10^{-8} s the wave has travelled the entire length of the domain. The time-integration is carried out via a BDF2 time-integration scheme with time-step length $\Delta t = 10^{-11}$ s, for a total simulation time $T_{\max} = 3.33 \times 10^{-8}$ s, such that the effects of the zero initial condition are transported outside the domain.

To visualize the results it is useful to transform the results from the time-domain to the frequency-domain. The transform makes it easier to compare results to those that can be found in the literature, see e.g. [67], as the time dependence is removed and the solution takes the form

$$
\hat{\mathbf{E}}_{\text{inc}}(\mathbf{x}, f) = \frac{1}{2}\cos\left(\sqrt{\varepsilon_0\mu_0}\,2\pi f_0 \mathbf{x}\right)\delta\left(f_0 - f\right), \tag{4.2}
$$

where $\delta\left(f_0 - f\right)$ is the Dirac delta function and f_0 is the frequency of the wave.

Given the frequency of the wave, $f_0 = 300$ MHz, the solution in the frequency-domain reads

$$
\hat{\mathbf{E}}_{\text{inc}}(\mathbf{x}, f_0) = \frac{1}{2}\cos\left(\sqrt{\varepsilon_0\mu_0}\,2\pi f_0 \mathbf{x}\right), \tag{4.3}
$$

and is related to the solution in the time-domain by

$$
\hat{\mathbf{E}}_{\text{inc}}(\mathbf{x}, f_0) = \frac{1}{2}\mathbf{E}_{\text{inc}}(\mathbf{x}, t = 0). \tag{4.4}
$$

The approximate solution in the frequency-domain is obtained via a Discrete Fourier Transform (DFT) using Numpy's implementation [144] of the Fast Fourier Transform (FFT) [145]. Once the DFT is computed, the coefficients of the Fourier transform relative to the frequency $f = 300$ MHz are extracted and plotted in Figure 4.1.
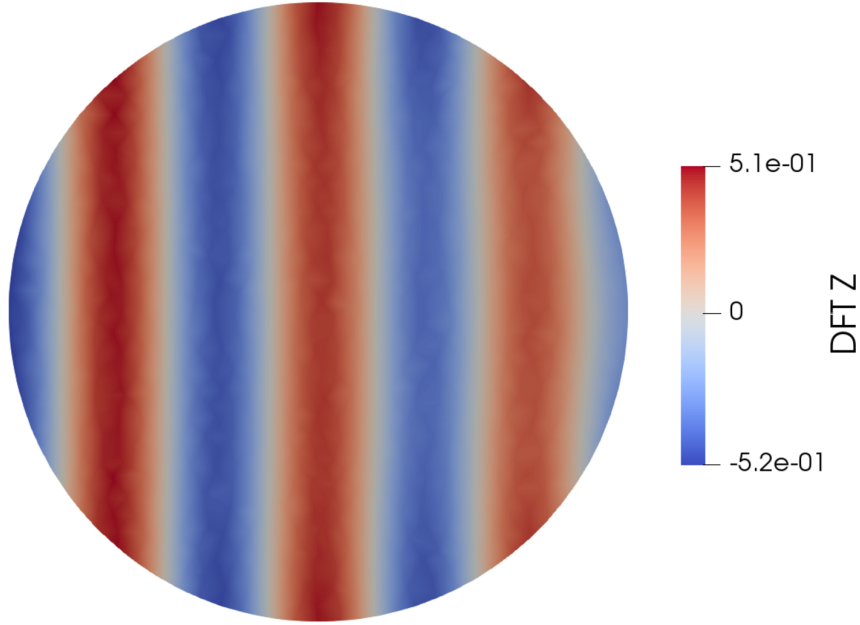
Figure 4.1: Wave propagation: Discrete Fourier transform of E_z.

The result in the frequency-domain is shown in Figure 4.1, where it is possible to notice how the plane wave propagates through the domain unperturbed. It is, however, possible to notice that the amplitude of the wave reduces as the wave travels along the y-axis. This is not only due to the dissipation introduced by the discretization but, as noticeable from the solution in the proximity of the boundaries near the positive end of the y-axis, mostly by the reflections introduced by the Absorbing boundary conditions. In fact, the ABCs used in this work are only first-order conditions [146, 147] and therefore, the incident wave is partly reflected from the surface. To reduce the surface reflection is possible to use second-order conditions including curvature terms in the definition of the ABCs [139, 146]. However, as the goal of this work is not an investigation of ABCs, second-order conditions are not implemented. For a more detailed review of higher-order ABCs see, e.g. [34, 36, 138].

4.2 Wave scattering by dielectric obstacle

In this section, the scattering of plane waves of different frequencies by a spherical dielectric scatterer is investigated. In the centre of the domain Ω described in Section 4.1, a spherical obstacle Ω_s, with radius $r = 0.5$, is introduced as shown in Figure 4.2. Absorbing boundary conditions are used to bound the domain Ω, while no condition is enforced on the interface between Ω and Ω_s. The incoming electromagnetic radiation is prescribed in the form of (4.1) and different frequencies are set in different test cases.

The electric properties set in Ω are the same used in Section 4.1, that is, $\varepsilon_0 = 8.854 \times 10^{-12}$ F/m, $\mu_0 = 1.257 \times 10^{-6}$ H/m and $\sigma = 0$ S/m. In the scatterer, Ω_s, the conductivity is left unchanged, $\sigma_s = 0$ S/m, while the permittivity and permeability are set to $\varepsilon_s = 2\varepsilon_0$
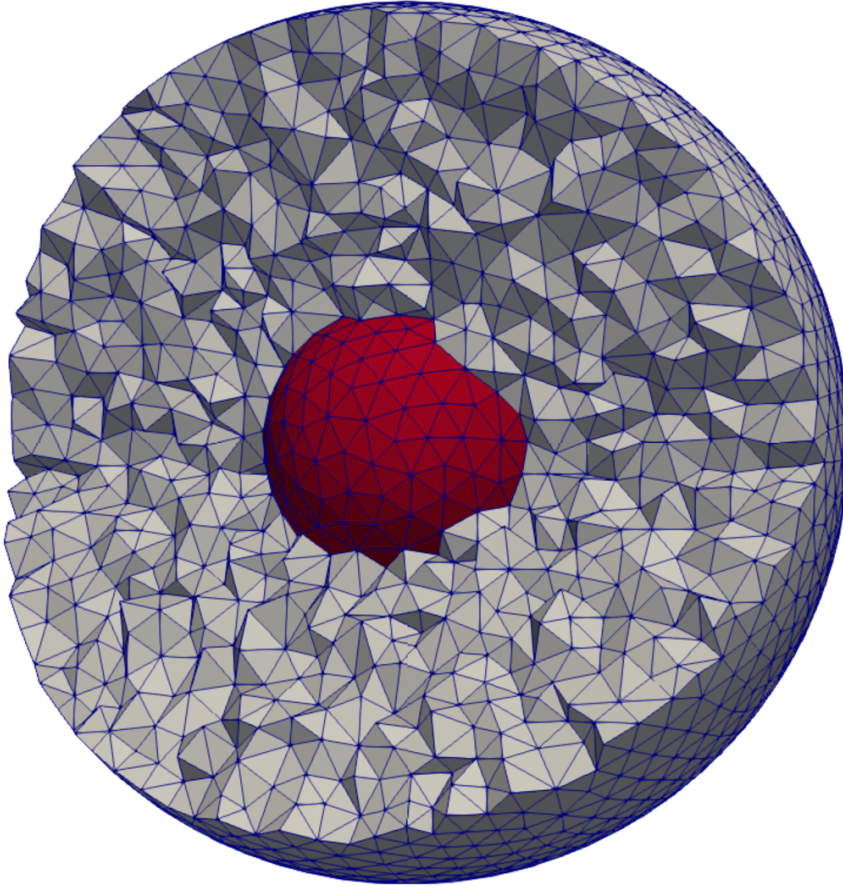
Figure 4.2: Discretization of the domain Ω used in the wave scattering examples. The electrical properties of free space are set in the external sphere. Different electrical properties are set in the scatterer to investigate the resulting scattering patterns.

and $\mu_s = \mu_0$, respectively, such that the wave velocity c_s and the wavelength λ_s in the scatterer are reduced by a factor of $\sqrt{2}$.

As first test case, a wave with the same frequency as in Section 4.1, that is, $f_1 = 300$ MHz, is enforced at the boundary. In the second case, a wave with double the frequency, $f_2 = 600$ MHz, is introduced. To maintain the same ratio between the sampling frequency, $f_s = {}^1/_{\Delta t}$, and the frequencies of the waves, two different time step length are used, $\Delta t_1 = 10^{-11}$ s and $\Delta t_2 = 5 \times 10^{-12}$ s. The total simulation time has also been changed according to the frequencies, $T_{\mathrm{max},1} = 3.33 \times 10^{-8}$ s and $T_{\mathrm{max},2} = 1.67 \times 10^{-8}$ s, such that the number of oscillation periods of the waves is the same in both simulations.

In Figure 4.3 the scattering patterns of the two waves are shown. It is possible to notice how in both test cases the planar wavefront is disturbed by the presence of the obstacle. From the scattering patterns is also possible to notice how the wavelength of the wave within the scatterer is reduced with respect to the wavelength of the unperturbed wave.

Additionally, the maximum amplitude of the wave just after the obstacle increases as the obstacle behaves as a ball lens [148]. The focal length of a ball lens f_{L}, from the centre

(a) Wave frequency $f_1 = 300$ MHz.

(b) Wave frequency $f_2 = 600$ MHz.
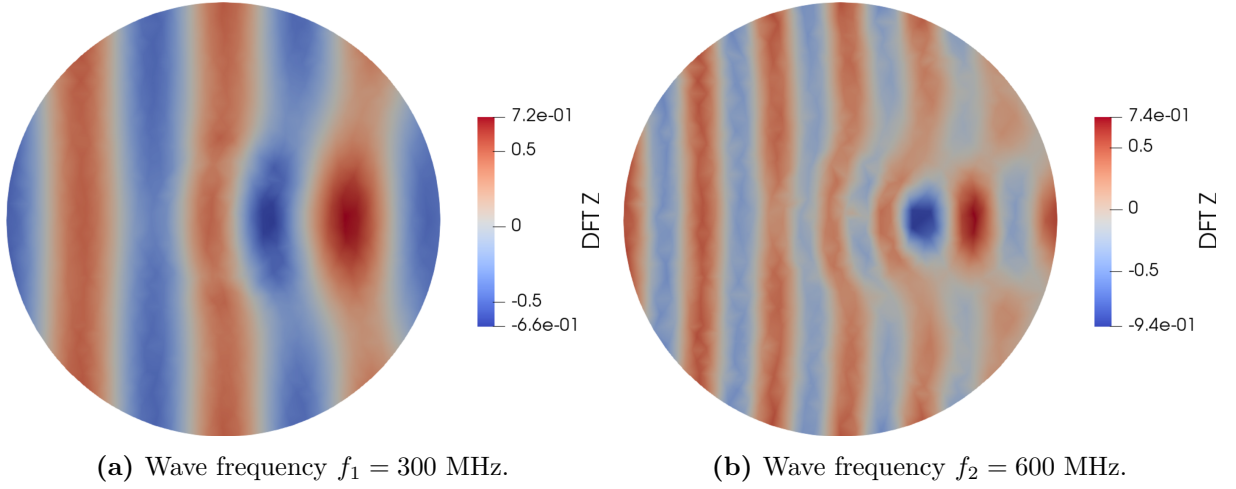
Figure 4.3: Wave scattering by a dielectric sphere: Discrete Fourier transform of E_z for different wave frequencies.

of the sphere, is given by the relation

$$f_{\mathrm{L}} = \frac{rn}{2\,(n-1)},$$

(4.5)

where r is the radius of the sphere and n is the *refractive index* of the material, defined as

$$n = \frac{c_0}{c_s} = \sqrt{\frac{\varepsilon_s \mu_s}{\varepsilon_0 \mu_0}}.$$

(4.6)

In (4.6), c_s is the speed of light in the lens. For a thorough investigation of the optical properties of a ball lens see e.g. [148].

Given the electrical properties of the lens, the refractive index is

$$n = \sqrt{\frac{2\varepsilon_0 \mu_0}{\varepsilon_0 \mu_0}} = \sqrt{2}$$

(4.7)

and a focal length of $f_{\mathrm{L}} \approx 0.85$ is obtained, that is, the lens focuses the radiation beyond its rear surface. However, given the ratio between the dimension of the lens, r, and the waves' wavelengths $\lambda_1 \approx 1$ and $\lambda_2 \approx 0.5$, $r/\lambda \approx 1$, the lens performs poorly with the given waves. Nonetheless, from Figure 4.4, it is possible to notice that the maximum absolute value of E_z over time, $\overline{E_z}(t)$, along the y-axis, is in the proximity of the rear surface of the sphere.

In the ideal case of perfect propagation in a dielectric medium, Figure 4.4 would result in a constant value, as the amplitude of the incoming wave is not affected during the propagation. In this test case instead, as the waves are focused and diffracted by the obstacle, the amplitude varies along the direction of propagation.

49
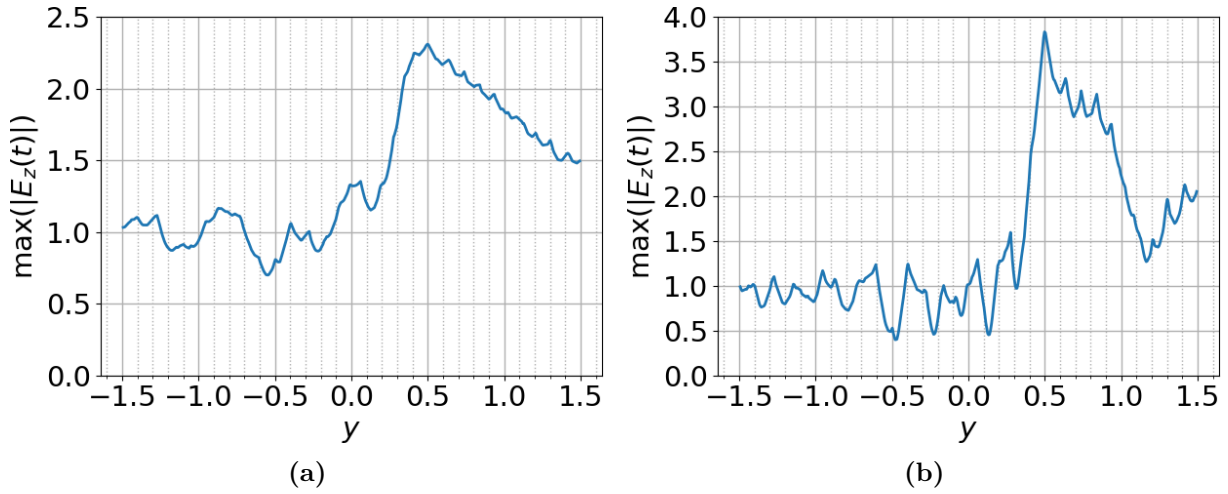
Figure 4.4: Wave scattering by a dielectric sphere: $\overline{|E_z|}$ along the y-axis for different wave frequencies: (a) $f = 300$ Mhz, (b) $f = 600$ Mhz.

4.3 Wave scattering by conductive obstacle

In this section, the dielectric obstacle of Section 4.2 is replaced by a conductive scatterer Ω_s with $\sigma_s \neq 0$. The values of permittivity and permeability of the obstacle are set to $\varepsilon_s = \varepsilon_0$ and $\mu_s = \mu_0$. Various values of conductivity are set in the scatterer to compare the response of the wave to the different conductivity values of the obstacle. The conductivities of choice are: $\sigma_{s,1} = 10^{-3}$ S/m, $\sigma_{s,2} = 10^{-2}$ S/m, $\sigma_{s,3} = 10^{-1}$ S/m. The electrical properties of the domain Ω are left unchanged. The spatial and temporal discretizations are the same used in previous test cases.

In the first test case, a plane wave with frequency $f_1 = 300$ MHz is imposed at the boundary and the scattering is investigated. In Figure 4.5 the results of the simulations for scatterers of increasing conductivities are shown both in terms of DFTs of the electric field and in terms of $\overline{|E_z|}$ along the y-axis. It is possible to notice how, increasing the conductivity of the obstacle, the value of $\overline{|E_z|}$ decreases in the scatter.

Additionally, in Figure 4.5(b), Figure 4.5(d) and Figure 4.5(f) it is possible to appreciate the amount of dissipation due to the conductive scatterers. In the obstacles with conductivity values $\sigma_{s,1}$ and $\sigma_{s,2}$ the value of $\overline{|E_z|}$ decreases approximately 10% and 60% respectively. In the obstacle of conductivity $\sigma_{s,3}$, the wave is almost entirely dissipated.

From the peaks of $\overline{|E_z|}$ for $y < -0.5$ in Figure 4.5(f), is possible to notice that while part of the wave is transmitted through the conductive media, part of it is reflected by the obstacle. The same is true also for the other values of conductivity but the effect in Figure 4.5(b) and Figure 4.5(d) is not as clearly visible as in Figure 4.5(f).

In the second test case the scattering of a wave of frequency $f_2 = 600$ MHz is investigated. The results of the wave scattering by the obstacles of different conductivities are presented in Figure 4.6, where the solutions in the form of the DFTs of the electric fields and the values of $\overline{|E_z|}$ along the propagation axis are shown.

As expected, as the conductivity of the obstacle increases, the amplitude of the wave is increasingly dissipated as it travels through the scatterer. For the scatterer with con-

ductivity $\sigma_{s,3}$, the wave is fully absorbed when, approximately, the coordinate $y = 0$ is reached. Similarly to the wave of frequency f_1, when the obstacle with the highest value of conductivity is used $\sigma_{s,3}$, in Figure 4.6(f) it is possible to notice how the wave is partly reflected by the scatterer towards the negative y-direction.

Comparing Figure 4.5 to Figure 4.6 is possible to notice how, given the same numerical discretization and electric properties in the domain, the waves of different frequencies f_1 and f_2 behave differently. From the graphs of $\overline{|E_z|}$ in the two different test cases, in fact, is possible to notice how the higher frequency wave is dissipated faster as it travels through the obstacle. The comparison between Figure 4.5(b) and Figure 4.6(b) shows that, while the amplitude of the wave of frequency f_2 is reduced to circa 80% of the initial value, the amplitude of the wave of frequency f_1 is reduced to circa 90%. Comparing the simulations with the scatterer of conductivity $\sigma_{s,2}$, Figure 4.5(d) to Figure 4.6(d) the amplitude reduction of the waves of f_1 and f_2 are, respectively, circa 40% and 10% of the original values. Finally, although for the obstacle with higher conductivity $\sigma_{s,3}$, the waves are completely dissipated within the obstacle, it is possible to notice a faster decay of the amplitude of the higher frequency wave.

This result is modeled by equation (2.45) that describes how the amplitude of the wave is damped by conductive media. In fact, in equation (2.45), the term $e^{-\sqrt{\frac{\omega\mu\sigma}{2}}x}$ depends on both the conductivity of the media and on the frequency of the wave. Finally, the reflection of the wave by the obstacle plays a role in the reduction of the amplitude of the transmitted wave.

Finally, it is worth to point out that the peaks in $\overline{|E_z|}$, mostly noticeable in Figure 4.6[(b), (d), (f)], are attributed to numerical artifacts due to the boundary conditions, especially in the early propagation times. In fact, while from the DFTs of the electric fields, Figure 4.6[(a), (c), (e)], it is not possible to notice any peak after the conductive scatterer, in the initial transient of the time evolution it is possible to notice high-amplitude peaks reflecting between the conductive scatterer and the boundaries in the positive region of the y-axis. Hence, to remove such peaks it would be necessary to further extend the simulations in time or extend the boundaries of the domain. However, a full and comprehensive treatise of the physics and numerics of wave scattering by buried objects is not the main goal of this work and is hence left to specialised literature.

(a)

(b)

(c)

(d)

(e)

(f)
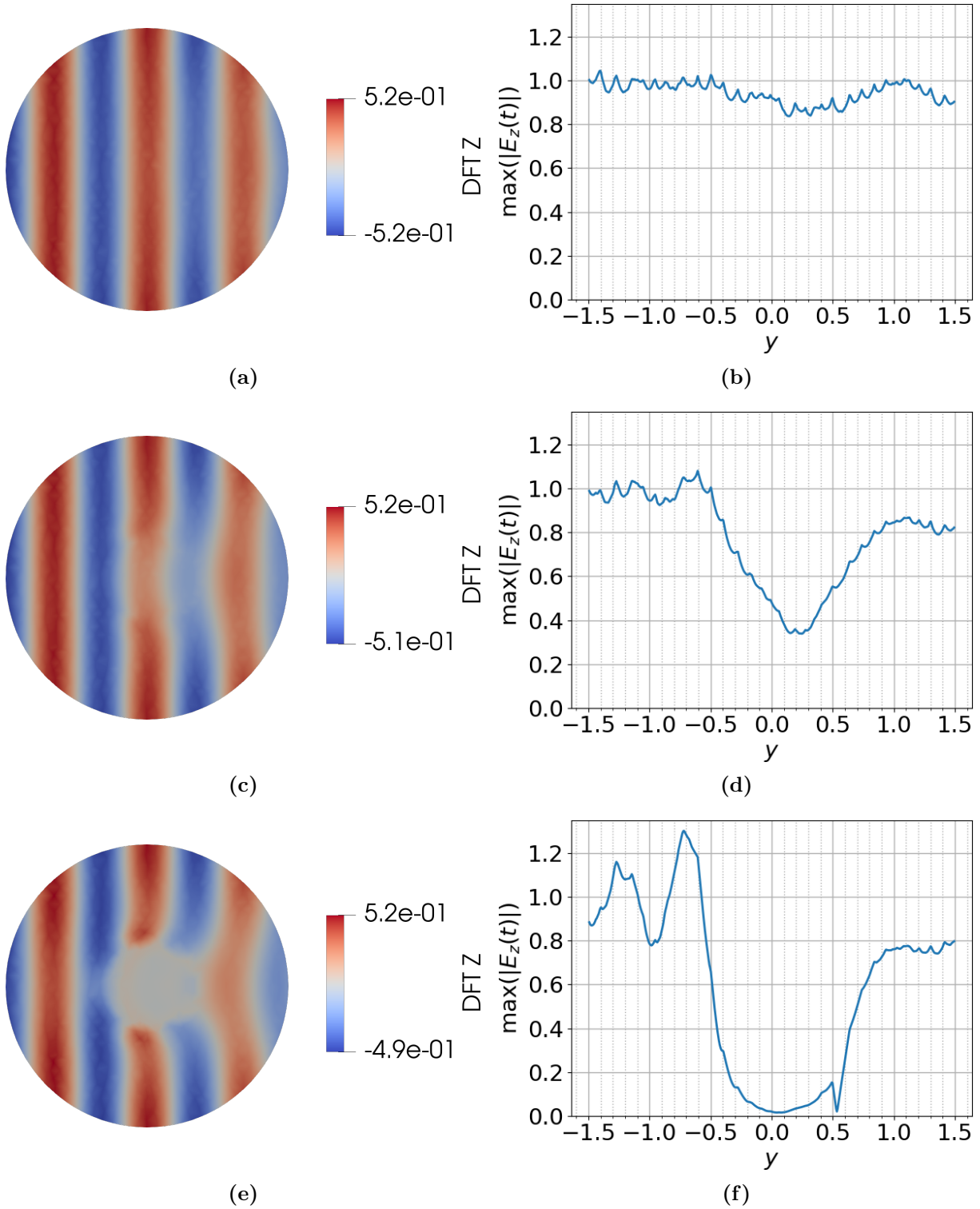
Figure 4.5: Scattering of a wave with frequency $f_1 = 300$ MHz by a conductive sphere. Comparison between discrete Fourier transform of E_z (left) and maximum amplitude of $|E_z|$ over the time (right) for different conductivity values: (a)-(b) $\sigma_{s,1} = 10^{-3}$ S/m; (c)-(d) $\sigma_{s,2} = 10^{-2}$ S/m; (e)-(f) $\sigma_{s,3} = 10^{-1}$ S/m.

(a)

(b)

(c)

(d)

(e)

(f)
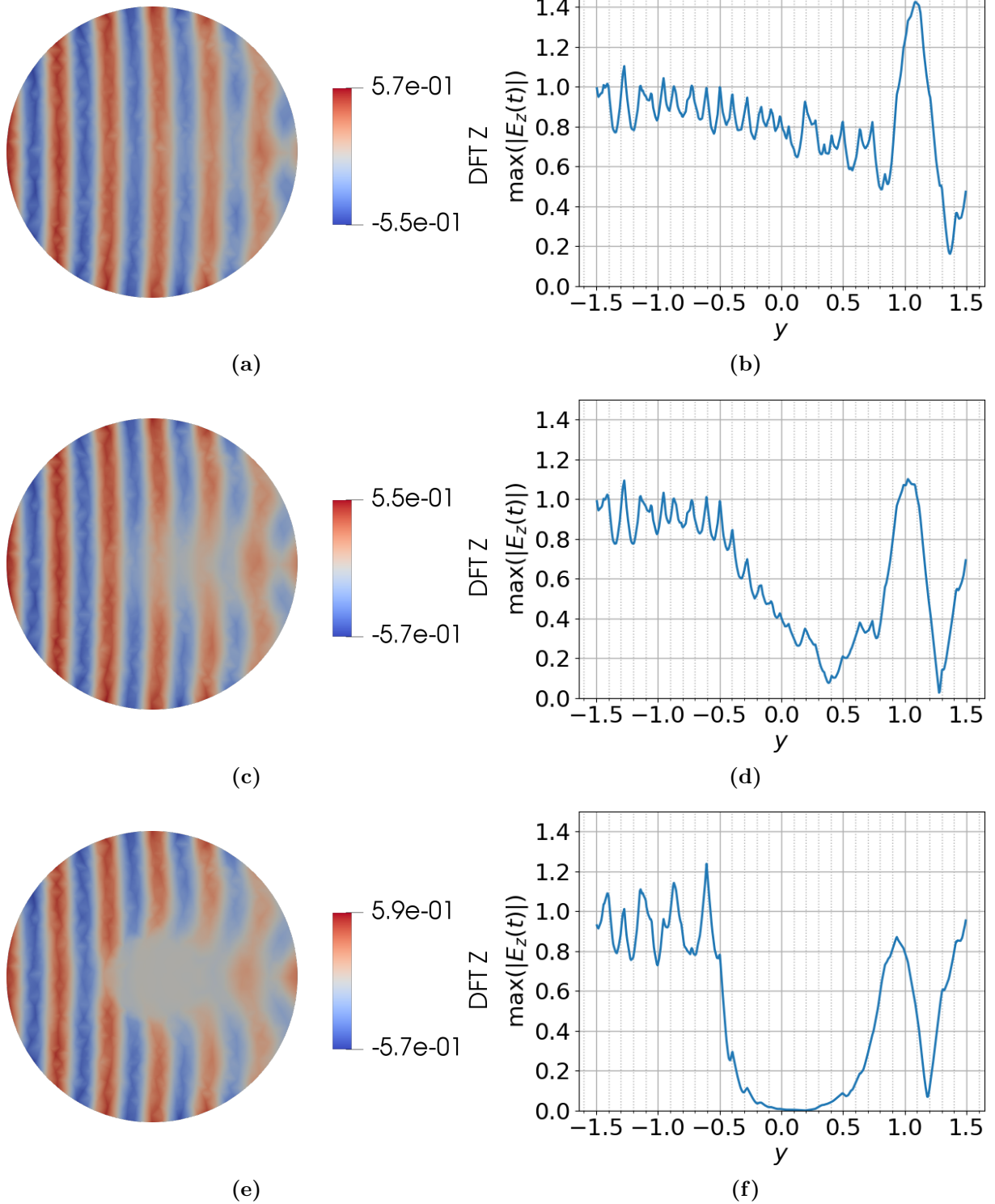
Figure 4.6: Scattering of a wave with frequency $f_2 = 600$ MHz by a conductive sphere. Comparison between discrete Fourier transform of E_z (left) and maximum amplitude of $|E_z|$ over the time (right) for different conductivity values: (a)-(b) $\sigma_{\mathrm{s},1} = 10^{-3}$ S/m; (c)-(d) $\sigma_{\mathrm{s},2} = 10^{-2}$ S/m; (e)-(f) $\sigma_{\mathrm{s},3} = 10^{-1}$ S/m.

5 Electromagnetic diffusion equation formulation

After the investigation of a general purpose HDG formulation for the Maxwell equations in Chapter 3-4, a formulation based on the EMD equation is developed.

In geophysical applications, electromagnetic signals typically propagate through conductive environment such as underground strata-formation or water. In these materials the presence of an electromagnetic field induces electric currents that dissipate the energy of the signals. As already seen in more detail in Chapter 4, high-frequency signals dissipate energy more than low-frequency ones, hence, only the latter propagate over large distances. Therefore, in geophysical applications, frequencies between 1 Hz and 10 Hz are typically used.

From a mathematical point of view, when modelling low-frequency signals in conductive environments, it is possible to neglect the displacement current term with respect to the conductive current obtaining a diffusion equation, as seen in Section 2.1.4 and Section 2.1.5. Therefore, in the proposed formulation the displacement current term is neglected in favour of the conduction current term. However, it is worth to point out that it is possible to extend the proposed formulation for problems with high-frequency signals by adding the displacement current term. The addition of the displacement current term, together with ABCs, would allow for the simulation of wave propagation and scattering problems such as those introduced in Chapter 3 and Chapter 4.

Unfortunately, the addition of a second derivative in time introduces the need for additional initial conditions on the electric field. These conditions can be provided in terms of the value of the time derivative at the initial time or as an additional step in the initialization procedure. Furthermore, BDF schemes for higher-order derivatives require more previous time-steps with respect to BDF schemes for first-order time derivatives. While initial conditions can easily be computed when analytic solutions are available, as in the case of convergence studies, in real-world application scenarios it is typically more complex. In fact, to compute initial conditions for engineering problems, additional problems have to be formulated such as, for example, the DC resistivity problem. For these reasons, the displacement current term will not be included in the proposed formulation.

This chapter is based on [69] and is organised as follows. In Section 5.1 a formulation based on the damped vector wave equation for the electric field is developed. In Section 5.2, a local post-processing algorithm to improve the convergence properties of the method is developed. In Section 5.3, a HDG formulation for the solution of the DC initial problem is introduced. Successively, in Section 5.4, the proposed formulation is modified to improve the condition number of the discretization matrix. Finally, in Section 5.5, the convergence properties of the method are shown.

5.1 Formulation derivation

Starting from the EMD equation (2.46), the auxiliary variable

$$\mathbf{u} = \frac{1}{\mu}\nabla\times\mathbf{E} \tag{5.1}$$

is introduced, obtaining the following set of partial differential equations

$$\mu\mathbf{u} - \nabla\times\mathbf{E} = \mathbf{0}, \tag{5.2a}$$

$$\sigma\partial_t\mathbf{E} + \nabla\times\mathbf{u} = -\partial_t\mathbf{i}_\mathrm{s}. \tag{5.2b}$$

From Faraday's law (2.19c) it is possible to notice that the auxiliary variable $\mathbf{u}$, is related to the magnetic field by the relation

$$\mathbf{u} = -\partial_t\mathbf{H}. \tag{5.3}$$

Moreover, notice that, while a solution in terms of the magnetic field is not directly obtained in this formulation, if proper initial conditions on the magnetic field are provided, it is still possible to reconstruct the field as

$$\mathbf{H} = -\int_{t_0}^{T_\mathrm{max}} \mathbf{u}\ \mathrm{d}t. \tag{5.4}$$

Using the notation introduced in Section 2.2.2, equations (5.2) are multiplied by (discrete) weighting functions $(\mathbf{v}^\mathrm{h}, \mathbf{w}^\mathrm{h}) \in \mathbf{V}^\mathrm{h} \times \mathbf{V}^\mathrm{h}$, and integrated over one element Ω_e with boundary $\partial\Omega_e$

$$\left(\mathbf{v}^\mathrm{h}, \mu\mathbf{u}^\mathrm{h}\right)_{\Omega_e} - \left(\mathbf{v}^\mathrm{h}, \nabla\times\mathbf{E}^\mathrm{h}\right)_{\Omega_e} = \mathbf{0}, \tag{5.5a}$$

$$\left(\mathbf{w}^\mathrm{h}, \sigma\partial_t\mathbf{E}^\mathrm{h}\right)_{\Omega_e} + \left(\mathbf{w}^\mathrm{h}, \nabla\times\mathbf{u}^\mathrm{h}\right)_{\Omega_e} = -\left(\mathbf{w}^\mathrm{h}, \partial_t\mathbf{i}_\mathrm{s}^\mathrm{h}\right)_{\Omega_e}, \tag{5.5b}$$

where $(\mathbf{u}^\mathrm{h}, \mathbf{E}^\mathrm{h}) \in \mathbf{V}^\mathrm{h} \times \mathbf{V}^\mathrm{h}$ are the approximations of the fields $\mathbf{u}$ and $\mathbf{E}$ in the space $\mathbf{V}^\mathrm{h}$ and $\mathbf{i}_\mathrm{s}^\mathrm{h}$ is an L^2 projection of $\mathbf{i}_\mathrm{s}$ onto $\mathbf{V}^\mathrm{h}$.

Summing all the element's contributions and integrating (5.5) by parts, yields

$$\left(\mathbf{v}^\mathrm{h}, \mu\mathbf{u}^\mathrm{h}\right)_{\mathcal{T}^\mathrm{h}} - \left(\nabla\times\mathbf{v}^\mathrm{h}, \mathbf{E}^\mathrm{h}\right)_{\mathcal{T}^\mathrm{h}} - \left\langle\mathbf{v}^\mathrm{h}\times\mathbf{n}, \hat{\mathbf{E}}^\mathrm{h}_{\ \mathrm{t}}\right\rangle_{\partial\mathcal{T}^\mathrm{h}} = \mathbf{0}, \tag{5.6a}$$

$$\left(\mathbf{w}^\mathrm{h}, \sigma\partial_t\mathbf{E}^\mathrm{h}\right)_{\mathcal{T}^\mathrm{h}} + \left(\nabla\times\mathbf{w}^\mathrm{h}, \mathbf{u}^\mathrm{h}\right)_{\mathcal{T}^\mathrm{h}} + \left\langle\mathbf{w}^\mathrm{h}, \mathbf{n}\times\hat{\mathbf{u}}^\mathrm{h}\right\rangle_{\partial\mathcal{T}^\mathrm{h}} = -\left(\mathbf{w}^\mathrm{h}, \partial_t\mathbf{i}_\mathrm{s}^\mathrm{h}\right)_{\mathcal{T}^\mathrm{h}}. \tag{5.6b}$$

The discrete hybrid variable $\mathbf{\Lambda}^\mathrm{h}$, as defined by (3.3), and the definition of the trace value of the auxiliary variable

$$\hat{\mathbf{u}}^\mathrm{h} := \mathbf{u}^\mathrm{h} + \tau\left(\mathbf{E}^\mathrm{h}_{\ \mathrm{t}} - \mathbf{\Lambda}^\mathrm{h}\right)\times\mathbf{n}, \tag{5.7}$$

are introduced in discretized form, obtaining the following

$$\left(\mathbf{v}^\mathrm{h}, \mu\mathbf{u}^\mathrm{h}\right)_{\mathcal{T}^\mathrm{h}} - \left(\nabla\times\mathbf{v}^\mathrm{h}, \mathbf{E}^\mathrm{h}\right)_{\mathcal{T}^\mathrm{h}} - \left\langle\mathbf{v}^\mathrm{h}\times\mathbf{n}, \mathbf{\Lambda}^\mathrm{h}\right\rangle_{\partial\mathcal{T}^\mathrm{h}} = \mathbf{0}, \tag{5.8a}$$

$$\left(\mathbf{w}^\mathrm{h}, \sigma\partial_t\mathbf{E}^\mathrm{h}\right)_{\mathcal{T}^\mathrm{h}} + \left(\nabla\times\mathbf{w}^\mathrm{h}, \mathbf{u}^\mathrm{h}\right)_{\mathcal{T}^\mathrm{h}} + \left\langle\mathbf{w}^\mathrm{h}, \mathbf{n}\times\mathbf{u}^\mathrm{h}\right\rangle_{\partial\mathcal{T}^\mathrm{h}}$$
$$+ \left\langle\mathbf{w}^\mathrm{h}, \tau\left(\mathbf{E}^\mathrm{h}_{\ \mathrm{t}} - \mathbf{\Lambda}^\mathrm{h}\right)\right\rangle_{\partial\mathcal{T}^\mathrm{h}} = -\left(\mathbf{w}^\mathrm{h}, \partial_t\mathbf{i}_\mathrm{s}^\mathrm{h}\right)_{\mathcal{T}^\mathrm{h}}. \tag{5.8b}$$

Notice that for the stabilization parameter τ, the same observations made in Section 3.1 hold, that is, values too close to zero yield ill-defined methods [54] while values that are too high can lead to poor solver efficiency [56, 123].

To close the system of equations, the continuity condition on the auxiliary variable

$$\llbracket \mathbf{n} \times \hat{\mathbf{u}}^{\mathrm{h}} \rrbracket = \mathbf{0} \quad \text{on } \mathcal{E}^0, \tag{5.9}$$

is introduced to enforce the tangential component of $\hat{\mathbf{u}}^{\mathrm{h}}$ to be continuous across inter-element boundaries and to ensure that the method is locally conservative [66].

In this formulation, the weak form of (5.9) has the opposite sign with respect to (3.9)

$$\left\langle \boldsymbol{\eta}^{\mathrm{h}}, \mathbf{u}^{\mathrm{h}} \times \mathbf{n} \right\rangle_{\partial \mathcal{T}^{\mathrm{h}}} - \left\langle \boldsymbol{\eta}^{\mathrm{h}}, \tau \mathbf{E}^{\mathrm{h}} \right\rangle_{\partial \mathcal{T}^{\mathrm{h}}} + \left\langle \boldsymbol{\eta}^{\mathrm{h}}, \boldsymbol{\Lambda}^{\mathrm{h}} \right\rangle_{\partial \mathcal{T}^{\mathrm{h}}} = \mathbf{0}, \tag{5.10}$$

to ensure symmetry in the matrix obtained from the discretization of the equations in the partition $\mathcal{T}^{\mathrm{h}}$ of the domain Ω.

The final problem then reads: find $\left(\mathbf{u}^{\mathrm{h}}, \mathbf{E}^{\mathrm{h}}, \boldsymbol{\Lambda}^{\mathrm{h}} \right) \in \mathbf{V}^{\mathrm{h}} \times \mathbf{V}^{\mathrm{h}} \times \mathbf{M}^{\mathrm{h}}_{\mathrm{t}}(\mathbf{0})$ such that

$$- \left(\mathbf{v}^{\mathrm{h}}, \mu \mathbf{u}^{\mathrm{h}} \right)_{\mathcal{T}^{\mathrm{h}}} + \left(\nabla \times \mathbf{v}^{\mathrm{h}}, \mathbf{E}^{\mathrm{h}} \right)_{\mathcal{T}^{\mathrm{h}}} + \left\langle \mathbf{v}^{\mathrm{h}} \times \mathbf{n}, \boldsymbol{\Lambda}^{\mathrm{h}} \right\rangle_{\partial \mathcal{T}^{\mathrm{h}}} = \mathbf{0}, \tag{5.11a}$$

$$\left(\mathbf{w}^{\mathrm{h}}, \sigma \partial_t \mathbf{E}^{\mathrm{h}} \right)_{\mathcal{T}^{\mathrm{h}}} + \left(\mathbf{w}^{\mathrm{h}}, \nabla \times \mathbf{u}^{\mathrm{h}} \right)_{\mathcal{T}^{\mathrm{h}}} + \left\langle \mathbf{w}^{\mathrm{h}}, \tau \mathbf{E}^{\mathrm{h}}_{\mathrm{t}} \right\rangle_{\partial \mathcal{T}^{\mathrm{h}}}$$

$$- \left\langle \mathbf{w}^{\mathrm{h}}, \tau \boldsymbol{\Lambda}^{\mathrm{h}} \right\rangle_{\partial \mathcal{T}^{\mathrm{h}}} = - \left(\mathbf{w}^{\mathrm{h}}, \partial_t \mathbf{i}_{\mathrm{s}}^{\mathrm{h}} \right)_{\mathcal{T}^{\mathrm{h}}} \tag{5.11b}$$

$$\left\langle \boldsymbol{\eta}^{\mathrm{h}}, \mathbf{u}^{\mathrm{h}} \times \mathbf{n} \right\rangle_{\partial \mathcal{T}^{\mathrm{h}}} - \left\langle \boldsymbol{\eta}^{\mathrm{h}}, \tau \mathbf{E}^{\mathrm{h}}_{\mathrm{t}} \right\rangle_{\partial \mathcal{T}^{\mathrm{h}}} + \left\langle \boldsymbol{\eta}^{\mathrm{h}}, \tau \boldsymbol{\Lambda}^{\mathrm{h}} \right\rangle_{\partial \mathcal{T}^{\mathrm{h}}} = \mathbf{0}, \tag{5.11c}$$

for all $\left(\mathbf{v}^{\mathrm{h}}, \mathbf{w}^{\mathrm{h}}, \boldsymbol{\eta}^{\mathrm{h}} \right) \in \mathbf{V}^{\mathrm{h}} \times \mathbf{V}^{\mathrm{h}} \times \mathbf{M}^{\mathrm{h}}_{\mathrm{t}}(\mathbf{0})$.

In matrix-vector form, (5.11) becomes

$$\begin{bmatrix} \mathbf{0} & \mathbf{0} & \mathbf{0} \\ \mathbf{0} & \mathbb{E} & \mathbf{0} \\ \mathbf{0} & \mathbf{0} & \mathbf{0} \end{bmatrix} \begin{bmatrix} \dot{\mathbf{u}} \\ \dot{\mathbf{E}} \\ \dot{\boldsymbol{\Lambda}} \end{bmatrix} + \begin{bmatrix} \mathbb{A} & \mathbb{B} & \mathbb{C} \\ \mathbb{B}^T & \mathbb{G} & \mathbb{H} \\ \mathbb{C}^T & \mathbb{H}^T & \mathbb{L} \end{bmatrix} \begin{bmatrix} \mathbf{u} \\ \mathbf{E} \\ \boldsymbol{\Lambda} \end{bmatrix} = \begin{bmatrix} \mathbf{0} \\ -\partial_t \mathbf{i}_{\mathrm{s}} \\ \mathbf{0} \end{bmatrix}. \tag{5.12}$$

It is worth pointing out that the proposed formulation can easily be extended to include the displacement current contribution by adding the term

$$\left(\mathbf{w}^{\mathrm{h}}, \varepsilon \partial_{t^2} \mathbf{E}^{\mathrm{h}} \right)_{\mathcal{T}^{\mathrm{h}}} \tag{5.13}$$

to the left-hand side of equation (5.11b) and, therefore, an additional matrix in (5.12). Additionally, it is possible to impose ABCs to this extended, full-wave, formulation in order to solve the wave problems of Chapter 4, previously addressed with the formulation derived in Chapter 3. However, as the current formulation provides enough accuracy for the problems encountered in the following chapters, such extension will be neglected.

5.1.1 Time discretization

The spatial discretization of the EMD equation (2.46) via the novel HDG formulation takes the form of the ODEs in (5.12). It is now necessary to discretize the resulting ODEs in time, in order to be able to numerically compute the solution.

Applying the BDF scheme introduced in (2.76) to the matrix-vector formulation in equation (5.12) takes the form

$$\begin{bmatrix} \mathbb{A} & \mathbb{B} & \mathbb{C} \\ \mathbb{B}^T & \mathbb{E} + \mathbb{G} & \mathbb{H} \\ \mathbb{C}^T & \mathbb{H}^T & \mathbb{L} \end{bmatrix} \begin{bmatrix} \mathbf{u}^n \\ \mathbf{E}^n \\ \mathbf{\Lambda}^n \end{bmatrix} = \begin{bmatrix} \mathbf{0} \\ \tilde{\mathbf{E}} - \partial_t \mathbf{i_s}^n \\ \mathbf{0} \end{bmatrix}, \tag{5.14}$$

where the term $\frac{1}{\beta \Delta t}$ is included in the definition of the matrix $\mathbb{E}$, and the term $\tilde{\mathbf{E}}$ is defined as

$$\tilde{\mathbf{E}} = -\sum_{k=1}^{s} \alpha_{n-k} \mathbb{E} \mathbf{E}^{n-k}. \tag{5.15}$$

One of the advantages of this formulation lies in the absence of the time derivative of the auxiliary variable. In fact, the absence of an evolution equation for the auxiliary variable eliminates the necessity for an initial condition on the auxiliary variable field. Whilst in the mixed-equation formulation the first equation of (3.13) relates the time evolution of the magnetic field to the electric and hybrid variable fields, in the EMD equation formulation, (5.11a) directly relates the value of the auxiliary variable to the electric and hybrid variable fields.

As thoroughly shown in Section 5.3, computing an initial condition for the electric field is a problem per se and requires both additional implementation and computational effort. The fact that the necessity of an initial condition on the magnetic field is eliminated, allows us to avoid the development and solution of an additional magnetostatic problem. Moreover, for time-integration schemes of order higher than two, where more than one previous step is necessary to initialize the algorithm, the computational advantage of the current formulation is further increased.

It is important to notice that, while the structures of the final discretization matrices (3.15) and (5.14) are the same, the definitions of the block matrices are different. For example, in (3.14) the matrix $\mathbb{A}$ contains the discretization of the time derivative of the magnetic field while in (5.12), the matrix $\mathbb{A}$ is a simple mass matrix for the auxiliary variable.

More importantly, the matrix resulting from the discretization of (5.11) is a symmetric matrix. It is therefore possible to reduce the number of block matrices that is necessary to compute and store. Furthermore, the solution of a sparse symmetric linear system matrix is typically more efficient, both by direct and iterative solvers, than the solution of a non-symmetric matrix.

5.1.2 Matrix condensation

As in Section 3.1.2, assembling the element matrices defined by (5.14) in the global stiffness matrix is very expensive and results in a matrix that is unnecessary large. Given the sparsity pattern of the matrix in (5.14), it is possible to condense the matrices at an element level and only assemble the condensed matrices.

In the matrix-vector formulation (5.14), it is possible to identify the blocks

$$
\left[
\begin{array}{cc|c}
\mathbb{A} & \mathbb{B} & \mathbb{C} \\
\mathbb{B}^T & \mathbb{E} + \mathbb{G} & \mathbb{H} \\
\hline
\mathbb{C}^T & \mathbb{H}^T & \mathbb{L}
\end{array}
\right]
\begin{bmatrix}
\mathbf{u}^n \\
\mathbf{E}^n \\
\mathbf{\Lambda}^n
\end{bmatrix}
=
\begin{bmatrix}
\mathbf{0} \\
\tilde{\mathbf{E}} - \mathbf{i_s}^n \\
\mathbf{0}
\end{bmatrix}
\tag{5.16}
$$

and, following the same rationale of Section 3.1.2, the Schur complement[1] can be used to condense the each element matrix, obtaining the equation

$$
\mathbb{K}\mathbf{\Lambda}^n = \mathbf{F}, \tag{5.17}
$$

where

$$
\mathbb{K} = \mathbb{L} - \begin{bmatrix} \mathbb{C}^T & \mathbb{H}^T \end{bmatrix}
\begin{bmatrix} \mathbb{A} & \mathbb{B} \\ \mathbb{B}^T & \mathbb{E} + \mathbb{G} \end{bmatrix}^{-1}
\begin{bmatrix} \mathbb{C} \\ \mathbb{H} \end{bmatrix}, \tag{5.18a}
$$

$$
\mathbf{F} = -\begin{bmatrix} \mathbb{C}^T & \mathbb{H}^T \end{bmatrix}
\begin{bmatrix} \mathbb{A} & \mathbb{B} \\ \mathbb{B}^T & \mathbb{E} + \mathbb{G} \end{bmatrix}^{-1}
\begin{bmatrix} \mathbf{0} \\ \tilde{\mathbf{E}} - \mathbf{i_s}^n \end{bmatrix}. \tag{5.18b}
$$

To further reduce cost of matrix inversion, it is possible to reduce the size of the matrices using the identity

$$
\begin{bmatrix} \mathbb{A} & \mathbb{B} \\ \mathbb{B}^T & (\mathbb{E} + \mathbb{G}) \end{bmatrix}^{-1}
= \begin{bmatrix} 1 & -\mathbb{A}^{-1}\mathbb{B} \\ 0 & 1 \end{bmatrix}
\begin{bmatrix} \mathbb{A}^{-1} & 0 \\ 0 & ((\mathbb{E} + \mathbb{G}) - \mathbb{B}^T\mathbb{A}^{-1}\mathbb{B})^{-1} \end{bmatrix}
\begin{bmatrix} 1 & 0 \\ -\mathbb{B}^T\mathbb{A}^{-1} & 1 \end{bmatrix},
\tag{5.19}
$$

obtaining the following relations

$$
\mathbb{K} = \mathbb{L} - \mathbb{C}^T\mathbb{X} - \mathbb{H}^T\mathbb{Y}, \tag{5.20a}
$$

$$
\mathbf{F} = \mathbb{C}^T\mathbf{x} - \mathbb{H}^T\mathbf{y}, \tag{5.20b}
$$

where the matrices $\mathbb{X}$ and $\mathbb{Y}$ are defined as

$$
\mathbb{X} = \mathbb{A}^{-1}(\mathbb{C} - \mathbb{B}\mathbb{Y}), \tag{5.21a}
$$

$$
\mathbb{Y} = ((\mathbb{E} + \mathbb{G}) - \mathbb{B}^T\mathbb{A}^{-1}\mathbb{B})^{-1}(\mathbb{H} - \mathbb{B}^T\mathbb{A}^{-1}\mathbb{C}), \tag{5.21b}
$$

and the definitions of the vectors $\mathbf{x}$ and $\mathbf{y}$ are the following

$$
\mathbf{x} = \mathbb{A}^{-1}\mathbb{B}\mathbf{y}, \tag{5.22a}
$$

$$
\mathbf{y} = ((\mathbb{E} + \mathbb{G}) - \mathbb{B}^T\mathbb{A}^{-1}\mathbb{B})^{-1}(\tilde{\mathbf{E}} - \mathbf{i_s}^n). \tag{5.22b}
$$

The matrix $\mathbb{K}$ and the vector $\mathbf{F}$ computed element-wise, are assembled in the global matrix. Then, the global system of equations can be solved using either direct or iterative solvers to obtain the solution of the hybrid variable $\mathbf{\Lambda}^n$ in the whole domain.

---

[1]A theoretical background, as well as possible applications of the Schur complement can be found in Appendix B.

Once $\mathbf{\Lambda}^n$ is known globally, the local problem

$$\begin{bmatrix} \mathbf{u}^n \\ \mathbf{E}^n \end{bmatrix} = \begin{bmatrix} \mathbb{A} & \mathbb{B} \\ \mathbb{B}^T & \mathbb{E} + \mathbb{G} \end{bmatrix}^{-1} \begin{bmatrix} -\mathbb{C}\mathbf{\Lambda}^n \\ \tilde{\mathbf{E}} - {\mathbf{i}_\text{s}}^n - \mathbb{H}\mathbf{\Lambda}^n \end{bmatrix}, \tag{5.23}$$

can be solved element-wise, obtaining the local values of $\mathbf{E}^n$ and $\mathbf{u}^n$.

As done for the matrix $\mathbb{K}$, it is possible to substitute (5.19) in (5.23) reducing the size of the matrix that has to be inverted

$$\mathbf{u}^n = \mathbb{A}^{-1}\left(-\mathbb{C}\mathbf{\Lambda}^n - \mathbb{B}\mathbf{E}^n\right), \tag{5.24}$$

$$\mathbf{E}^n = \left((\mathbb{E} + \mathbb{G}) - \mathbb{B}^T\mathbb{A}^{-1}\mathbb{B}\right)^{-1}\left(\tilde{\mathbf{E}} - {\mathbf{i}_\text{s}}^n + \left(\mathbb{B}^T\mathbb{A}^{-1}\mathbb{C} - \mathbb{H}\right)\mathbf{\Lambda}^n\right). \tag{5.25}$$

Again, notice that the local problem is solved individually for each element and is therefore well suited for parallelization.

5.2 Local post-processing

The optimal convergence rates achieved by HDG methods in both the primary variable and auxiliary variable allow to improve the accuracy of the approximation of the primary variable via post-processing algorithms, see e.g. [53, 54, 57–59, 61, 66, 69, 140, 149]. With post-processing, the approximation of the primary variable is enhanced exploiting the accuracy of the approximation of the auxiliary variable. In order to obtain an improved solution of the primary variable, in fact, it is necessary to obtain optimal convergence of both the primary and the auxiliary variable. In this section, the post-processing algorithm of [69] is presented. Notice that the algorithm is adapted for the current formulation from [59], where it is developed for a mixed-equation formulation.

With post-processing, we seek an approximation for the electric field, $\mathbf{E}^*$, that converges with order $k+1$ in the H^curl-norm. The improved approximation of the electric field, $\mathbf{E}^*$, is obtained as the solution to the problem: find $\mathbf{E}^* \in \mathcal{P}^d_{k+1}(\Omega_e)$ such that

$$(\nabla\times\mathbf{w}^\text{h}, \nabla\times\mathbf{E}^*) = (\nabla\times\mathbf{w}^\text{h}, \mu\mathbf{u}^\text{h}), \tag{5.26a}$$

$$(\nabla\psi^\text{h}, \mathbf{E}^*) = (\nabla\psi^\text{h}, \mathbf{E}^\text{h}), \tag{5.26b}$$

$\forall(\mathbf{w}^\text{h}, \psi^\text{h}) \in \mathcal{P}^d_{k+1}(\Omega_e) \times \mathcal{P}_{k+2}(\Omega_e)$.

It is worth to point out that, in equation (5.26), only quantities that are local both in time and space appear. It is therefore possible to compute the improved solution at an element level independently for each time-step. This does not only result in implementations that are well suited for parallelization but, also, provides the flexibility of allowing the computation of the improved solution only in regions of the domain, and for time-steps, where higher accuracy is required.

Notice that in the local post-processing problem (5.26), the fields $\mathbf{E}^\text{h}, \mathbf{E}^*, \mathbf{w}^\text{h}$ and ψ^h belong to spaces of polynomials of different orders. It is therefore important to choose carefully the numerical integration rules, and the number of integration points used to integrate the products in (5.26). Furthermore, the resulting linear system of equations is overdetermined and can not be solved by standard direct linear solvers. For the solution of this system we use LAPACK's least-square solver [150] via the Trilinos package [151].

5.3 Direct current problem

For the solution of time-dependent problems, appropriate initial conditions are necessary. In electromagnetics, the initial conditions have to satisfy the divergence-free conditions on the magnetic (2.1a) and electric (2.1b) fields. Unless the initial conditions are manufactured to satisfy these conditions, such as, for example, zero fields or analytical solutions, it is necessary to obtain a stationary solution that can be used as initial field.

One way of producing suitable initial conditions, is to simulate the transient response of a zero field to a source signal until the stationary state is reached. However, while this approach is perfectly sound from a mathematical point of view, it is not the most efficient way to obtain a stationary solution in a numerical setting. Long-term numerical integration of evolution equations, necessarily results in a loss of accuracy of the solution as, at each time-step, different sources of errors sum-up. This phenomenon is well known in any field that requires long-term numerical integration of evolution equations, see e.g. [116,117,152,153]. To reduce the errors introduced by long-term integration, different approaches have been used in different fields. Examples of such approaches are those developed for meteorological simulations and fluid mechanics where energy conserving finite difference schemes, spectral methods and structure-preserving discretizations have been developed and used, see e.g. [153–158].

Another way to obtain initial conditions for the electromagnetic fields, is to develop solvers based on the equations of electrostatics and magnetostatics. While in this approach it is necessary to implement additional solvers, the computational cost is typically lower than that of long-term numerical integration.

A stationary electric field satisfying (2.1b) can be obtained as the solution of the DC resistivity problem (2.23) introduced in Section 2.1.3, see e.g. [97,98,105,106]. To obtain the solution of static magnetic fields in conductive media, it is necessary to solve a magnetostatic problem such as those presented in [108,119,120], to cite a few. However, given that the proposed formulation only includes the evolution equation for the electric field, see Section 5.1, the solution of a magnetostatic problem is not required.

The DC resistivity problem can be solved with any discretization technique and the solution interpolated to the discretization used by the HDG method. However, as the solution of the DC problem is to be used as the initial condition in our geophysical application, it is necessary to be able to solve the DC problem in the same domain. Therefore, to ensure that it is possible to compute a solution of the DC problem in any domain, it is necessary to use a discretization method that allows the same flexibility of the HDG method used to discretize the EMD equation. Once again, our choice is to discretize the EMD equation making use of an HDG method. The property of HDG methods to obtain high-order approximations on the primary and flux variables, is of particular importance in our application, where the interest is not in the primary variable, ϕ, but rather its derivatives, $\mathbf{E} = -\nabla\phi$.

In standard FEM methods, the electric field can be obtained from the solution of the DC problem computing the gradient of the electric potential along the edges of the elements [105]. However, the derivatives of the approximated electric potential have a lower-order of accuracy with respect to the field they are computed from. The lower-

order approximation of the electric field can then be interpolated on the nodes of the HDG discretization to be used as an initial condition.

Solving the DC problem via the HDG method instead, provides an electric field that converges with the same order as the electric potential and the solution is computed in the nodes of the discretization, rather than along the edges. Hence, the solution of the DC problem via an HDG method can directly be used as initial condition for the EMD equation. Additionally, with HDG methods, it is possible to locally increase the order of approximation obtaining a more accurate approximation in parts of the domain where higher accuracy is necessary, such as near sources, receivers and in the presence of highly heterogeneous media, while reducing the computational cost by reducing the polynomial order of approximation where a lower accuracy is required.

Furthermore, it could be possible to take advantage of the superconvergence of properties of HDG methods as an error estimator for polynomial adaptivity in regions of the domain that require additional accuracy, as proposed in [61, 124, 125]. post-processing algorithms for diffusion equations have been extensively investigated in the past [53, 54, 60], to cite a few.

5.3.1 Hybridizable Discontinuous Galerkin formulation

The HDG formulation used to solve the EMD problem, is a diffusion equation formulation for the electric potential. The application of HDG methods to diffusion equation has been investigated thoroughly in a variety of different fields, see e.g. [53, 54, 57, 61, 159].

For the derivation of the HDG formulation we start by introducing the auxiliary variable, $\mathbf{u}$, in the diffusion equation for the electric potential (2.23)

$$\Delta\left(\sigma\phi\right) = \nabla\cdot\mathbf{i}_\mathrm{s},$$

obtaining the following set of equations

$$\sigma\nabla\phi - \mathbf{u} = \mathbf{0}, \tag{5.27a}$$
$$\nabla\cdot\mathbf{u} = \nabla\cdot\mathbf{i}_\mathrm{s}. \tag{5.27b}$$

Given the definitions of the auxiliary variable (5.27a) and of the electric potential (2.22), the relation between the auxiliary variable and the electric field is given by

$$\mathbf{u} = -\sigma\mathbf{E}. \tag{5.28}$$

Using the notation introduced in Section 2.2.2, we substitute the fields ϕ and $\mathbf{u}$ by discrete approximations $(\phi^\mathrm{h}, \mathbf{u}^\mathrm{h}) \in V^\mathrm{h} \times \mathbf{V}^\mathrm{h}$, multiply the equations with discrete weighting functions $(\mathbf{v}^\mathrm{h}, r^\mathrm{h}) \in \mathbf{V}^\mathrm{h} \times V^\mathrm{h}$ and integrate over one element Ω_e, obtaining

$$\left(\mathbf{v}^\mathrm{h}, \sigma\nabla\phi^\mathrm{h}\right)_{\Omega_e} - \left(\mathbf{v}^\mathrm{h}, \mathbf{u}^\mathrm{h}\right)_{\Omega_e} = \mathbf{0}, \tag{5.29a}$$
$$\left(r^\mathrm{h}, \nabla\cdot\mathbf{u}^\mathrm{h}\right)_{\Omega_e} - \left(r^\mathrm{h}, \nabla\cdot\mathbf{i}_\mathrm{s}^\mathrm{h}\right)_{\Omega_e} = 0. \tag{5.29b}$$

The hybrid variable Λ^h is now defined as

$$\begin{aligned}\Lambda^\mathrm{h} &:= \hat{\phi}^\mathrm{h} \quad \forall F \in \mathcal{E}^0,\\ \Lambda^\mathrm{h} &:= 0 \quad\ \ \forall F \in \mathcal{E}^\partial \cap \Gamma_D,\end{aligned} \tag{5.30}$$

such that $\Lambda^h \in M^h(0)$.

Introducing the definition of the hybrid variable (5.30) and the definition of the numerical flux of the auxiliary variable

$$\hat{\mathbf{u}}^h := \mathbf{u}^h + \tau(\Lambda^h - \phi^h)\mathbf{n}, \qquad (5.31)$$

in (5.29), integrating by parts and summing all the element contributions yields

$$\left(\mathbf{v}^h, \sigma^{-1}\mathbf{u}^h\right)_{\mathcal{T}^h} + \left(\nabla\cdot\mathbf{v}^h, \phi^h\right)_{\mathcal{T}^h} - \left\langle\mathbf{v}^h\cdot\mathbf{n}, \Lambda^h\right\rangle_{\partial\mathcal{T}^h} = \mathbf{0}, \qquad (5.32a)$$

$$\left(r^h, \nabla\cdot\mathbf{u}^h\right)_{\mathcal{T}^h} - \left\langle r^h, \tau\phi^h\right\rangle_{\partial\mathcal{T}^h} + \left\langle r^h, \tau\Lambda^h\right\rangle_{\partial\mathcal{T}^h} = -\left(r^h, \nabla\cdot\mathbf{i}_s^{\ h}\right)_{\mathcal{T}^h}. \qquad (5.32b)$$

The continuity condition is introduced, similary to (3.9) and (5.10), as

$$\left\langle\mu, \mathbf{u}^h\cdot\mathbf{n}\right\rangle_{\partial\mathcal{T}^h} - \left\langle\mu, \tau\phi^h\right\rangle_{\partial\mathcal{T}^h} + \left\langle\mu, \tau\Lambda^h\right\rangle_{\partial\mathcal{T}^h} = 0, \qquad (5.33)$$

to weakly enforce the continuity of the auxiliary variable across elements.

Finally, the DC problem reads: find $(\mathbf{u}^h, \phi^h, \Lambda^h) \in \mathbf{V}^h \times V^h \times M^h(0)$ such that:

$$\left(\mathbf{v}^h, \sigma^{-1}\mathbf{u}^h\right)_{\mathcal{T}^h} + \left(\nabla\cdot\mathbf{v}^h, \phi^h\right)_{\mathcal{T}^h} - \left\langle\mathbf{v}^h\cdot\mathbf{n}, \Lambda^h\right\rangle_{\partial\mathcal{T}^h} = \mathbf{0}, \qquad (5.34a)$$

$$\left(r^h, \nabla\cdot\mathbf{u}^h\right)_{\mathcal{T}^h} - \left\langle r^h, \tau\phi^h\right\rangle_{\partial\mathcal{T}^h} + \left\langle r^h, \tau\Lambda^h\right\rangle_{\partial\mathcal{T}^h} = -\left(r^h, \nabla\cdot\mathbf{i}_s^{\ h}\right)_{\mathcal{T}^h}, \qquad (5.34b)$$

$$-\left\langle\mu^h, \mathbf{u}^h\cdot\mathbf{n}\right\rangle_{\partial\mathcal{T}^h} + \left\langle\mu^h, \tau\phi^h\right\rangle_{\partial\mathcal{T}^h} - \left\langle\mu^h, \tau\Lambda^h\right\rangle_{\partial\mathcal{T}^h} = 0, \qquad (5.34c)$$

for all $(\mathbf{v}^h, r^h, \mu^h) \in \mathbf{V}^h \times V^h \times M^h(0)$.

Notice that

$$M^h(f) = \{\mu \in M^h : \mu = \Pi(f) \text{ on } \partial\Omega\}, \qquad (5.35)$$

where $\Pi(f)$ is a projection of f onto M^h.

The proposed formulation can be expressed in matrix-vector form as

$$\begin{bmatrix} \mathbb{A} & \mathbb{B} & \mathbb{C} \\ \mathbb{B}^T & \mathbb{G} & \mathbb{H} \\ \mathbb{C}^T & \mathbb{H}^T & \mathbb{L} \end{bmatrix} \begin{bmatrix} \mathbf{u}^h \\ \phi^h \\ \Lambda^h \end{bmatrix} = \begin{bmatrix} \mathbf{0} \\ -\nabla\cdot\mathbf{i}_s^{\ h} \\ 0 \end{bmatrix}. \qquad (5.36)$$

Notice that the discretization matrix (5.36) is a symmetric matrix.

Similarly to the formulations proposed in Section 3.1 and Section 5.1, the element matrix (5.36) can be assembled in a global matrix containing both the global and local problems. However, assembling (5.36) as is, results in an unnecessarily large matrix. On the contrary, it is possible to condense the element matrices such that a smaller matrix has to be solved, thus improving the performances of the solver. The condensation procedure follows the same rationale of Section 3.1.2 and Section 5.1.2 and is therefore not shown for this formulation.

Finally, it is worth to point out that, as the current formulation is developed for a stationary problem, the spatial discretization of the equations does not result in an ODE in time. Hence, it is possible to compute a solution to the problem as is without additional discretization steps.

5.3.2 Boundary conditions

To make the DC problem well posed, boundary conditions have to be enforced on the boundaries of the domain. Different types and combinations of boundary conditions have been developed for DC resistivity problems, from the simplest Dirichlet and Neumann boundary conditions, to more complex mixed-boundary conditions [84, 95, 98, 103, 105].

In our electric field time-domain approach, we opted for the simpler PEC boundary conditions and extend the boundaries of the domain far enough from the area of interest, such that possible boundary effects do not interfere with the solution, see Section 2.2.3. Consequently, as the DC problem is solved in the same domain in which the EMD equation is solved, it is possible to take advantage of the already extended domain and employ Dirichlet boundary conditions avoiding the implementation of ad-hoc boundary conditions, following the same rationale used in [105].

However, as different boundary conditions can lead to substantially different approximations, with Neumann BC overestimating and Dirichlet BC underestimating the solution of the electric potential [103], we investigated the effect of the different boundary conditions on the electric field. In Figure 5.1, the solutions obtained imposing Dirichlet and Neumann BC are compared. As expected, in our tests the difference between the solutions increases, for both $|\phi|$ and $|E_x|$, as we get closer to the boundaries, see Figure 5.1(a) and Figure 5.1(c). However, the differences in the approximations of $|\phi|$ and $|E_x|$ obtained imposing different BCs are not appreciable in the area of interest, see Figure 5.1(b) and Figure 5.1(d), justifying our approach.

5.4 Implementation aspects and condition number improvement

The numerical solution of the EMD problem (5.11), is obtained solving the linear system (5.14) for all $n > 0$ such that $n\Delta t \leq T_{\max}$. Hence, for typical values of $T_{\max}$ and Δt, a large number of linear solutions is required. Additionally, as the computational cost of the solution of linear systems increases with the matrix size, in real-world applications the computational cost of each simulation is dominated by the cost of the linear solver. While the development of linear solvers is not the main interest of this work, it is essential to have a basic understanding of the available solvers with their advantages and disadvantages in order to be able to obtain solutions in a reasonable time.

The simplest linear solvers available are direct solvers. Direct solvers are the most robust solvers available. Their solution does not depend on the structure of the matrix and the solution accuracy is controlled by the condition number of the matrix and the machine precision [160]. The computational cost of direct solvers is mostly influenced by the size and not by the properties of the matrices and, therefore, these solvers are mostly used for the solution of small linear system of equations. In fact, direct solvers are memory intensive and their computational cost is approximately that of matrix multiplication. Although in FEM applications it is typically possible to store matrices in a sparse fashion, reducing both the memory requirement and the computational cost of their solution, their application to larger system is usually impractical.
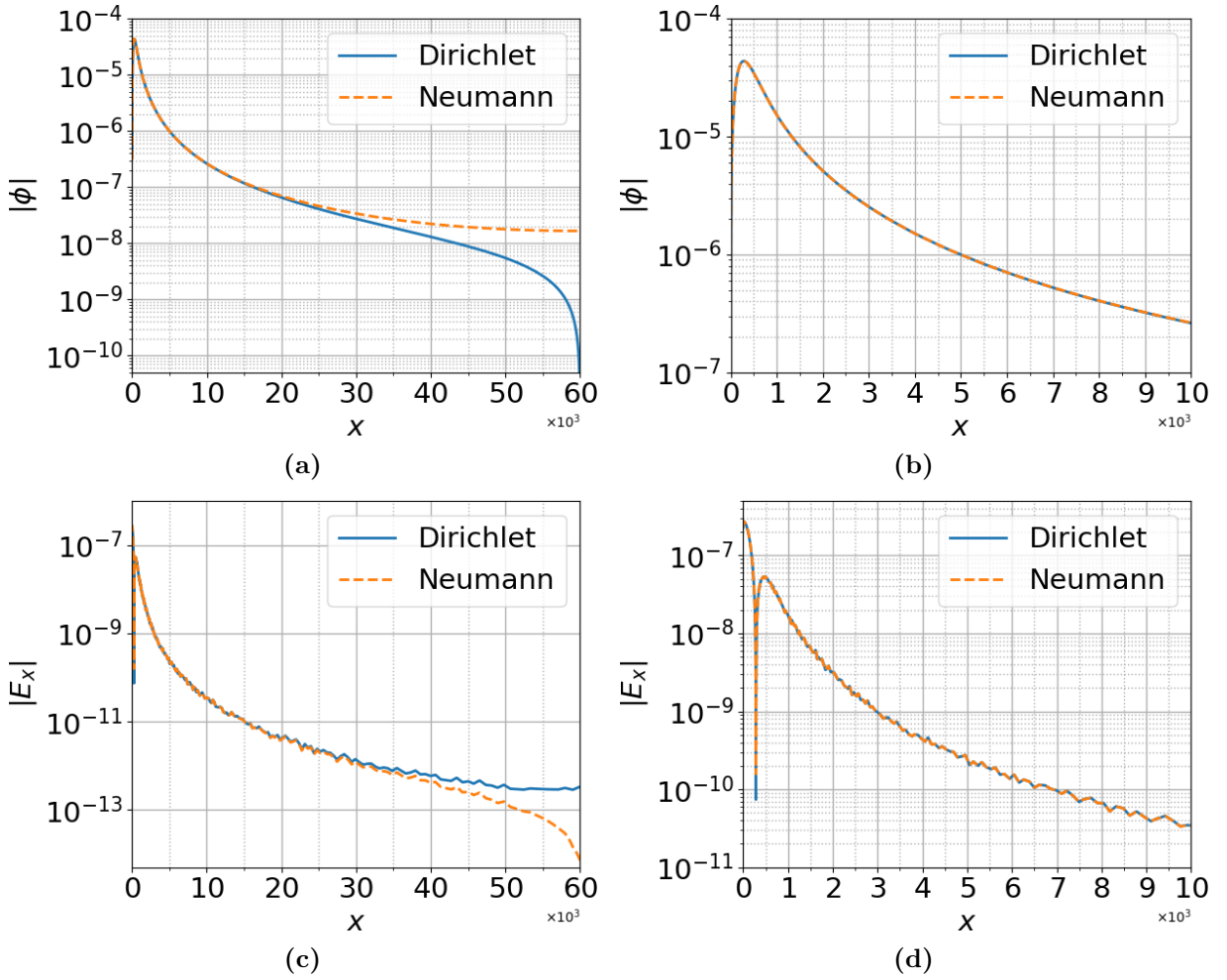
Figure 5.1: Absolute value of the potential and x-component of the electric field along the x-direction at a depth of 10 m. (a) $|\phi|$ from the origin to the boundaries of the domain. (b) $|\phi|$ in the area of interest. (c) $|E_x|$ from the origin to the boundaries of the domain. (d) E_x in the area of interest.

Whereas simple direct solvers can efficiently be used on small system of equations, for large systems, as those resulting from the discretization of the EMD equation on large domains, iterative solvers are typically used. In iterative solvers, the solution is obtained by iteratively improving a provided initial guess, until some user-defined stopping criteria is met. The different iterative methods differ in the algorithms used to update the solution at each iteration.

The computational cost of iterative solvers can mostly be reconducted to the cost of matrix-vector multiplication $O(n^2)$, rather than matrix-matrix multiplication or matrix inversion $O(n^3)$, hence these methods are better suited for the solution of large system of equations. The matrices resulting from the discretization of PDEs are typically sparse, hence the computational cost of matrix-vector multiplication necessary to solve the system is further decreased. Additionally, in iterative solvers it is not necessary to store large,

full, decomposition matrices, as is the case in direct solvers, thus reducing both memory usage and overall computational cost.

Unfortunately, however, the number of iterations necessary to obtain acceptable solutions, depends on the structure and properties of the matrices, on the condition number and on the preconditioning techniques used. It is therefore important, while developing novel formulations, to make sure that the matrix resulting from the discretization of the equations can efficiently be solved by modern solvers.

Of utmost importance to improve the efficiency of iterative linear solvers, is the application of appropriate preconditioners to the system of equations. An efficient preconditioner is a matrix that is a good approximation of the inverse of the linear system matrix, is computationally inexpensive to compute and, at the same time, contains a small number of non-zero entries, reducing the memory necessary for storage and the number of operations for matrix-matrix multiplications [161, 162]. Because of the different properties of linear system matrices resulting from different engineering problems, several preconditioner have been developed, see e.g. [161, 163–169].

The preconditioner that provides convergence with the smallest number of iterations, however, is not necessarily the most computationally efficient one. In fact, even though Algebraic multigrid (AMG), see e.g. [169], preconditioners are a necessary prerequisite for the solution of complex problems such as those shown in Chapter 6-7, it was noticed that the ILU, see e.g. [167, 170], preconditioner provides solver performances comparable to AMG preconditioners when applied to smaller test cases such as those used for convergence studies in Section 5.5. However, while the small test cases presented in Section 5.5 can be solved both via direct and iterative solvers, for those presented in Chapter 6 and Chapter 7, iterative solvers are typically more efficient. Hence, to achieve acceptable solution times in the aforementioned problems, it is necessary to build an efficient setup for preconditioners and solvers.

Unfortunately, in the real-world scenarios modeled in Chapter 6 and Chapter 7, the low value of magnetic permeability, $\mu_0 \approx 10^{-6}$ H/m, the heterogeneous distribution of electric conductivity and the unstructured meshes, make the matrices extremely ill-conditioned and, thus, not well suited for iterative solvers. Moreover, because of the size of the system, solution via direct solvers is prohibitive. In fact, in our first tests for the solution of the problem described in Chapter 6, it was noticed that carefully setting up AMG preconditioners did not improve the condition number enough to make the simulations affordable.

A careful investigation revealed that, while the condition number worsens with a decreasing value of magnetic permeability, the opposite effect can be obtained decreasing the time-step size. This behaviour is to be expected as both the time-step, Δt, and the magnetic permeability, μ, are present in the diagonal entries of the matrix. Furthermore, the terms present in the first row of the matrix equation (5.14) are extremely unbalanced because of the extremely small permeability value. Assuming a uniform, structured, mesh with element size $h = 1$, the matrices $\mathbb{B}$ and $\mathbb{C}$ have entries of the order $O(1)$, while the matrix $\mathbb{A}$ has entries of the order $O(\mu)$, that is, circa 6 orders of magnitude smaller. In a similar way, in the second row of the matrix equation (5.14), while the matrices $\mathbb{B}^T$ and $\mathbb{H}$ have entries of the order $O(1)$, the matrix $\mathbb{G} + \mathbb{E}$ has entries of the order $\sigma/\Delta t$, that

is, several orders of magnitude bigger. Additionally, the stark difference in coefficients leads to rows that have very different norms and, as a consequence, iterative linear solvers cannot be successfully and efficiently applied to the system [171].

5.4.1 Formulation-conditioning

To improve the efficiency of iterative solvers, it is possible to rebalance the rows' norms of the matrix by row equilibration or performing a "formulation-preconditioning" before the application of preconditioners. In the formulation-preconditioning approach, the equations are reorganised in order to smoothen the differences between equations.

In the matrix-vector formulation (5.14) the balancing can be achieved expressing the permeability coefficient as the product

$$\mu = \mu^{1-\alpha}\mu^{\alpha} \tag{5.37}$$

where the coefficient α is chosen such that

$$\frac{\mu^{\alpha}}{\Delta t} = \mu^{1-\alpha}, \tag{5.38}$$

and can be obtained from the relation

$$\alpha = \frac{1}{2}\left(1 + \log_{\mu}(\Delta t)\right) = \frac{1}{2}\left(1 + \frac{\log(\Delta t)}{\log(\mu)}\right). \tag{5.39}$$

Notice that for a value $\mu = 1$ equation (5.39) is undefined. Therefore the proposed algorithm is used only for $\mu \leq 10^{-1}$ H/m.

Substituting (5.37) and rearranging the coefficients (5.41) between the equations (5.11a) and (5.11b) the following is obtained

$$-\left(\mathbf{v}^{\mathrm{h}}, \mu^{1-\alpha}\mathbf{u}^{\mathrm{h}}\right)_{\mathcal{T}^{\mathrm{h}}} + \left(\nabla\times\mathbf{v}^{\mathrm{h}}, \mathbf{E}^{\mathrm{h}}\right)_{\mathcal{T}^{\mathrm{h}}} + \left\langle\mathbf{v}^{\mathrm{h}}\times\mathbf{n}, \mathbf{\Lambda}^{\mathrm{h}}\right\rangle_{\partial\mathcal{T}^{\mathrm{h}}} = \mathbf{0}, \tag{5.40a}$$

$$\left(\mathbf{w}^{\mathrm{h}}, \sigma\mu^{\alpha}\partial_t\mathbf{E}^{\mathrm{h}}\right)_{\mathcal{T}^{\mathrm{h}}} + \left(\mathbf{w}^{\mathrm{h}}, \nabla\times\mathbf{u}^{\mathrm{h}}\right)_{\mathcal{T}^{\mathrm{h}}} + \left\langle\mathbf{w}^{\mathrm{h}}, \tau\hat{\mathbf{E}}^{\mathrm{h}}_{\mathrm{t}}\right\rangle_{\partial\mathcal{T}^{\mathrm{h}}}$$
$$-\left\langle\mathbf{w}^{\mathrm{h}}, \tau\mathbf{\Lambda}^{\mathrm{h}}\right\rangle_{\partial\mathcal{T}^{\mathrm{h}}} = -\left(\mathbf{w}^{\mathrm{h}}, \mu^{\alpha}\partial_t\mathbf{i}_{\mathrm{s}}^{\mathrm{h}}\right)_{\mathcal{T}^{\mathrm{h}}} \tag{5.40b}$$

Notice that the coefficient μ^{α} is also present on the right-hand side of (5.40b). However, the right-hand side does not contribute to the condition number of the matrix and can hence be seen as a simple scale factor.

We can now define the coefficients $C_{\mathbb{A}}$ and $C_{\mathbb{E}}$

$$C_{\mathbb{A}} = \mu^{1-\alpha}, \tag{5.41a}$$

$$C_{\mathbb{E}} = \frac{\mu^{\alpha}}{\Delta t}. \tag{5.41b}$$

that are responsible for the order of magnitude of the matrices $\mathbb{A}$ and $\mathbb{E}$. Notice that the coefficient Δt in $C_{\mathbb{E}}$ derives from the discretization of the time derivative of the electric field. From (5.38), follows that

$$C_{\mathbb{A}} = C_{\mathbb{E}}, \tag{5.42}$$

and, substituting (5.41) in (5.37), the following relation is obtained

$$\mu = C_{\mathbb{A}} C_{\mathbb{E}} \Delta t. \tag{5.43}$$

Furthermore, it is worth to point out that, as the coefficients $C_{\mathbb{A}}$ and $C_{\mathbb{E}}$ only appear in the diagonal blocks of the matrix (5.14), its structure is not modified by the algorithm. Hence, the matrix resulting from the discretization of (5.40) is still a symmetric matrix.

The rows and columns of the matrix-vector equation resulting form (5.40) are better balanced than those in (5.14). Additionally, notice that the first term of (5.11a) and (5.11b) differ by the factors σ and β. The coefficient β, obtained discretizing the time derivative via BDF schemes, can be neglected in the definition (5.38) as it is of the order $O(1)$ in the BDF schemes up to the fourth-order used in this work. Moreover, accounting for the value of electric conductivity by replacing (5.38) with

$$\sigma \frac{\mu^{\alpha}}{\Delta t} = \mu^{1-\alpha}, \tag{5.44}$$

did not show an improvement on the number of iterations necessary to solve the problems of Chapter 6 and Chapter 7 and was, therefore, not further investigated. Further investigation, however, is required to explore the effect of (5.44) in problems with extreme values of electrical conductivity.

5.4.2 Effects of formulation-conditioning on the condition number

Given the relation (5.42) between the coefficients $C_{\mathbb{A}}$ and $C_{\mathbb{E}}$, we can study the order of magnitude of the first term of equation (5.11a) or, similarly, (5.11b) computing the value of the $C_{\mathbb{A}}$ only. Therefore, in Figure 5.2 the dependence of the coefficient $C_{\mathbb{A}}$ on the magnetic permeability and time-step length are shown. The case of $\alpha = \frac{1}{2}$, obtained for $\Delta t = 1$ s, is added for comparison.
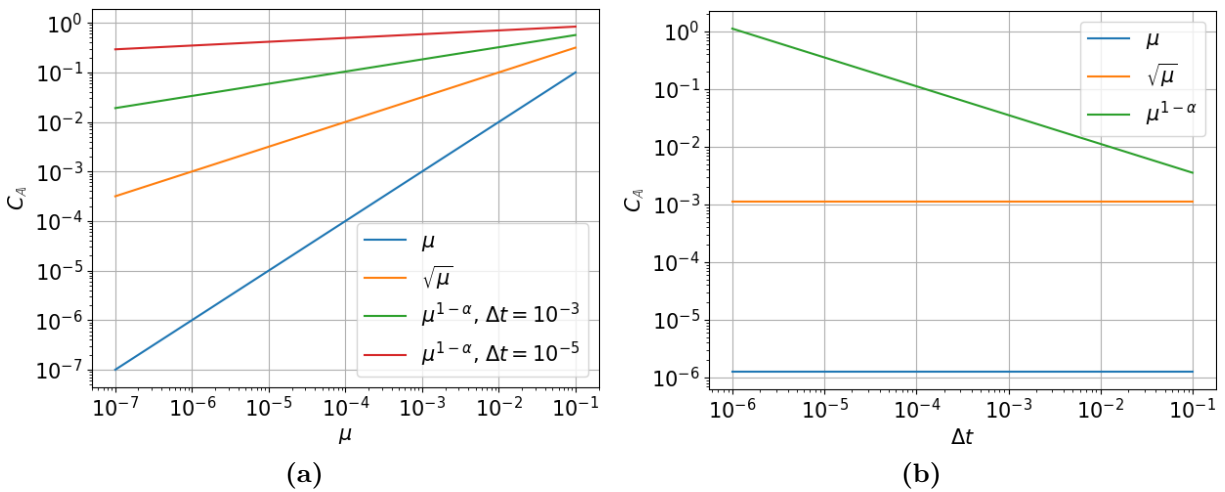
Figure 5.2: $C_{\mathbb{A}}$ coefficients' values for different definitions of the coefficient.(a) $C_{\mathbb{A}}$ as a function of the magnetic permeability. (b) $C_{\mathbb{A}}(\mu = \mu_0)$ as a function of the time-step length.

From Figure 5.2 is evident how making use of $C_\mathbb{A}$ and $C_\mathbb{E}$ balances the rows and the columns of the matrix. For example, assuming the values $\sigma = 1$ S/m, $\mu = 10^{-5}$ H/m and $\Delta t = 10^{-3}$ s, from Figure 5.2(a), we can immediately see that the order of magnitude of the matrices $\mathbb{A}$ and $\mathbb{E}$ coefficients in (5.14) is approximately 10^{-5} and 10^3 respectively. The coefficients $C_\mathbb{A}$ and $C_\mathbb{E}$ in equations (5.40a) and (5.40b) instead, are equal and approximately of the order of 10^{-1}. From Figure 5.2(b) is clear how, reducing the time-step size, the coefficients of the equations tend to increase in value.

The number of iterations necessary to solve the system of equations (5.40) by iterative solvers is smaller than that of (5.14) and the performance improvement can be explained by a reduction of the condition number, $\kappa(\mathbb{K})$, of the matrix. In Figure 5.3 the dependence of the condition number on the magnetic permeability for different definitions of $C_\mathbb{A}$ and different values of the time-step length are shown. The condition numbers shown in Figure 5.3 are obtained with a value of conductivity $\sigma = 1$ S/m. Comparing Figure 5.2 with Figure 5.3 is possible to notice how a higher value of the coefficient $C_\mathbb{A}$ results in a better conditioned matrix. Furthermore, it is noticeable that the choice of $C_\mathbb{A} = \mu$ results in an inversely proportional growth of the condition number with the permeability value. Adoption of the definition $C_\mathbb{A} = \sqrt{\mu}$ significantly improves the condition number, especially with smaller values of Δt. Finally, using the definitions (5.41) helps maintain the condition number to approximately the same order of magnitude for permeability values $\mu \geq \Delta t$, before drastically increasing.
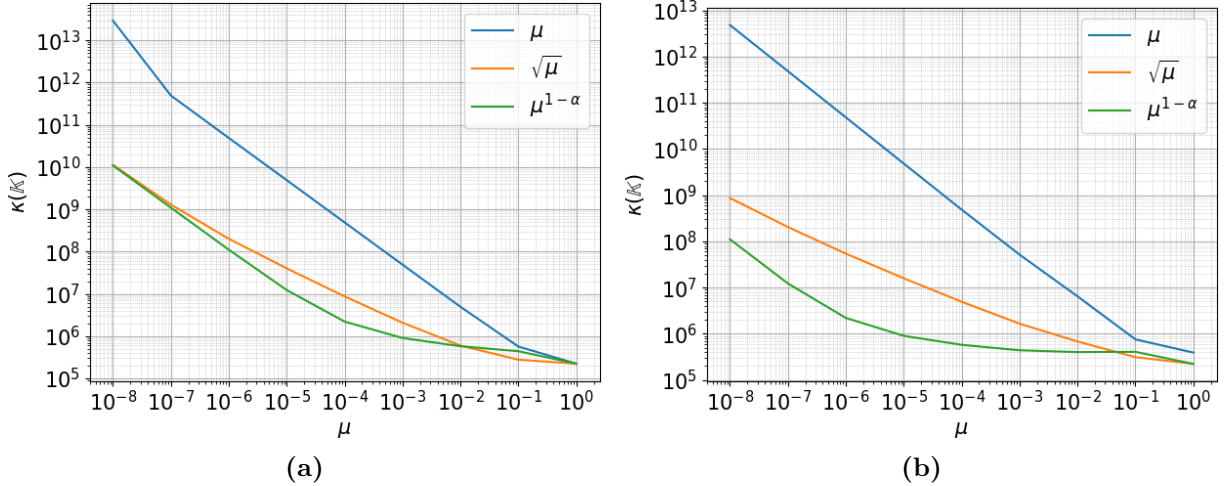
Figure 5.3: Condition number of the linear system matrix, $\kappa(\mathbb{K})$, as a function of the magnetic permeability for different definitions of the coefficient $C_\mathbb{A}$. (a) $C_\mathbb{A}(\Delta t = 10^{-3}\,\text{s})$. (b) $C_\mathbb{A}(\Delta t = 10^{-5}\,\text{s})$.

Finally, in Figure 5.4, the dependence of the condition number on the conductivity of the material and on the time-step size is shown. Figure 5.4(a) is obtained setting the permeability value to that of vacuum $\mu = \mu_0$ and using the modified formulation (5.40). From this figure is interesting to see how the condition number proportionally increases with the inverse of the electrical conductivity value, explaining why the number of iterations necessary to solve the linear system is substantially larger for the test cases of Chapter 7 than those of Chapter 6, where higher values of electrical conductivities are
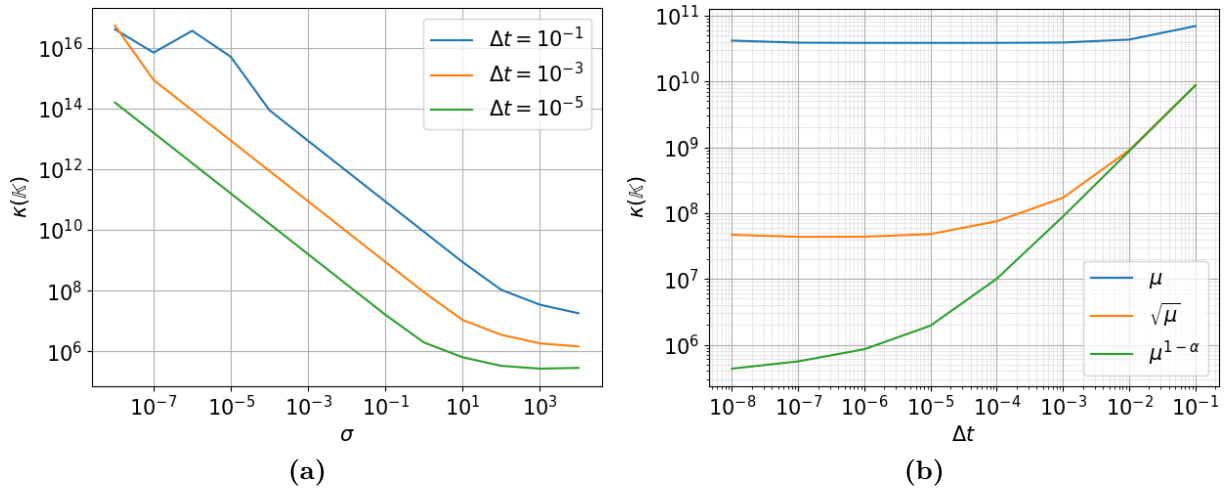
Figure 5.4: Condition number of the linear system matrix, $\kappa(\mathbb{K})$, dependence on the electrical conductivity value and time-step sizes. (a) $\kappa(\mathbb{K})$ as a function of σ for different time-step lengths. (b) $\kappa(\mathbb{K})$ as a function of Δt.

set. Figure 5.4(b) is obtained setting $\mu = \mu_0$ and $\sigma = 1$ S/m and shows that, while a reduction of time-step size does not improve the condition number of the matrix in the case $C_{\mathbb{A}} = \mu$, the same reduction leads to an improvement of the condition number in the other cases. Both definitions of the coefficient $C_{\mathbb{A}}$ lead to an initial reduction of the condition number and a subsequent stabilization at constant values, higher for the case $C_{\mathbb{A}} = \sqrt{\mu}$ and lower for the case $C_{\mathbb{A}} = \mu^{1-\alpha}$.

5.5 Convergence studies

In this section the convergence properties of the formulation introduced in Section 5.1, and modified in Section 5.4, are assessed.

The test case used to study the convergence properties models the dissipation of an electric field by means of a conductive material. The numerical domain is a unit cube bounded by PEC boundary conditions. The electrical and magnetic properties of the media are set to $\sigma = 50$ S/m and $\mu = 50$ H/m. Notice that with the chosen electrical properties, the problem being solved is that described in Section 5.1 rather than that of Section 5.4. In fact, the formulation described in Section 5.1 is modified only for values of magnetic permeability $\mu \leq 0.1$ H/m.

To simplify the derivation of an analytical solution, the convergence studies are carried out in a source free domain, that is, $\mathbf{i}_\mathrm{s} = \mathbf{0}$ A/m^2 and $\partial_t \mathbf{i}_\mathrm{s} = \mathbf{0}$ $\frac{A}{\mathrm{m}^2\mathrm{s}}$, such that the electric field is solenoidal

$$\nabla \cdot \mathbf{E} = 0, \tag{5.45}$$

and the EMD equation can be written as (2.47), to simplify the derivation of the analytical solution. Taking into account the divergence-free condition (5.45) and the PEC boundary

conditions (2.64), the following analytical solution can be obtained

$$
\mathbf{E}^{\mathrm{a}} =
\begin{bmatrix}
\sin(\pi x)\cos(\pi y)\cos(\pi z)e^{-\frac{3\pi^2}{\sigma\mu}t} \\
0 \\
-\cos(\pi x)\cos(\pi y)\sin(\pi z)e^{-\frac{3\pi^2}{\sigma\mu}t}
\end{bmatrix}.
\tag{5.46}
$$

The analytic solution (5.46) can be used to study the behaviour of a system in the limit case of a perfect conductor. In fact, for $\sigma \to \infty$, equation (5.46) models the case of a good conductor that does not dissipate the electric field's energy. In this case, the term $\frac{3\pi^2}{\sigma\mu} \to 0$ and the dissipation of the electric field happens over extremely long time periods. However, recalling Ohm's law (2.18), in the limit for $\sigma \to \infty$, the conductor sustains extremely large currents and no electric fields.

In dielectric environments instead, where $\sigma \to 0$ and the term $\frac{3\pi^2}{\sigma\mu} \to \infty$, the transient becomes extremely fast. However, in this limit, the assumption that the displacement current term is neglectable with respect to the conduction current term is no longer valid and, therefore, the EMD equation is no longer a good approximation for this type of physical phenomena. In fact in dielectric media, the electric field is propagating through the domain rather than being dissipated.

5.5.1 Spatial convergence

To asses the spatial convergence properties of the novel method the domain are discretized with increasingly finer structured meshes with elements of size h. Additionally, polynomial approximations of different degrees, k, are used. The time integration is carried out using a BDF4 time integration scheme, with a time-step small enough to ensure that the error introduced by the time discretization is neglectable with respect to the error due to the spatial discretization.

The errors as a function of the inverse of the elements' size in different norms and for different degrees of polynomial approximation are reported in Figure 5.5.

Figure 5.5(a) and Figure 5.5(b) show the achieved convergence rates of $k + 1$, in the L^2-norm, for both the electric field and auxiliary variable fields. In Figure 5.5(c) the errors and the achieved convergence rates of k for the electric field in the H^{div}-norm are reported. In Figure 5.5(d) the errors are computed in the H^{curl}-norm for the electric field and for the post-processed solution $\mathbf{E}^*$. As expected, while only a convergence rate of k is achieved for the electric field, the post-processed solution achieves a convergence rate of $k + 1$. A closer comparison of the convergence rates achieved by the auxiliary variable and by the post-processed solution reveals that, as expected, the convergence of the latter is strongly influenced by the convergence rate of the former.

Finally, Table 5.1 collects all the numerical values of the electric field errors for all the test cases in the different norms.
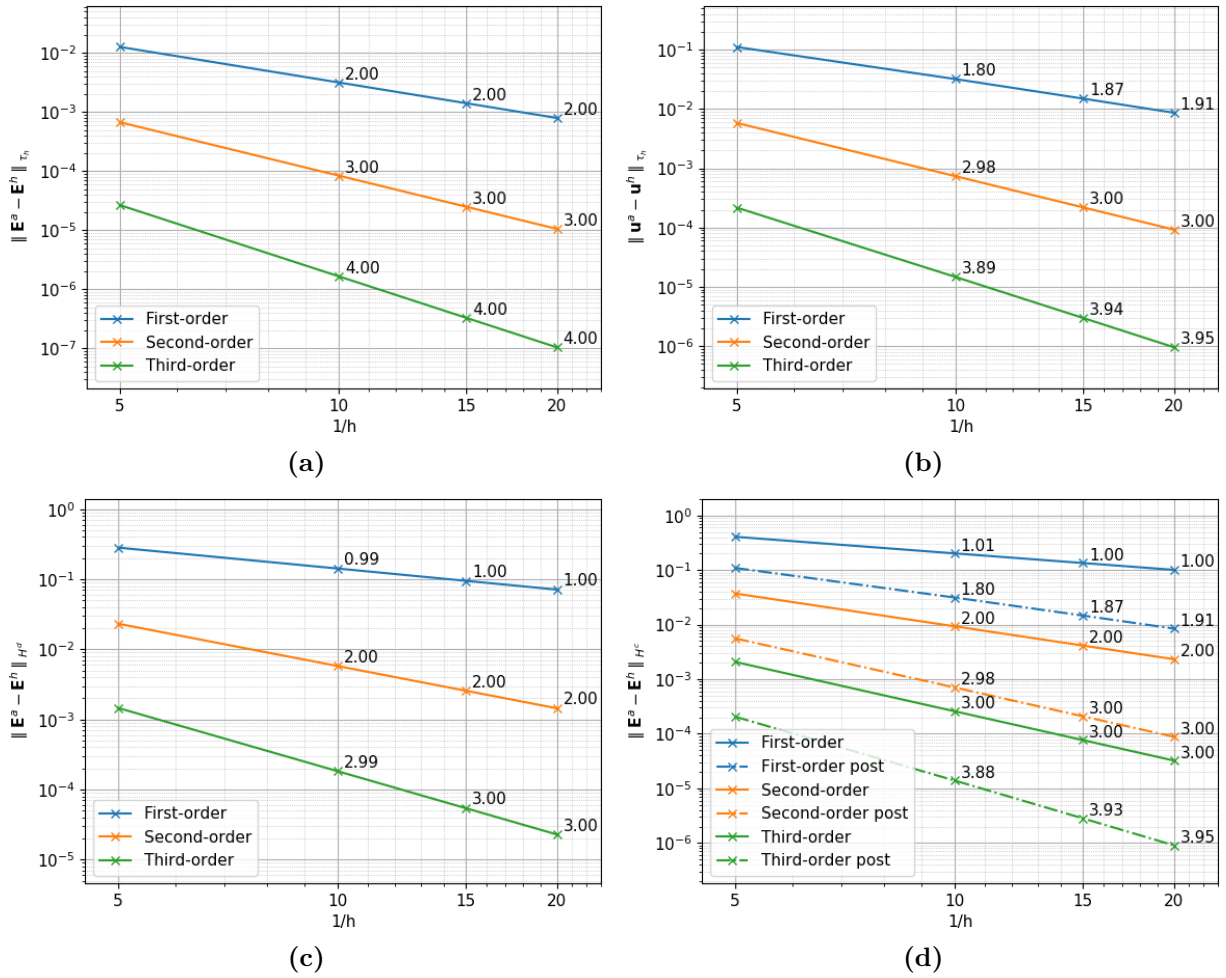
Figure 5.5: Space convergence properties of the method in the different error norms. (a) L^2-norm error. (c) H^{div}-norm error. (d) H^{curl}-norm error for $\mathbf{E}^{\mathrm{h}}$ (solid line) and $\mathbf{E}^*$ (dash-dot line). Post-processing does not improve the errors in the L^2-norm and H^{div}-norm and are therefore not shown.

k	$1/h$	$\|\mathbf{E}^{\mathrm{a}} - \mathbf{E}^{\mathrm{h}}\|$		$\|\mathbf{E}^{\mathrm{a}} - \mathbf{E}^{\mathrm{h}}\|_{H^{\mathrm{div}}}$		$\|\mathbf{E}^{\mathrm{a}} - \mathbf{E}^{\mathrm{h}}\|_{H^{\mathrm{curl}}}$		$\|\mathbf{E}^{\mathrm{a}} - \mathbf{E}^{*}\|_{H^{\mathrm{curl}}}$	
		Error	Order	Error	Order	Error	Order	Error	Order
1	5	$1.27e-02$	–	$2.82e-01$	–	$4.06e-01$	–	$1.09e-01$	–
	10	$3.18e-03$	2.00	$1.42e-01$	0.99	$2.02e-01$	1.01	$3.14e-02$	1.80
	15	$1.42e-03$	2.00	$9.49e-02$	1.00	$1.34e-01$	1.00	$1.47e-02$	1.87
	20	$7.96e-04$	2.00	$7.12e-02$	1.00	$1.01e-01$	1.00	$8.47e-03$	1.91
2	5	$6.74e-04$	–	$2.32e-02$	–	$3.71e-02$	–	$5.59e-03$	–
	10	$8.45e-05$	3.00	$5.78e-03$	2.00	$9.31e-03$	2.00	$7.07e-04$	2.98
	15	$2.50e-05$	3.00	$2.57e-03$	2.00	$4.14e-03$	2.00	$2.10e-04$	3.00
	20	$1.06e-05$	3.00	$1.44e-03$	2.00	$2.33e-03$	2.00	$8.84e-05$	3.00
3	5	$2.67e-05$	–	$1.46e-03$	–	$2.07e-03$	–	$2.06e-04$	–
	10	$1.67e-06$	4.00	$1.83e-04$	2.99	$2.59e-04$	3.00	$1.40e-05$	3.88
	15	$3.31e-07$	4.00	$5.43e-05$	3.00	$7.68e-05$	3.00	$2.83e-06$	3.93
	20	$1.05e-07$	4.00	$2.29e-05$	3.00	$3.24e-05$	3.00	$9.09e-07$	3.95

Table 5.1: Error table for the convergence study.

6 Homogeneous seabed model

Once the convergence properties of the methods are assessed, it is possible to use the methods to simulate real-world application scenarios. One possible application of the proposed methods is the simulation of CSEM surveys. We call the model of the CSEM survey simulated in this chapter Homogeneous Seabed Model (HSM).

In CSEM surveys, a time-varying electromagnetic signal is generated by a dipole source that is towed just above the seabed surface and propagates through the sea and seabed. The propagation of the electric field is affected by the formations that are present in the seabed and, therefore, given the signal received by receivers placed in known positions on the seabed, it is possible to reconstruct the underlying formations solving an inverse problem. However, for the correct and efficient solution of the inverse problem, a forward problem solver is necessary.

Even though the primary objective of this work is not that of the development of an inverse problem solver but, rather, that of the development of a forward problem solver for the simulation of electromagnetic signal propagation in geophysical applications, CSEM simulations are common in the specialised literature and a wide range of results is available, making it a great validation example. In fact, in this chapter, the results obtained with the proposed novel formulation are compared with the analytic results published in [105, 106] and kindly provided by Dr. Evan S. Um.

The main characteristics of marine CSEM surveys are given by the high conductivity values of the materials that are being modelled. In such high-conductive environments, the only frequencies that propagate over long distances are those in the low-frequency spectrum. The signals used in these surveys are typically impulsive as the goal of the surveys is to investigate the formations present in-situ, rather than signal transmission. The high-frequency signals generated by impulsive sources are dissipated in the proximity of the source shortly after the impulses. Once the high-frequency content of the signal is dissipated, the displacement current term in the equations loses importance in favour of the conductive current term. Therefore, if the near-field solution of the problem is not of interest, the propagation of low-frequency signals can be accurately modeled by a diffusion equation. Therefore, in this chapter, the EMD equation formulation proposed in Chapter 5 is chosen.

The chapter is organised as follows. In Section 6.1, a thorough description of geometry, material parameters as well as the spatial and temporal discretizations of the HSM problem is provided. Then, in Section 6.2, the numerical results are shown and compared to the analytical solution presented in [105]. Finally, Section 6.3 contains some concluding remarks and an outlook of potential future work related to the proposed HDG method and its application to the homogeneous seabed model.

6.1 Problem description
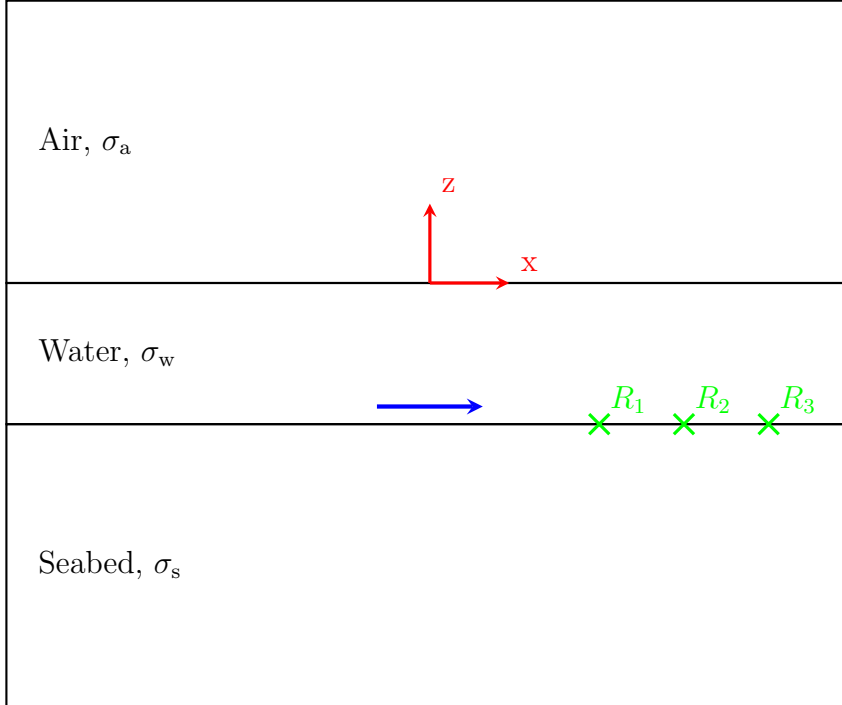
Figure 6.1: Homogeneous seabed model schematical representation (xz-plane at $y = 0$). The blue arrow represents the current source. The green crosses indicate the positions of the three inline receivers, R_1, R_2 and R_3. Notice that the representation is not to scale.

The domain of the HSM is a cube of side $L = 120$ km, composed of three rectangular prisms stacked on top of each other in the $z-$direction, each of which extending until the boundary of the domain in the $x-$ and $y-$directions. The top layer represents air and extends from the origin of the $z-$axis to top boundary at $z = 60$ km. The second layer extends 400 m in the regative region of the $z-$axis and represents the sea. In the water layer, a 250 m long dipole, oriented along the $x-$direction, is placed 50 m above the seabed, that is, $z = -350$ m. Lastly, the bottom layer, extends from $z = -400$ m to $z = -60$ km and represents the underlying seabed.

On the interface between water and seabed, a total of 6 receivers, R_1-R_6, are used to measure the electromagnetic field generated by the dipole. The receivers R_1 to R_3 are inline receivers, that is, are placed along the positive region of the $x-$axis at distances of $x_1 = 2$ km, $x_2 = 4$ km and $x_3 = 6$ km. The receivers R_4 to R_6 are broadside receivers, that is, are placed along the positive region of the $y-$axis, at distances of $y_4 = 2$ km, $y_5 = 4$ km and $y_6 = 6$ km. In Figure 6.1, a not-to-scale schematical representation of the side view of the HSM is provided. Figure 6.2 instead, provides a top-side view of the configuration of the receivers on the water-seabed interface. Notice that the source and the receivers lay on distinct $xy-$planes 50 m apart.
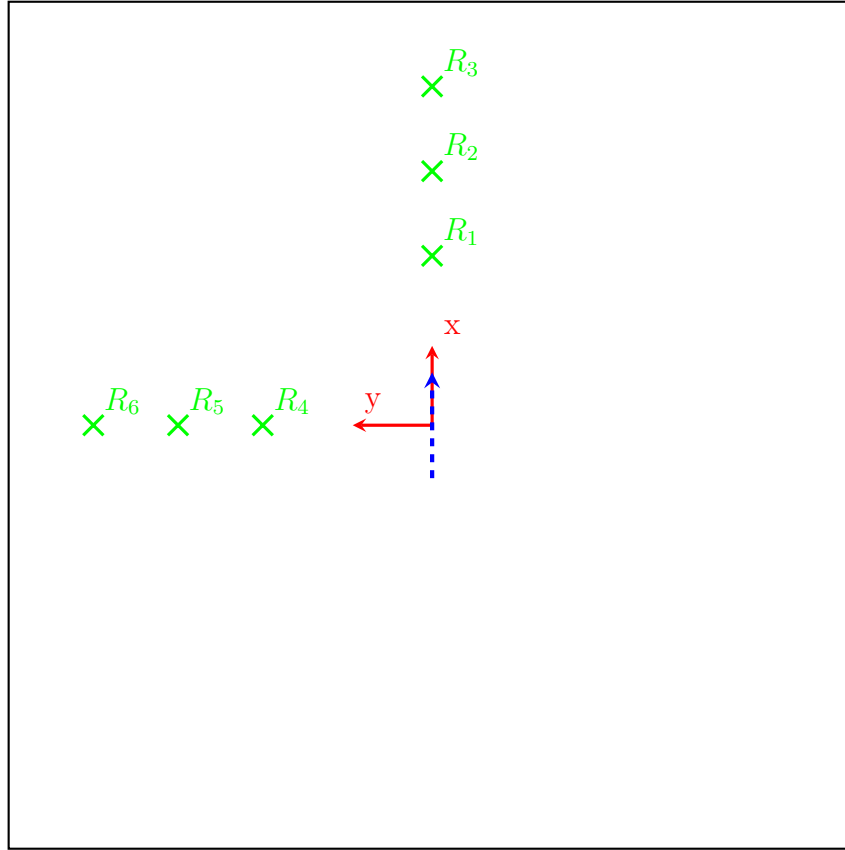
Figure 6.2: Position of the receivers on the water-seabed interface ($xy-$plane at $z = -400$m). The green crosses represent the positions of the receivers R_1-R_6 while the dashed blue arrow is the projection of the dipole on the represented plane.

The electrical properties of the materials are set to be homogeneous within each layer but can be discontinuous between the different layers. The magnetic permeability value, homogeneous across the whole domain, is set to $\mu = \mu_0$. The electrical conductivity of the water and seabed are set to the same used in [105, 106], i.e., $\sigma_w = 3.33$ S/m and $\sigma_s = 1.43$ S/m, such that it is possible to compare the results. In the air layer, the electrical conductivity is set to $\sigma_a = 10^{-7}$ S/m. Notice that σ_a is not set to the physical conductivity value of air, i.e., 10^{-12} S/m, as very low values of electrical conductivity make the problem ill-conditioned, see Figure 5.4(a), without appreciably improving the solution [106]. The value $\sigma_a = 10^{-7}$ S/m is found to be a good compromise between solution efficiency and accuracy. For an overview of the effects of the electrical properties on the condition number of the matrix, see Section 5.4.

Finally, the source is a 250 m long cylinder of radius $r = 1$ m. At the time $t_0 = 0$ s, a total current of $|\mathbf{I}_s| = 1$ A flows in the $x-$direction through the source, and is then turned off via a 0.01 s ramp-off signal starting at $t_s = 0.01$ s, as shown in Figure 6.5(b). Notice that, being $\mathbf{i}_s$ a current density and $r = 1$ m, then $\mathbf{I}_s = \mathbf{i}_s \pi$.

6.1.1 Spatial discretization

The domain is discretized using geometrically linear tetrahedral elements. PEC boundary conditions are applied to the boundaries of the domain. The element size varies within the domain to make sure that the geometry is well approximated, see Figure 6.3. The number of elements necessary to discretize the domain is increased by the necessity to properly discretize the geometry of the source and the water layer. In fact, as the water layer extends for 120 km in the $x-$ and $y-$ directions, while extending only 400 m in the $z-$ direction, it is impossible to increase the element size within this layer to more than approximately 400 m without obtaining extremely deformed tetrahedral elements. Therefore, while accounting for less than 1% of the total volume, the water layer contains approximately 1/3 of the total number of elements. To reduce the number of elements,
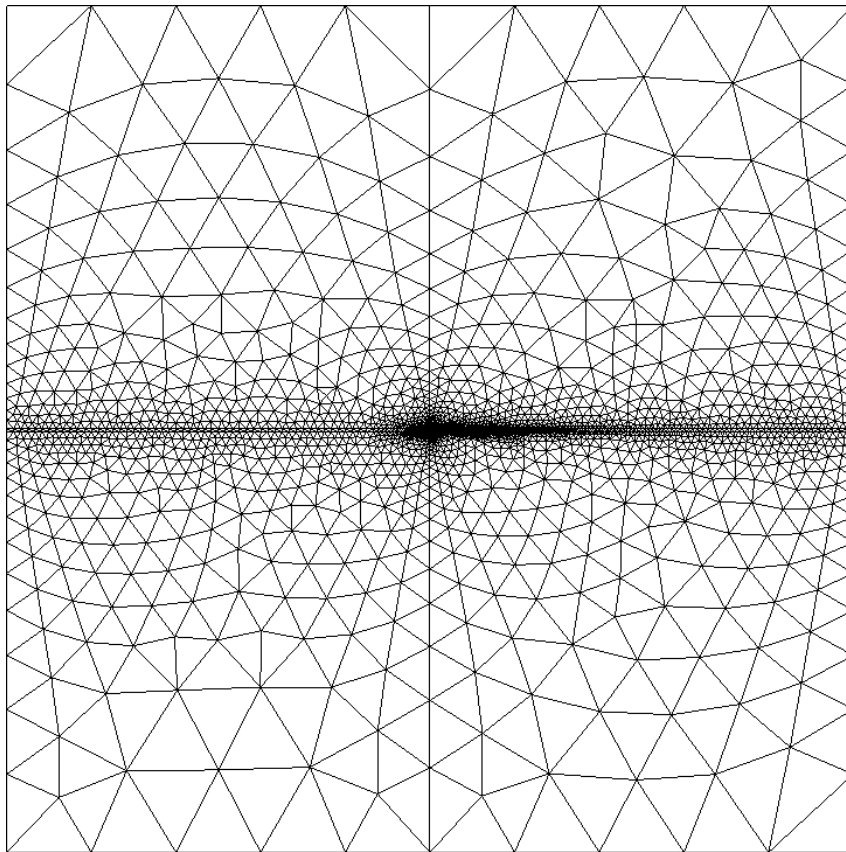
Figure 6.3: Section of the numerical discretization on the xz-plane. The mesh size in the water layer is controlled by the height of the water layer itself, increasing the number of elements. In the water layer and in the seabed the mesh is refined in the vicinity of the source and of the receivers. Towards the boundaries the mesh is coarsened as the distance from the water layer increases.

however, outside the water layer the mesh is coarsened where the solution is not of interest and close to the boundary where the surface triangulation reaches a characteristic length of approximately 12 km, as noticeable in Figure 6.3.

(a)

(b)
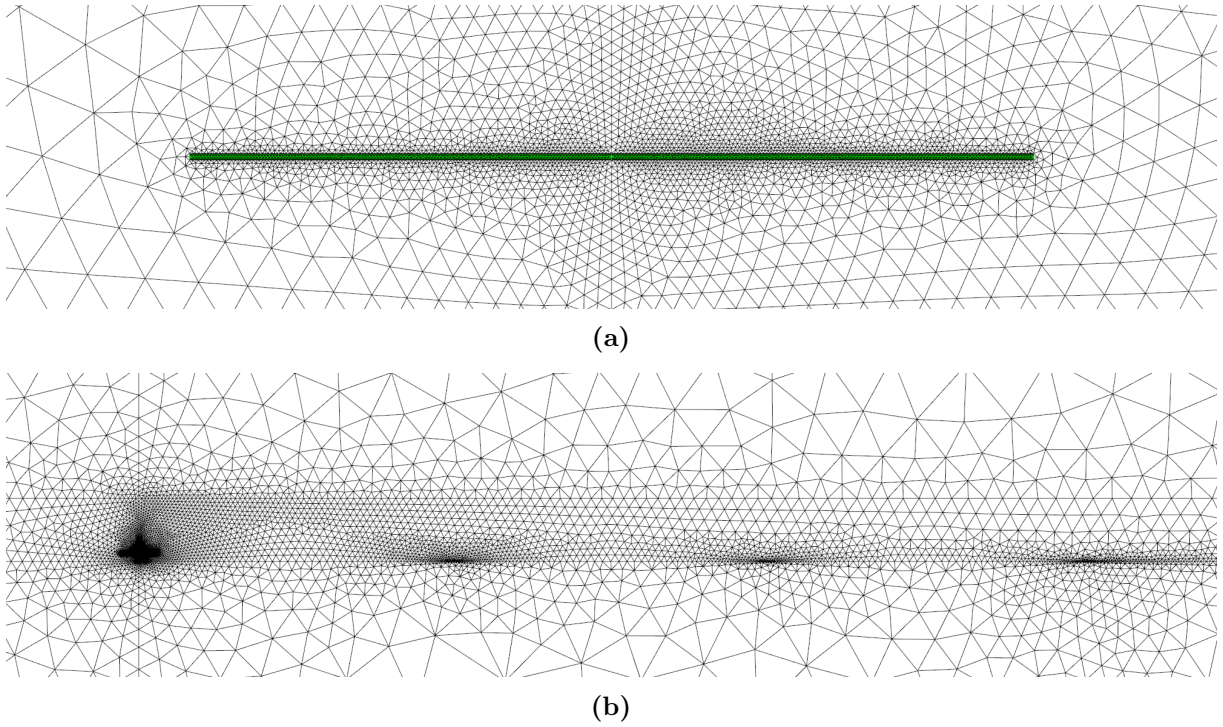
Figure 6.4: Mesh refinement in the proximity of interest zones. (a) Dipole. (b) Dipole and receivers R_1 to R_3.

A coarser mesh near the boundary has the additional effect of damping possible numerical artifacts due to the PEC boundary conditions near the boundaries. Therefore, the possibility of the solution, in the proximity of the receivers, being affected by numerical boundary effects is reduced. In fact, using PEC boundary conditions can lead to unwanted artificial boundary effects at the receiver positions, if the boundaries are not far enough from receivers and sources. To reduce such possibility the boundaries of the domain are placed at a distance of 10 times the maximum source-receiver offset [105]. In Section 5.3.2 the effects of different boundary conditions in the vicinity of the receivers, $|\mathbf{x}| < 10$ km, and near the boundaries of the domain are presented.

Due to the extension of the domain and the size of its geometrical details, such as the source, the domain is discretized in circa 1.2 millions tetrahedral elements. Depending on the order of polynomial approximation used within the elements the number of DOFs can vary. The discretization of the formulation (5.11) with first-order polynomials in the discretized domain results in a total number of unknowns, the sum of the local unknowns and the global ones, of approximately 43 millions. Applying the condensation procedure introduced in Section 5.1.2, the condensed system (5.17) is assembled instead of (5.16), reducing the number of unknowns to be solved by the linear solver to circa 14 millions unknowns. The remaining 29 millions local unknowns are successively computed via (5.23) on an element basis and, therefore, with a fraction of the computational cost.

Given the size of the problem at hand, an AMG preconditioned GMRES method [172] implemented in the Trilinos packages [151] ML and AztecOO is used. The AMG preconditioner is based on a full Petrov–Galerkin unsymmetric smoothed aggregation method and

the iterative solution at each time-step is terminated when the L^2-norm of the residual vector falls below the value 10^{-11}.

6.1.2 Time discretization

As previously mentioned, the EMD equation is a stiff equation, making the time-integration via explicit schemes prohibitive, as it requires very small time-step sizes. Implicit time-integration schemes, on the other hand, are unconditionally stable and the choice of time-step size is only limited by the condition number of the matrix and by the solver choice, see Section 5.4, Figure 5.4(b).

The time-integration of the problem presented in this chapter is carried out via the BDF2 scheme introduced in Section 2.2.4. It has to be noticed though, that as the source excitation waveform, $f(t)$, is only $f(t) \in C_0$, i.e., continuous function with discontinuous first derivatives, it is only possible to achieve first-order convergence [105, 142]. However, even though lower-order integration schemes can be dissipative, the dissipation introduced by these schemes is not of concern here as the dissipation is mostly noticeable on the higher frequencies of the spectrum, while our interest is on the low frequency spectrum. To control the numerical dissipation introduced by the time-integration scheme, it is possible to make use of schemes such as the Generalized-α method that allows control over the dissipation of the scheme through a set of coefficients, see e.g. [173–175].

Regardless of the chosen time-integration scheme, it is necessary to provide an initial condition that satisfies the electromagnetic diffusion equation (2.46) and the divergence-free condition (2.5) in order to initialize the simulation. The initial condition can be obtained integrating (2.46) until a stationary state is achieved or, alternatively, solving the direct current resistivity problem defined in Section 5.3.

In the first approach, the EMD equation is used to simulate the diffusion of a field generated by a source following a smooth ramp-on signal, as shown in Figure 6.5(a). The simulation is extended until a steady state is reached, and the results are used as initial conditions for following simulations. Although this approach has been employed to obtain initial conditions with meaningful results, its computational cost makes it of impractical use and will therefore not be further discussed in this work.

To save computational time, the initial condition for this test case is obtained following the second approach, that is, solving the DC resistivity problem. The direct current problem is solved on the same geometrically linear mesh used for the solution of the EMD problem. The order of polynomial approximation matches that used in the EMD problem.

In the HSM, the interest is on the responses to a source that is turned off with a ramp-off signal. The ramp-off is initiated at $t_r = 0.01$ s and has a duration of 0.01 s, as shown in Figure 6.5(b). The time-step length is chosen to be $\Delta t = 10^{-3}$ s such that the ramp-off signal is discretized by 10 time-steps. The total simulation time is set to $T_{\max} = 20$ s.

It is worth to point out that, given the time-step size and total simulation time, the time evolution of this problem is discretized in 20000 time-steps. Hence, the global and local problems (5.17) and (5.23) are solved 20000 times. To reduce the number of linear solutions necessary to complete a simulation it is possible to introduce an adaptive time-
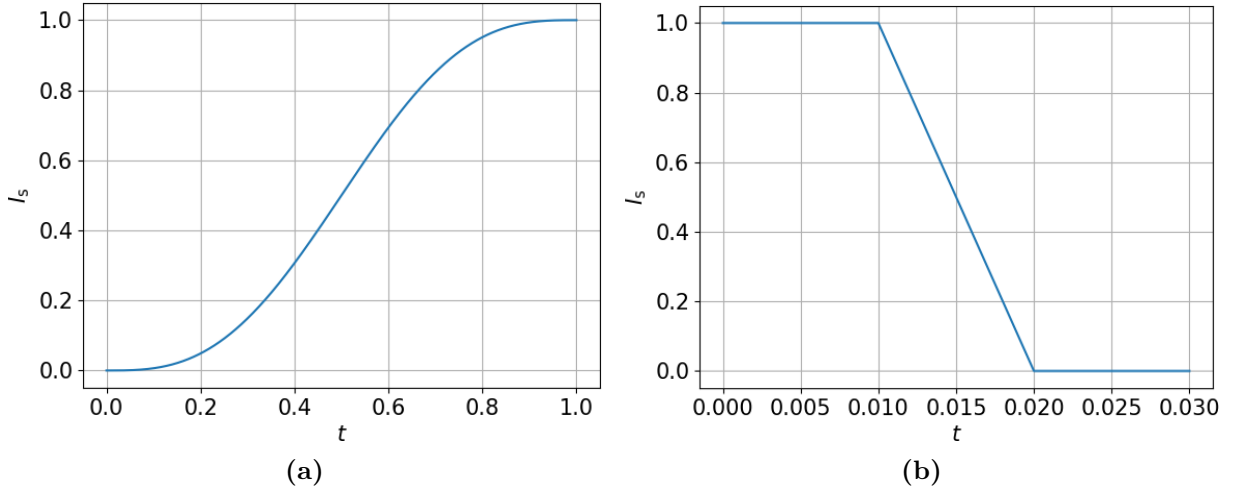
Figure 6.5: Source signal waveform. (a) Smooth power-on signal. (b) Ramp-off signal

step size as proposed in Section 6.1.2.1. However, for the validation of the method, a constant time-step size is adopted.

6.1.2.1 Adaptive time-step size

The solution for the validation scenario in Section 6.2 is obtained with a constant time-step of $\Delta t = 10^{-3}$ s. However, given the relatively long-term time-integration necessary to describe electromagnetic diffusion phenomena, $T_{\max} > 10$ s, the number of time-steps necessary to compute the complete transient makes the simulation computationally very expensive.

To reduce the computational cost of the simulations, it is possible to adapt the time-step size to the characteristic times of the physical processes being modeled. Particularly, in the case of marine electromagnetic diffusion encountered in the HSM, the high-frequency components of the fields are rapidly attenuated in the early times by the highly conductive water layer in which the source is immersed. Thus, once the high-frequency content of the signal has been dissipated, it is possible to increase the time-step size without losing accuracy of the solution in later times, see, e.g. [105, 106].

Albeit different methods are available in the literature to compute the most appropriate time-step size for the problem, or to determine the optimal conditions under which it is possible to increase the time-step in a particular simulation, in our experiment we adopt the same algorithm used in [105]. In this elementary algorithm, the user defines the ratio between the time-step sizes

$$a = \frac{\Delta t_{\mathrm{new}}}{\Delta t_{\mathrm{old}}} \tag{6.1}$$

and the number of iterations, m, after which the time-step is modified. Although being simple, if properly set-up, this method has the potential to consistently reduce the computational cost of the simulation, as shown in [105].

Notice that, when the time-step size is modified, every m time-steps, it is necessary to recompute the discretization matrix, therefore introducing a computational overhead

to the method. Hence, it is necessary to set the coefficients a and m such that the computational cost of the matrix assembly is balanced by the computational advantage of the bigger time-step size. Furthermore, when a variable time-step size is employed, the coefficients in Table 2.1 of the time-integration schemes have to be modified to retain the accuracy and stability of the methods [176, 177].

6.2 Results

The solution of the EMD equation formulation represent an approximation of the electric and auxiliary variable fields. While the electric field can be directly compared to the results present in the literature, the auxiliary variable is used to obtain the values of $\partial_t \mathbf{B}^{\mathrm{h}}$ and $\partial_t \mathbf{H}^{\mathrm{h}}$ thanks to the relations (5.3) and (2.9b). It is important to notice that, while in the proposed formulation the $\partial_t \mathbf{B}^{\mathrm{h}}$ field can be obtained directly as $\partial_t \mathbf{B}^{\mathrm{h}} = -\mu \mathbf{u}^{\mathrm{h}}$, it is common, for other methods, to obtain the magnetic and magnetic induction fields and their time derivatives post-processing the electric field. The latter approach can increase the complexity of such methods and reduce the accuracy of the approximation. It is worth to point out that, if the formulation is modified as proposed in Section 5.4, given the definition (5.40a), the magnetic induction field is obtained by $\partial_t \mathbf{B}^{\mathrm{h}} = -\mu^{1-\alpha} \mathbf{u}^{\mathrm{h}}$.

In Figure 6.6 the time evolution of the fields $\mathbf{E}^{\mathrm{h}}$ and $\partial_t \mathbf{B}^{\mathrm{h}}$ at the different receivers positions are shown. In Figure 6.6(a) and Figure 6.6(b) the fields measured by the inline receivers R_1-R_3 are shown. The choice of showing the E_x and E_z components is made considering the emission pattern of a dipole source. In fact, in the inline direction, the other components of the electric field are neglectable. Figure 6.6(c) and Figure 6.6(d) show the time evolution of the E_x and $\partial_t B_z$ fields as measured by the receivers R_4-R_6 in the broadside configuration. As for the inline receivers, in the broadside configuration only the non-zero components of the fields are shown.

The initial condition obtained via the solution of the DC problem, in terms of electric field measured at the receivers R_1 to R_6 locations, is accurate within 4% accuracy in each location with the exception for the E_z field measured at the receiver R_2 position, for which the error is approximately 7%. It is worth to point out that it is impossible to compute a relative error for the time derivative of the magnetic induction field at $t = 0$ s. In fact, the time derivative of a stationary field is equally zero. Moreover, an initial condition on the time derivative of the magnetic field is not necessary in the proposed formulation, hence the approximation of $\partial_t \mathbf{B}$ is only available for $t > 0$ s. These results show that the accuracy of the solution of DC resistivity problem by a total potential approach is accurate enough when considering receivers locations that are far enough from the source. However, as a secondary potential approach can improve the solution in the vicinity of the source [97, 105], it would be of great interest to compare the solutions obtained by the different approaches with high-order methods such as the one proposed in this work.

At $t = t_s$ the source is turned off following the ramp-off waveform described in Figure 6.5(b). The received electric field is not noticeably affected by the signal until a later time due to the finite diffusion velocity. After circa 0.3 s, the effect of the source becomes appreciable in the electric field strength received in the closer receivers, R_1 and R_4, and, later on, on the further receivers, in good agreement with the analytical solu-
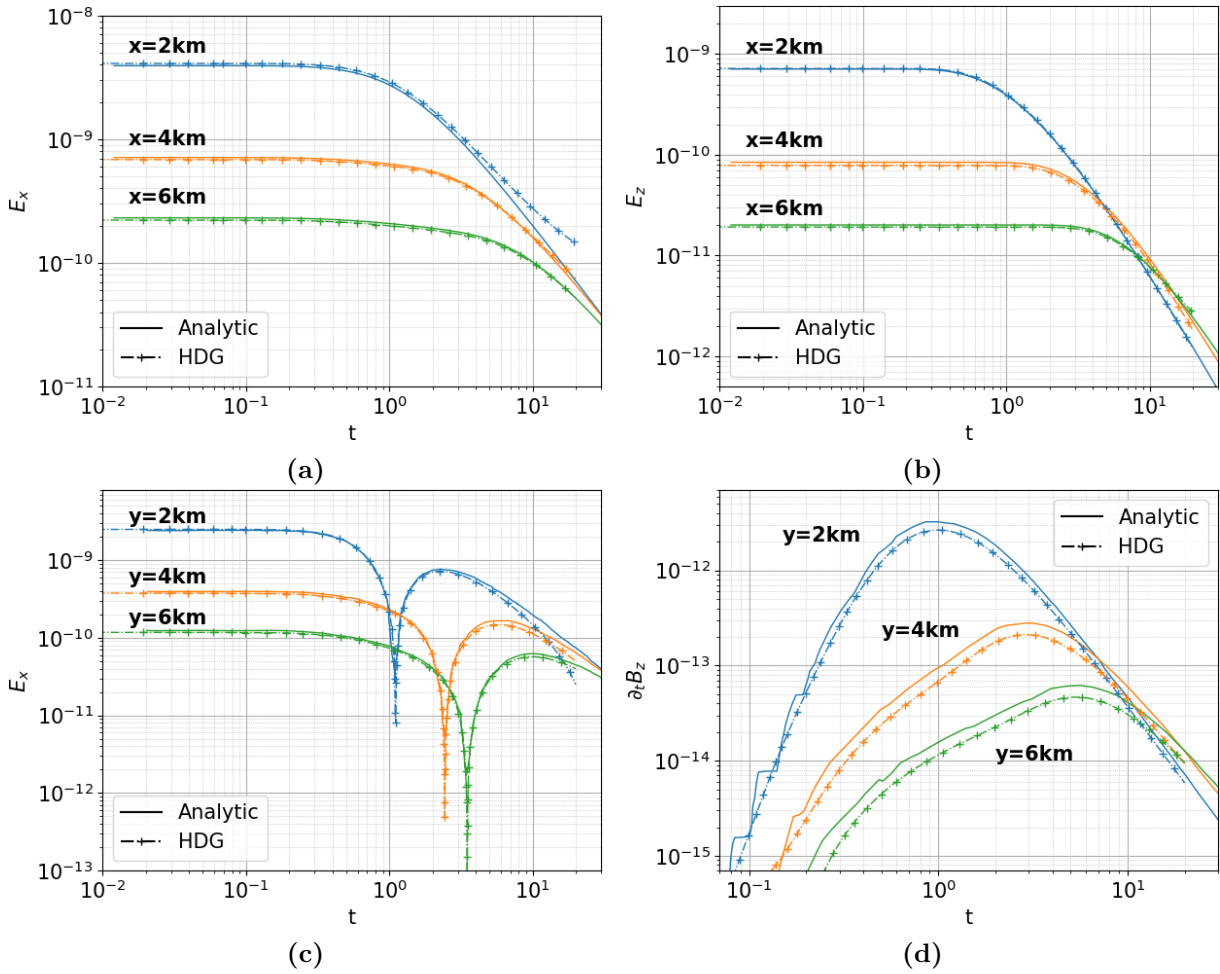
Figure 6.6: Inline and broadside field responses to a step-off source signal at the receivers positions. The solid line is the solution obtained with the proposed method while the dash-dot line represents the reference solution. (a) Inline E_x. (b) Inline E_z. (c) Broadside E_x. (a) Broadside $\partial_t B_z$.

tion. In Figure 6.6(a) and Figure 6.6(b) is possible to notice how the numerical solution accurately reproduces the transient predicted by the analytic solution. In Figure 6.6(c) it is possible to notice that the sign reversal in the E_x component, observed in the broadside configuration in the early time $t < 1$ s, is accurately represented by the numerical approximation.

The time derivative of the magnetic induction field is contaminated by numerical noise in the early time range $0 < t < 0.1$ s. Starting from $t \approx 10^{-1}$ s, the $\partial_t B_z$ field reaches intensities that can be discerned from the numerical noise, $|\partial_t B_z| \approx 10^{-15}$ T/s, and the time evolution of the field can be observed to reproduce the expected transient. Although the behaviour is correctly represented, it is possible to notice and offset between the numerical approximation and the solution provided in [105], hence the relative error is still relatively high. Moreover, given the small amplitude of the signal, it is expected

that the approximation of the time derivative of the magnetic induction field is the most affected by numerical errors.

Interestingly, as the simulation advances in time, $t > 5$ s, the time evolution of some components of the fields departs from the expected behaviour. This behaviour can be observed mainly in the $x-$component of the electric field measured at the receivers R_1 and R_4, as indicated by the blue lines in Figure 6.6(a) and Figure 6.6(c). A careful study of the behaviour of the solution with respect to solver tolerances and different meshes revealed that in late times, $t > 10$ s, the solution is affected by spurious oscillations due to the numerical contamination. In fact, it is worth to point out that the accuracy of the linear solution is affected by the condition number of the matrix and by the solver tolerances adopted as stopping criteria. As the system is solved repeatedly, the errors cumulate and, after several time-steps, it is possible that the error reaches the significant digits of the solution. This effect is more pronounced in low quality meshes and in the components of the fields with magnitudes close to the magnitude of machine precision.

It is a known drawback of the solution of the EMD equation via iterative solvers to obtain spurious solutions in the static limit [99, 106]. This effect is attributed to the introduction of non-physical values of divergence of the electric field. In fact, as already stated in Section 2.1.1, solutions of Maxwell's equations have to satisfy the divergence-free condition at all times. Unfortunately, numerical methods can introduce a finite value of divergence in numerical approximations of electromagnetic fields. To address this problem, several divergence-cleaning techniques have been developed in different fields, see, e.g. [106, 116, 117]. In this thesis however, none are implemented as it would extend beyond the scope of this work.

6.3 Discussion of the benchmark problem and takeaways

In this chapter, a description of the homogeneous seabed model benchmark and its accurate solution have been presented. However, many interesting aspects of the solution of this benchmark have not yet been addressed. In fact, various different experiments have been carried out to study the effects of different factors on solution accuracy. In Section 6.3.1 the adaptive time-step algorithm proposed in Section 6.1.2.1 is employed in the solution of the HSM problem and the effects of the time-step size on the solution are investigated. In Section 6.3.2, the effects of mesh quality and the degree of the polynomial approximation on the accuracy of the solution are presented. Finally, the takeaways from the solution of the HSM problem are illustrated in Section 6.3.3.

6.3.1 Effect of the time-step size on the solution

In this experiment, the solution obtained employing an adaptive time-step size are compared to the solution presented in Section 6.2, obtained using a constant time-step size. In the adaptive algorithm, the initial time-step is set to $\Delta t_0 = 10^{-3}$ s, the factor a between the new and old time-steps is set to $a = 2$ and the number of time-steps between each time-step size update is chosen as $m = 1000$. With these parameters the time-step size is doubled every 1000 time-steps and therefore doubled 4 times through the simulation.
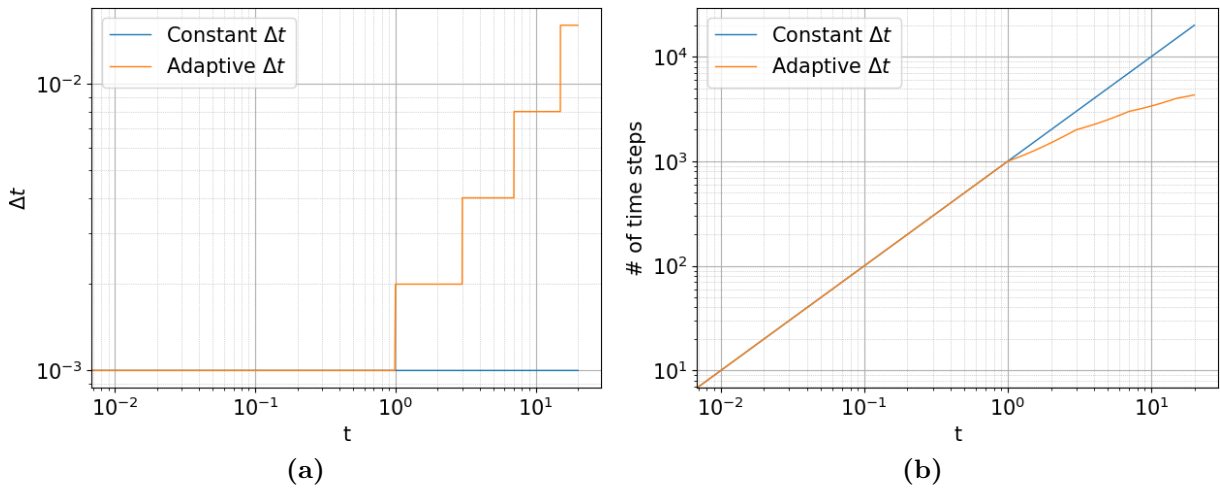
Figure 6.7: Effect of the adaptive time-step on the time-step size and number of necessary time-steps. (a) Time-step size over time. (b) Number of time-steps over time.

In Figure 6.7 the time-step size and the total number of time-steps necessary to complete a simulation making use of the adaptive time-step algorithm are shown and compared to those necessary in a simulation that makes use of a constant-time step size.

Notice that, while with a constant time-step size the number of time-steps to compute is 20000, using the adaptive algorithm with the given parameters reduces the number of time-steps to circa 4300, that is, a reduction of approximately 80%. However, it is worth to point out that an 80% reduction in the number of computed time-steps does not necessarily translate into an 80% reduction in compute time. In fact, as already stated, the refactorization of the linear systems' matrix introduces a computational overhead and the modified matrix can be harder to solve, as will be seen later in this section.

Ideally, the update of the time-step size should leave the solution of the problem unaffected. Indeed, in the early times, the adaptive time-step size algorithm does not affect the solution of the HSM. Additionally, the approximations of the E_x and $\partial_t B_z$ remain accurate through the whole simulation. Unexpectedly, however, some components of the solution loose accuracy in later times. Figure 6.8 shows the time evolution of the electric field and the derivative of the magnetic induction field in each receiver location.

The introduction of an error is clearly noticeable in the E_z component of the solution at the receiver R_1 location for $t > 5$ s. The behaviour observed in electric field component normal to the water-seabed interface, E_z, at the R_1 receiver location, is consistent with the errors introduced by a poor quality of the mesh, see Section 6.3.2, and/or an excessively ill-conditioned problem, see Section 7.2.1.

In fact, although the formulation preconditioning presented in Section 5.4 has been adopted, a large time-step can still negatively affect the condition number of the matrix, and thus the solution accuracy. Notice that the dependence of the condition number of the matrix on different numerical parameters has already been investigated in Section 5.4.2. Particularly, Figure 5.4(b) shows the dependence of the condition number on the time-step size used. It is possible to notice how a bigger time-step size increases the condition number of the matrix and vice-versa. Therefore, the reduced accuracy noticed in Fig-
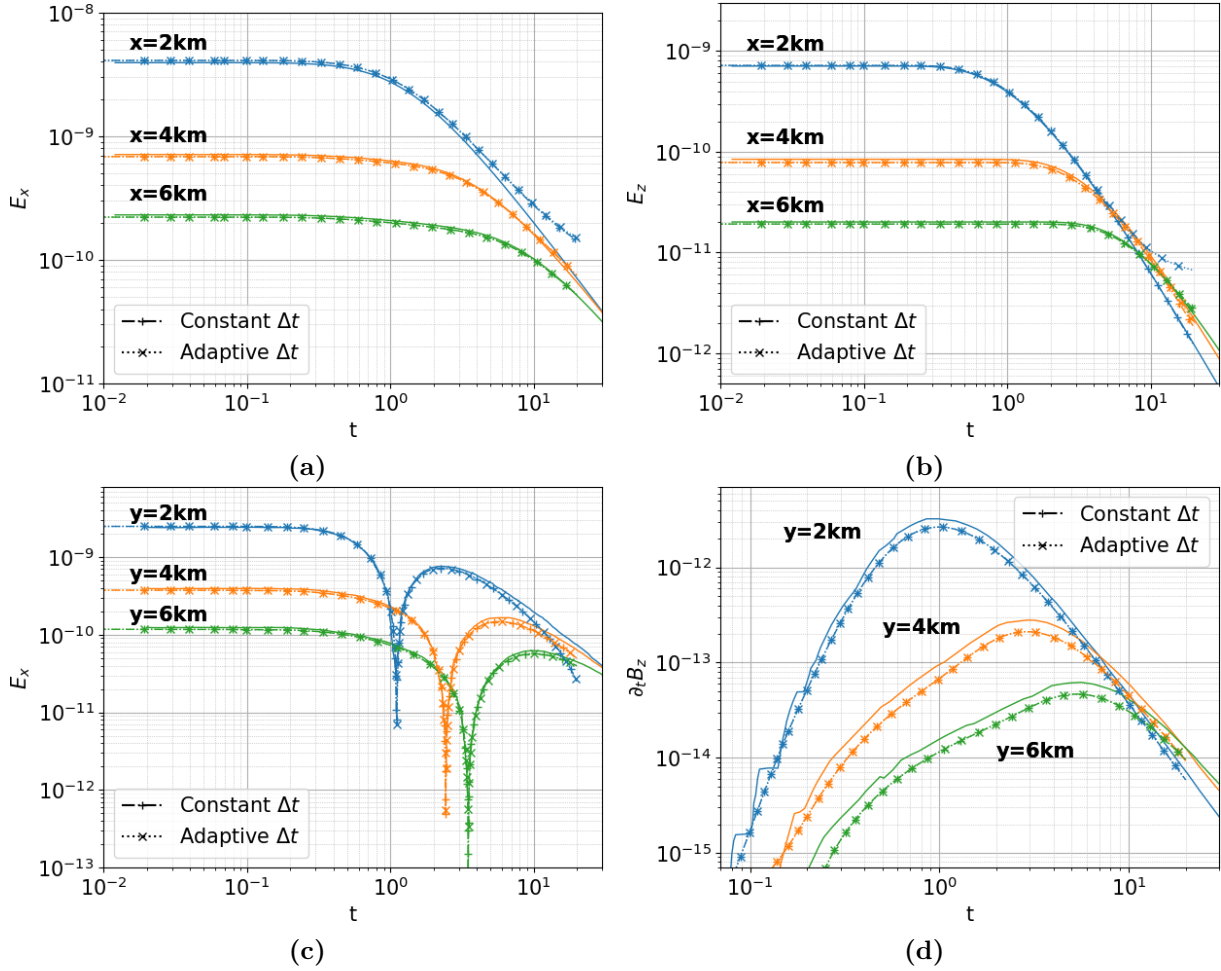
Figure 6.8: Inline and broadside field responses to a step-off source signal at the receivers positions. The solid line is the solution obtained with the proposed method while the dash-dot line represents the reference solution. (a) Inline E_x. (b) Inline E_z. (c) Broadside E_x. (a) Broadside $\partial_t B_z$.

ure 6.8(b) can be attributed to an increase in the condition number of the matrix due to the increased time-step size with respect to the case with constant time-step. In Section 6.3.2 the effect of the condition number on the accuracy of the solution in long-term time-integration is more thoroughly discussed.

The effect of the increased time-step size can also be noticed in the number of iterations necessary to solve the linear system. In fact, each time the time-step size is doubled, the number of iterations necessary for the convergence of the iterative linear solver increases, as seen in Figure 6.9. The increased number of iteration partially is due to the greater difference between the initial guess provided to the iterative solver and the actual solution of the current step as a consequence of the increased time-step size. Additionally, the matrix obtained from the refactorization after the time-step size update is expected to have a higher condition number, see Figure 5.4(b). Hence, doubling the time-step size is expected to negatively affect the number of iterations necessary for each solution. Addi-
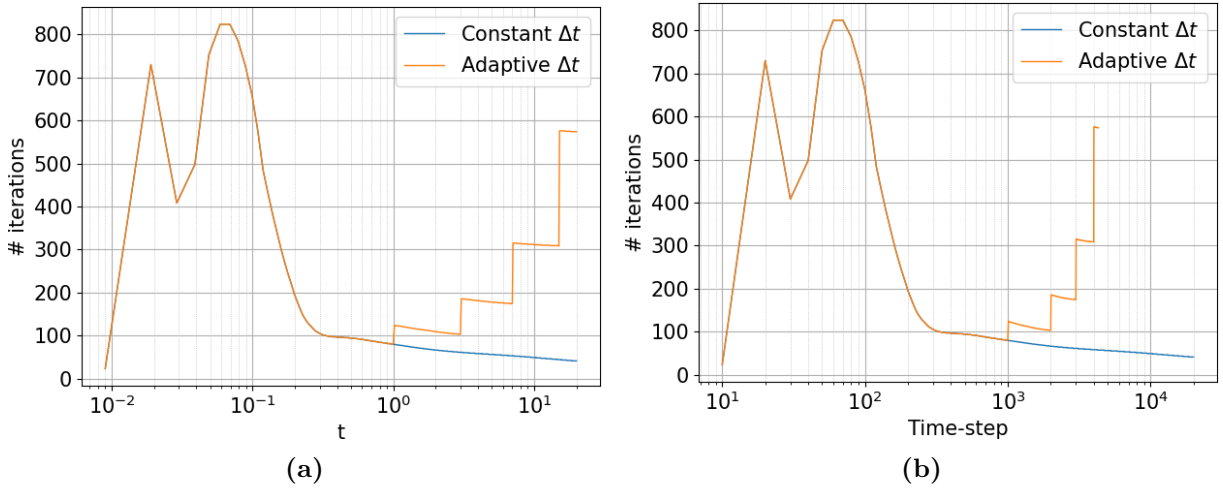
Figure 6.9: Effect of the adaptive time-step on the linear solver's iteration count. (a) Iterations over simulation time. (b) Iterations over time-step number.

tionally, it is worth to point out that, if the time-step is increased over a certain threshold, the solution accuracy can be degraded to unacceptable levels and, in extreme cases, the matrix can be become extremely ill-conditioned, therefore preventing a full convergence of the iterative solver.

The larger number of iterations necessary to solve the system, together with the need to recompute the linear system's matrix each time the time-step is modified, increases the computational cost of the algorithm. Therefore, to reduce the overall computational cost, it is important to set the parameters a and m carefully, striking the right balance between time-step size and the achievable efficiency of available linear solvers.

6.3.2 Mesh quality and order of polynomial approximation

The discretization of the domain by tetrahedral elements allows an accurate discretization of small geometrical objects as the source and the receivers. At the same time, unstructured meshes allow a reduction of the number of elements in regions of the domain where high accuracy is not needed. In fact, while in the proximity of the boundaries large elements are used, in the vicinity of source and receivers the element size is decreased to achieve the higher accuracy required. However, reducing the element size makes the process of mesh generation more complex and, possibly, prone to generate lower quality elements.

To show the effects of mesh quality on the solution, the HSM is discretized using different meshes. Two different geometrical discretizations consisting of a similar number (less than 10% difference) of geometrically linear tetrahedral elements are employed. In the different meshes, the elements have a similar spatial distribution, that is, are refined in the proximity of source and receivers and are coarsened towards the boundaries. However, the different discretizations contain elements with different quality, measured in the shape metric [178], especially in the vicinity of the receivers. Figure 6.10 shows a comparison of the higher quality mesh, HDG_H, and lower quality mesh, HDG_L, in proximity of the

87

receiver R_1, together with the distribution of the elements in element quality ranges for each mesh. A comparison of Figure 6.10(a) to Figure 6.10(b) shows that, in HDG_L, the elements' quality in the vicinity of the receivers is sacrificed in favour of a higher element count. In fact, while the lowest element quality that can be found in HDG_H is 0.450, in HDG_L this value drops to 0.418, as shown in Figure 6.10(c) and Figure 6.10(d), respectively.


(a)   (b)

(c)   (d)
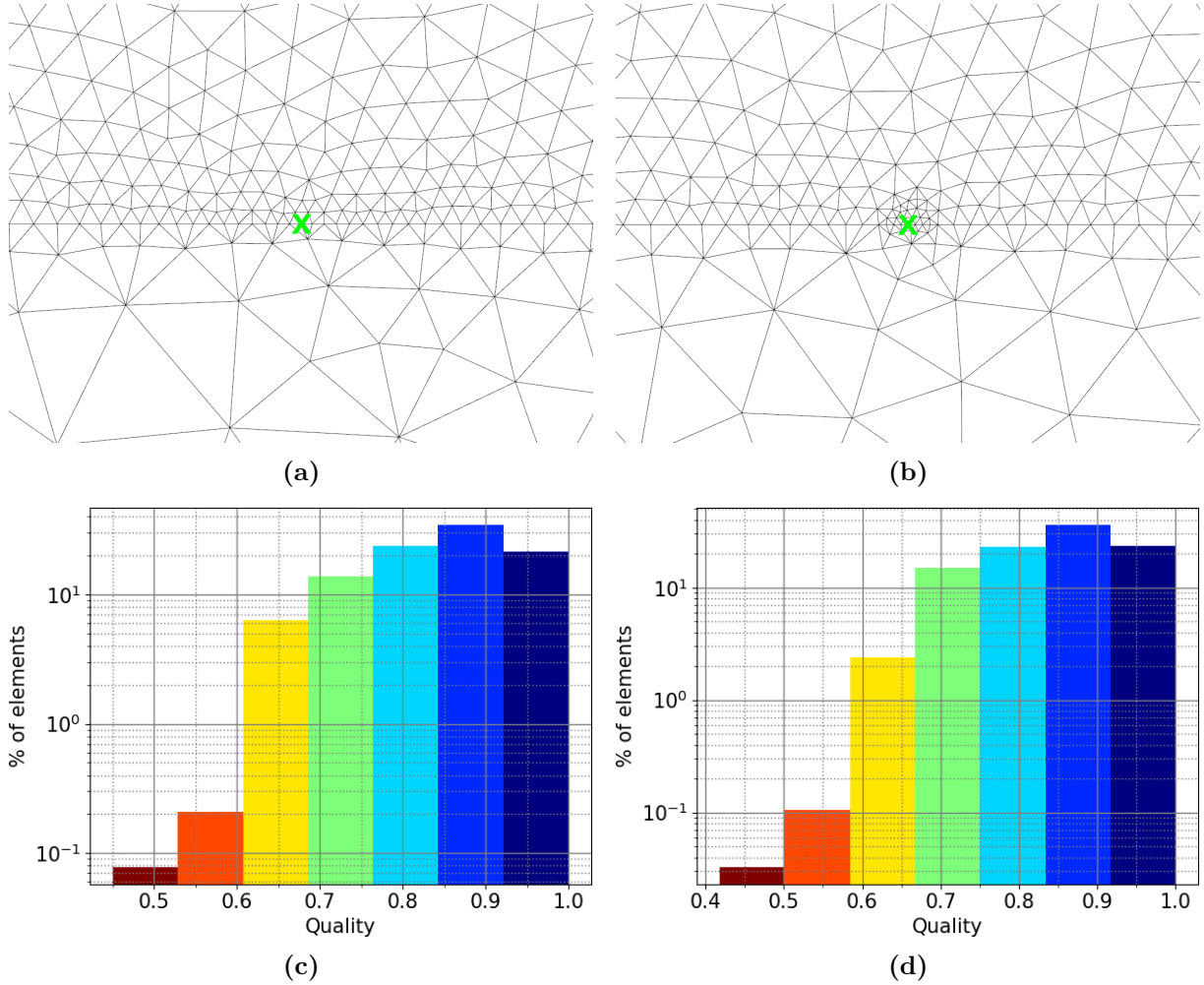
Figure 6.10: Comparison of the HDG_H and HDG_L meshes. (a) HDG_H mesh near R_1. (b) HDG_L mesh near R_1. (c) HDG_H elements' quality ranges. (d) HDG_L elements' quality ranges.

Additionally, to compare the effects of the polynomial order on the accuracy of the solution in long-term time-integration, in each of the two geometrical discretizations the solutions are approximated by polynomials of different orders k. In the first case, second-order, $k = 2$, polynomials are used, whilst in the second configuration, a first-order, $k = 1$, polynomial approximation is employed. Thus, a total of four different discretizations are used.

Considering the discretizations employing second-order polynomial approximation, the solution obtained with the lower-quality mesh is, in the early times, almost indistinguish-

able from the solution obtained with the higher-quality mesh. However, it was noticed that, the quality of the solution of the low-quality mesh degrades. This effect is evident in regions of the mesh where the low quality elements are present, where spurious oscillations in the solution begin to appear. In Figure 6.11 is possible to notice how the different solutions, initially identical, diverge noticeably from one another for $t > 1$ s in the proximity of R_1.
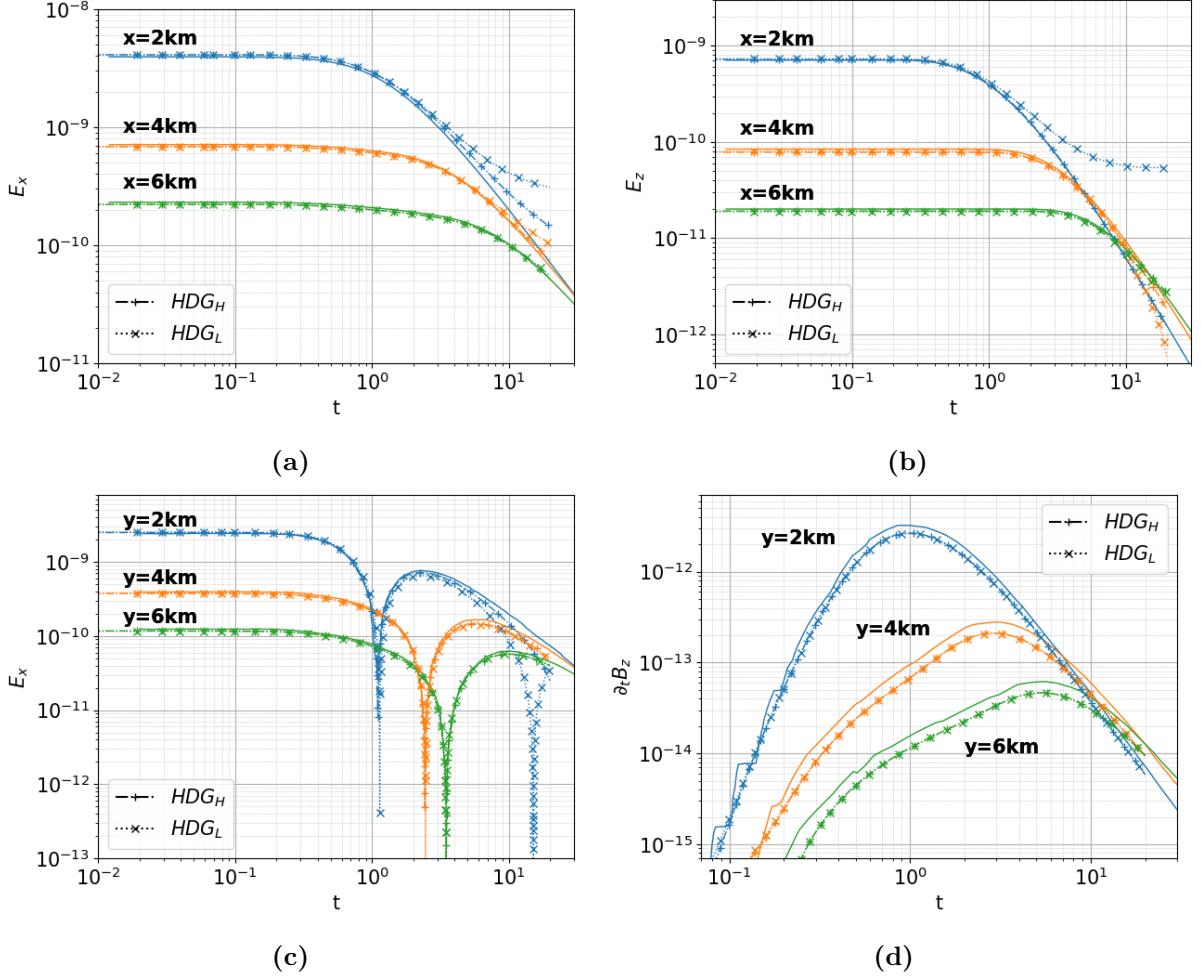
Figure 6.11: Comparison of analytical solution and HDG solution with different meshes. (a) Inline E_x. (b) Inline E_z. (c) Broadside E_x. (d) Broadside $\partial_t B_z$.

It is worth to point out that, although both the E_x and E_z components are affected by spurious oscillations, the different components are affected in different measure. In fact, in the inline receivers, while the approximated E_x component is affected by spurious oscillations in both cases, the approximate E_z component is inaccurate only when computed with the low-quality mesh, see Figure 6.11(a) and Figure 6.11(b). In the broadside configuration, the E_x component has vastly different behaviours at the different receivers' locations, with the closer receivers more affected by spurious oscillations. Moreover, in these tests, the time derivative of the magnetic induction field is not affected by the mesh quality, see Figure 6.11(d).

The same loss of accuracy is noticeable comparing the high-quality mesh employing first-order polynomial approximation, HDG_H^1, to that employing second-order polynomial approximation HDG_H^2. In fact, whilst in early times both solution have similar accuracy, the HDG_H^1 mesh is affected by error migration earlier than HDG_H^2 mesh is.
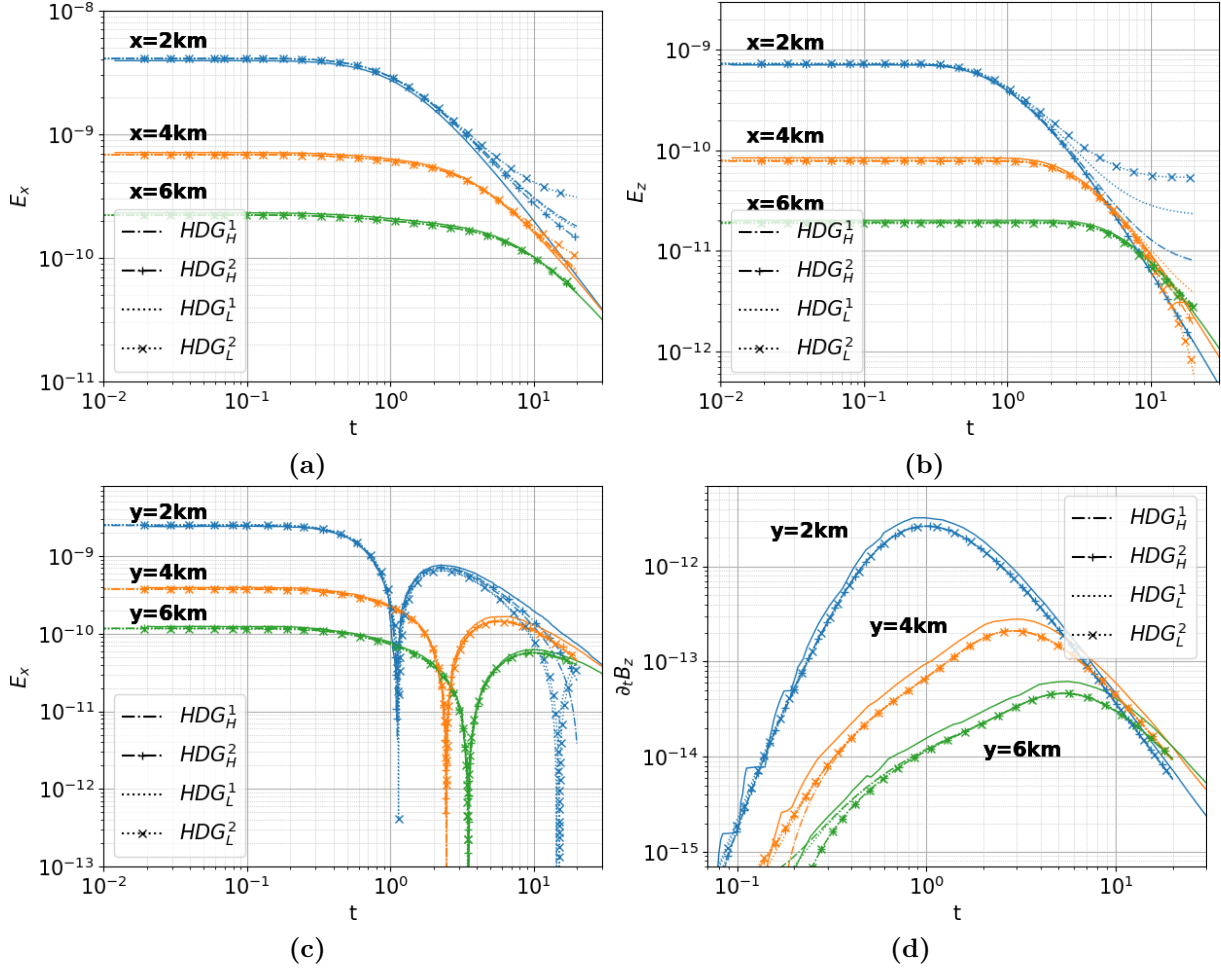
Figure 6.12: Comparison of solutions obtained with different meshes and different orders of polynomial approximation. (a) Inline E_x. (b) Inline E_z. (c) Broadside E_x. (d) Broadside $\partial_t B_z$.

Despite being affected by spurious oscillations, the solutions obtained with the low-quality meshes exhibit an opposite behaviour with respect to the high-quality meshes. In fact, the solution obtained with the HDG_L^1 mesh appears to be more accurate than that obtained with the HDG_L^2 mesh in each component of the electric field and at each receiver location. However, the time derivative of the magnetic induction field remains unaffected. Figure 6.12 shows the results for each combination of mesh quality and polynomial order of approximation used.

The loss of accuracy can be attributed to the amplification of the errors due to the repetitive solution of the linear system of equations via iterative solvers, whose accuracy is governed by a user-specified tolerance and by the condition number of the system's

matrix. Hence, despite the fact that both the HDG$_\text{H}$ and the HDG$_\text{L}$ meshes provide an accurate solution in early times, the lower quality HDG$_\text{L}$ mesh suffers more from error migration in later times.

The comparison between first- and second-order polynomial approximation is more complex as no information about the condition number of the system is available.

6.3.3 Conclusions and outline

In Section 6.3.2, the main factors contributing to a fast and reliable solution of an EMD problem are shown. From these results is possible to extract a few key points and remarks that could be used to improve the accuracy of the proposed method.

Time-step size   It has been seen that in long-term integration of the equations the effects of the time-step size are numerous. The main factor in the choice of the time-step size is the physical process being modeled and its frequency content. For physical processes with fast changing fields and high-frequency contents, small time-step are necessary. For problems with slower transients, and frequencies in the low-frequency spectrum, larger time-steps can be employed. However, it has to be considered that for long-term integration, the time-step size plays a role in the long-term evolution of the fields. Finally, the time-step size influences the condition number of the matrix, hence affecting the performance of the solver and its accuracy.

Mesh quality   It is widespread knowledge that mesh quality plays an important role in the numerical solution of PDEs. The results of Section 6.3.2 show that mesh quality plays an even more important role when long-term integration of the equations is necessary. In fact, even though a lower quality mesh might provide satisfactory results in early times, it is possible, in later times, to obtain results that no longer represent the correct behaviour of the system. Hence, from an accuracy point of view, it is more important to generate a high quality mesh than unnecessarily refine the mesh.

High-order polynomial approximation   Similarly to mesh quality, using a higher order polynomial approximation leads to more accurate results in long-term integration of PDEs. In fact, once again, Section 6.3.2 shows that even though a first-order polynomial approximation produces accurate results in early times, the accuracy of the solution reduces as we move to later times. Hence, the advantages of high-order HDG methods are appreciable in problems that require long-term integration.

Divergence cleaning   From a closer inspection of the solution, it is possible to notice that, as the magnitude of the solution decreases, spurious oscillations appear in the solution. These oscillations are more pronounced where the element size and quality is reduced and in proximity of material interfaces. In fact, the appearance of spurious solutions in the static limit is a known problem of the solution of EMD equations via iterative solvers [105]. Hence, the development of divergence cleaning techniques could lead to an

improvement of the accuracy of the proposed method when long-term time-integration is necessary.

7 Fracking model

The goal of this work is to develop a novel, efficient, approach to the simulation of the propagation of electromagnetic signal in underground strata-formations.

An accurate simulation of the propagation of electromagnetic signals in earth is a necessary prerequisite for the economic and safe, in situ, deployment of measure-while-drilling technologies. Prior knowledge of the electrical characteristics of the local geological formations, though not indispensable, leads to improved solutions and therefore more effective MWD transmissions. Once the transmission properties of the MWD telemetry module are known, simulating the current configuration of the drill site provides important information regarding the best transmission setup. In fact, modern MWD transmission velocities are typically bounded by the transmission technology and by the properties of the formations encountered during the operations.

In mud-pulse telemetry, the data is encoded in pressure signals and transmitted by the drilling fluid. In electromagnetic telemetry, the signals are transmitted via electromagnetic signals propagating through the underground formations. Depending on the location, and on the geometry of the drill site, it might be favourable to use mud-pulse over EM telemetry and vice-versa. However, when possible, EM telemetry is preferred as the transmission is typically faster and does not require production down-times. Therefore, simulating the transmission beforehand can provide the operator information about the feasibility and achievable performances of EM telemetry.

To achieve our goals, in Chapter 3 and Chapter 5 novel formulations have been developed and thoroughly tested with simple test cases, for which analytical solutions are available. In Chapter 4 and Chapter 6 the formulations are validated against more complex real-world scenarios and the performances evaluated. Finally, in this chapter, an application to signal propagation simulation of the most promising of the two formulations, the one based on the EMD equation discussed in Chapter 5, is shown.

The chapter is organised as follows. In Section 7.1 the geometry and the properties of the model are presented. A detailed description of spatial and time discretizations is also part of this section. In Section 7.2 the results of different configurations are analysed. This section can be split in two sub-parts. In the first part, Section 7.2.1, the relation between the electrical properties of the materials and the numerical performance and accuracy of the method are investigated. Within this section, the effects of electric conductivity and of time-step size on the condition number of the matrix and on the solution accuracy are explored. In the second part, Section 7.2.2 and Section 7.2.3 the effect of application-specific properties, such as in-situ electrical conductivity and signal frequency, on transmission efficacy are thoroughly investigated.

7 Fracking model

7.1 Problem description
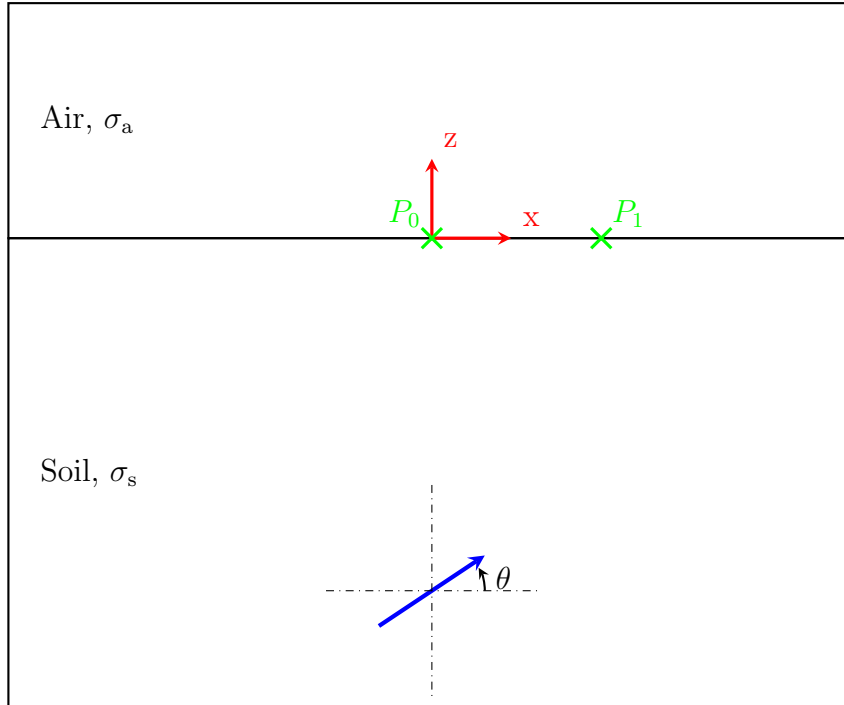
Figure 7.1: Fracking model schematical representation (xz-plane at $y = 0$). The blue arrow represents the current source laying at an angle $\theta = 30°$, from the horizontal. The green crosses indicate the positions of the antenna poles P_0 and P_1. Notice that the representation is not to scale.

In this fracking example the domain is a cube of side $L = 50$ km vertically divided in two identical rectangular prisms. The top rectangular prism represents air, while the bottom one represents the ground. The interface between the two half-spaces is the xy-plane, and divides the domain in two halves.

A 6 m long current source of radius $r = 1$ m is buried in the earth layer. The barycentric coordinates of the dipole are placed along the z-axis at a depth of $z_D = -2500$ m. The longitudinal axis of the source lies on the xz-plane and has an inclination $\theta = 30°$ with respect to the x-axis.

At the interface between air and soil, two antenna poles, P_0 and P_1, are placed in the origin of the axis, P_0, and at a distance $x_1 = 100$ m along the x-axis, P_1. Figure 7.1 provides a not-to-scale representation of the geometry of the problem.

The magnetic permeability is set to $\mu = \mu_0$ in the whole domain. The electrical conductivity is homogeneous only within each half-space and the effects of the values of electrical conductivity of the different layers are investigated. Initially different conductivity values are set in the air layer $\sigma_a = [10^{-5}, 10^{-6}, 10^{-7}, 10^{-8}, 10^{-9}, 10^{-10}]$ S/m are to evaluate the effect of the electrical conductivity of the air on the solution accuracy and efficiency. The effects of the electrical conductivity of the soil layer are also explored. Hence, the values $\sigma_s = [1, 10^{-1}, 10^{-2}, 10^{-3}]$ S/m are employed in different test cases.

The current source is excited with a 20 A pk-pk alternate current with a sinusoidal waveform. The signal transmission at the frequencies $f = [1, 2, 4, 8, 16]$ Hz are simulated to study the dependency of the received electric field and electric potential on the transmission frequency.

7.1.1 Spatial discretization

The domain is discretized in 146228 geometrically linear tetrahedral elements. In this chapter only first-order polynomial approximation is used hence, the discretization of the EMD equation results in 1760796 global unknowns and 3509472 local unknowns. Notice that the computational cost of the simulation is mostly dependent on the number of unknowns of the global problem. In fact, after the condensation of the matrices following the algorithm described in Section 5.1.2, the size of the linear system's matrix (5.17) is equal to the number of unknowns of the global problem. Once the global problem is solved, the unknowns of the local problem can be computed in a parallel fashion computing the matrix-vector multiplications of (5.23).

The numerical domain's boundaries are extended 10 times the source-receiver distance from the centre of the domain, that is, 25 km from the origin of the axis. On the boundaries of the domain PEC boundary conditions are enforced. Extending the boundaries away from the area where the source and antenna poles are, ensures that artificial boundary effects do not affect the solution in the area of interest, as seen in Section 5.3.2. The mesh used to discretize the fracking model is shown in Figure 7.2 and Figure 7.3.

It is important to notice that, despite structured meshes can be used to discretize the domain and account for the source, their application is not advised. The discretization of the domain described in Section 7.1 with structured meshes, just as for the problem described in Section 6.1, would result in an unnecessarily large number of elements. In fact, with structured meshes it is typically necessary to extend the region containing small elements all the way to the boundaries, see [95, 99]. Unstructured meshes, on the contrary, allow a fine representation of the geometry of source and a coarser discretization in the vicinity of the boundaries. Figure 7.3(a) shows the fine discretization of the source with tetrahedral elements. In Figure 7.3(b) it is possible to notice how the unstructured discretization allows for a reduction of the number of elements increasing the size of the elements away from small geometrical features.

Notice that, in order to obtain accurate solutions, it is necessary to smoothly increase the size of adjacent elements. In fact, steep changes in elements' sizes and heavily distorted tetrahedrons, reduce the quality of the approximation. This effect can be measured directly, computing the condition number of the matrix or, indirectly, from an analysis of the number of iterations necessary to solve the linear system. In the discretization of the domain, therefore, the growth rate of the elements is maintained below 2 in the whole mesh and the elements are modified until each element has a quality, in the shape metric [178], above the threshold set to 0.4. The mesh was generated via the software Cubit 13.2 [179]. Figure 7.4 shows the distribution of the elements in the different element's shape quality ranges. The lowest element quality range is the range comprising
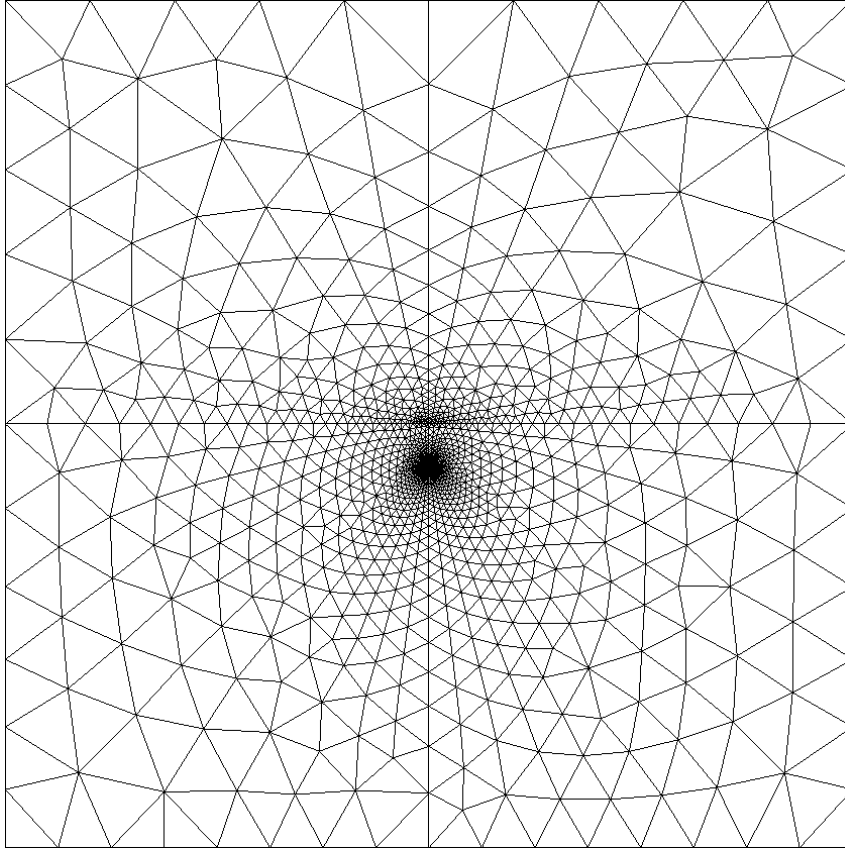
Figure 7.2: Section of the spatial discretization on the xz-plane.

elements with quality between 0.56 and 0.62 and contains 106 elements, that is, 0.072% of the elements. Approximately 90% of the elements have a quality of more than 0.75.

7.1.2 Time discretization

In this test case a MWD scenario in which a downhole transmitter is turned on to transmit data to the surface is modeled. As the transmission is initiated during the simulation, the initial condition represents a stationary, identically zero, electric and magnetic field. Hence, there is no need to initialize the field to an electric field solving a EMD problem.

At the time $t_s = 10^{-3}$ s a current is forced through the source, following a sinusoidal waveform. The transmission is maintained until the end of the simulation at $T_{max} = 2.2$ s. T_{max} is chosen such that, with the source excited with the lowest frequency signal, $f = 1$ Hz, approximately two periods of the wave are received at the antenna poles' locations.

Signals with different frequencies, $f = [1, 2, 4, 8, 16]$ Hz, are used in different test cases, to investigate the effect of the frequency of the source on the received signal. Notice that, as the waveform $\mathbf{i}_s(t) \in C^\infty$, it is beneficial to use a higher-order time-integration scheme. Therefore, for all the simulations, the BDF2 time-integration scheme introduced in Section 2.2.4 is used.
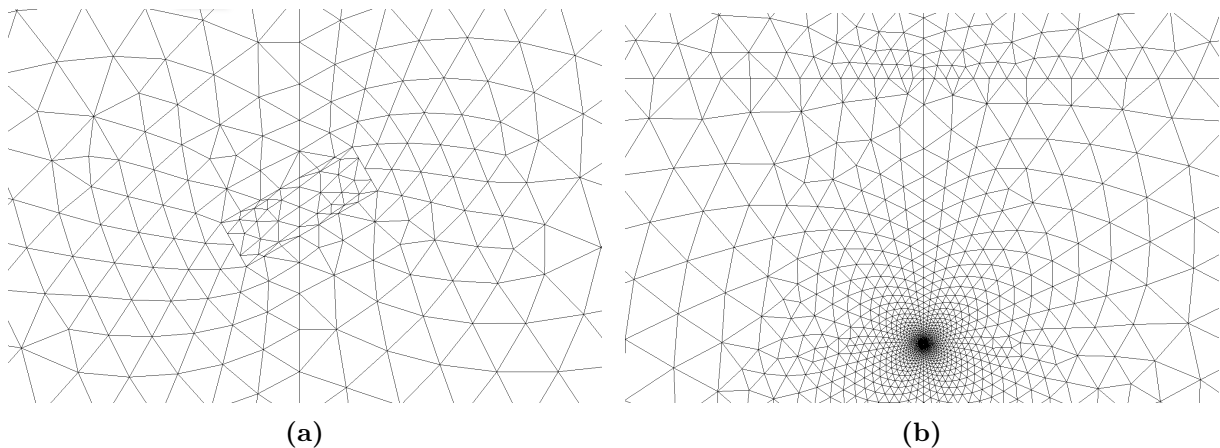
Figure 7.3: Details of the fracking model mesh. (a) Discretization of the source. (b) Mesh in the source-receiver area.

The time-step size is set to $\Delta t = 10^{-3}$ s, to ensure a proper resolution for $f = 16$ Hz and to improve the condition number of the linear system's matrix, see Section 5.4.

In fact, it was observed that, depending on the electrical properties of the different regions of the domain, especially for low values of electrical conductivity of the soil, a very small time-step was necessary to achieve convergence in the iterative solvers. In fact, when more resistive earth $\sigma_{\mathrm{s}} = 0.01$ S/m is simulated, the condition number of the matrix increases until the point in which it is impossible to obtain a solution by iterative solvers. Given that the formulation proposed in Section 5.4 and AMG preconditioners are already being used, it is only possible to improve the condition number of the matrix decreasing the time-step size, with obvious repercussions on execution times.

7.2 Results

In this section different numerical experiments are presented with the goal to explore the dependency of the electric field and the electric potential at the antenna poles' locations on the different electrical properties.

The fields are generated by an electrical current source excited by a current density flowing parallel to the dipole longitudinal axis with the intensity given by

$$|\mathbf{i}_{\mathrm{s}}(t)| = \begin{cases} 0 & t < t_s, \\ \frac{10}{\pi}\sin(2\pi f(t - t_s)) & t \geq t_s. \end{cases} \tag{7.1}$$

The electric field presented in the following sections is measured at the P_1 antenna pole location while the electric potential, that is not a solution of the proposed method, is obtained integrating the electric field over the line $P_0 - P_1$

$$\phi = -\int_{P_0}^{P_1} \mathbf{E}^{\mathrm{h}} \cdot \mathbf{dl}. \tag{7.2}$$
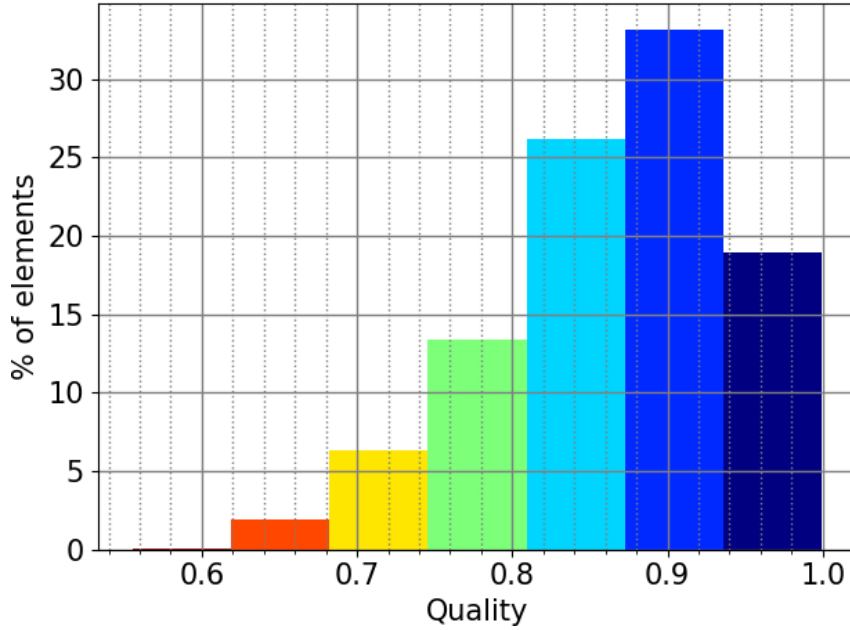
Figure 7.4: Element's shape quality distribution.

It is worth to point out that the segment $P_0 - P_1$ is parallel to the $x-$axis. Hence, in the line integral (7.2), only the $x-$component of the electric field is being considered.

Finally, in the following tests, the linear system of equations is solved via a direct solver as it was found that, for the size of the problems and the electrical parameters set in the domain, these are more efficient than iterative solvers. In fact, despite the fact that direct solvers make intensive use of system memory, the reduced number of elements and globally coupled unknowns of the current problem with respect to the homogeneous seabed model allows employing direct solver. Additionally, the linearity of the formulation (5.11) allows us to compute the factorization of the linear system's matrix $\mathbb{K}$ (5.17) and reuse it in each time-step, therefore reducing the computational cost of the solution. The solver used is the SuperLU [180] accessed via the Trilinos package [151] wrapper. However, the experiments of Section 7.2.1 have also been solved by iterative solvers to investigate the dependency of their performance on the conductivity value of the air layer.

7.2.1 Air conductivity value

As already seen in Chapter 6, the electrical conductivity of the air layer is not set to its physical value of $\sigma_{\mathrm{a}} \approx 10^{-12}$ S/m. In fact, such a small value of electrical conductivity would increase the condition number of the matrix without necessarily improving the accuracy of the solution, see e.g. [105, 106]. However, the air layer is necessary to avoid the introduction of boundary conditions on the interface between air and soil. In order to achieve accurate solutions, the air layer has to provide enough electrical resistivity contrast with the ground to avoid unwanted signal dissipation or reflection [20, 95, 99, 105, 106]. If the electric conductivity of the air layer is set to be higher than the physical conductivity value, $\sigma_{\mathrm{a}} > 10^{-12}$ S/m, while still being much more resistive than the earth layer, $\sigma_{\mathrm{a}} \ll \sigma_{\mathrm{s}}$,

the signals received at the antenna location are accurate enough. To prove this point and ensure that the results provided in Section 7.2.2 and Section 7.2.3 can be accepted, different values of σ_a are set in the different simulations described in this section and the results carefully analysed.

In the all the test cases described here the magnetic permeability is set to $\mu = \mu_0$ and the electric conductivity of the ground is set to $\sigma_s = 0.1$ S/m. The time-step size is set to $\Delta t = 10^{-3}$ s. Considering the frequency of excitation of the source, $f = 2$ Hz, a larger time-step could be used to accurately discretize the response of the system. However, given the magnitude of the received signals, and the studies in Section 5.4.2 on the effect of the electrical conductivity value on the condition number of the matrix, a smaller time-step size is chosen. The air conductivity value spans the order of magnitudes from $\sigma_a = 10^{-5}$ S/m to $\sigma_a = 10^{-10}$ S/m.
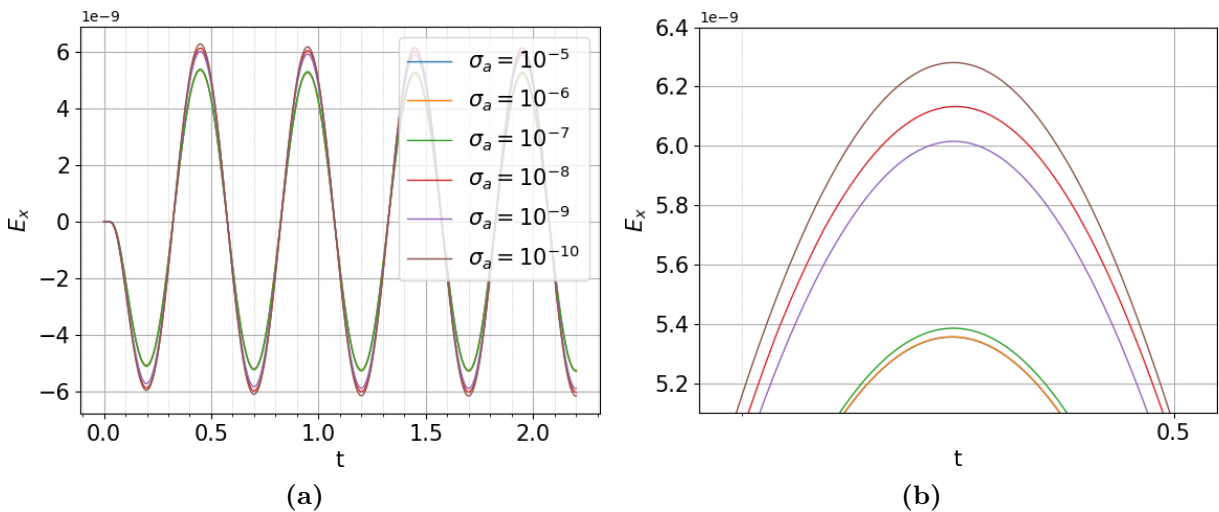
Figure 7.5: Comparison between the received E_x for different values of σ_a. (a) Time evolution of E_x. (b) Close up on the first positive peak of E_x.

The results of the parameter study are reported in Figure 7.5 where a comparison between the x-components of the electric fields over time, measured at the antenna pole P_1, is provided. In Figure 7.5(a) is possible to notice that the results obtained with conductivity values $\sigma_a \geq 10^{-7}$ S/m are very close to each other and follow the expected behaviour, that is, the amplitude of the signal increases with a decrease in air conductivity. In fact, the amplitude of the signals is expected to be inversely proportional to the electrical conductivity of the air layer, such that a lower value of σ_a results in a higher amplitude of the received electric field, and vice-versa. The expected reduction in signal strength is due to the increased diffusion of the electric field in a more conductive air layer. In fact, higher values of electric conductivity increase the amount of energy being dissipated.

However, for $\sigma_a < 10^{-7}$ S/m, the results become noticeably different and the expected relation between the amplitude of the received electric signal and the air conductivity can not be observed anymore. In fact, as shown in Figure 7.5(b), while the difference between the signals obtained with $\sigma_a = 10^{-5}$ S/m and $\sigma_a = 10^{-7}$ S/m is, as measured at the first

positive peak, less than 1%, between signals obtained with $\sigma_\mathrm{a} = 10^{-7}$ S/m and $\sigma_\mathrm{a} = 10^{-10}$ S/m grows to approximately 16%.

Although, at first impression, these results might indicate that the higher conductivity values, $\sigma_\mathrm{a} \geq 10^{-7}$ S/m, do not provide the necessary conductivity contrast between the air and soil layers, the sudden increase in the E_x value, the presence of an anomaly between the results obtained with $\sigma_\mathrm{a} = 10^{-7}$ S/m, $\sigma_\mathrm{a} = 10^{-8}$ S/m and $\sigma_\mathrm{a} = 10^{-9}$ S/m, and the results presented in Section 5.4, raise a question on the reliability of these results. Hence, in Section 7.2.1.1 the same study is repeated with a different time-step to investigate the effect of the time-step length on the solution accuracy.

Finally, although the results presented in this section are obtained making use of a direct solver, to remove the dependence of the solution on the tolerances set by the user, the configurations with $\sigma_\mathrm{a} = 10^{-5}$ S/m to $\sigma_\mathrm{a} = 10^{-8}$ S/m have been simulated using iterative solvers to investigate the dependence of the iteration count on σ_a. The number of iterations necessary to solve the linear system was observed to be extremely large and mostly constant among the different simulations. However, a more detailed study will not be provided here.

7.2.1.1 Effect of the time-step length on the solution

In Section 5.4, the effect of different physical and numerical parameters on the condition number of the matrix are presented. In particular, Figure 5.4 shows the effect of the electric conductivity and of the time-step size on the condition number of the matrix.

Although it is not possible to directly compare the condition numbers in Figure 5.4 to those of the problem at hand, since the current problem includes different values of conductivities and different meshes are used, it is nonetheless possible to extract meaningful information on the behaviour of the condition number. In fact, Figure 5.4 shows that, for $\Delta t = 10^{-3}$ s and very low values of σ_a, that is, $\sigma_\mathrm{a} \leq 10^{-7}$ S/m, the condition number of the matrix has an order of magnitude close to that of machine precision. Hence, to investigate the source of the anomaly found in Figure 7.5, the same experiments are repeated with the reduced time-step size $\Delta t = 10^{-4}$ s, such that, according to Figure 5.4, the condition number is decreased by approximately one order of magnitude.

Figure 7.6 shows the results of the parameter study employing the reduced time-step length, $\Delta t = 10^{-4}$ s. It is possible to notice how, while for $\sigma_\mathrm{a} \geq 10^{-7}$ S/m the results are mostly unaffected by the reduced time-step size, the results for $\sigma_\mathrm{a} < 10^{-7}$ S/m are. The result for $\sigma_\mathrm{a} = 10^{-8}$ S/m becomes closer to those for $\sigma_\mathrm{a} \geq 10^{-7}$ S/m and the anomaly observed in Section 7.2.1 disappears. However, the results for $\sigma_\mathrm{a} \leq 10^{-9}$ S/m are negatively affected by the change in time-step size and the difference between the results for $\sigma_\mathrm{a} = 10^{-7}$ S/m and $\sigma_\mathrm{a} = 10^{-10}$ S/m increases to approximately 40%. A close-up on the first received electric field peak is shown in Figure 7.6(b) and, in greater detail, in Figure 7.7.

These results are consistent with the hypothesis that with small values of air conductivity, $\sigma_\mathrm{a} < 10^{-8}$ S/m, the condition number of the matrix becomes too large to obtain reliable results. In fact, decreasing the time-step size affects mostly the simulations employing $\sigma_\mathrm{a} \leq 10^{-8}$ S/m. As a comparison, whilst the difference of the results for $\sigma_\mathrm{a} = 10^{-8}$ S/m in the two test cases is approximately 8%, the difference for $\sigma_\mathrm{a} \geq 10^{-7}$ S/m is less
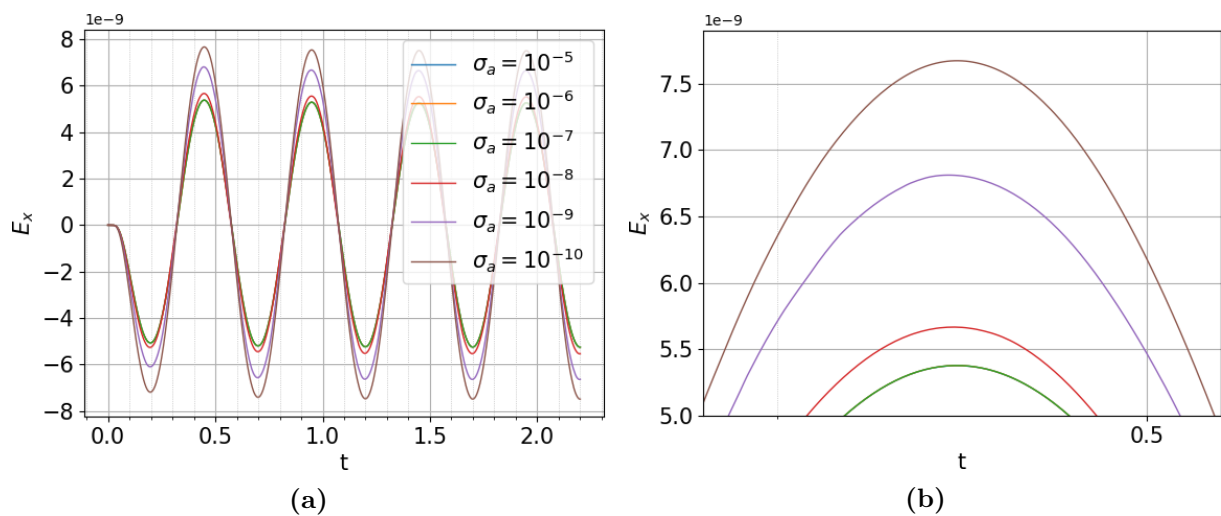
Figure 7.6: Comparison between the received E_x for different values of σ_a for $\Delta t = 10^{-4}$ s. (a) Time evolution of E_x. (b) Close up on the first positive peak of E_x.

than 1%. Finally, while the results for $\sigma_a = 10^{-8}$ S/m improve, the results for $\sigma_a \leq 10^{-9}$ S/m do not. Hence, for the aforementioned reasons, the cases with $\sigma_a \leq 10^{-9}$ S/m are believed to be mostly affected by numerical errors.

Furthermore, it is important to point out that the influence of the electrical conductivity of the air layer on the time transient is neglectable. Hence, the reduction of the time-step size does not influence the accuracy of the time-integration scheme. In fact, the invariance of the solutions for $\sigma_a > 10^{-7}$ S/m in the different test cases, indicates that the time-step size $\Delta t = 10^{-3}$ s is already accurate enough.

The results of this parameter study indicate that the values $\sigma_a = 10^{-7}$ S/m and $\Delta t = 10^{-3}$ s provide the best trade-off between accuracy and computational time. Hence, in the experiments of the following sections, these values will be employed.

7.2.2 Soil conductivity value

In this test case, the effect of the electric conductivity of the underground formations on the received signal strength is investigated.

The decreased value of electrical conductivity of the current problem with respect to the HSM of Chapter 6 negatively affects the performances of iterative solvers. In fact, in our experiments, it was noticed that the value $\sigma_s = 0.1$ S/m is the threshold for an efficient solution via iterative solvers. Lower values of $\sigma_s > 0.1$ S/m degrade the performances of the solvers until the convergence is lost. Hence, the solutions of the test cases presented in this section is computed via direct solvers.

In Figure 7.8 the time evolution of the received electric field and of the electric potential's absolute value are shown for different values of soil's electrical conductivity. The results clearly show how the more conductive underground formations, from the lowest value $\sigma_s = 10^{-3}$ S/m to the highest conductivity value of $\sigma_s = 1$ S/m, increasingly atten-
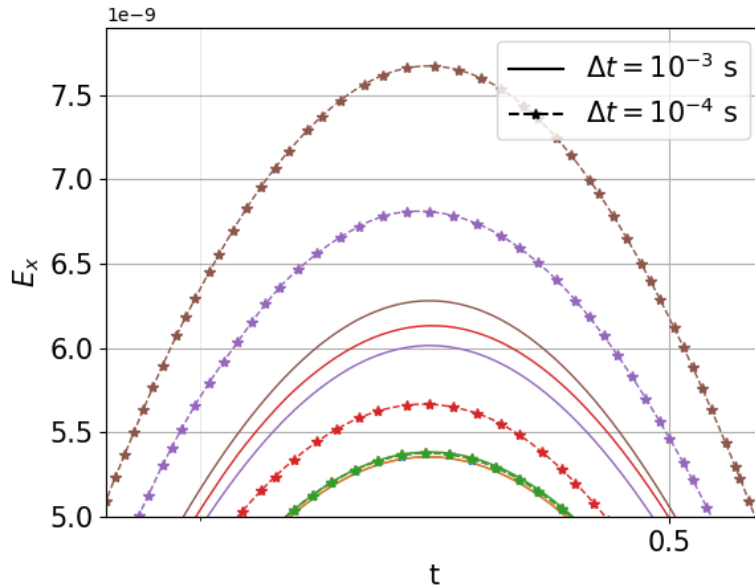
Figure 7.7: Comparison between the received E_x for different values of σ_a and Δt. The color scheme is the same adopted in Figure 7.5 and Figure 7.6.

uate the signal amplitude. Therefore, given a source with a finite power, more resistive formations are better suited the transmission of telemetry signals to the ground.

Additionally, in Figure 7.8(b), it is also possible to notice the dependence of the signal propagation velocity on the conductivity of the medium. In fact, the peaks and the zeros of the electric potential are shifted towards later times for formations with higher electric conductivity values.

In conclusion, these results indicate that when using electromagnetic telemetry for MWD purposes, resistive formations are advantageous with respect to more conductive environments. In practical applications, the lower signal absorption of a more resistive formation can be exploited by: reducing the transmission power, therefore reducing costs; increasing the transmission frequency, obtaining faster transmission rates; communications can be established on longer ranges, hence deeper wells.

7.2.3 Source frequency

One of the parameters that on-field operators can set in their transmission apparatus is the signal frequency. The choice of the carrier frequency is forced by the trade-off between transmission speeds and signal attenuation. Higher frequencies allow for faster data transmission rates but are also subject to higher signal attenuation. Lower frequency transmissions allow for communications over longer distances but with a reduced speed with respect to higher frequency signals. Therefore, given the configuration of the drilling site and of the performances of the transmission instrumentation, simulation of signal propagation can provide meaningful information for the setup of the transmission link.
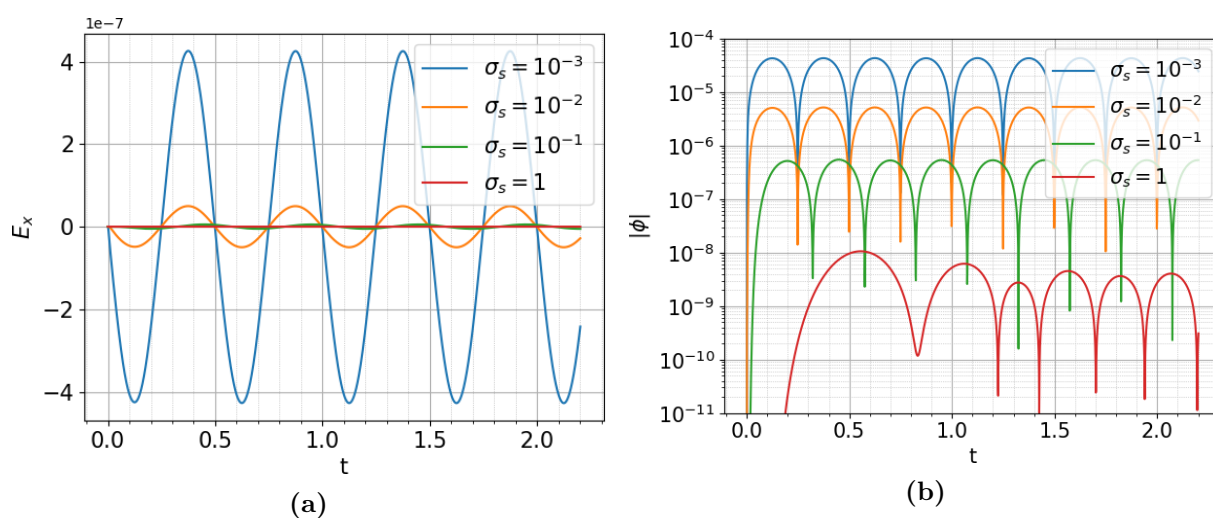
Figure 7.8: Received signal strength as a function of soil electric conductivity over time. (a) Electric field. (b) Absolute value of the electric potential.

In this section, an exemplary study of the dependence of the strength of the received signal on the frequency of the source is shown. The electrical conductivity of the air and earth layers are set to $\sigma_a = 10^{-7}$ S/m and $\sigma_s = 0.1$ S/m, respectively, and the magnetic permeability in the entire domain is set to $\mu = \mu_0$. The source is excited with a total current $|\mathbf{I}_s| = 20$ A pk-pk following the relation (7.1). The frequencies employed are chosen in the frequency range that is typical in MWD applications, that is, $f = [1, 2, 4, 8, 16]$ Hz.

Figure 7.9 shows the comparison between signals received from sources excited with different frequencies as electric field over time. The received electric potentials closely follow the behaviour of the electric field and are therefore not shown.

As expected, for sources excited with low frequencies currents, $1 - 2$ Hz, the received signal strengths are higher than those of the sources excited with higher frequencies currents, $8 - 16$ Hz. It is worth to point out that the relation of the amplitudes of the received signals on the source frequency is nonlinear. Hence, doubling the source frequency does not reduce the signal strength by half.
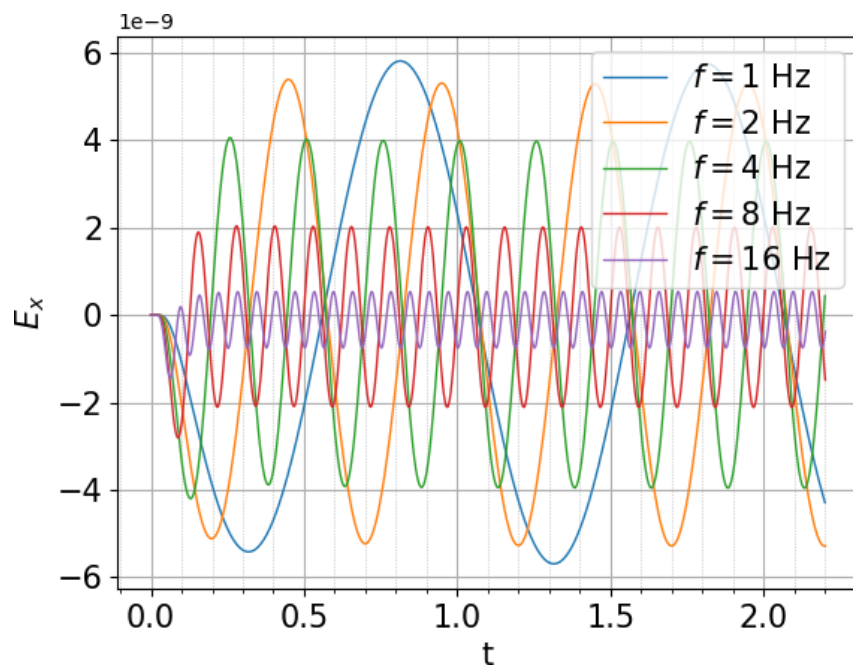
Figure 7.9: Received signal strength over time for different source excitation frequencies.

8 Conclusion & Outlook

This thesis lays the groundwork for the application of high-order methods in the field of geophysics. In fact, in the previous chapters, different schemes for the solution of electromagnetic propagation phenomena in conductive media are presented. The novel methods are complemented with convergence studies on simple test cases for verification purposes. Finally, real-world application scenarios are simulated to validate the proposed approximation schemes.

In this chapter, the conclusions that can be drawn from this work and additional research ideas are presented. The chapter is organised as follows. In Section 8.1, the overall achievements of this work are summarised. However, many of the ideas proposed in this work can be extended or improved with further research. Hence, a short outlook of some of the areas that, in the author's opinion, are worth investigating are listed in Section 8.2.

8.1 Conclusions

In this thesis, two novel schemes for the solution of electromagnetic phenomena in geophysical applications have been developed. The equations that model electromagnetic wave and diffusion phenomena in conductive media are discretized by means of novel high-order Hybridizable Discontinuous Galerkin (HDG) methods and are used to solve real-world application scenarios.

The first proposed scheme is based on a mixed-equation formulation of the Maxwell equations. This general-purpose method allows the solution of electromagnetic wave and diffusion phenomena. This set of equations includes Faraday's law of induction and Maxwell–Ampere's law, and has been successfully used in the past to model wave propagation in dielectric media [59, 67] and electromagnetic diffusion problems in geophysical applications [21, 142]. However, to the best of the author's knowledge, the first high-order HDG method, based on these equations, for the solution of electromagnetic wave propagation in conductive media is proposed in the author's publication [68] on which this work is based. The scheme proposed in the third chapter combines the high-order approximation properties of HDG discretizations, with the possibility to simulate complex geological formations with embedded current sources. Appropriate boundary conditions for diffusion problems, in the form of Perfect Electric Conductor (PEC) Boundary Conditions (BC), and wave phenomena, in the form of Absorbing Boundary Conditions (ABC), are proposed for use in different test cases. In this work, the derivation of the formulation is shown in detail. The problem of electromagnetic wave propagation in a resonant cavity is used to thoroughly assess the convergence properties of the method for several orders of polynomial approximation. Finally, the scheme is used to simulate an electromagnetic

diffusion problem in a unit cube of conductive material containing a current source for which the analytic solution is available to further prove its accuracy properties.

In the fourth chapter, the proposed formulation is applied to different test cases representing wave propagation and scattering problems. First, the wave propagation in a dielectric sphere, for which analytical solutions are available, is used to further validate the method and the ABCs. Successively, the scattering of waves of different frequencies by a spherical obstacle is investigated. Initially, a dielectric obstacle modelling a ball lens is used, and the observed optical properties are qualitatively compared to the expected values. Finally, conductive obstacles of different values of electrical conductivity are employed and the absorption characteristics on waves of different frequencies are evaluated.

The second high-order HDG scheme proposed is based on the Electromagnetic Diffusion (EMD) equation, and can be obtained from the damped vector wave equation neglecting the displacement current term. The electromagnetic diffusion equation is typically used in geophysical applications for the simulation of transient electromagnetic responses to galvanic sources [105, 106]. In geophysical applications, the EMD equation is typically discretized by finite differences and edge-based finite element [83, 105]. Hence, to the best of the author's knowledge, the first application of HDG methods in this field can be found in the author's publication [69]. A step-by-step derivation of the HDG formulation is provided and a post-processing algorithm to improve solution accuracy is proposed. To compute the initial conditions necessary for the initialization of the time-integration scheme, an additional HDG scheme is proposed for the solution of the Direct Current (DC) resistivity problem. Once again, to the best of the author's knowledge, this is the first application of an HDG scheme to the solution of the DC problem in geophysical applications. Moreover, the effect of the electrical properties on the condition number of the discretization matrices are investigated. As a result, it was found that the electrical properties of the materials usually encountered in geophysical applications cause the discretization matrices to be ill-conditioned. Therefore, a modified formulation of the EMD equation, in which the time-step length is used to balance the negative effects of the magnetic permeability, is proposed. The modified version of the EMD equation is shown to sharply reduce the condition number in applications that use real-world electrical properties. Finally, the convergence rates achieved by the primary, auxiliary and post-processed variables for different orders of polynomial approximation are assessed.

The focus of Chapter 6, is on the validation of the proposed discretization scheme via the so-called Homogeneous Seabed Model (HSM). In this test case, the electromagnetic transient response to a ramp-off galvanic source signal is simulated in a marine scenario in which layers of materials with different conductivity values are present. The simulation of this model problem is made complex by the necessity of using unstructured meshes to discretize the geometrical details of the domain and by the presence of a strong conductivity contrast between the air layer and the water layer. As a consequence of these properties, the formulation based on the EMD equation is employed to successfully reproduce the results present in the literature [105, 106].

In conclusion, an application of the proposed HDG method to Measure-While-Drilling (MWD) scenarios is presented. In this model, an arbitrarily oriented source buried in a homogeneous, conductive stratum, transmits electromagnetic signals to a surface receiver.

The effects of different materials and signal properties on the signal transmission efficacy, in this exemplary fracking configuration, are investigated. First, the effects of different conductivity values for the air layer on the solution time and accuracy are explored. Then, the conductivity value of the soil is modified and its consequences on the received signals are considered. Finally, the effects of the source's excitation frequency on the received signal amplitude are considered.

8.2 Outlook

Together with its novelty elements, this thesis brings to light additional questions that, in the author's opinion, are worth investigating in future research.

In real-world application scenarios, as those presented in Chapter 6 and Chapter 7, given the choice of implicit time-integration schemes, it is typically necessary to solve large systems of equations by means of iterative solvers. However, as a consequence of the strong non diagonally dominant matrix structure of HDG methods [123], standard preconditioning techniques as ILU and Algebraic multigrid (AMG) lose their efficiency and, therefore, the solution of the linear system quickly becomes troublesome. Hence, a thorough investigation of the best preconditioning practices available for HDG methods [181], specially in conjunction with unstructured meshes and heterogeneous electrical properties, and the development of preconditioner specifically developed for geophysical applications, would greatly expand the applicability of the proposed high-order methods.

To further improve the computational efficiency of the proposed HDG method, it is possible to explore the performances of matrix-free implementations, as already implemented in the discretization of Poisson's equation via HDG methods, where a matrix-free evaluation is shown to reduce the computational cost [123]. In the matrix-free approach the goal is to maximise the number of arithmetic operations that the processor has to execute before loading additional data, reducing the bottleneck caused by the limited memory bandwidth [182]. The extension of the matrix-free approach to the discretization of the electromagnetic diffusion equation could therefore improve solvers' efficiency.

Closely related to the topic of solver efficiency, is the performance comparison of the proposed HDG schemes to edge-based Continuous Galerkin (CG) methods. In fact, while a lot of effort was put in the past into exploring performances comparisons of HDG and node-based CG methods [55,56,122,123], to the best of the author's knowledge, not much was done comparing HDG schemes to their direct competitors in the field of electromagnetics. In fact, the HDG is known to compare well with respect to CG when high-order polynomial approximation is used. Therefore, the increased number of unknowns present in edge-based CG methods, coupled with the increased complexity of generating high-order approximations, could make HDG methods increasingly advantageous.

To improve the solution accuracy and, potentially, improve the convergence of iterative solvers, it is possible to introduce a divergence cleaning technique as done in [106]. In their approach, the DC problem, without a current source, is solved during the iterations of the Conjugate Gradient Solver (CGS) to ensure the electric field to be solenoidal. Different divergence cleaning techniques have been developed for different use cases, see,

e.g. [116, 117]. Therefore, an investigation of the most appropriate techniques for use in geophysical applications would be of great interest in subsequent work.

An additional way to reduce the computational cost of the simulations could be the implementation of explicit methods instead of implicit ones, as detailed in [128]. In fact, it was shown that the time-step size limit necessary for the stability of explicit methods does not necessarily result in a higher computational cost of the simulation. Although the comparison in [128] was specific for acoustic problems, the same results could apply to a performance comparison between implicit and explicit time-integration schemes applied to the problems investigated in this thesis.

In this work, it was found that the HDG scheme based on the EMD equation performs better than the one based on the mixed-equation formulation. However, HDG methods based on the full-wave wave formulation could benefit by the use of efficient time-integration schemes such as Implicit-Explicit (IMEX), in which the hyperbolic and parabolic terms of the equation are discretized by explicit and implicit schemes respectively, see e.g. [43, 183].

Finally, we motivate our choice of an implicit time-integration scheme with the rationale that low-order Backward Differentiation Formula (BDF) schemes dissipate the high-frequency content of the excitation source. However, to control the dissipation of the numerical method, it is possible to discretize the Ordinary Differential Equation (ODE)s by means of the Generalized-α method [173–175] that allows to control the high-frequency damping via a set of parameters. Hence, the application of the Generalized-α to geophysical applications could bring increased control in the simulation setup.

A Conservativity of the methods

To prove that the methods derived in Section 3.1 and Section 5.1 are locally conservative, it is necessary to show that $\hat{\mathbf{H}}^{\mathrm{h}}$ and $\hat{\mathbf{u}}^{\mathrm{h}}$, respectively, are single-valued across inter-element boundaries [66]. This condition is ensured by the definitions (3.5) and (5.7) of $\hat{\mathbf{H}}^{\mathrm{h}}$ and $\hat{\mathbf{u}}^{\mathrm{h}}$, respectively, togher with the continuity equations (3.7) and (5.9). In this chapter, the prof of the continuity of the magnetic trace field is provided. The prof for the $\hat{\mathbf{u}}^{\mathrm{h}}$ field follows the same rationale.

Substituting (3.5) in (3.7), the following relation is obtained

$$\left[\!\left[\mathbf{n} \times \mathbf{H}^{\mathrm{h}}\right]\!\right] + \tau^{+}\mathbf{E}_{\mathrm{t}}^{h+} + \tau^{-}\mathbf{E}_{\mathrm{t}}^{h-} - (\tau^{+} + \tau^{-})\boldsymbol{\Lambda}^{\mathrm{h}} = \mathbf{0}, \tag{A.1}$$

from which is possible to obtain the following equation for the hybrid variable

$$\boldsymbol{\Lambda}^{\mathrm{h}} = \frac{\tau^{+}\mathbf{E}_{\mathrm{t}}^{h+} + \tau^{-}\mathbf{E}_{\mathrm{t}}^{h-}}{\tau^{+} + \tau^{-}} + \frac{1}{\tau^{+} + \tau^{-}}\left[\!\left[\mathbf{n} \times \mathbf{H}^{\mathrm{h}}\right]\!\right]. \tag{A.2}$$

Substituting (A.2) in (3.5), the following equation is obtained

$$\hat{\mathbf{H}}^{\mathrm{h}} = \mathbf{H}^{\mathrm{h}} + \tau\left(\hat{\mathbf{E}}_{\mathrm{t}}^{\mathrm{h}} - \frac{\tau^{+}\mathbf{E}_{\mathrm{t}}^{h+} + \tau^{-}\mathbf{E}_{\mathrm{t}}^{h-}}{\tau^{+} + \tau^{-}} - \frac{1}{\tau^{+} + \tau^{-}}\left[\!\left[\mathbf{n} \times \mathbf{H}^{\mathrm{h}}\right]\!\right]\right) \times \mathbf{n}, \tag{A.3}$$

eventually yielding

$$\hat{\mathbf{H}}^{h-} = \hat{\mathbf{H}}^{h+} = \hat{\mathbf{H}}^{\mathrm{h}} = \frac{\tau^{-}\mathbf{H}_{\mathrm{t}}^{h+} + \tau^{+}\mathbf{H}_{\mathrm{t}}^{h-}}{\tau^{+} + \tau^{-}} + \frac{\tau^{+}\tau^{-}}{\tau^{+} + \tau^{-}}\left[\!\left[\mathbf{E}^{\mathrm{h}} \times \mathbf{n}\right]\!\right]. \tag{A.4}$$

Hence, the trace value of the magnetic field on the faces of the discretization is single valued. Note that to obtain (A.4), the relation $\mathbf{n}^{+} = -\mathbf{n}^{-}$ is used.

B Schur complement

The stiffness matrices resulting from the HDG formulations presented in this work greatly benefit from static condensation. The procedure of static condensation via Schur complement is shown here. An in-depth mathematical treatment and additional applications of the Schur complement can be found in [184].

B.1 Schur complement

Suppose $\mathbb{A}, \mathbb{B}, \mathbb{C}, \mathbb{D}$ are respectively $p \times p, p \times q, q \times p$, and $q \times q$ matrices, and $\mathbb{D}$ (respectively $\mathbb{A}$) is invertible. Let

$$\mathbb{M} = \begin{bmatrix} \mathbb{A} & \mathbb{B} \\ \mathbb{C} & \mathbb{D} \end{bmatrix}, \tag{B.1}$$

than the Schur complement of the block $\mathbb{D}$ (respectively $\mathbb{A}$) of the matrix $\mathbb{M}$ is the $q \times q$ (respectively $p \times p$) matrix is defined as

$$\begin{aligned} \mathbb{M}/\mathbb{D} &= \mathbb{A} - \mathbb{B}\mathbb{D}^{-1}\mathbb{C}, \\ \mathbb{M}/\mathbb{A} &= \mathbb{D} - \mathbb{C}\mathbb{A}^{-1}\mathbb{B}. \end{aligned} \tag{B.2}$$

Note that, if the matrix $\mathbb{D}$ (respectively $\mathbb{A}$) is itself a block matrix, as in (B.1), it is possible to reduce the size of the matrix to invert, making use of the following identity

$$\begin{aligned} \begin{bmatrix} \mathbb{A} & \mathbb{B} \\ \mathbb{C} & \mathbb{D} \end{bmatrix}^{-1} &= \begin{bmatrix} 1 & -\mathbb{A}^{-1}\mathbb{B} \\ 0 & 1 \end{bmatrix} \begin{bmatrix} \mathbb{A}^{-1} & 0 \\ 0 & (\mathbb{D} - \mathbb{C}\mathbb{A}^{-1}\mathbb{B})^{-1} \end{bmatrix} \begin{bmatrix} 1 & 0 \\ -\mathbb{C}\mathbb{A}^{-1} & 1 \end{bmatrix} \\ &= \begin{bmatrix} 1 & 0 \\ -\mathbb{D}^{-1}\mathbb{C} & 1 \end{bmatrix} \begin{bmatrix} (\mathbb{A} - \mathbb{B}\mathbb{D}^{-1}\mathbb{C})^{-1} & 0 \\ 0 & \mathbb{D}^{-1} \end{bmatrix} \begin{bmatrix} 1 & -\mathbb{B}\mathbb{D}^{-1} \\ 0 & 1 \end{bmatrix}. \end{aligned} \tag{B.3}$$

that requires the inversion of a single block and matrix-matrix multiplications rather than the inversion of the full matrix.

B.2 Schur complement for linear sytems solution

Suppose we have the following linear system:

$$\begin{bmatrix} \mathbb{A} & \mathbb{B} \\ \mathbb{C} & \mathbb{D} \end{bmatrix} \begin{bmatrix} x \\ y \end{bmatrix} = \begin{bmatrix} a \\ b \end{bmatrix}. \tag{B.4}$$

Multiplying the second equation by $\mathbb{B}\mathbb{D}^{-1}$ and subtracting it from the first, the following equation is obtained

$$(\mathbb{A} - \mathbb{B}\mathbb{D}^{-1}\mathbb{C})x = a - \mathbb{B}\mathbb{D}^{-1}b. \tag{B.5}$$

If it is possible to compute the inverse of the Schur complement, and of the $\mathbb{D}$ matrix, it is then possible to compute x. Once x is known, it is possible to compute y

$$\mathbb{D}y = b - \mathbb{C}x. \tag{B.6}$$

In a similar fashion, it is possible to solve for y first, multiplying the first equation by $\mathbb{C}\mathbb{A}^{-1}$ and subtracting it to the second equation

$$(\mathbb{D} - \mathbb{C}\mathbb{A}^{-1}\mathbb{B})y = b - \mathbb{C}\mathbb{A}^{-1}a, \tag{B.7}$$

and then solving for x

$$\mathbb{A}x = a - \mathbb{B}y. \tag{B.8}$$

B.2.1 Computational complexity of the linear solution

It is interesting to study how solving the system of equations using the Schur complement compares to the direct solution via LU decomposition and backward (or forward) substitution.

The computational cost of the direct solution of a linear system is dominated by the cost of the LU decomposition. The LU decomposition of a dense matrix has a computational cost of the order of $O(n^3)$, where n is the number of rows or columns of the matrix. Additionally it is possible to show that the cost of inverting a matrix, $O(n^3)$, is equivalent to that of matrix-matrix multiplication [185]. Hence, faster matrix-matrix multiplication algorithms result in faster matrix inversion algorithms.

Let the matrices $\mathbb{A}, \mathbb{B}, \mathbb{C}, \mathbb{D}$ in (B.1) be $n \times n$ matrices and the matrix $\mathbb{A}$ be invertible. Then, the computational cost of solving the system (B.4) is approximately $(2n)^3$. The computational cost of computing the solution via (B.7) and (B.8) is given by the number of matrix-matrix multiplications and is therefore approximately $5n^3$.

The ratio between the cost of a direct solution and a solution using the Schur complement is then

$$\frac{(2n)^3}{5n^3} = \frac{8}{5} = 1.6, \tag{B.9}$$

indicating that the computational cost of the direct solution is higher than that of the solution via Schur complement by approximately 60%.

Notice that the actual execution time of a solver based on the two different algorithms does not only depend on the computational cost but also on implementation details and on the specific hardware, therefore, using an algorithm based on the Schur complement does not guarantee faster execution times.

Bibliography

[1] S. L. Miller. A Production of Amino Acids Under Possible Primitive Earth Conditions. *Science*, 117(3046):528–529, 1953. URL: `https://science.sciencemag.org/content/117/3046/528`, `doi:10.1126/science.117.3046.528`.

[2] J. L. Bada and A. Lazcano. Prebiotic Soup–Revisiting the Miller Experiment. *Science*, 300(5620):745–746, 2003. URL: `https://science.sciencemag.org/content/300/5620/745`, `doi:10.1126/science.1085145`.

[3] J. Venter. *Life at the Speed of Light: From the Double Helix to the Dawn of Digital Life*. Little, Brown Book Group, 2013.

[4] E. Whittaker. *A History of the Theories of Aether and Electricity from the Age of Descartes to the Close of the Nineteenth Century*. Dublin University Press series. Longmans, Green and Company, 1910.

[5] J. D. Jackson. *Classical electrodynamics*. Wiley, New York, NY, 3rd ed. edition, 1999.

[6] C. S. Herrmann. Human EEG responses to 1–100 Hz flicker: resonance phenomena in visual cortex and their potential correlation to cognitive phenomena. *Experimental Brain Research*, 137:346– 353, 2001. URL: `https://doi.org/10.1007/s002210100682`, `doi:10.1007/s002210100682`.

[7] M. Rausch, M. Gebhardt, M. Kaltenbacher, and H. Landes. Computer-aided design of clinical magnetic resonance imaging scanners by coupled magnetomechanical-acoustic modeling. *IEEE Transactions on Magnetics*, 41(1):72–81, 2005. `doi:10.1109/TMAG.2004.839727`.

[8] Y. Zhang, Z. Ren, and D. Lautru. Finite element modeling of current dipoles using direct and subtraction methods for EEG forward problem. *COMPEL: The International Journal for Computation and Mathematics in Electrical and Electronic Engineering*, 33:210–223, 2014. URL: `https://doi.org/10.1108/COMPEL-11-2012-0329`, `doi:10.1108/COMPEL-11-2012-0329`.

[9] M. W. Asten. The Down-hole Magnetometric Resistivity (DHMMR) Method. *Exploration Geophysics*, 19(1-2):12–16, 1988. URL: `https://doi.org/10.1071/EG988012`, `doi:10.1071/EG988012`.

[10] J. Macnae and R. J. Irvine. Inductive Source Resistivity: A tool for outlining silicification in gold exploration. *Exploration Geophysics*, 19(4):471–480, 1988. URL: `https://doi.org/10.1071/EG988471`, `doi:10.1071/EG988471`.

[11] S. Constable. Ten years of marine CSEM for hydrocarbon exploration. *GEO-PHYSICS*, 75(5):75A67–75A81, 2010. URL: `https://doi.org/10.1190/1.3483451`, `doi:10.1190/1.3483451`.

[12] D. Yang and D. W. Oldenburg. Electric field data in inductive source electromagnetic surveys. *Geophysical Prospecting*, 66(1):207–225, 2018. URL: `https://onlinelibrary.wiley.com/doi/abs/10.1111/1365-2478.12529`, `doi:https://doi.org/10.1111/1365-2478.12529`.

[13] J. Maxwell. *A Treatise on Electricity and Magnetism*. Clarendon Press, 1873.

[14] R. F. Harrington. Matrix methods for field problems. *Proceedings of the IEEE*, 55(2):136–149, 1967. `doi:10.1109/PROC.1967.5433`.

[15] R. F. Harrington. *Field Computation by Moment Methods*. Wiley-IEEE Press, 1993.

[16] W. Gibson. *The Method of Moments in Electromagnetics*. CRC Press, 2007. URL: `https://books.google.de/books?id=uQITMQtmGOwC`.

[17] K. Yee. Numerical solution of inital boundary value problems involving maxwell's equations in isotropic media. *IEEE Transactions on Antennas and Propagation*, 14:302–307, May 1966. `doi:10.1109/TAP.1966.1138693`.

[18] A. Taflove and M. E. Brodwin. Numerical Solution of Steady-State Electromagnetic Scattering Problems Using the Time-Dependent Maxwell's Equations. *IEEE Transactions on Microwave Theory and Techniques*, 23(8):623–630, 1975. `doi:10.1109/TMTT.1975.1128640`.

[19] A. Taflove. Application of the Finite-Difference Time-Domain Method to Sinusoidal Steady-State Electromagnetic-Penetration Problems. *IEEE Transactions on Electromagnetic Compatibility*, EMC-22(3):191–202, 1980. `doi:10.1109/TEMC.1980.303879`.

[20] M. L. Oristaglio and G. W. Hohmann. Diffusion of electromagnetic fields into a two-dimensional earth: A finite-difference approach. *GEOPHYSICS*, 49(7):870–894, 1984. URL: `https://doi.org/10.1190/1.1441733`, `doi:10.1190/1.1441733`.

[21] M. Commer and G. Newman. A parallel finite-difference approach for 3D transient electromagnetic modeling with galvanic sources. *GEOPHYSICS*, 69(5):1192–1202, 2004. URL: `https://doi.org/10.1190/1.1801936`, `doi:10.1190/1.1801936`.

[22] K. Kunz and R. Luebbers. *The Finite Difference Time Domain Method for Electromagnetics*. Taylor & Francis, 1993. URL: `https://books.google.de/books?id=00on9fRvJqIC`.

[23] B. T. DeWitt and W. D. Burnside. Electromagnetic scattering by pyramidal and wedge absorber. *IEEE Transactions on Antennas and Propagation*, 36(7):971–984, 1988. `doi:10.1109/8.7202`.

[24] G. H. Shortley and R. Weller. The Numerical Solution of Laplace's Equation. *Journal of Applied Physics*, 9(5):334–348, 1938. URL: `https://doi.org/10.1063/1.1710426`, `doi:10.1063/1.1710426`.

[25] F. Gibou, R. P. Fedkiw, L.-T. Cheng, and M. Kang. A Second-Order-Accurate Symmetric Discretization of the Poisson Equation on Irregular Domains. *Journal of Computational Physics*, 176(1):205–227, 2002. URL: `https://www.sciencedirect.com/science/article/pii/S0021999101969773`, `doi:https://doi.org/10.1006/jcph.2001.6977`.

[26] Z. Jomaa and C. Macaskill. The embedded finite difference method for the Poisson equation in a domain with an irregular boundary and Dirichlet boundary conditions. *Journal of Computational Physics*, 202(2):488–506, 2005. URL: `https://www.sciencedirect.com/science/article/pii/S0021999104002955`, `doi:https://doi.org/10.1016/j.jcp.2004.07.011`.

[27] R. Kramer, C. Pantano, and D. Pullin. Nondissipative and Energy-Stable High-Order Finite-Difference Interface Schemes for 2-D Patch-Refined Grids. *J. Comput. Phys.*, 228(14):5280–5297, aug 2009. URL: `https://doi.org/10.1016/j.jcp.2009.04.010`, `doi:10.1016/j.jcp.2009.04.010`.

[28] K. Mattsson and M. H. Carpenter. Stable and Accurate Interpolation Operators for High-Order Multiblock Finite Difference Methods. *SIAM Journal on Scientific Computing*, 32(4):2298–2320, 2010. URL: `https://doi.org/10.1137/090750068`, `doi:10.1137/090750068`.

[29] A. Nissen, K. Kormann, M. Grandin, and K. Virta. Stable Difference Methods for Block-Oriented Adaptive Grids. *J. Sci. Comput.*, 65(2):486–511, nov 2015. URL: `https://doi.org/10.1007/s10915-014-9969-z`, `doi:10.1007/s10915-014-9969-z`.

[30] J. C. Nédélec. Mixed finite elements in R3. *Numerische Mathematik*, 35(3):315–341, 1980. URL: `https://doi.org/10.1007/BF01396415`, `doi:10.1007/BF01396415`.

[31] J. C. Nédélec. A new family of mixed finite elements in R3. *Numerische Mathematik*, 50(1):57–81, 1986. URL: `https://doi.org/10.1007/BF01389668`, `doi:10.1007/BF01389668`.

[32] J. B. Davies, F. A. Fernandez, and G. Y. Philippou. Finite Element Analysis of All Modes in Cavities with Circular Symmetry. *IEEE Transactions on Microwave Theory and Techniques*, 30(11):1975–1980, 1982. `doi:10.1109/TMTT.1982.1131353`.

[33] G. Mur. Edge elements, their advantages and their disadvantages. *IEEE Transactions on Magnetics*, 30(5):3552–3557, 1994. `doi:10.1109/20.312706`.

[34] P. Monk. *Finite Element Methods for Maxwell's Equations*. Oxford University Press, Oxford, 2003. URL: `https://www.oxfordscholarship.com/10.1093/acprof:`

```
oso/9780198508885.001.0001/acprof-9780198508885,    doi:10.1093/acprof:
oso/9780198508885.001.0001.
```

[35] G. Mur and A. de Hoop. A finite-element method for computing three-dimensional electromagnetic fields in inhomogeneous media. *IEEE Transactions on Magnetics*, 21(6):2188–2191, 1985. `doi:10.1109/TMAG.1985.1064256`.

[36] J. Jin. *The Finite Element Method in Electromagnetics*. Wiley, 2002. URL: `https://www.wiley.com/en-al/The+Finite+Element+Method+in+Electromagnetics%2C+3rd+Edition-p-9781118841983`.

[37] J. Jin and D. Riley. *Finite Element Analysis of Antennas and Arrays*. Wiley - IEEE. Wiley, 2009. URL: `https://www.wiley.com/en-al/Finite+Element+Analysis+of+Antennas+and+Arrays-p-9780470409725`.

[38] O. Biro and K. Preis. On the use of the magnetic vector potential in the finite-element analysis of three-dimensional eddy currents. *IEEE Transactions on Magnetics*, 25(4):3145–3159, 1989. `doi:10.1109/20.34388`.

[39] A. Napolitano, S. Ferracin, R. Gerbaldo, G. Ghigo, L. Gozzelino, D. Torsello, and F. Laviano. Multiphysics simulation of a superconducting bolometer working in a portable cryostat. *Journal of Physics: Conference Series*, 1559:012019, 2020. URL: `https://doi.org/10.1088/1742-6596/1559/1/012019`, `doi:10.1088/1742-6596/1559/1/012019`.

[40] W. H. Reed and T. R. Hill. Triangular mesh methods for the neutron transport equation, 1973. URL: `https://www.osti.gov/biblio/4491151`.

[41] D. N. Arnold, F. Brezzi, B. Cockburn, and L. D. Marini. Unified Analysis of Discontinuous Galerkin Methods for Elliptic Problems. *SIAM J. Numer. Anal.*, 39(5):1749–1779, 2001. URL: `https://doi.org/10.1137/S0036142901384162`, `doi:10.1137/S0036142901384162`.

[42] P.-O. Persson, J. Bonet, and J. Peraire. Discontinuous Galerkin solution of the Navier–Stokes equations on deformable domains. *Computer Methods in Applied Mechanics and Engineering*, 198(17):1585–1595, 2009. URL: `https://www.sciencedirect.com/science/article/pii/S0045782509000450`, `doi:https://doi.org/10.1016/j.cma.2009.01.012`.

[43] M. Restelli and F. X. Giraldo. A Conservative Discontinuous Galerkin Semi-Implicit Formulation for the Navier–Stokes Equations in Nonhydrostatic Mesoscale Modeling. *SIAM Journal on Scientific Computing*, 31(3):2231–2257, 2009. URL: `https://doi.org/10.1137/070708470`, `doi:10.1137/070708470`.

[44] B. Krank, N. Fehn, W. A. Wall, and M. Kronbichler. A high-order semi-explicit discontinuous Galerkin solver for 3D incompressible flow with application to DNS and LES of turbulent channel flow. *Journal of Computational Physics*,

348:634–659, 2017. URL: `https://www.sciencedirect.com/science/article/pii/S0021999117305478`, `doi:https://doi.org/10.1016/j.jcp.2017.07.039`.

[45] N. Fehn, W. A. Wall, and M. Kronbichler. A matrix-free high-order discontinuous Galerkin compressible Navier-Stokes solver: A performance comparison of compressible and incompressible formulations for turbulent incompressible flows. *International Journal for Numerical Methods in Fluids*, 89(3):71–102, 2019. URL: `https://onlinelibrary.wiley.com/doi/abs/10.1002/fld.4683`, `doi:https://doi.org/10.1002/fld.4683`.

[46] J. Hesthaven and T. Warburton. Nodal High-Order Methods on Unstructured Grids: I. Time-Domain Solution of Maxwell's Equations. *Journal of Computational Physics*, 181(1):186–221, 2002. URL: `https://www.sciencedirect.com/science/article/pii/S0021999102971184`, `doi:https://doi.org/10.1006/jcph.2002.7118`.

[47] J. S. Hesthaven and T. Warburton. High-order nodal discontinuous Galerkin methods for the Maxwell eigenvalue problem. *Philosophical Transactions of the Royal Society of London. Series A: Mathematical, Physical and Engineering Sciences*, 362(1816):493–524, 2004. URL: `https://royalsocietypublishing.org/doi/abs/10.1098/rsta.2003.1332`, `doi:10.1098/rsta.2003.1332`.

[48] L. Fezoui, S. Lanteri, S. Lohrengel, and S. Piperno. Convergence and stability of a discontinuous Galerkin time-domain method for the 3D heterogeneous Maxwell equations on unstructured meshes. *ESAIM: M2AN*, 39(6):1149–1176, 2005. URL: `https://doi.org/10.1051/m2an:2005049`, `doi:10.1051/m2an:2005049`.

[49] P. Houston, I. Perugia, and D. Schotzau. Mixed Discontinuous Galerkin Approximation of the Maxwell Operator. *SIAM Journal on Numerical Analysis*, 42(1):434–459, 2004. URL: `https://doi.org/10.1137/S003614290241790X`, `doi:10.1137/S003614290241790X`.

[50] B. Cockburn, F. Li, and C.-W. Shu. Locally divergence-free discontinuous Galerkin methods for the Maxwell equations. *Journal of Computational Physics*, 194(2):588–610, 2004. URL: `https://www.sciencedirect.com/science/article/pii/S0021999103004960`, `doi:https://doi.org/10.1016/j.jcp.2003.09.007`.

[51] H. Fahs and S. Lanteri. A high-order non-conforming discontinuous Galerkin method for time-domain electromagnetics. *Journal of Computational and Applied Mathematics*, 234(4):1088–1096, 2010. URL: `https://www.sciencedirect.com/science/article/pii/S0377042709003070`, `doi:https://doi.org/10.1016/j.cam.2009.05.015`.

[52] B. Cockburn and J. Gopalakrishnan. New hybridization techniques. *GAMM-Mitteilungen*, 28(2):154–182, 2005. URL: `https://onlinelibrary.wiley.com/doi/abs/10.1002/gamm.201490017`, `doi:https://doi.org/10.1002/gamm.201490017`.

[53] B. Cockburn, B. Dong, and J. Guzmán. A Superconvergent LDG-Hybridizable Galerkin Method for Second-Order Elliptic Problems. *Mathematics of Computation*, 77(264):1887–1916, 2008. URL: http://www.jstor.org/stable/40234595.

[54] B. Cockburn, J. Gopalakrishnan, and R. Lazarov. Unified Hybridization of Discontinuous Galerkin, Mixed, and Continuous Galerkin Methods for Second Order Elliptic Problems. *SIAM Journal on Numerical Analysis*, 47(2):1319–1365, 2009. URL: https://doi.org/10.1137/070706616, doi:10.1137/070706616.

[55] R. M. Kirby, S. J. Sherwin, and B. Cockburn. To CG or to HDG: A Comparative Study. 51:183–212, 2012. URL: https://doi.org/10.1007/s10915-011-9501-7, doi:10.1007/s10915-011-9501-7.

[56] S. Yakovlev, D. Moxey, R. M. Kirby, and S. J. Sherwin. To CG or to HDG: A Comparative Study in 3D. *Journal of Scientific Computing*, 67(1):192–220, Apr 2016. URL: https://doi.org/10.1007/s10915-015-0076-6, doi:10.1007/s10915-015-0076-6.

[57] M. Giacomini, A. Karkoulias, R. Sevilla, and A. Huerta. A Superconvergent HDG Method for Stokes Flow with Strongly Enforced Symmetry of the Stress Tensor. *Journal of Scientific Computing*, 77:1679–1702, 2018.

[58] A. La Spina, M. Giacomini, and A. Huerta. Hybrid coupling of CG and HDG discretizations based on Nitsche's method. *Computational Mechanics*, pages 1432–0924, 2019. URL: https://doi.org/10.1007/s00466-019-01770-8, doi:10.1007/s00466-019-01770-8.

[59] G. Nehmetallah, S. Lanteri, S. Descombes, and A. Christophe. An Explicit Hybridizable Discontinuous Galerkin Method for the 3D Time-Domain Maxwell Equations. In S. J. Sherwin, D. Moxey, J. Peiró, P. E. Vincent, and C. Schwab, editors, *Spectral and High Order Methods for Partial Differential Equations ICOSAHOM 2018*, pages 513–523, Cham, 2020. Springer International Publishing.

[60] B. Cockburn, J. Gopalakrishnan, and F.-J. Sayas. A projection-based error analysis of HDG methods. *Mathematics of Computation*, 79:1351–1367, 2010. URL: https://www.ams.org/journals/mcom/2010-79-271/S0025-5718-10-02334-3, doi:https://doi.org/10.1090/S0025-5718-10-02334-3.

[61] R. Sevilla and A. Huerta. HDG-NEFEM with Degree Adaptivity for Stokes Flows. *Journal of Scientific Computing*, 77:1953–1980, 2018. URL: https://doi.org/10.1007/s10915-018-0657-2, doi:10.1007/s10915-018-0657-2.

[62] S. Schoeder, M. Kronbichler, and W. A. Wall. Arbitrary High-Order Explicit Hybridizable Discontinuous Galerkin Methods for the Acoustic Wave Equation. *Journal of Scientific Computing*, 76:969–1006, August 2018. URL: https://doi.org/10.1007/s10915-018-0649-2, doi:10.1007/s10915-018-0649-2.

[63] F. Vidal-Codina, N. Nguyen, S.-H. Oh, and J. Peraire. A hybridizable discontinuous Galerkin method for computing nonlocal electromagnetic effects in three-dimensional metallic nanostructures. *Journal of Computational Physics*, 355:548–565, 2018. URL: `https://www.sciencedirect.com/science/article/pii/S002199911730863X`, `doi:https://doi.org/10.1016/j.jcp.2017.11.025`.

[64] L. Li, S. Lanteri, and R. Perrussel. A Hybridizable Discontinuous Galerkin Method for Solving 3D Time-Harmonic Maxwell's Equations. In A. Cangiani, R. L. Davidchack, E. Georgoulis, A. N. Gorban, J. Levesley, and M. V. Tretyakov, editors, *Numerical Mathematics and Advanced Applications 2011*, pages 119–128, Berlin, Heidelberg, 2013. Springer Berlin Heidelberg.

[65] L. Li, S. Lanteri, and R. Perrussel. A Hybridizable Discontinuous Galerkin Method Combined to a Schwarz Algorithm for the Solution of 3d Time-Harmonic Maxwell's Equation. *J. Comput. Phys.*, 256(C):563–581, 2014.

[66] N. Nguyen, J. Peraire, and B. Cockburn. Hybridizable discontinuous Galerkin methods for the time-harmonic Maxwell's equations. *Journal of Computational Physics*, 230(19):7151 – 7175, 2011. URL: `http://www.sciencedirect.com/science/article/pii/S0021999111003226`, `doi:https://doi.org/10.1016/j.jcp.2011.05.018`.

[67] A. Christophe, S. Descombes, and S. Lanteri. An implicit hybridized discontinuous Galerkin method for the 3D time-domain Maxwell equations. *Applied Mathematics and Computation*, 319:395 – 408, 2018. URL: `http://www.sciencedirect.com/science/article/pii/S0096300317302758`, `doi:https://doi.org/10.1016/j.amc.2017.04.023`.

[68] L. Berardocco, M. Kronbichler, and V. Gravemeier. A hybridizable discontinuous Galerkin method for electromagnetics with a view on subsurface applications. *Computer Methods in Applied Mechanics and Engineering*, 366:113071, 2020. URL: `http://www.sciencedirect.com/science/article/pii/S0045782520302553`, `doi:https://doi.org/10.1016/j.cma.2020.113071`.

[69] L. Berardocco, M. Kronbichler, and V. Gravemeier. A hybridizable discontinuous Galerkin time-domain method for simulating three-dimensional electromagnetic diffusion in earth. *In preparation*, 2021.

[70] H. Inoue, Y. Fukao, K. Tanabe, and Y. Ogata. Whole mantle P-wave travel time tomography. *Physics of the Earth and Planetary Interiors*, 59(4):294–328, 1990. URL: `https://www.sciencedirect.com/science/article/pii/003192019090236Q`, `doi:https://doi.org/10.1016/0031-9201(90)90236-Q`.

[71] D. Zhao, A. Hasegawa, and S. Horiuchi. Tomographic imaging of P and S wave velocity structure beneath northeastern Japan. *Journal of Geophysical Research: Solid Earth*, 97(B13):19909–19928, 1992. URL: `https://agupubs.onlinelibrary.wiley.com/doi/abs/10.1029/92JB00603`, `doi:https://doi.org/10.1029/92JB00603`.

[72] M. K. Salah. Upper crustal structure beneath Southwest Iberia north of the convergent boundary between the Eurasian and African plates. *Geoscience Frontiers*, 5(6):845–854, 2014. URL: `https://www.sciencedirect.com/science/article/pii/S1674987113001369`, `doi:https://doi.org/10.1016/j.gsf.2013.10.002`.

[73] J. H. Coggon and H. F. Morrison. ELECTROMAGNETIC INVESTIGATION OF THE SEA FLOOR. *GEOPHYSICS*, 35(3):476–489, 1970. URL: `https://doi.org/10.1190/1.1440109`, `doi:10.1190/1.1440109`.

[74] A. D. Chave, S. C. Constable, and R. N. Edwards. *12. Electrical Exploration Methods for the Seafloor*, pages 931–966. 2012. URL: `https://library.seg.org/doi/abs/10.1190/1.9781560802686.ch12`, `doi:10.1190/1.9781560802686.ch12`.

[75] A. G. Jones. Static shift of magnetotelluric data and its removal in a sedimentary basin environment. *GEOPHYSICS*, 53(7):967–978, 1988. URL: `https://doi.org/10.1190/1.1442533`, `doi:10.1190/1.1442533`.

[76] M. N. Nabighian, editor. *Electromagnetic Methods in Applied Geophysics: Volume 1, Theory*. Society of Exploration Geophysicists, 1988.

[77] M. N. Nabighian and J. C. Macnae. TIME DOMAIN ELECTROMAGNETIC PROSPECTING METHODS. In *Electromagnetic Methods in Applied Geophysics: Volume 2, Application, Parts A and B*. Society of Exploration Geophysicists, 1991. URL: `https://doi.org/10.1190/1.9781560802686.ch6`, `doi:10.1190/1.9781560802686.ch6`.

[78] A. Hibbs, T. Petrov, J. Pendleton, S. Milberger, G. Eiskamp, and G. A. Wilson. *New electromagnetic sensors for magnetotelluric and induced polarization geophysical surveys*, pages 1–5. 2012. URL: `https://library.seg.org/doi/abs/10.1190/segam2012-1478.1`, `doi:10.1190/segam2012-1478.1`.

[79] Nabighian, Misac N. Time-domain electromagnetic methods of exploration; foreword and introduction. *Geophysics*, 49(7):849–853, 1984. URL: `https://doi.org/10.1190/1.1441730`, `doi:10.1190/1.1441730`.

[80] W. L. Anderson. Calculation of transient soundings for a central induction loop system (Program TCILOOP). Technical report, U.S. Geological Survey, 1981. URL: `http://pubs.er.usgs.gov/publication/ofr811309`, `doi:10.3133/ofr811309`.

[81] Anderson, W.L. Nonlinear least-squares inversion of transient soundings for a central induction loop system (program NLSTCI). Technical report, U.S. Geological Survey, 1982. URL: `http://pubs.er.usgs.gov/publication/ofr821129`, `doi:10.3133/ofr821129`.

[82] G. A. Newman, G. W. Hohmann, and W. L. Anderson. Transient electromagnetic response of a three-dimensional body in a layered earth. *GEOPHYSICS*, 51(8):1608–1627, 1986. URL: `https://doi.org/10.1190/1.1442212`, `doi:10.1190/1.1442212`.

[83] G. A. Newman and D. L. Alumbaugh. Frequency-domain modelling of airborne electromagnetic responses using staggered finite differences. *Geophysical Prospecting*, 43(8):1021–1042, 1995. URL: `https://onlinelibrary.wiley.com/doi/abs/10.1111/j.1365-2478.1995.tb00294.x`, `doi:https://doi.org/10.1111/j.1365-2478.1995.tb00294.x`.

[84] Y. Li and K. Spitzer. Three-dimensional DC resistivity forward modelling using finite elements in comparison with finite-difference solutions. *Geophysical Journal International*, 151(3):924–934, 2002. URL: `https://doi.org/10.1046/j.1365-246X.2002.01819.x`, `doi:10.1046/j.1365-246X.2002.01819.x`.

[85] L. B. Slichter. An Inverse Boundary Value Problem in Electrodynamics. *Physics*, 4(12):411–418, 1933. URL: `https://doi.org/10.1063/1.1745154`, `doi:10.1063/1.1745154`.

[86] R. E. Langer. An inverse problem in differential equations. *Bullettin of the American Mathematical Society*, 39(10):814–820, 1933. URL: `https://doi.org/10.1090/S0002-9904-1933-05752-X`, `doi:10.1090/S0002-9904-1933-05752-X`.

[87] A. F. Stevenson. On the Theoretical Determination of Earth Resistance from Surface Potential Measurements. *Physics*, 5(4):114–124, 1934. URL: `https://doi.org/10.1063/1.1745237`, `doi:10.1063/1.1745237`.

[88] S. Bukhari and D. Lennox. Geometric coefficients for use in numerical resistivity analysis. *Research Council of Alberta, Bulletin*, 19, 1966. URL: `https://ags.aer.ca/publications/BUL_019.html#summary`.

[89] A. P. Annan. *The equivalent source method for electromagnetic scattering analysis and its geophysical application*. PhD thesis, Memorial University of Newfoundland, 1974.

[90] G. W. Hohmann. THREE-DIMENSIONAL INDUCED POLARIZATION AND ELECTROMAGNETIC MODELING. *GEOPHYSICS*, 40(2):309–324, 1975. URL: `https://doi.org/10.1190/1.1440527`, `doi:10.1190/1.1440527`.

[91] P. E. Wannamaker, G. W. Hohmann, and W. A. SanFilipo. Electromagnetic modeling of three-dimensional bodies in layered earths using integral equations. *GEOPHYSICS*, 49(1):60–74, 1984. URL: `https://doi.org/10.1190/1.1441562`, `doi:10.1190/1.1441562`.

[92] W. A. SanFilipo and G. W. Hohmann. Integral equation solution for the transient electromagnetic response of a three-dimensional body in a conductive half-space. *GEOPHYSICS*, 50(5):798–809, 1985. URL: `https://doi.org/10.1190/1.1441954`, `doi:10.1190/1.1441954`.

[93] D. B. Avdeev, A. V. Kuvshinov, O. V. Pankratov, and G. A. Newman. Three-dimensional induction logging problems, part i: An integral equation solution and

model comparisons. *GEOPHYSICS*, 67(2):413–426, 2002. URL: `https://doi.org/10.1190/1.1468601`, `doi:10.1190/1.1468601`.

[94] A. C. Tripp and G. W. Hohmann. Block Diagonalization of the Electromagnetic Impedance Matrix of a Symmetric Buried Body Using Group Theory. *IEEE Transactions on Geoscience and Remote Sensing*, GE-22(1):62–69, 1984. `doi:10.1109/TGRS.1984.350580`.

[95] A. DEY and H. F. MORRISON. RESISTIVITY MODELLING FOR ARBITRARILY SHAPED TWO-DIMENSIONAL STRUCTURES. *Geophysical Prospecting*, 27(1):106–136, 1979. URL: `https://onlinelibrary.wiley.com/doi/abs/10.1111/j.1365-2478.1979.tb00961.x`, `doi:https://doi.org/10.1111/j.1365-2478.1979.tb00961.x`.

[96] A. Dey and H. F. Morrison. Resistivity modeling for arbitrarily shaped three-dimensional structures. *GEOPHYSICS*, 44(4):753–780, 1979. URL: `https://doi.org/10.1190/1.1440975`, `doi:10.1190/1.1440975`.

[97] T. Lowry, M. B. Allen, and P. N. Shive. Singularity removal: A refinement of resistivity modeling techniques. *GEOPHYSICS*, 54(6):766–774, 1989. URL: `https://doi.org/10.1190/1.1442704`, `doi:10.1190/1.1442704`.

[98] K. Spitzer. A 3-D finite-difference algorithm for DC resistivity modelling using conjugate gradient methods. *Geophysical Journal International*, 123(3):903–914, 1995. URL: `https://onlinelibrary.wiley.com/doi/abs/10.1111/j.1365-246X.1995.tb06897.x`, `doi:https://doi.org/10.1111/j.1365-246X.1995.tb06897.x`.

[99] T. Wang and G. W. Hohmann. A finite-difference, time-domain solution for three-dimensional electromagnetic modeling. *GEOPHYSICS*, 58(6):797–809, 1993. URL: `https://doi.org/10.1190/1.1443465`, `doi:10.1190/1.1443465`.

[100] J. T. Smith. Conservative modeling of 3-D electromagnetic fields, Part I: Properties and error analysis. *GEOPHYSICS*, 61(5):1308–1318, 1996. URL: `https://doi.org/10.1190/1.1444054`, `doi:10.1190/1.1444054`.

[101] J. T. Smith. Conservative modeling of 3-D electromagnetic fields, Part II: Biconjugate gradient solution and an accelerator. *GEOPHYSICS*, 61(5):1319–1324, 1996. URL: `https://doi.org/10.1190/1.1444055`, `doi:10.1190/1.1444055`.

[102] G. A. Newman and D. L. Alumbaugh. Three-dimensional induction logging problems, part 2: A finite-difference solution. *GEOPHYSICS*, 67(2):484–491, 2002. URL: `https://doi.org/10.1190/1.1468608`, `doi:10.1190/1.1468608`.

[103] J. H. Coggon. ELECTROMAGNETIC AND ELECTRICAL MODELING BY THE FINITE ELEMENT METHOD. *GEOPHYSICS*, 36(1):132–155, 1971. URL: `https://doi.org/10.1190/1.1440151`, `doi:10.1190/1.1440151`.

[104] D. F. Pridmore, G. W. Hohmann, S. H. Ward, and W. R. Sill. An investigation of finite-element modeling for electrical and electromagnetic data in three dimensions. *GEOPHYSICS*, 46(7):1009–1024, 1981. URL: `https://doi.org/10.1190/1.1441239`, `doi:10.1190/1.1441239`.

[105] E. S. Um, J. M. Harris, and D. L. Alumbaugh. 3D time-domain simulation of electromagnetic diffusion phenomena: A finite-element electric-field approach. *GEOPHYSICS*, 75(4):F115–F126, 2010. URL: `https://doi.org/10.1190/1.3473694`, `doi:10.1190/1.3473694`.

[106] E. Um, J. Harris, and D. L. Alumbaugh. An iterative finite element time-domain method for simulating three-dimensional electromagnetic diffusion in earth. *Geophysical Journal International*, 190:871–886, 2012. `doi:10.1111/j.1365-246X.2012.05540.x`.

[107] E. Um, M. Commer, G. A. Newman, and G. Hoversten. Finite element modelling of transient electromagnetic fields near steel-cased wells. *Geophysical Journal International*, 202:901–913, 05 2015. `doi:10.1093/gji/ggv193`.

[108] E. Haber. A mixed finite element method for the solution of the magnetostatic problem with highly discontinuous coefficients in 3D. *Computational Geosciences*, 4(4):323–336, 2000. URL: `https://doi.org/10.1023/A:1011540222718`, `doi:10.1023/A:1011540222718`.

[109] Z. Bing and S. A. Greenhalgh. Finite element three dimensional direct current resistivity modelling: accuracy and efficiency considerations. *Geophysical Journal International*, 145(3):679–688, 06 2001. URL: `https://doi.org/10.1046/j.0956-540x.2001.01412.x`, `doi:10.1046/j.0956-540x.2001.01412.x`.

[110] J. Chen, E. Haber, and D. W. Oldenburg. Three-dimensional numerical modelling and inversion of magnetometric resistivity data. *Geophysical Journal International*, 149(3):679–697, 2002. URL: `https://doi.org/10.1046/j.1365-246X.2002.01688.x`, `doi:10.1046/j.1365-246X.2002.01688.x`.

[111] Y. Li and K. Spitzer. Finite element resistivity modelling for three-dimensional structures with arbitrary anisotropy. *Physics of the Earth and Planetary Interiors*, 150(1):15–27, 2005. URL: `https://www.sciencedirect.com/science/article/pii/S0031920104003607`, `doi:https://doi.org/10.1016/j.pepi.2004.08.014`.

[112] N. Vieira da Silva, J. V. Morgan, L. MacGregor, and M. Warner. A finite element multifrontal method for 3D CSEM modeling in the frequency domain. *GEOPHYSICS*, 77(2):E101–E115, 2012. URL: `https://doi.org/10.1190/geo2010-0398.1`, `doi:10.1190/geo2010-0398.1`.

[113] S. Ansari and C. G. Farquharson. 3D finite-element forward modeling of electromagnetic data using vector and scalar potentials and unstructured grids. *GEOPHYSICS*, 79(4):E149–E165, 2014. URL: `https://doi.org/10.1190/geo2013-0172.1`, `doi:10.1190/geo2013-0172.1`.

[114] E. Um, M. Commer, and G. A. Newman. Efficient pre-conditioned iterative solution strategies for the electromagnetic diffusion in the Earth: finite-element frequency-domain approach. *Geophysical Journal International*, 193:1460–1473, 2013. `doi: 10.1093/gji/ggt071`.

[115] J. Rosen. Redundancy and superfluity for electromagnetic fields and potentials. *American Journal of Physics*, 48(12):1071–1073, 1980. URL: `https://doi.org/10.1119/1.12289`, `doi:10.1119/1.12289`.

[116] C.-D. Munz, P. Omnes, R. Schneider, E. Sonnendrücker, and U. Voß. Divergence Correction Techniques for Maxwell Solvers Based on a Hyperbolic Model. *Journal of Computational Physics*, 161(2):484 – 511, 2000. URL: `http://www.sciencedirect.com/science/article/pii/S0021999100965070`, `doi:https://doi.org/10.1006/jcph.2000.6507`.

[117] A. Dedner, F. Kemm, D. Kröner, C.-D. Munz, T. Schnitzer, and M. Wesenberg. Hyperbolic Divergence Cleaning for the MHD Equations. *Journal of Computational Physics*, 175(2):645–673, 2002. URL: `https://www.sciencedirect.com/science/article/pii/S002199910196961X`, `doi:https://doi.org/10.1006/jcph.2001.6961`.

[118] R. N. Edwards, H. Lee, and M. N. Nabighian. On the theory of magnetometric resistivity (MMR) methods. *GEOPHYSICS*, 43(6):1176–1203, 1978. URL: `https://doi.org/10.1190/1.1440887`, `doi:10.1190/1.1440887`.

[119] P. Dular, J.-F. Remacle, F. Henrotte, A. Genon, and W. Legros. Magnetostatic and magnetodynamic mixed formulations compared with conventional formulations. *IEEE Transactions on Magnetics*, 33(2):1302–1305, 1997. `doi:10.1109/20.582494`.

[120] I. Perugia, V. Simoncini, and M. Arioli. Linear algebra methods in a mixed approximation of magnetostatic problems. *SIAM J. Sci. Comput.*, 21(3):1085–1101, 1999.

[121] G. Newman. Crosswell electromagnetic inversion using integral and differential equations. *GEOPHYSICS*, 60(3):899–911, 1995. URL: `https://doi.org/10.1190/1.1443825`, `doi:10.1190/1.1443825`.

[122] M. Paipuri, S. Fernández-Méndez, and C. Tiago. Comparison of high-order continuous and hybridizable discontinuous Galerkin methods for incompressible fluid flow problems. *Mathematics and Computers in Simulation*, 153:35–58, 2018. URL: `https://www.sciencedirect.com/science/article/pii/S0378475418301241`, `doi:https://doi.org/10.1016/j.matcom.2018.05.012`.

[123] M. Kronbichler and W. Wall. A Performance Comparison of Continuous and Discontinuous Galerkin Methods with Fast Multigrid Solvers. *SIAM Journal on Scientific Computing*, 40(5):A3423–A3448, 2018. URL: `https://doi.org/10.1137/16M110455X`, `doi:10.1137/16M110455X`.

[124] G. Giorgiani, S. Fernández-Méndez, and A. Huerta. Hybridizable discontinuous Galerkin p-adaptivity for wave propagation problems. *International Journal for Numerical Methods in Fluids*, 72(12):1244–1262, 2013. URL: `https://onlinelibrary.wiley.com/doi/abs/10.1002/fld.3784`, doi: `https://doi.org/10.1002/fld.3784`.

[125] G. Giorgiani, S. Fernández-Méndez, and A. Huerta. Hybridizable Discontinuous Galerkin with degree adaptivity for the incompressible Navier–Stokes equations. *Computers & Fluids*, 98:196–208, 2014. URL: `https://www.sciencedirect.com/science/article/pii/S0045793014000188`, doi:`https://doi.org/10.1016/j.compfluid.2014.01.011`.

[126] J. Schöberl and S. Zaglmayr. High order Nédélec elements with local complete sequence properties. *COMPEL - The international journal for computation and mathematics in electrical and electronic engineering*, 24:374–384, 2005. URL: `https://doi.org/10.1108/03321640510586015`, doi:`10.1108/03321640510586015`.

[127] C. Lehrenfeld and J. Schöberl. High order exactly divergence-free Hybrid Discontinuous Galerkin Methods for unsteady incompressible flows. *Computer Methods in Applied Mechanics and Engineering*, 307:339–361, 2016. URL: `https://www.sciencedirect.com/science/article/pii/S004578251630264X`, doi:`https://doi.org/10.1016/j.cma.2016.04.025`.

[128] M. Kronbichler, S. Schoeder, C. Müller, and W. A. Wall. Comparison of implicit and explicit hybridizable discontinuous Galerkin methods for the acoustic wave equation. *International Journal for Numerical Methods in Engineering*, 106(9):712–739, 2016. URL: `https://onlinelibrary.wiley.com/doi/abs/10.1002/nme.5137`, doi:`https://doi.org/10.1002/nme.5137`.

[129] M. Kronbichler and K. Kormann. A generic interface for parallel cell-based finite element operator application. *Computers & Fluids*, 63:135–147, 2012. URL: `https://www.sciencedirect.com/science/article/pii/S0045793012001429`, doi:`https://doi.org/10.1016/j.compfluid.2012.04.012`.

[130] A. T. Barker and T. Kolev. Matrix-free preconditioning for high-order H(curl) discretizations. *Numerical Linear Algebra with Applications*, 28(2):e2348, 2021. URL: `https://onlinelibrary.wiley.com/doi/abs/10.1002/nla.2348`, doi:`https://doi.org/10.1002/nla.2348`.

[131] M. Kronbichler and K. Kormann. Fast Matrix-Free Evaluation of Discontinuous Galerkin Finite Element Operators. *ACM Trans. Math. Softw.*, 45(3), aug 2019. URL: `https://doi.org/10.1145/3325864`, doi:`10.1145/3325864`.

[132] F. Byron and R. Fuller. *Mathematics of Classical and Quantum Physics.* Number v. 1-2 in Dover books on physics and chemistry. Dover Publications, 1992.

[133] P. Dennery and A. Krzywicki. *Mathematics for Physicists.* Dover Books on Physics. Dover Publications, 2012.

[134] P. Bettess and O. C. Zienkiewicz. Diffraction and refraction of surface waves using finite and infinite elements. *International Journal for Numerical Methods in Engineering*, 11(8):1271–1290, 1977. URL: `https://onlinelibrary.wiley.com/doi/abs/10.1002/nme.1620110808`, `doi:https://doi.org/10.1002/nme.1620110808`.

[135] R. J. Astley. Wave envelope and infinite elements for acoustical radiation. *International Journal for Numerical Methods in Fluids*, 3(5):507–526, 1983. URL: `https://onlinelibrary.wiley.com/doi/abs/10.1002/fld.1650030506`, `doi:https://doi.org/10.1002/fld.1650030506`.

[136] L. Demkowicz and M. Pal. An infinite element for Maxwell's equations. *Computer Methods in Applied Mechanics and Engineering*, 164(1):77–94, 1998. Exterior Problems of Wave Propagation. URL: `https://www.sciencedirect.com/science/article/pii/S0045782598000474`, `doi:https://doi.org/10.1016/S0045-7825(98)00047-4`.

[137] G. Bunting, A. Prakash, T. Walsh, and C. Dohrmann. Parallel Ellipsoidal Perfectly Matched Layers for Acoustic Helmholtz Problems on Exterior Domains. *Journal of Theoretical and Computational Acoustics*, 26(02):1850015, 2018. URL: `https://doi.org/10.1142/S2591728518500159`, `doi:10.1142/S2591728518500159`.

[138] B. Engquist and A. Majda. Absorbing Boundary Conditions for the Numerical Simulation of Waves. *Mathematics of Computation*, 31(139):629–651, 1977. URL: `http://www.jstor.org/stable/2005997`.

[139] H. Barucq, F. Delaurens, and B. Hanouzet. Method of Absorbing Boundary Conditions: Phenomena of Error Stabilization. *SIAM Journal on Numerical Analysis*, 35(3):1113–1129, 1998. URL: `http://www.jstor.org/stable/2587124`.

[140] M. Stanglmeier, N. Nguyen, J. Peraire, and B. Cockburn. An explicit hybridizable discontinuous Galerkin method for the acoustic wave equation. *Computer Methods in Applied Mechanics and Engineering*, 300:748 – 769, 2016. URL: `http://www.sciencedirect.com/science/article/pii/S0045782515003941`, `doi:https://doi.org/10.1016/j.cma.2015.12.003`.

[141] U. Ascher and L. Petzold. *Computer methods for ordinary differential equations and differential-algebraic equations*. Society for Industrial and Applied Mathematics, 1998.

[142] E. Haber, U. M. Ascher, and D. W. Oldenburg. Inversion of 3D electromagnetic data in frequency and time domain using an inexact all-at-once approach. *GEOPHYSICS*, 69(5):1216–1228, 2004. URL: `https://doi.org/10.1190/1.1801938`, `doi:10.1190/1.1801938`.

[143] T. F. Chan, W. Wang, and L. L. Lai. Performance of an Axial-Flux Permanent Magnet Synchronous Generator From 3-D Finite-Element Analysis. *IEEE Transactions on Energy Conversion*, 25(3):669–676, 2010. `doi:10.1109/TEC.2010.2042057`.

[144] T. Oliphant. NumPy: A guide to NumPy. USA: Trelgol Publishing, 2006. URL: `http://www.numpy.org/`.

[145] J. Cooley and J. W. Tukey. An algorithm for the machine calculation of complex Fourier series. *Mathematics of Computation*, 19:297–301, 1965.

[146] H. Barucq and B. Hanouzet. Asymptotic behavior of solutions to Maxwell's system in bounded domains with absorbing Silver–Müller's condition on the exterior boundary. *Asymptotic Analysis*, 15:25– 40, 1997. `doi:10.3233/ASY-1997-15102`.

[147] B. Hanouzet and M. Sesques. *Absorbing Boundary Conditions for Maxwell's Equations*, pages 315–322. Vieweg+Teubner Verlag, Wiesbaden, 1993. URL: `https://doi.org/10.1007/978-3-322-87871-7_37`, `doi:10.1007/978-3-322-87871-7_37`.

[148] M. Riedl. *Optical Design Fundamentals for Infrared Systems*. SPIE tutorial texts. SPIE Press, 2001. URL: `https://spie.org/Publications/Book/412729`.

[149] N. Nguyen, J. Peraire, and B. Cockburn. High-order implicit hybridizable discontinuous Galerkin methods for acoustics and elastodynamics. *Journal of Computational Physics*, 230(10):3695 – 3718, 2011. URL: `http://www.sciencedirect.com/science/article/pii/S002199911100060X`, `doi:https://doi.org/10.1016/j.jcp.2011.01.035`.

[150] E. Anderson, Z. Bai, C. Bischof, S. Blackford, J. Demmel, J. Dongarra, J. Du Croz, A. Greenbaum, S. Hammarling, A. McKenney, and D. Sorensen. *LAPACK Users' Guide*. Society for Industrial and Applied Mathematics, Philadelphia, PA, third edition, 1999.

[151] T. Trilinos Project Team. *The Trilinos Project Website*, 2020 (acccessed May 22, 2020). URL: `https://trilinos.github.io`.

[152] A. Milani and A. M. Nobili. Integration error over very long time spans. *Celestial mechanics*, 43:1–34, 1987. URL: `https://doi.org/10.1007/BF01234550`, `doi:10.1007/BF01234550`.

[153] A. Arakawa. Computational design for long-term numerical integration of the equations of fluid motion: Two-dimensional incompressible flow. Part I. *Journal of Computational Physics*, 1(1):119–143, 1966. URL: `https://www.sciencedirect.com/science/article/pii/0021999166900155`, `doi:https://doi.org/10.1016/0021-9991(66)90015-5`.

[154] V. Naulin and A. H. Nielsen. Accuracy of Spectral and Finite Difference Schemes in 2D Advection Problems. *SIAM Journal on Scientific Computing*, 25(1):104–126, 2003. URL: `https://doi.org/10.1137/S1064827502405070`, `doi:10.1137/S1064827502405070`.

[155] C. Canuto, M. Hussaini, A. Quarteroni, and J. Thomas A. *Spectral Methods in Fluid Dynamics*. Scientific Computation. Springer Berlin Heidelberg, 2012. URL: `https://link.springer.com/book/10.1007/978-3-642-84108-8`, `doi:https://doi.org/10.1007/978-3-642-84108-8`.

[156] M. Kraus and O. Maj. Variational integrators for nonvariational partial differential equations. *Physica D: Nonlinear Phenomena*, 310:37–71, 2015. URL: `https://www.sciencedirect.com/science/article/pii/S0167278915001499`, `doi:https://doi.org/10.1016/j.physd.2015.08.002`.

[157] M. Kraus, K. Kormann, P. Morrison, and E. Sonnendrücker. GEMPIC: geometric electromagnetic particle-in-cell methods. *Journal of Plasma Physics*, 83(4):905830401, 2017. `doi:10.1017/S002237781700040X`.

[158] K. Kormann and E. Sonnendrücker. Energy-conserving time propagation for a structure-preserving particle-in-cell Vlasov–Maxwell solver. *Journal of Computational Physics*, 425:109890, 2021. URL: `https://www.sciencedirect.com/science/article/pii/S0021999120306641`, `doi:https://doi.org/10.1016/j.jcp.2020.109890`.

[159] J. M. Hoermann, C. Bertoglio, M. Kronbichler, M. R. Pfaller, R. Chabiniok, and W. A. Wall. An adaptive hybridizable discontinuous Galerkin approach for cardiac electrophysiology. *International Journal for Numerical Methods in Biomedical Engineering*, 34(5):e2959, 2018. URL: `https://onlinelibrary.wiley.com/doi/abs/10.1002/cnm.2959`, `doi:https://doi.org/10.1002/cnm.2959`.

[160] J. H. Wilkinson. *The algebraic eigenvalue problem*. Clarendon Press, 1988.

[161] E. D'Azevedo, P. Forsyth, and W. Tang. Towards a cost-effective ILU preconditioner with high level fill. *BIT Numerical Mathematics*, 32:442–463, 1992.

[162] O. Axelsson. *Solution of linear systems of equations: Iterative methods.*, volume 572. Springer, Berlin, Heidelberg., 1977. `doi:https://doi.org/10.1007/BFb0116614`.

[163] E. E. Osborne. On Pre-Conditioning of Matrices. *J. ACM*, 7(4):338–345, 1960. URL: `https://doi.org/10.1145/321043.321048`, `doi:10.1145/321043.321048`.

[164] T.-Y. Chen and J. W. Demmel. Balancing sparse matrices for computing eigenvalues. *Linear Algebra and its Applications*, 309(1):261–287, 2000. URL: `https://www.sciencedirect.com/science/article/pii/S0024379500000148`, `doi:https://doi.org/10.1016/S0024-3795(00)00014-8`.

[165] J. Meijerink and H. Vorst. An iterative solution method for linear systems of which the coefficient matrix is a symmetric -matrix. *Mathematics of Computation*, 31:148–162, 1977.

[166] T. A. Manteuffel. Incomplete factorization technique for positive definite linear systems. *Mathematics of Computation*, 34:473–497, 1980. URL: `https://www.osti.gov/biblio/5346805`, `doi:10.1090/S0025-5718-1980-0559197-0`.

[167] J. Wallis. Incomplete Gaussian Elimination as a Preconditioning for Generalized Conjugate Gradient Acceleration. volume All Days of *SPE Reservoir Simulation Conference*, 1983. URL: `https://doi.org/10.2118/12265-MS`, `doi:10.2118/12265-MS`.

[168] P. Wesseling and C. Oosterlee. Geometric multigrid with applications to computational fluid dynamics. *Journal of Computational and Applied Mathematics*, 128(1):311–334, 2001. URL: `https://www.sciencedirect.com/science/article/pii/S0377042700005173`, `doi:https://doi.org/10.1016/S0377-0427(00)00517-3`.

[169] K. Stüben. A review of algebraic multigrid. *Journal of Computational and Applied Mathematics*, 128(1):281–309, 2001. URL: `https://www.sciencedirect.com/science/article/pii/S0377042700005161`, `doi:https://doi.org/10.1016/S0377-0427(00)00516-1`.

[170] H. P. Langtangen. Conjugate gradient methods and ILU preconditioning of non-symmetric matrix systems with arbitrary sparsity patterns. *International Journal for Numerical Methods in Fluids*, 9(2):213–233, 1989. URL: `https://onlinelibrary.wiley.com/doi/abs/10.1002/fld.1650090207`, `doi:https://doi.org/10.1002/fld.1650090207`.

[171] R. Fang, M. Kronbichler, M. Wurzer, and W. A. Wall. Parallel, physics-oriented, monolithic solvers for three-dimensional, coupled finite element models of lithium-ion cells. *Computer Methods in Applied Mechanics and Engineering*, 350:803–835, 2019. URL: `https://www.sciencedirect.com/science/article/pii/S004578251930146X`, `doi:https://doi.org/10.1016/j.cma.2019.03.017`.

[172] Y. Saad and M. H. Schultz. GMRES: A Generalized Minimal Residual Algorithm for Solving Nonsymmetric Linear Systems. *SIAM Journal on Scientific and Statistical Computing*, 7(3):856–869, 1986. URL: `https://doi.org/10.1137/0907058`, `doi:10.1137/0907058`.

[173] J. Chung and G. M. Hulbert. A Time Integration Algorithm for Structural Dynamics With Improved Numerical Dissipation: The Generalized-α Method. *Journal of Applied Mechanics*, 60(2):371–375, 1993. URL: `https://doi.org/10.1115/1.2900803`, `doi:10.1115/1.2900803`.

[174] K. E. Jansen, C. H. Whiting, and G. M. Hulbert. A generalized-α method for integrating the filtered Navier–Stokes equations with a stabilized finite element method. *Computer Methods in Applied Mechanics and Engineering*, 190(3):305–319, 2000. URL: `https://www.sciencedirect.com/science/article/pii/S0045782500002036`, `doi:https://doi.org/10.1016/S0045-7825(00)00203-6`.

[175] V. Gravemeier, M. W. Gee, M. Kronbichler, and W. A. Wall. An algebraic variational multiscale–multigrid method for large eddy simulation of turbulent

flow. *Computer Methods in Applied Mechanics and Engineering*, 199(13):853–864, 2010. URL: `https://www.sciencedirect.com/science/article/pii/S0045782509002059`, `doi:https://doi.org/10.1016/j.cma.2009.05.017`.

[176] G. G. Dahlquist, W. Liniger, and O. Nevanlinna. Stability of Two-Step Methods for Variable Integration Steps. *SIAM Journal on Numerical Analysis*, 20(5):1071–1085, 1983. URL: `https://doi.org/10.1137/0720076`, `doi:10.1137/0720076`.

[177] R. D. Grigorieff. Stability of Multistep-Methods on Variable Grids. *Numer. Math.*, 42(3):359–377, oct 1983. URL: `https://doi.org/10.1007/BF01389580`, `doi:10.1007/BF01389580`.

[178] P. M. Knupp. Algebraic mesh quality metrics for unstructured initial meshes. *Finite Elements in Analysis and Design*, 39(3):217–241, 2003. URL: `https://www.sciencedirect.com/science/article/pii/S0168874X02000707`, `doi:https://doi.org/10.1016/S0168-874X(02)00070-7`.

[179] Sandia Corporation. Cubit 13.2. https://cubit.sandia.gov/, 3023.

[180] X. S. Li and J. W. Demmel. SuperLU_DIST: A scalable distributed-memory sparse direct solver for unsymmetric linear systems. *ACM Trans. Mathematical Software*, 29(2):110–140, 2003.

[181] B. Cockburn, O. Dubois, J. Gopalakrishnan, and S. Tan. Multigrid for an HDG method. *IMA Journal of Numerical Analysis*, 34(4):1386–1425, 2013. URL: `https://doi.org/10.1093/imanum/drt024`, `doi:10.1093/imanum/drt024`.

[182] D. A. Patterson and J. L. Hennessy. *Computer Organization and Design, Fifth Edition: The Hardware/Software Interface*. Morgan Kaufmann Publishers Inc., San Francisco, CA, USA, 5th edition, 2013.

[183] U. M. Ascher, S. J. Ruuth, and R. J. Spiteri. Implicit-explicit Runge-Kutta methods for time-dependent partial differential equations. *Applied Numerical Mathematics*, 25(2):151–167, 1997. URL: `https://www.sciencedirect.com/science/article/pii/S0168927497000561`, `doi:https://doi.org/10.1016/S0168-9274(97)00056-1`.

[184] F. Zhang. *The Schur Complement and its Applications*, volume 4 of *Numerical Methods and Algorithms*. Springer, New York, 2005. `doi:10.1007/b105056`.

[185] T. Cormen, C. Leiserson, R. Rivest, and C. Stein. *Introduction To Algorithms*. Introduction to Algorithms. MIT Press, 2001.